THE UNIVERSITY *of* EDINBURGH

X-ray Constraints on the Population of High-redshift Active Galactic Nuclei and prospects with NewAthena

Cassandra Louise Barlow-Hall

Doctor of Philosophy
The University of Edinburgh
August 2024

Lay Summary

Our Universe is vast, containing billions of galaxies, made of trillions of stars much like our own Sun and extending far beyond our reach. Yet we can learn much from studying the cosmos, through the lens of Astrophysics, to better understand how the vastness in which we live came to be.

Amongst the most mysterious of objects within the Universe are black holes; astronomical sources which are so dense that not even light, the fastest thing in the Universe, can escape their gravitational pull. At the centre of every galaxy, including our own Milky Way Galaxy, resides a massive black hole. Such black holes are known as Supermassive Black Holes and likely helped to shape the galaxies they are in. These Supermassive Black Holes grow through the accumulation of matter that has been pulled down onto their surface by an extremely high gravitational force. As this matter is drawn towards the black hole, it releases large amounts of energy across many wavelengths of light. When a Supermassive Black Hole grows very quickly, a huge amount of light is generate by the in-falling matter. We call this an Active Galactic Nucleus.

Active Galactic Nuclei power the emission of X-rays in particular, typically enough to outshine their galaxy. Thus, Astrophysicists often use X-ray Telescopes to find Active Galactic Nuclei.

Exactly how Supermassive Black Holes were able to grow to the extreme mass we have measured, whilst the Universe was still very young, remains a mystery. By understanding the numbers of Active Galactic Nuclei in existence at such early epochs, we can begin to understand how these Supermassive Black Holes grew and the impact they would have had on each galaxy that hosts them. This forms the focus of my thesis and the work contained therein. Using X-ray images of the distant, early Universe and information about galaxies that have been found at such early times, I push the limits of our current X-ray telescopes in order to

determine the population of Active Galactic Nuclei.

Using this population of Active Galactic Nuclei, I can mathematically predict the number of quickly growing Supermassive Black Holes that will be found by the European Space Agency's next big X-ray telescope, NewAthena.

Abstract

Supermassive Black Holes (SMBHs) play an important role within their host galaxies, however little is known about their initial formation and growth. X-ray luminosity functions (XLFs) of actively accreting SMBHs, known as Active Galactic Nuclei (AGN), trace the growth and evolution of SMBH populations across cosmic time. However, due to limitations in survey depth and sky area with current telescopes, current XLF models are poorly constrained at redshifts of $z > 4$, until now. This thesis presents new measurements of the high-redshift XLF, using Swift-XRT, Chandra and looking to the future with NewAthena.

I place limits on the bright-end of the XLF at $z = 5.7 - 6.4$ using high-redshift AGN identified within the Extragalactic Serendipitous Swift Survey (ExSeSS), covering $\sim 2000\,\mathrm{deg}^2$. Within ExSeSS I find one spectroscopically confirmed, serendipitously X-ray detected $z > 6$ AGN, with an X-ray luminosity of $L_X = 8.47^{+3.40}_{-3.13} \times 10^{44}\,\mathrm{erg\,s^{-1}}$ and $z = 6.31 \pm 0.03$, and calculate an upper limit on the space density at higher luminosities where no additional sources are found, with which I place constraints on the shape of the XLF. These results are consistent with the rapid decline in the space densities of high-luminosity AGN. I also find these X-ray based measurements are consistent with estimates of the bolometric quasar luminosity function based on UV measurements at $z \gtrsim 6$, although a large X-ray to bolometric correction factor is required at these high luminosities.

I performed measurements of the $z = 4 - 10$ XLF at intermediate luminosities, using deep Chandra observations of X-ray selected AGN within the COSMOS2020 galaxy survey. I first performed a cross-match to a deep Chandra source list, for which the X-ray sensitivity can be accurately quantified, before exploiting the available X-ray data further through direct extraction of X-ray counts at the positions of COSMOS2020 galaxies. With the resulting $z = 4 - 10$ X-ray AGN sample, comprised of 21 blind detections and a further 11 directly extracted detections, I have measured the early space density of AGN at

moderate-luminosities where the majority of early SMBH growth occurred. These measurements reveal higher space-densities than expected, based on the extrapolation of XLF models from lower redshifts. Whilst my measured space densities at $z = 4 - 5$ are consistent with the model predictions, at $z = 5 - 7$ I find space densities of the order of 10× the extrapolated model predictions which rises to $\sim$ 250× the model extrapolations at $z = 7 - 10$. In addition I find evidence that a large fraction of the early AGN population is heavily obscured with an obscured fraction of $0.982^{+0.007}_{-0.008}$; correcting for this obscuration further increases the measured space densities. Comparing to recent JWST results, these measurements begin to bridge the gap between the bright-end of the quasar luminosity function and the latest JWST observations of very early, low-luminosity AGN, indicating that a larger fraction of the first galaxies likely play host to a rapidly growing SMBH than previously thought.

With these observational measurements of the XLF, I determine predictions for the source numbers detected with a survey performed by the Wide Field Instrument (WFI) on ESA's next large X-ray mission, NewAthena. I perform full simulations of NewAthena WFI survey pointings for a small number of exposure times, using the SIXTE software. I then use these to calibrate an analytical description of the survey sensitivity of NewAthena. The resulting analytical sensitivity (which includes important source confusion effects) enables rapid predictions for a wider range of exposure times. Combining this model sensitivity and my XLF measurements I predict the number of high redshift X-ray AGN that will be visible to NewAthena, identifying a survey strategy that can be expected to find 1159 unabsorbed, 2748 absorbed and 1091 Compton thick AGN at $z = 4 - 10$ within approximately one year of observing time. NewAthena can be expected to observe an area of sky two orders of magnitude larger than Chandra, to similar survey depths, and yield unprecedented samples of early AGN. The large number of observed X-ray AGN predicted indicates the power of NewAthena for investigating the high-redshift XLF.

Acknowledgements

First I would like to thank my supervisor, Dr. James Aird, for all his guidance and support during my PhD, encouraging me when I judged myself too harshly. He has played an immeasurable role in helping me throughout this PhD and beyond.

I acknowledge the financial support from an STFC PhD studentship, and travel grant from AHEAD 2020.

To my family; thank you for helping me reach where I am today. I cherish all the laughs and good times and craziness, I love you all. Mummy and Daddy, you showed me the stars and I have never stopped looking up.

A special thanks to all the friends who have been there for me during the PhD. You had faith in me even when I did not. You have brought me strength, reassurance and encouragement throughout. I would have gone insane without you!

Finally, thank you to Amy Rankine and Keir Birchall for their last minute proof-reading.

Contents

List of Figures

List of Tables

Chapter 1

Background

Some of the most violent and esoteric objects within the known Universe are Supermassive Black Holes (SMBHs). Although only parsecs across, these extremely dense objects can have a major impact upon the host galaxy they reside at the centre of (Kormendy & Ho, 2013). They grow through the accretion of gas, increasing their mass, and powering emissions across X-ray to Radio wavelengths. When undergoing rapid growth SMBHs can easily outshine their hosts (wavelength dependent) and are known as Active Galactic Nuclei (AGN). These AGN form the focus of this thesis.

The formation of SMBHs and their subsequent rapid growth as AGN within the early Universe remains an open question, with observations indicating they must undergo several orders of magnitude in mass growth. The X-ray Luminosity Function (XLF) provides a tracer of this growth within the AGN population, however limitations in current X-ray telescopes mean it is poorly constrained across the regime of this rapid growth. This thesis utilises existing X-ray data in order to place new constraints on the XLF within the early Universe (at redshifts $z \geq 4$).

This opening chapter will present the background theory of SMBHs and AGN, characteristic of their emissions at different wavelengths and their appearance at high redshifts (early cosmic times). In section 1.1 I will provide an overview of the formation of host galaxies, before providing an outline of the underlying physics of black holes in section 1.2. In section 1.3 I will detail the main theories of SMBH formation. I will then outline the mechanisms by which SMBHs grow through the accretion of gas (in section 1.4), then the structure and different wavelength

emissions powered by actively accreting SMBHs, or AGN (in section 1.5). I will outline the measurement of the mass of SMBHs across cosmic time in section 1.6, which allowed the high masses of SMBHs within AGN at high-redshifts to be discovered. I will then outline the appearance and observations of high-redshift AGN in section 1.7, and of X-ray AGN and the XLF in section 1.8. Finally, section 1.9 will summarise the chapter and outline the structure of the Thesis that follows.

1.1 The Cosmological Formation of Galaxies

The Universe began with an event known as The Big Bang, a singularity when time began and from which all space began to expand (see Peebles et al., 2009, for a summary of the studies leading to this theory). As the Universe rapidly expanded and cooled, baryonic matter formed from quarks. This was followed by further cooling and the formation of Hydrogen and Helium (as well as trace amounts of Lithium and Beryllium) from free protons and neutrons (Mukhanov, 2005) and subsequently underwent recombination with electrons, releasing photons and producing what is now the Cosmic Microwave Background (CMB) (Liddle, 2015; Combes et al., 2002; Planck Collaboration et al., 2014). Despite the homogeneous and isotropic nature of the matter distribution within the 380 000 yr old Universe, local inhomogeneities allowed matter to slowly coalesce into defined structures (see e.g. Combes et al., 2002; Mukhanov, 2005; Longair, 1998).

Unimpeded by collisions with baryons, photons or itself, the dark matter content of the Universe fell towards regions of localised over-density and away from under-dense regions, forming dark matter halos. As the baryonic matter continued to cool it followed the flow of the dark-matter, falling towards the centre of gravity within the dark-matter halos. Through interactions with itself, the primordial gas within dark matter halos continued to cool, coalescing into clouds which continued to collapse under their own self-gravity. As the gas collapsed, reaching a density of $\sim 200\times$ the critical density of the Universe (e.g. Cole & Lacey, 1996), it fragmented into smaller clouds. Virialising as they collapse, these clouds of primordial gas subsequently formed the first stars (White & Rees, 1978; Clark et al., 2011), theorised to have occurred around 100 Myr after the Big Bang (see Klessen & Glover, 2023).

Dark matter halos, hosting clouds of primordial gas and the first stellar clusters, gravitationally interacted and built up mass through hierarchical merging[1] (Carroll, 2013). Through this merging and the continued formation of stars within the dark matter halos, at around 400 Myr [2] after the Big Bang, the first galaxies are considered to have formed (see Johnson, 2013, for a detailed summary of theories). This process is outlined in summary by figure 1.1. As these early galaxies formed stars the photons escaping from them began to re-ionise the cold gas surrounding them, until the Universe was fully ionised once more around 942 Myrs ago (redshift $z \sim 7-5$) at what is known as the epoch of reionisation (see e.g. Carroll, 2013).

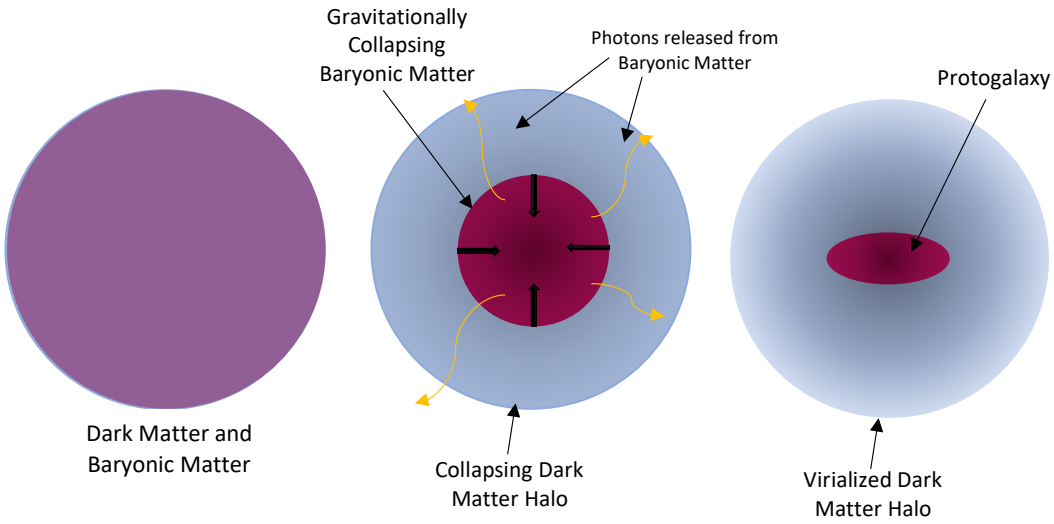

Figure 1.1 *Schematic of the gravitational collapse of baryonic matter within a dark matter protogalaxy halo, to form a protogalaxy within a Virialised DM halo.*

Galaxies continue to build up their stellar mass through star formation, however this rate of growth dropped with cosmic time as less gas remained available to fuel such star formation. Removal of gas from a galaxy, through processes such as stellar death or bursts of star formation, can result in the rapid reduction in the star formation rate, know as quenching. This has resulted in a significant population of "quiescent" (passively evolving) galaxies, with very low star formation rates. Observations of the most massive quiescent galaxies, such as those of Thomas et al. (2010), suggest these giants formed the earliest within

[1] The merging of smaller halos or galaxies into ever more massive ones.

[2] The age of the Universe at $z = 10-12$ was $\sim 372-478$ Myrs, however new observations of very high redshift sources by JWST are already identifying sources within this redshift range (e.g. Donnan et al., 2024, and references therein), indicating the first galaxies may have formed earlier.

cosmic time, contrary to what is expected in hierarchical formation. Simply modelling the stellar mass growth of galaxies through the hierarchical assembly of dark matter halos, in ΛCDM cosmology, cannot alone reproduce the population of massive quiescent galaxies observed (see figure 1.2). The observed low-mass slope in the distribution of galaxy masses is well explained by the inclusion of feedback due to stellar processes, specifically the release of energy by supernova suppressing star formation in low-mass halos (e.g. see Carroll & Ostlie, 2017; Somerville & Davé, 2015, and references therein). However, in order to suppress the formation of stars within the most massive halos, and reproduce the observed number of massive galaxies, significantly more energy must be released.

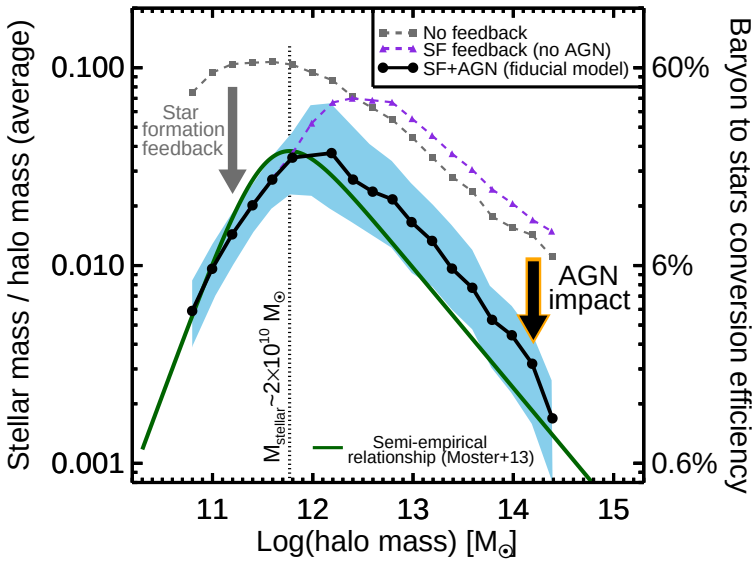

Figure 1.2 *The stellar mass to halo mass ratio with respect to halo mass, given by the simulations of Somerville et al. (2008) performed without feedback (grey dashed), with feedback due to star formation processes only (purple dashed) and resulting from feedback due to AGN and star formation included (black solid, with 16th and 84th percentiles in blue). A semi-analytic model, also accounting for AGN and star formation feedback, is shown by the dark green line. As can be clearly seen from comparison to the cases including AGN feedback, these processes are required to reproduce the observed galaxy mass function. Figure reproduced from Harrison (2017).*

The only mechanism, in the Universe, known to release sufficient energy to over come the escape velocity of gas within the most massive galaxies is that of Active Galactic Nuclei; powered by the in-fall of material onto a black hole $\sim 10^6 - 10^{10}$ times the mass of the Sun (see Kormendy & Richstone, 1995, for a summary of

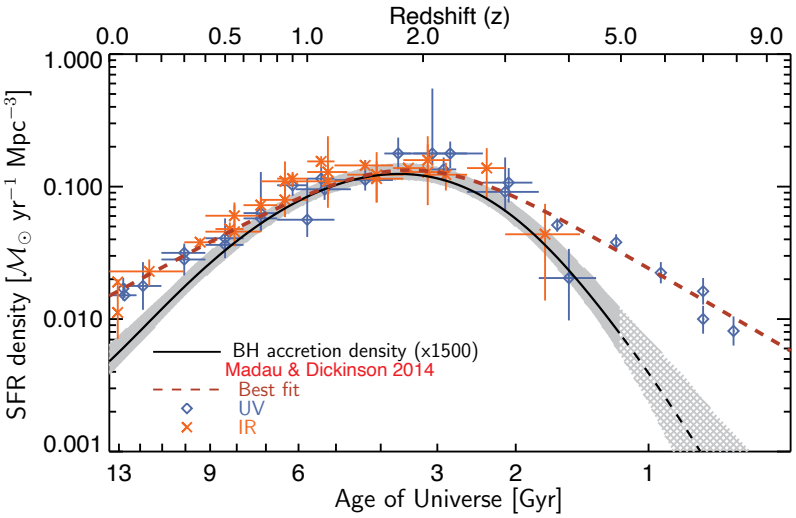

Figure 1.3 *The Black Hole Accretion rate Density across cosmic time (black line) scaled up by a factor of 1500, for comparison to the SFRD from Madau & Dickinson (2014) (red dashed line) of galaxies. UV and IR observations that contributed to the SFRD fit are shown by the blue diamonds and orange crosses, respectively. Figure reproduced from Aird et al. (2015).*

older reviews). This requirement of feedback by Active Galactic Nuclei (AGN) to limit the stellar mass growth of galaxies at the high mass end has been clearly demonstrated by Cosmological Hydrodynamic simulations of galaxy formation (Somerville & Davé, 2015).

The mass growth of galaxies is known to peak at a redshift of $z \sim 2$, referred to as Cosmic Noon, as can be seen from measurements of the Star Formation Rate Density (SFRD) by studies such as that of Madau & Dickinson (2014). Studies have found that the rate of accretion in the AGN population, the Black Hole Accretion Density (BHAD), follows the same trend as the SFRD (e.g. Boyle & Terlevich, 1998; Ueda et al., 2014; Aird et al., 2015), with the work of Aird et al. (2015) finding the $z \sim 0-5$ BHAD peaks only slightly later than the SFRD found by Madau & Dickinson (2014) (see figure 1.3). As such, there is expected to be a co-evolution of galaxies and AGN hosted within them (Heckman & Best, 2014; Kormendy & Ho, 2013), theorised to arise due to AGN activity being fuelled by the same gas reservoirs as star formation.

With observations identifying many of these AGN and massive black holes within local galaxies, it is now typically accepted that at the centre of every galaxy there resides a supermassive black hole (SMBH) (Rees, 1984; Kormendy & Ho, 2013).

1.2 The Nature of SMBHs

A Black Hole is an object so dense that not even light can escape from its surface. Although Black Holes were only relatively recently discovered, with Cygnus X1 thought to be the first BH observationally discovered (Carroll, 2013; Camenzind, 2007), the theoretical concept of an object for which the velocity required to escape is equal or greater than the speed of light was first conceived over 240 years ago, by John Mitchell in 1783.

Within classical Newtonian gravity, for an object of a given mass (M) the radius at which the velocity required to escape from the gravitational force of the mass is the speed of light (c) is given by the Schwarzschild radius (R_S),

$$R_S = \frac{2GM}{c^2}, \tag{1.1}$$

where G is the gravitational constant (see e.g. Carroll & Ostlie, 2017, for details). For the majority of objects this radius lies within the physical extent of the object ($R_{object} > R_S$), and as such the mass contributing to the required escape velocity at this distance from the centre of mass is less than the total mass of the object. However, if an object was sufficiently dense that all mass is contained within this radius, even light would not be able to escape from it's gravitational pull; this is a black hole.

Black Holes arise as a direct prediction from General Relativity (GR); developed in 1915 by Albert Einstein as an alternative theory of gravity, with which observed gravitational phenomena such as the orbit of Mercury[3] that defy the classical theory of Gravity could be explained. GR describes the gravitational force due to a mass as a curvature of spacetime, caused by the mass, which affects how other masses (or light) move within spacetime (see e.g. Carroll, 2013; Camenzind, 2007, for mathematical explanation of GR). Shortly after its discovery, Karl Schwarzschild found the GR solution for the spacetime metric corresponding to a stationary point mass (see e.g. review by Fabian & Lasenby, 2019), recovering the equation for the Schwarzschild radius (equation 1.1). Later the rotating point mass solution was determined by Roy Kerr (Kerr, 1963).

[3]Using GR, Einstein (1916) explained the 43 s time lag in Mercury's orbit, that arrises from relativistic effects due to it's close proximity to the massive body it orbits (the Sun).

With the law of Hawking's Singularity (Hawking, 1965) stating that a space-time singularity is formed once an object is contained within it's Schwarzschild radius, a Black Hole can thus be described as; a region of space-time, bound by an event horizon, at the centre of which lies a singularity, from which *nothing* can escape (Camenzind, 2007).

Black holes are characterised by only three key properties; Mass, Angular Momentum (also referred to as spin) and an Electromagnetic field. Despite only being characterised by these three properties, there is a plethora of variations in the Black Hole population, due to the differences in the environment and properties of the material falling into the gravitational influence of the black hole.

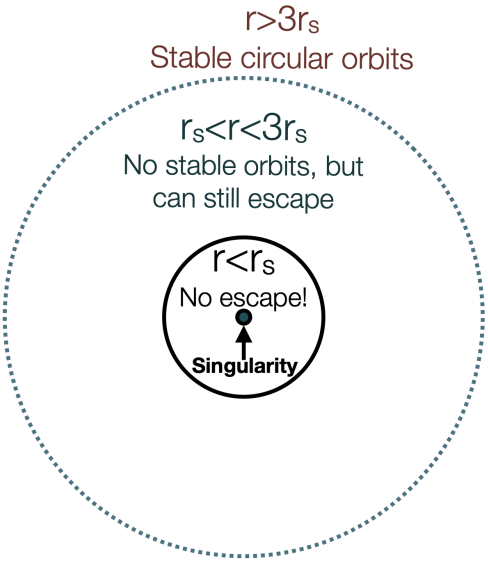

Figure 1.4 *Sketch of orbital radius (r) around a black hole indicating the distance at which material will can orbit in a stable circular orbit ($r > 3R_s$), an unstable orbit from which it can still escape ($R_s < r < 3R_s$) and the event horizon ($r = R_s$)*

Neglecting the electromagnetic field of a black hole, the two extremes of Black Hole spin models are that of the minimally spinning (or stationary) Schwarzschild Black Hole and the maximally spinning Kerr Black Hole (Fabian & Lasenby, 2019). The last stable orbit around a black hole depends on its spin, with a higher spin resulting in a smaller radius of this orbit. The larger the radius at which this orbit lies the less angular momentum that must be lost from in-falling material for it to fall into the black hole. Thus more mass can be accreted by Black Holes with smaller spins, as less energy must be lost by in-falling material, and they grow faster (Carroll & Ostlie, 2017). However, the accretion of material

with angular momentum will transfer that angular momentum to the black hole and it will spin up. I will discuss the accretion of material onto a black hole in more detail in section 1.4.

Black holes can be split into different mass ranges (stellar mass, intermediate mass and supermassive) typically being found in different locations throughout the Universe. The smallest black holes are known as Stellar-Mass Black Holes, with masses of $3 - 15\,M_\odot$, resulting from the death of sufficiently massive supergiant stars. Oppenheimer & Snyder (1939) first theorised that black holes could form from the collapse of stars, with Chandrasekhar deducing (in 1930) that at a mass of $\gtrsim 2\,M_\odot$ the self gravity of a neutron star would overcome the degeneracy pressures and a black hole would be formed (Fabian & Lasenby, 2019; Camenzind, 2007). Due to the presence of certain elements that cause the star to cool too rapidly as it dies, a star within a specific mass range will explode upon death (Carroll, 2013). As such, no remnant black hole will be formed, and this results in a gap in possible black hole masses. Intermediate Black Holes have masses of the order of $100 - 1000\,M_\odot$, with Ultra-luminous X-ray sources potentially providing evidence of their existence (see Carroll, 2013; Greene et al., 2020, and references therein) and gravitational wave detections by LIGO providing mass measurements of $> 100\,M_\odot$ black holes.

Finally, with masses of $\sim 10^5 - 10^9\,M_\odot$ are the so called Supermassive Black Holes (SMBHs). SMBHs reside within the centre of most galaxies, co-evolving with the galaxies themselves. These sources were first identified through early observations of Quasars (bright AGN) in 1960-1970, for which only a supermassive black hole can provide as much energy as is seen radiated by these objects. Whilst there has been significant evidence for SMBHs, such as broad iron lines at X-ray wavelengths (Tanaka et al., 1995), it was only in the last few years that imaging of these sources at the scale of their event horizon has been obtained using the Event Horizon Telescope (I will discuss the observation of SMBHs and AGN powered by them later, in section 1.5). Despite having been identified, the mechanism of SMBH formation remains a subject of much debate with multiple theories as to the mechanisms behind their formation (see §1.3 for details). Placing observational constraints on the growth of such SMBHs, seen as Active Galactic Nuclei, in the early ($z \gtrsim 6$) Universe forms the focus of the work presented in this Thesis.

1.3 The formation of SMBHs in the early Universe

Following the discovery of Supermassive Black Holes (SMBHs), these powerful objects are now thought to reside at the centres of most galaxies and play a crucial role in the build up of the most massive galaxies (Rees, 1984; Kormendy & Ho, 2013). Despite their major impact upon the galaxies hosting them, how these massive singularities formed remains a mystery.

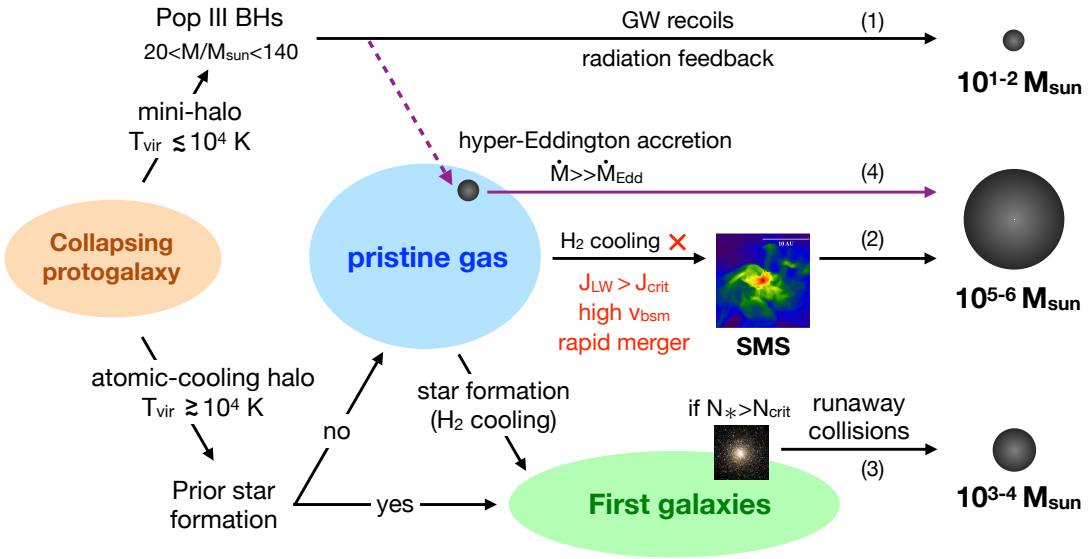

Figure 1.5 *Formation channels of seed Black Holes, from a primordial protogalaxy halo through Direct Collapse into a massive seed, collapse into a Population III star and subsequently low mass Black Hole remnant, or collapse into a stellar cluster then Black Hole seed through the runaway collapse of the stellar cluster. Figure reproduced from Inayoshi et al. (2020).*

Multiple formation pathways for SMBHs have been proposed over the years, from the collapse of gas clouds or stellar clusters to residuals from cosmic inflation in the very early Universe, resulting in various different masses of the initial black hole (known as the seed black hole) from which will grow a supermassive black hole. These mechanisms for SMBH seeding were first summarised by Rees (1984), with multiple possible intermediate objects presented, such as Supermassive Stars and dense stellar clusters, as shown in figure 1.5 (see also Inayoshi et al., 2020, for more recent summaries). However, even with recent advancements of our telescopes, seed Black Holes have remain undetected[4].

[4]Barrow et al. (2018) suggest that signatures of very massive black hole seeds may be detectable with state of the art observations by JWST, however such observations have yet to be confirmed.

In this section I will outline the three main mechanisms of black hole seeding; Population III stellar remnants (see §1.3.1), Direct Collapse black holes (see §1.3.2) and collapse of young stellar clusters (as outlined in §1.3.3). Other theories of SMBH seeding have also been proposed, which will be summarised in §1.3.4.

1.3.1 Population III Stellar Remnants

One of the main theories of Black Hole seeding is the formation of black hole remnants following the death of massive Population III stars, the first stars in the Universe (e.g. Whalen & Fryer, 2012; Greif, 2015).

Population III stars formed from the metal free gas reservoirs within the very early Universe, and synthesized the first metals (Carroll & Ostlie, 2017). Although studies have, thus far, been unable to observe these first stars, simulations have been performed in order to better understand them. Cosmological simulations, modelling the collapse of primordial gas, predict the formation of Population III stars to have occurred at redshifts of $z \sim 20 - 35$ (Haiman et al., 1996; Tegmark et al., 1997), with the typically assumed ΛCDM cosmology predicting the formation of these first stars at $z \gtrsim 30$.

Due to the lack of metals in the very early Universe primordial gas clouds are theorised to have cooled quasi-statically, through molecular hydrogen channels, reducing their fragmentation into lower mass halos (Madau & Rees, 2001). Without fragmentation of the collapsing gas cloud, massive stars are formed with compact cores that are expected to lose less mass when the star eventually dies (Woosley & Weaver, 1995). Lacking the metals that typically catalyse fusion in massive stars, fusion of hydrogen to helium proceeds rapidly, releasing large quantities of energy and exhausting the hydrogen fuel within their core. Thus these first stars are more unstable and shorter lived than the later Population I and II stars. However, simulations by Kudritzki & Puls (2000) find that, despite this instability, less mass is lost from metal poor stars as the momentum transfer that drives mass loss in stars proceeds through a metal absorption line.

Due to the large masses of population III stars, once they have exhausted all fuel for fusion within their core and their self-gravity causes them to collapse (as occurs in later stars), the remnant of the compact core left following the explosion will be a black hole with mass $\sim 10 - 10^3\,\mathrm{M}_\odot$ (e.g. Madau & Rees, 2001). Simulations show that stars with masses of around $25\,\mathrm{M}_\odot \lesssim \boldsymbol{M}_\star \lesssim 80\,\mathrm{M}_\odot$ and $\boldsymbol{M}_\star \gtrsim 200\,\mathrm{M}_\odot$

will result in a BH remnant (Hirano et al., 2014), whilst pair instabilities will result in the explosion of the core of stars with masses of $100\,\mathrm{M}_\odot \lesssim \boldsymbol{M}_\star \lesssim 250\,\mathrm{M}_\odot$ (Heger & Woosley, 2002).

Population III stars are often proposed as the seeding mechanism of SMBHs, with many studies predicting the number of these seeds. Larson (1998) predict that the number of population III stars would be significant enough to produce many SMBH seeds, whilst other studies suggest that additional seeding mechanisms are required (see Greene et al., 2019, and references therein)

1.3.2 Direct Collapse BHs

Alternative to seeding through Population III stars, Black Hole seeds are also theorised to form directly, through the gravitational collapse of large gas reservoirs in the very early Universe (Volonteri & Begelman, 2010). This process produces what are known as Direct Collapse Black Hole (DCBH) seeds, which are theorised to be much more massive than the seeds predicted by Population III simulations.

Similar to the formation of proto-stellar clusters (see section 1.1) protogalaxy gas halos merge within the early Universe, increasing in mass and density. Once a critical density is reached, found by Wise et al. (2019) to be $10^{-15}\,\mathrm{g\,cm^{-3}}$ (however this value remains controversial—see Maio et al., 2019), the gas halo begins to collapse, monatonically, under it's own self-gravity (Woods et al., 2019). Unlike during the formation of stars, continual ionisation of the protogalaxy halo by a nearby source of Lyman-Werner radiation (of energy $\sim 11 - 15\mathrm{eV}$), such as a stellar cluster, prevents the formation of molecular hydrogen channels which would allow for more rapid cooling of the metal free gas. Thus the collapse of the gas proceeds near isothermally, and no virialisation of the collapsing gas into smaller clouds occurs. The gas instead collapses into a supermassive disk which subsequently collapses into a supermassive star (Begelman, 2010), or passes the stellar stage entirely to directly form the seed black hole (Begelman et al., 2006).

In order for the continued collapse of the protogalaxy gas cloud into a black hole the angular momentum of the cloud must remain low. Simulations of this collapse have shown that this is achieved through gravitational torques, whilst Koushiappas et al. (2004) theorise that Toomre instabilities in the gas allow for the transfer of angular momentum to the edges of the cloud, by driving the viscosity of the cloud.

Simulations of the formation of direct collapse black hole seeds produced black hole seeds with masses of the order of $\sim 10^3 - 10^6\,\mathrm{M}_\odot$ (see e.g. Koushiappas et al., 2004), although it should be noted that such predictions are highly dependent on the assumptions made in the simulations, resulting in significant uncertainty in the frequency with which direct collapse black hole seeds occur. In addition, the direct collapse of protogalaxies halos into black hole seeds requires specific conditions under which the process can occur. Thus a number of factors could reduce or inhibit the formation of a DCBH; such as gas self shielding, cosmic rays or the enhancement of molecular Hydrogen formation by UV and X-ray photons resulting in a need for stronger Lyman-Werner radiation. As such DCBHs are expected to be rarer than those of Pop III stellar remnants. Maio et al. (2019) theorise that although direct collapse black holes may not be the main formation mechanism of SMBHs, they likely contribute to the full SMBH population.

1.3.3 Collapse of Young Stellar clusters

Within a highly dense stellar cluster, collisions between stars occur over timescales shorter than the life-time of even the most massive stars (e.g. Katz et al., 2015). Through such collisions a dense stellar cluster can undergo efficient runaway core collapse to produce a single massive star, the remnant of which will be the seed of a supermassive black hole (see e.g. Nakauchi et al., 2020).

When a protogalaxy gas halo collapses under it's own self gravity, as occurs with Direct Collapse Black Holes (see section 1.3.2), the presence of metals or dust within the gas will allow it to cool more rapidly, resulting in fragmentation of the gas cloud. Such fragmentation can occur in gas clouds of density as extreme as $n_\mathrm{H} \sim 10^{11-13}\,\mathrm{cm}^{-3}$, for highly metal poor protogalaxy halos (see Inayoshi et al., 2020). The fragmented collapse of the protogalaxy halo will result in an ultra dense cluster of low-mass, metal-poor stars. Alternatively a lower density cluster may form, with more massive fragments becoming massive short lived stars.

At high redshift, inflow of gas as the cloud collapses results in stars with highly accreting, bloated photospheres; Davies et al. (2011) predict the cluster will shrink by a factor of ~ 10 due to this gas inflow. This shrinking results in a number of processes within the cluster, taking $\sim 100\,\mathrm{Myrs}$ to form a seed black hole: Binary stars will either be split into single stars, or when they are more closely bound the stars of the binary will merge through gravitational in-spiralling or direct collisions. More massive stars migrate towards the centre of the cluster,

through mass segregation, and subsequently the core of the cluster contains black hole and Neutron star remnants of these massive short lived stars. As stellar collisions continue and energy is transferred out of the cluster core, the number of dense stellar remnants increases. These black holes and neutron stars are then gravitationally captured and merge into a single black hole seed of mass $\gtrsim 500\,\mathrm{M}_\odot$ (Nakauchi et al., 2020).

1.3.4 Other Models of SMBH seeding

In addition to the main three theories of SMBH seeding presented above, there are a number of other less widely accepted theories. Building on the theory of Direct Collapse Black Holes, heating of a collapsing protogalaxy halo by a primordial magnetic field has been proposed as a mechanisms by which fragmentation might be prevented during gravitational collapse, requiring a magnetic field strength of $\sim 1\,\mathrm{nG}$ (Schleicher et al., 2009). Whilst freezing out of the flux within the collapsing gas could amplify the magnetic field, it is still expected that this effect would be rare, occurring only in $\lesssim 3\sigma$ regions where molecular hydrogen cooling channels are fully suppressed by a primordial magnetic field (see reviews of Inayoshi et al., 2020; Widrow, 2002; Subramanian, 2016). Begelman et al. (2006) also proposed a variation of the Direct Collapse method; "bars within bars instability", where by a gas cloud of virial temperature $> 10^4\,\mathrm{K}$ forms a quasi-star with a black hole core. This black hole core rapidly grows to a mass of $\sim 10^6\,\mathrm{M}_\odot$ as matter is accreted onto the quasi-star.

Alternatively, mechanisms of SMBH seeding involving Dark Matter such as Dark Stars (powered by the self-annihilation of Dark Matter) or collisional Dark Matter, which could allow BHs to form with masses of $\sim 10^6\,\mathrm{M}_\odot$ by $z \sim 10$, have been postulated (see Inayoshi et al., 2020, for a summary). However, these require very specific conditions and forms of Dark Matter the existence of which, to date, have not been confirmed.

Primordial BHs

A more esoteric, yet frequently referenced theory of SMBH seeding is through Primordial Black holes. These singularities occur as a result of the inflation of the Universe and local inhomogeneities, but likely only represent around 0.3% of the SMBHs mass-density today (see Inayoshi et al., 2020, and references therein)

During the rapid early expansion of the Universe, regions of high density fluctuation decoupled from the overall expansion as they were carried outside the event horizon of the Universe. Once the expanding event horizon encompassed them once again, these primordial density fluctuations have a much higher density than the surrounding space, thus forming black holes. These Primordial Black Holes subsequently undergo efficient mass accretion within the very early Universe, and may grow as massive as $10^5\,M_\odot$ (Bean & Magueijo, 2002; Dolgov, 2018).

1.4 The Growth of SMBHs

Regardless of their formation mechanism, once formed Black Hole seeds must subsequently undergo significant growth to produce Supermassive Black Holes (SMBHs). This growth occurs through the accumulation of mass energy. In SMBHs this mass growth can occur via the accretion of material (gas, dust and larger object such as stars; see e.g. Alexander & Hickox, 2012), or through merging with another SMBH (Schulz & Komossa, 1999; Booth & Schaye, 2009).

The increase in black hole mass via merging can be significant, of the order of the merging black hole masses, as seen through gravitational wave observations by LIGO (Abbott et al., 2016). However, the time scale of the collision between two SMBHs (e.g. following a galaxy merger) is very long. Whilst growth via BH merging may dominate the gravitational wave background, it is the accretion of material that has long been observationally identified as the dominant SMBH growth channel (see e.g. Soltan, 1982). The accretion of material onto a SMBH is thus, typically considered to be one of the most important channels of growth in SMBHs, with this growth fuelled by a rotationally supported disk of accreting gas (Lynden-Bell, 1969; Bailey & Clube, 1978) that is fed by hydrogen gas reservoirs within the host galaxy (Gunn, 1978). Figure 1.6 shows simulations of the overall process of SMBH accretion, demonstrating the inflow of gas around and within the host galaxy and very close to the SMBH itself.

The gravitational influence of a SMBH only dominates within the very central regions of the host galaxy (Ciotti & Pellegrini, 2018; Carroll & Ostlie, 2017). In order to feed the continued growth of a SMBH, gas within the galaxy must be driven down from the kpc galaxy scales to the pc scales at which the gravitational influence of the SMBH begins to dominate (at $\sim 10\,\mathrm{pc}$). For this to occur, the

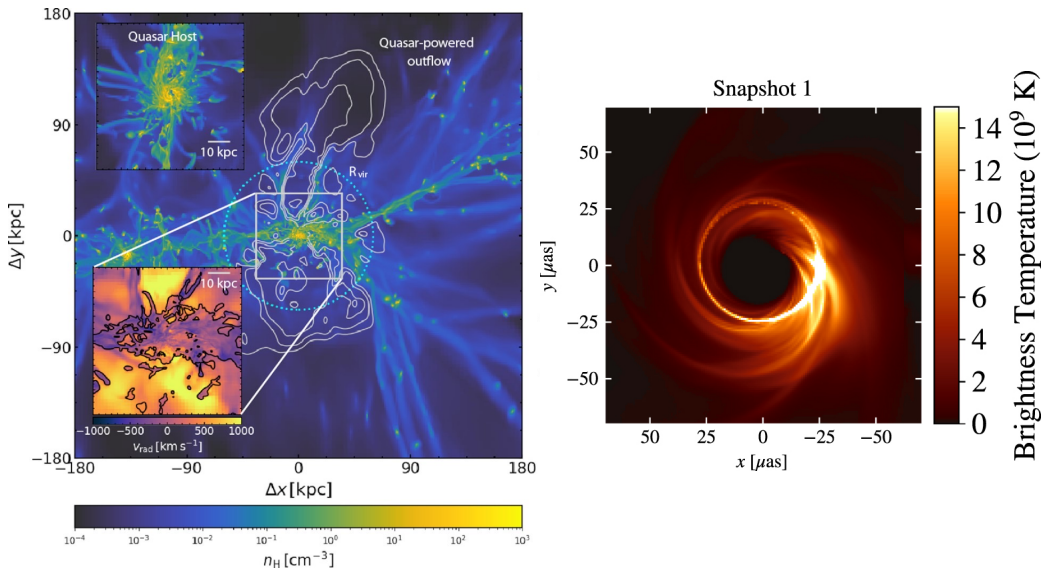

Figure 1.6 *Left: Simulation of the large scale gas flow around a rapidly growing SMBH (quasar), showing cold and dense gas inflows. The virial radius of the SMBH-host galaxy system is shown by the blue dotted circle, and outflowing gas due to the SMBH is shown by the white contours. The inset plots show a zoom in of the gas around and within the host galaxy (top left) and the radial gas velocity within the inner ~ 70 kpc of the system (bottom left). Figure reproduced from Costa et al. (2022). Right: Snapshot from a simulation of the flow of material close to a SMBH, as seen at Radio wavelengths. Figure reproduced from Event Horizon Telescope Collaboration et al. (2022).*

gas must lose almost all of it's angular momentum (see Alexander & Hickox, 2012, and references therein). The main cause of this is large-scale gravitational torques, arising as a result of non-axisymmetric morphologies (see e.g. Alexander & Hickox, 2012; Inayoshi et al., 2020), occurring in both stochastic or merger and tidal interaction driven gas accretion.

As the infalling gas experiences gravitational effects due to the galaxy as a whole, it falls towards the galactic plane, forming a disk. In addition, bar-like structures formed as the gas becomes self gravitating (see Inayoshi et al., 2020, and references therein) or turbulence caused by the large-scale instabilities (see Hickox & Alexander, 2018, and references therein) have been proposed to facilitate the continued inflow of gas towards the galaxy's centre of mass, where the SMBH resides. Once the gas reaches the influence of the central SMBH it is no longer subject to such instabilities and a gravitationally stable disc, known as the accretion disk, is expected to form (Netzer, 2013).

The simplest model of accretion onto an isolated central point mass, such as a black hole, is Spherical (Bondi) accretion (Bondi & Hoyle, 1944; Edgar, 2004). Bondi & Hoyle (1944) describe Bondi accretion as the radial free-fall of gas, initially at rest a large distance from the central mass, from an isothermal, non-rotating spherical distribution about the central mass (see e.g. Zhu et al., 2022; Netzer, 2013, for details). This model represents a perfectly idealised scenario of gas accretion onto a central mass, defining the boundary of the sphere of isothermal gas at infinity. In reality the accretion of material onto a black hole is more complex than this, with the accreting gas subject to gravitational effects of the galaxy around a black hole and other nearby gravitational sources. In general, more complex models describe an accretion disk with thick or thin geometry as well as how dense the gas is, all of which presents its own set of consequences on the rate of accretion (see e.g. Netzer, 2013; Hicks & Malkan, 2008).

The final accretion of gas onto the central SMBH occurs via the accretion disc, on sub-pc scales, the basic theory of which has been around for many years (e.g. Shakura, 1973). As the accretion disk rotates, due to the remaining angular momentum of the gas, viscous stress between layers of gas moving at different speeds results in the transport of angular momentum away from the inner regions of the system, allowing the gas to fall towards the SMBH. The friction between layers within the accretion disk also allow for kinetic energy in the particles to be radiated away through thermal emission of photons. This radiation can also result in particles being ejected from the disk or causing the disk to "puff up" as the energy is transferred to other regions of the disk (Netzer, 2013). Once gas within the disk loses sufficient energy to fall to an orbit around the SMBH at a radius equal to the last stable orbit of the SMBH (see section 1.2) it will fall, inevitably, into the black hole. The complex processes involved in the accretion of material has been the subject of many studies, modelling the accretion disk shape and opacity as well as the overall flow of gas within the system.

Two fundamental quantities relating to the process of accretion onto massive objects, such as SMBHs, are the Eddington Luminosity and Accretion Rate (Netzer, 2013). As material accretes, the energy lost as it falls towards the centre of gravity is emitted as radiation. This radiation exerts a pressure upon the in-falling material (radiation pressure) through electron scattering. The Eddington Luminosity (L_{Edd}) is defined as the energy emitted at the limit of accretion, where the gravitational force causing the material to in fall is balanced by the outwards radiation pressure. The Eddington Accretion Rate (M_{Edd}) is thus the

rate of mass accretion required to produce a Luminosity equal to the Eddington Luminosity, for a given accretion efficiency (η).

$$L_{\mathrm{Edd}} = \frac{4\pi c G M_{\mathrm{BH}} \mu m_p}{\sigma_T}, \qquad \dot{M}_{\mathrm{Edd}} = \frac{L_{\mathrm{Edd}}}{\eta c^2}, \tag{1.2}$$

where M_{BH} is the instantaneous mass of the black hole, m_p is the mass of a proton and σ_T is the cross sectional area of a photon. The accretion efficiency, η, of the black hole is linked in particular to the spin (angular momentum) of the black hole. As discussed in section 1.2, the radius of the last stable orbit around a black hole is smaller for more rapidly spinning black holes. As a result, more mass energy must be lost in order for matter to fall into the black hole.

Above this emission limit, known as the Eddington Limit, the radiation pressure of the dissipating energy is such that it prevents the gravitational collapse of gas onto the SMBH (e.g. Begelman et al., 1984). The definition of the Eddington Luminosity and Accretion Rate, however, contains a number of assumptions. Specifically it is assumed that all matter, comprised only of hydrogen, accretes radially from a spherical distribution with no winds of material being blown out. In reality, the accreting material can include dust, which would have a larger cross-section than Hydrogen upon which radiation pressure would act, and winds can allow for localised violations of the Eddington Limit.

If a SMBH accretes mass at a rate faster than that allowed by the Eddington limit it is said to be undergoing Super-Eddington accretion, a phenomenon that has been observed in only a few sources (e.g. Tang et al., 2019; Jin et al., 2017; Komossa et al., 2006; Berdina et al., 2021) and is seen more readily in X-ray Binaries (e.g. Greiner et al., 2001; Margon, 1984). The mechanism that would allow for such rapid accretion onto a SMBH is the subject of much debate, requiring conditions under which gas can reach the SMBH faster than allowed by the Eddington Limit (see Mayer, 2019, for a summary). Moffat (2020) theorise that the high gas content of the early Universe was such that the density of ambient gas and material accreting through the simple process of Bondi accretion would be sufficient to trap radiation around the black hole and reduce the radiative efficiency of the accretion process, thus result in Super-Eddington accretion rates (see also Liu et al., 2021).

Processes such as radiation driven winds or particle jets are expected to act

against the accretion of mass onto a SMBH. Such mechanisms are typically described as removing material from around the SMBH, preventing it from accreting further mass until the driver of these winds or jets has reduced in power. The driver of these mechanisms stem from the process of accretion, such that an actively accreting SMBH is often considered to regulating its own growth (e.g. Booth & Schaye, 2009; Costa et al., 2020, 2022, and references therein).

All of these processes involved in and resulting from the accretion of material onto a SMBH lead to a distinctive structure around highly accreting SMBHs. This structure produces characteristic emissions, with which SMBHs can be identified and characterised.

1.5 Physical Structure and Multiwavelength emission of AGN

Until very recently with the Event Horizon Telescope (Event Horizon Telescope Collaboration et al., 2019a,b,c), supermassive black holes (SMBH) could only be indirectly observed through their gravitational effect on the nearby stars or by the energy released when the SMBH is undergoing periods of high accretion. When actively accreting, SMBHs power emissions across a range of wavelengths from hard-band X-rays to the Radio wavelengths, with an almost constant power per unit decade (Reines & Comastri, 2016). When the emissions of an accreting SMBH contribute to the emissions of the galaxy such that a significant fraction of the total observed emissions from the galaxy are not due to stellar processes, the system is known as an Active Galactic Nuclus (AGN).

AGN are typically very luminous, with bolometric luminosities of $\log L_{bol}\,\mathrm{erg\,s^{-1}} = 42 - 45$ and $\log L_{bol}\,\mathrm{erg\,s^{-1}} > 45$ often used to classify AGN as Seyfert Galaxies (Seyfert, 1943) and Quasars (Schmidt, 1968) respectively (Hickox & Alexander, 2018). The Spectral Energy Distribution (SED) of an AGN can be modelled across a narrow wavelength range, very simply, as a power-law of the form $f_\nu \sim \nu^{-\alpha}$ (e.g Bañados et al., 2015). In X-ray studies this SED is typically modelled as a power law between the number of photons and their energy ($N(E) \propto E^{-\Gamma}$), with the photon index Γ assumed to be between $\Gamma = 2.0$ and $\Gamma \sim 1.4$. In reality the Spectral Energy Distribution (SED) of an AGN is more complex, and different wavelength emissions are produced by different components within the physical

structure of the AGN, as shown in figure 1.7.

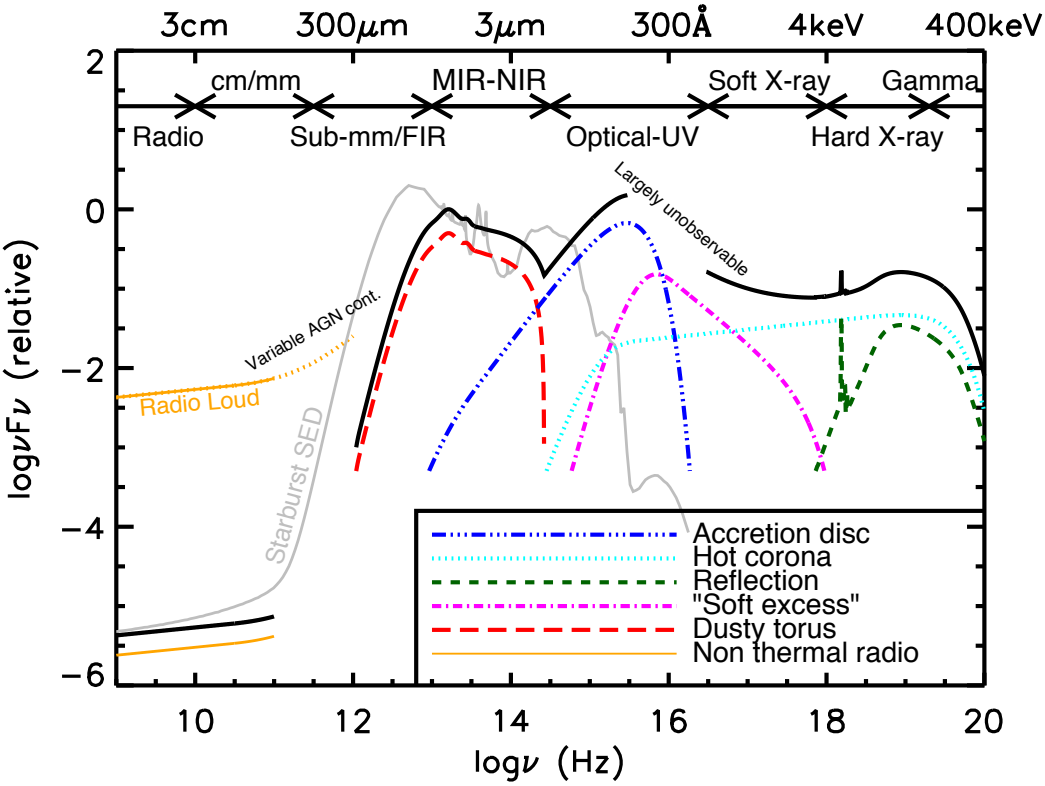

Figure 1.7 *Schematic of the Spectral Energy Distribution (SED) of an accreting SMBH, with contributions to the SED by the components of an AGN indicated by the different coloured lines. The total SED of the AGN is shown by the solid black line, with the SED of a galaxy undergoing bursty star formation shown in grey for comparison. The shape of the Radio end of the SED will depend on radio loudness, with the total SED shown for a radio quiet AGN. Figure reproduced from Harrison (2014).*

As discussed in §1.4, accreting SMBHs are fuelled by a rotationally supported disk of accreting gas (Lynden-Bell, 1969; Bailey & Clube, 1978), fed by a hydrogen gas reservoir (Gunn, 1978). As energy is dissipated from the infalling material, through viscosities within the accretion disk, it is thermally emitted as UV/Optical photons. Thus the majority of the UV/Optical emissions from an AGN are directly due to the feeding of the SMBH by the accretion disk (see e.g. Hickox & Alexander, 2018; Padovani et al., 2017; Rees, 1984).

Just beyond the edge of the accretion disk, within the sublimation radius of dust and under the gravitational influence of the SMBH itself, is theorised to be a region of dense dust-free gas clouds. This gas is ionised by the UV photons from the accretion disk and re-emits through recombination lines, with it's high

density preventing the occurrence of forbidden transitions within this gas (Netzer, 2013). These recombination lines are subsequently Doppler broadened by the Keplarian motion of the gas, resulting in broad emission lines with velocity widths of $\sim 10^3 - 10^4\,\mathrm{km\,s^{-1}}$. This region of dust-free gas is thus is known as the Broad Line Region (BLR). The Broad Line Profile of this region suggests a disk-like geometry, with studies such as Kuhn et al. (2024) determining constraints on the structure and geometric size of the BLR. AGN observed to have the broad emission line features characteristic of the BLR are known as Type I Seyfert galaxies or Broad Line AGN (BLAGN).

Further out, under greater influence from the host galaxy's gravity than the SMBH (Ho, 2009), is theorised to be a complex region of non-uniform gas (due to uneven illumination) know as the Narrow Line Region (NLR). In contrast to the BLR, the NLR is a region of low density gas and dust (Zhu et al., 2023), moving at low velocities. As with the BLR, it is illuminated by the UV light from the accretion disk, and re-emits photons following recombination, with intense forbidden lines due to transitions within the fine structure of the gas and dust Netzer (2013). Due to the low velocity of the material in the NLR, emission lines remain narrow with velocity widths of only $\sim 100 - 500\,\mathrm{km\,s^{-1}}$. Type II Seyfert galaxies, or Narrow Line AGN (NLAGN), are AGN observed to have only narrow emission lines within their spectra.

Matter distributed outside the accretion disk, can absorb or reflect the thermally emitted photons from the accretion disc. This surrounding dust is defined by Antonucci (1993) as a central, axis-symmetric dust structure with column density sufficient to entirely obscure the central SMBH. This dusty obscuring "torus" reprocesses the UV/Optical light from accretion into IR wavelengths, and polarising emissions through collisions with dust grains and free electrons. The so called "torus" is often modelled as a simple smooth distribution of material the inner boundary of which is set by the sublimation temperature of the dust grains (Barvainis, 1987). However, more complex torus models containing clumps (as shown in figure 1.8), in the form of optically and geometrically thick clouds, or a combination of clumps and a smooth distribution of material are more favoured by observations of accreting SMBHs. However, the exact nature of this surrounding dusty material has remained the subject of much debate.

Close in to the SMBH, within only a few Schwarzchild Radii (see section 1.2) from the event horizon, a corona of charged relativistic particles produces strong X-ray emission through the inverse Compton scattering of UV photons from the

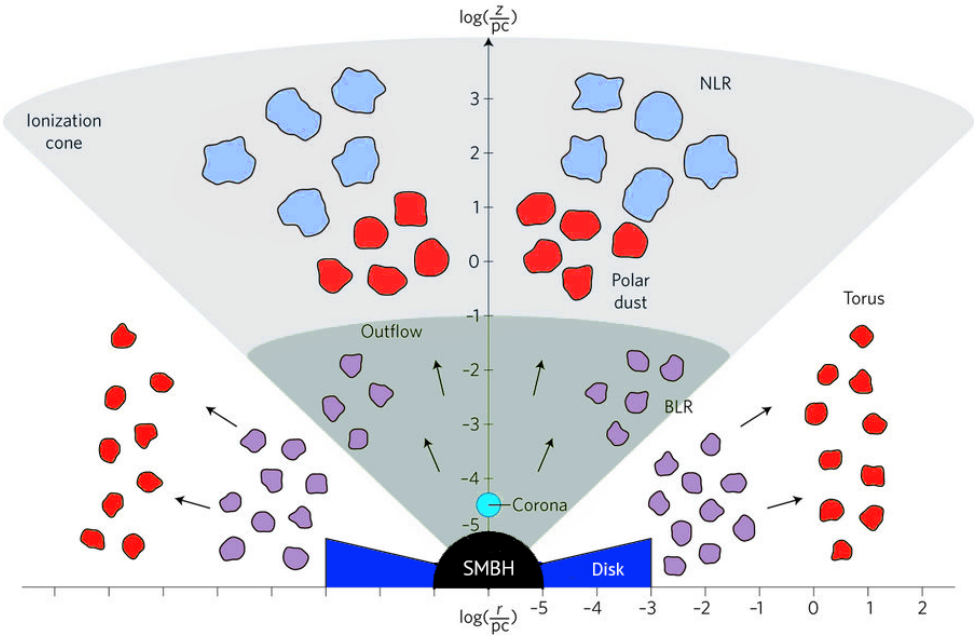

Figure 1.8 *Diagram of the unified model of AGN structure, showing the extent and location of the components with respect to the central SMBH. The BLR is indicated by the purple patches and the NLR is shown by the light blue patches, with both regions assumed to be clumpy in nature. The X-ray corona, located very close to the SMBH, is indicated by the cyan circle. Figure reproduced from Hickox & Alexander (2018)*

accretion disk itself. The exact form of this corona remains the subject of many studies (e.g. Tagliacozzo et al., 2023; Marinucci et al., 2022; Fabian et al., 2015; Wilkins, 2023). The X-ray emissions from the corona have been found to be tightly linked to the accretion of mass onto the SMBH, due to it's close proximity, indicating that X-ray emission from AGN is near universal and can be used as a direct tracer of the accretion rate of an AGN (Brandt & Alexander, 2015, and references therein).

The structure of an AGN is known, in general, to consist of an accretion disk (see section 1.4) surrounded by obscuring dusty gas (Hickox & Alexander, 2018). Studies have shown the orientation of an AGN, along the line of sight, to have a significant effect on its observed SED. This dependence upon the orientation of an accreting SMBH, along the line of sight, forms the basis of the Unified model of AGN classifications, originally proposed by Antonucci (1993). Within the unified model type-II AGN are described as those viewed through the obscuring material whilst type-I AGN are viewed from above the plane of the accretion disk and obscurer. Radio unification theories stem from the addition of a relativistic jet to this description (see e.g. Heckman & Best, 2014; Urry & Padovani, 1995).

A simplified diagram of the structure of an AGN, assuming the Unified model holds is shown in figure 1.8. Many observations support this Unified model of AGN (e.g. Ananna et al., 2019), however other studies suggest alternative models are required to reproduce the variety of observed AGN (e.g. Lawrence, 2007; Lawrence, 1991). Specific to this the exact nature of the dusty obscurer, vital to the unified model, is not well known (see Netzer, 2015, for a summary of models), although it is generally expected to exhibit clumpiness (i.e. patches/clumps of denser gas or dust) as shown in figure 1.8. It is possible that some aspects of AGN appearance can form a unified model, depending upon the angle relative to the plane of the accretion disk at which the AGN are viewed, whilst others require intrinsic differences between AGN.

AGN can also exhibit outflows, which are driven out from the accreting SMBH by radiation pressure (see Fabian, 2012, for a review), occurring most strongly when the continuum emissions from the accretion disk are absorbed by bound-bound absorption lines. Outflows have been observed to have a range of velocities and size scales, such as Ultra Fast Outflows moving at $10\% - 30\%$ the speed of light (e.g. Tombesi et al., 2014) or extended multi-phase ionised outflows which move at only $\sim 100\,\mathrm{km\,s^{-1}}$ (e.g. Singha et al., 2022).

Some AGN have jets of high energy particles (e.g. Bañados et al., 2018a), launched from the inner regions of the accretion disk and extending kpcs out from the AGN. These charged particles gyrate through the magnetic field of the SMBH, moving at relativistic velocities, and emit at radio wavelengths through synchrotron radiation as a result. AGN observed at radio wavelengths can fall into Radio Loud or Radio Quiet classifications, depending on the strength of their emissions, which is theorised to arise from the efficiency of accretion within these sources (see Heckman & Best, 2014, for review). The high energy of these particle jets can also result in the emission of X-rays as surrounding material becomes shock heated by the high speed jet.

The presence of material between the accretion disk and the observer, which absorbs or scatters the photons emitted close to the SMBH, is known as an obscurer (see Hickox & Alexander, 2018, for a review). This is often assumed to take the form of the dusty torus, however the host galaxy of an AGN may also obscure the AGN emissions. Typically it can be assumed that regions of dense gas obscure X-ray emissions whilst dust obscures UV/Optical emission, although this may be a simplification.

Finally, it should be noted that the variability of AGN has been identified as a main characteristic of these objects (see e.g. Angione, 1973; Marshall et al., 1981), with aperiodic flux variability over a range of timescales (minutes to years). However the cause of such variability remains a subject of much debate, with some studies finding the variability in AGN flux occurs more rapidly when observed at higher energy wavelengths (see Padovani et al., 2017, for summary). For studies beyond the nearby Universe, however, it is must be assumed that the measured luminosity of each source is not due to some random variation increasing or decreasing the flux. This is due to the effect of time dilation, by the expansion of the Universe, dramatically slowing the apparent speed at which AGN vary and the averaging out of AGN emissions by the prolonged exposures used in X-ray observations in particular.

The structures within AGN, detailed here, all contribute to the broad range of wavelengths across which they can be observed. The resulting spectral energy distribution of an AGN is summarised in Figure 1.7.

1.6 SMBH Mass Measurements

Supermassive Black Holes (SMBHs) are, crucially, defined by their mass (see section 1.2). The growth of SMBHs is the increase in this mass. As such mass measurements of SMBHs can provide significant insight into these powerful objects. Although the mass of SMBHs cannot be measured directly, there are a number of methods used to infer their masses from observations of nearby stars, gas and the Broad Line Region (BLR) in Active Galactic Nuclei (AGN).

For SMBHs within the nearby Universe, up to $\sim 150\,\mathrm{Mpc}$ (Gültekin et al., 2009), dynamical motion of stars and gas within the central region of the host galaxy can be used to measure the black hole mass. Typically this is done using IR observations of the stellar or gas dynamics, in order to reduce the contamination by non-stellar emission (Hicks & Malkan, 2008). For the SMBH at the centre of the Milky Way, Sagittarius A*, individual stars can be resolved. Through mapping of the motions of these stars the mass of Sagittarius A* is inferred to be $\sim 4\times10^6\,\mathrm{M}_\odot$ (e.g. Do et al., 2019). For SMBHs in other galaxies, they are too distant for the individual stars cannot be spatially resolved. Instead SMBH mass can be similarly determined from the dynamical motion of gas within $\sim 10\,\mathrm{pc}$ of the host galaxy's centre (e.g. Hicks & Malkan, 2008, where the gas is spatially

resolved), or from stellar velocity dispersion (e.g. McConnell & Ma, 2013) applying Schwarzschild modelling of the stellar dynamics in order to measure the mass (see e.g. Davies et al., 2006). Similarly, water masers emitting from the gas around SMBHs can be used to measure the central gravitational potential, and infer the mass of the SMBH (Miyoshi et al., 1995).

Alternatively, in particular for the case of more distant SMBHs, the black hole mass can be determined using Reverberation Line Mapping (RLM) of the Broad Line Region (BLR) of AGN (see Blandford & McKee, 1982; Peterson, 1993; Cackett et al., 2021). RLM determines the radius of the BLR (see 1.5 for details on BLR) using the time delay between changes in the light curve of the AGN's UV/Optical continuum and the light curve of broad emission lines from the BLR (Onken et al., 2007; Netzer, 2013), assuming the light-travel time across the BLR is within an observable range and the relationship between the observed UV/Optical continuum and the continuum emission which is driving emissions from the BLR is known. The mass of the SMBH is then calculated from the BLR radius and velocity broadening of the relevant emission line, given a scale factor which depends upon the geometry and kinematics of the BLR. This scale factor is obtained through calibration of RLM mass to the masses observed using the observations of stellar or gas dynamics, and extrapolated from those sources where both methods are possible out to higher redshifts.

Finally, when only one observation of the SMBH is available single epoch mass measurements must be relied on (e.g. McLure & Dunlop, 2004; Vestergaard & Peterson, 2006). Given the relation between the BLR widths (from which the RLM mass is determined) and corresponding continuum luminosity, the luminosity of an AGN as measured in a single observation can provide an estimate of the black hole mass (under the assumption this relation holds). It is through this method of single epoch mass measurements, of the SMBH within AGN, that the mass of the most distant SMBHs are determined (see Shen, 2013, for review).

1.7 AGN at high-z

Beyond the local Universe Active Galactic Nuclei (AGN) form the basis of Supermassive Black Hole (SMBH) studies, thanks to their high emissions across a very broad wavelength regime, making them observable at the centre of their host galaxies across cosmic time (Padovani et al., 2017). AGN are observed throughout

the Universe, from redshifts $z \lesssim 1$ out into the early Universe at redshifts $z \geq 6$. Some of the highest redshift AGN found to date are those of Bogdan et al. (2023) and Larson et al. (2023), at $z \sim 10.3^{+0.6}_{-1.3}$ and $z = 8.679$ respectively

Being at high redshift has a visible effect on the observed, and potentially the intrinsic spectrum, of AGN. The simplest, but most important consideration, is that the distance to an emission source reduces the flux received by the observer. As such, AGN which are further from the observer (i.e. at higher-redshifts) must be intrinsically brighter in order to be observed over the background (see chapter 2). In addition, redshifting of the emitted spectrum shifts it to longer wavelengths (see e.g. Carroll, 2013). Thus the typical peak in an AGN's continuum emissions at rest frame UV/optical wavelengths (AGN having a stronger blue continuum than stars Warren et al., 1991) is shifted towards observed Infrared (IR) wavelengths.

Absorption of source emissions by molecular hydrogen between galaxies can be seen as a redshift dependent drop in the source continuum, blue-wards of the rest-frame Lyman-α line (i.e. at $(z+1)1215\,\text{Å}$, see Netzer, 2013). Studies such as Gilli et al. (2022) also suggest that, due to an increase in the gas content within early galaxies, AGN are more likely to show evidence of obscuration (see section 1.5 for an explanation of obscuration). Obscuration by gas and dust around the SMBH, or within the host galaxy itself, will reduce the intrinsic spectrum of the AGN which may then be further diluted by the host galaxy (Hickox & Alexander, 2018). Thus, in order to observe high-redshift AGN imaging at IR wavelengths or high energies (such as hard-band X-ray wavelengths) which are not completely absorbed by the obscuring material are required.

Despite the difficulties involved in finding high-redshift AGN, 100s of sources at $z > 5$ have been found to date (Inayoshi et al., 2020). However, as can be seen in plots such as that in figure 1.9, the number of observed AGN rapidly declines with redshift as only the brightest sources are easily visible (see also Vestergaard & Osmer, 2009; Pons et al., 2020; Matsuoka et al., 2023). Following the work of Schmidt et al. (1995), who found that the space density of AGN above $z = 3$ is declining, it is also typically expected that larger areas of sky must be imaged in order to find the few high-redshift AGN observable with current instruments.

Following the methods described in section 1.6, studies such as Willott et al. (2010) have performed mass measurements of high-redshift AGN finding them to have black hole masses of around $10^8 - 10^9\,\text{M}_\odot$ (see table 1 in Zubovas & King,

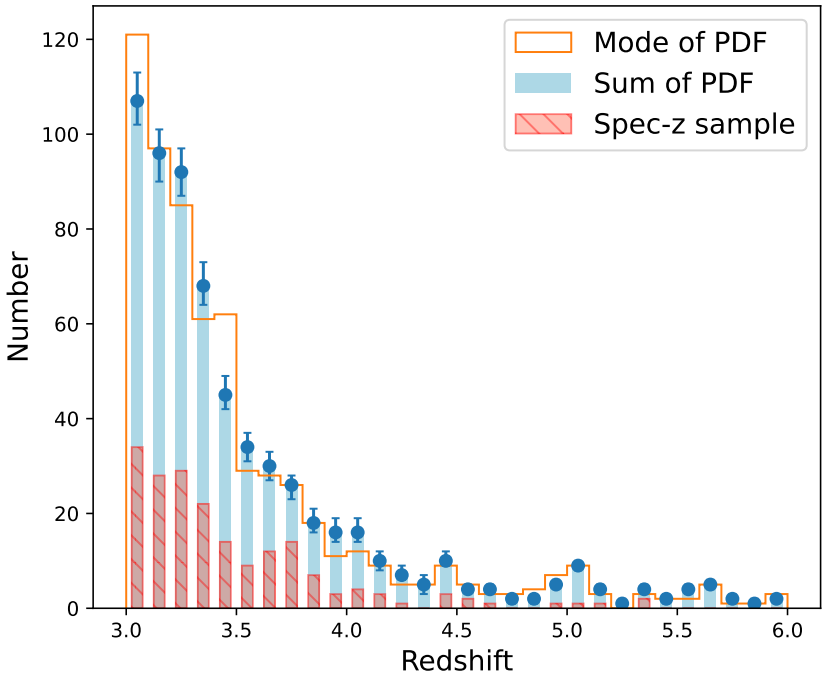

Figure 1.9 *Number of AGN with respect to redshift, as selected at $z \geq 3$ by Pouliasis et al. (2024) (based on soft-band X-ray detections), within the Chandra Deep Fields South (Luo et al., 2017) and North (Xue, 2017), Chandra COSMOS Legacy Survey (Civano et al., 2016), and XMM-Newton XXL survey North (Pierre et al., 2016). A rapid decline in the number of sources with increasing redshift can be clearly seen. It should also be noted that the large majority of AGN sources are found at $z < 3$, and thus would not enter into the sample plotted. Figure reproduced from (Pouliasis et al., 2024)*

2021, and references therein). These masses are comparable to those observed for SMBHs within the local Universe. From the SMBH seeding mechanisms discussed in §1.3, the initial mass of a SMBH will be several orders of magnitude smaller than these observed masses. Assuming a constant accretion rate at the Eddington limit the growth of a high-redshift AGN, of given observed SMBH mass and luminosity, can be traced back through time (see figure 1.10). Studies such as that by Orofino et al. (2018) find that, even if accretion proceeds continuously at the Eddington limit, it is not possible to attain all observed masses, with Zhu et al. (2020) finding that even with super-critical accretion black hole seeds of $\lesssim 10^4\,\mathrm{M}_\odot$ cannot reach observed masses. Assuming growth at the Eddington limit with different radiative efficiencies, corresponding to the spin of the SMBH, also impacts the rate of growth occurring, as shown in the left-hand of figure 1.10, with minimally spinning black holes accreting mass faster than those with some spin.

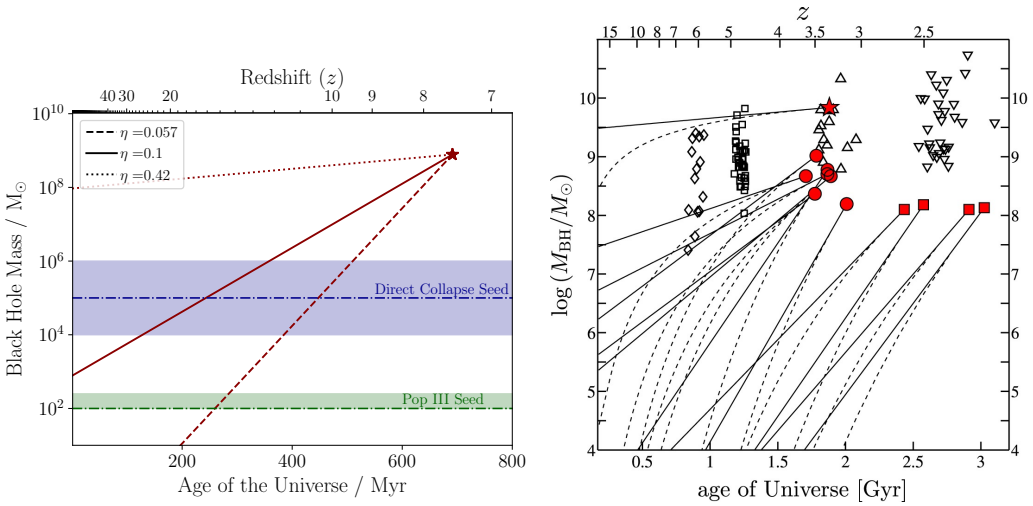

Figure 1.10 *Left: The predicted exponential growth of the Bañados et al. (2018b) $z = 7.5413$ AGN, assuming accretion at the Eddington limit with radiative efficiencies of a non-spinning Black hole, $\nu = 0.057$ (dashed), a maximally spinning black hole, $\nu = 0.42$ (dotted), and the typically assumed radiative efficiency, $\nu = 0.1$. The black hole seed mass ranges, $M_{seed} = 10^4 - 10^6\,M_\odot$ and $M_{seed} = 100 - 250\,M_\odot$, of DCBH (blue) and Population III remnant (green) respectfully, are shown. It can be seen that a non-spinning black hole is able to grow from both direct collapse and Pop III seeds, whilst a only direct collapse seeds can grow to the observed mass with a radiative efficiency of $\nu = 0.1$. A maximally spinning black hole is unable to attain the observed mass from either seeding mechanism. Right: Evolutionary tracks of known $z \sim 3.3$ AGN (red), assuming a radiative efficiency of $\nu = 0.1$ and a constant (solid) or $(1+z)^2$ evolving (dashed) accretion rate. Figure reproduced from Trakhtenbrot et al. (2016).*

With an accretion rate that evolves as $(1+z)^2$, but prevented from rising above the Eddington limit, Trakhtenbrot et al. (2016) find that continual AGN growth does allow for solar mass BH seeds to attain the observed masses (see right-hand of figure 1.10). In reality, however, no black hole will accrete at a constant or smoothly increasing rate. Instead AGN are expected to go through periods of high and low accretion (see e.g. Sharma & Sharma, 2024, and references therein). Thus, in order for the black hole to attain the observed masses, even greater mass growth is required during these periods of accretion. **So, how were these first black holes able to grow to the masses observed within only a few 100 Myrs?**

The growth of AGN populations and the evolution of accretion rate within these AGN, across cosmic time, can be traced by the Quasar Luminosity Function (QLF). The QLF describes the comoving space density of AGN as a function of

redshift and luminosity (e.g. Page et al., 1996; Boyle et al., 2000; Kalfountzou et al., 2014) and is measured using surveys of AGN selected using optical, IR, or X-ray data (Hopkins et al., 2007; Ross et al., 2013). The X-ray QLF will be discussed further in section 1.8.

With the recent launch of JWST, studies are beginning to identify AGN within the $z \gtrsim 6$ early Universe (e.g. Greene et al., 2023; Fujimoto et al., 2023; Bogdan et al., 2023; Matthee et al., 2024); through processes such as colour selection (identifying Little Red Dots), spectroscopic follow up of photometrically identified candidates and blanket spectroscopic follow-up revealing broad or narrow emission lines. These $z \gtrsim 6$ AGN hint at a substantial population of growing SMBH seeds. Due to the small areas surveyed so far, however, only the relatively low luminosity sources could be expected to be found. It is still only early days, but the spectral capabilities of JWST will be invaluable to future studies of high-z AGN.

1.8 X-ray observations of high-redshift AGN

As mentioned above (section 1.7), supermassive black holes must undergo a significant amount of mass growth within the early Universe. Study of the AGN population and its evolution with cosmic time, as is traced by the Quasar Luminosity Function (QLF), provides an insight into how such growth occurs. In order to obtain accurate measurements of the QLF, large unbiased samples of AGN across a wide redshift and luminosity range are required (Aird et al., 2015).

Many AGN have been identified through rest-frame UV/Optical selection, thanks to high resolution and large area surveys performed by IR and optical telescopes. However, this selection method is strongly biased towards the brightest sources, which are able to outshine their host galaxies, and are contaminated by stellar and gas processes within the host. X-ray selected AGN samples do not suffer from these effects; with very few processes within the host galaxy emitting at X-ray wavelengths it is only the very faintest AGN that are contaminated by the galactic X-ray emissions from X-ray Binaries (see e.g. Padovani et al., 2017).

The X-ray emissions from an AGN are produced by mechanisms very close in to the SMBH (see section 1.5), and thus will provide a very close tracer of the instantaneous accretion rate of the AGN and changes to this rate. As such, studies often perform X-ray follow-up of AGN identified within optical and IR samples in

order to further investigate the nature of these sources (e.g. Vignali et al., 2001; Brandt et al., 2002; Vito et al., 2019). The sensitivity of X-ray surveys is also, typically, well defined.

Although X-ray emissions from an AGN are affected by obscuration, this depends strongly on the rest-frame energy. Lower energy (soft-band) X-rays can be more easily absorbed than higher energy (hard-band) X-rays (Hickox & Alexander, 2018). Thus, as the same process of Compton up-scattering by the corona of the AGN produces hard and soft band energies (see section 1.5) the obscuration within an AGN can be determined from the observed ratio of hard to soft band energies, known as the Hardness Ratio. The effect of redshifting then causes harder rest-frame energies to be observed at soft-band energies.

It is the uncontaminated selection of AGN by X-ray observations, and their well defined sensitivity, that make X-ray surveys particularly useful for determining the QLF. Indeed, Lusso et al. (2023) found that X-ray observations may also uncover a population of AGN which cannot be identified at rest-frame UV/Optical (i.e. X-ray bright and optically normal galaxies as first discovered by Elvis et al., 1981). The X-ray QLF is known as the X-ray Luminosity Function (XLF), and forms the basis of the research I perform within this thesis.

The XLF is, simply, an observational characteristic of the AGN population which quantifies the number of AGN (per unit co-moving volume of the Universe) of a given X-ray luminosity and redshift, and can be modelled as a function of these two properties. Understanding the functional form of the XLF can provide a better understanding of the growth occurring across the AGN population throughout cosmic time. In figure 1.11 the change in appearance of the XLF with redshift, under different evolutionary dependencies can be seen. If the XLF shows evolution only in luminosity this indicates a change in the overall growth rate of the population (figure 1.11 shows such evolution as an increase in population accretion activity from $z = 0$ or $z = 2$), where as evolution within only the space density of AGN suggests a change in the number of AGN (figure 1.11 shows the apparent density evolution of an increasing number of AGN from $z = 0$ or $z = 2$). Other proposed forms of the XLF consider both the overall accretion rate and size of the population to evolve with cosmic time.

Many studies have performed fits of the XLF at different redshifts, using different X-ray surveys and parametric functional forms. Early observations of the evolutionary trends in AGN populations, such as that of Page et al. (1996),

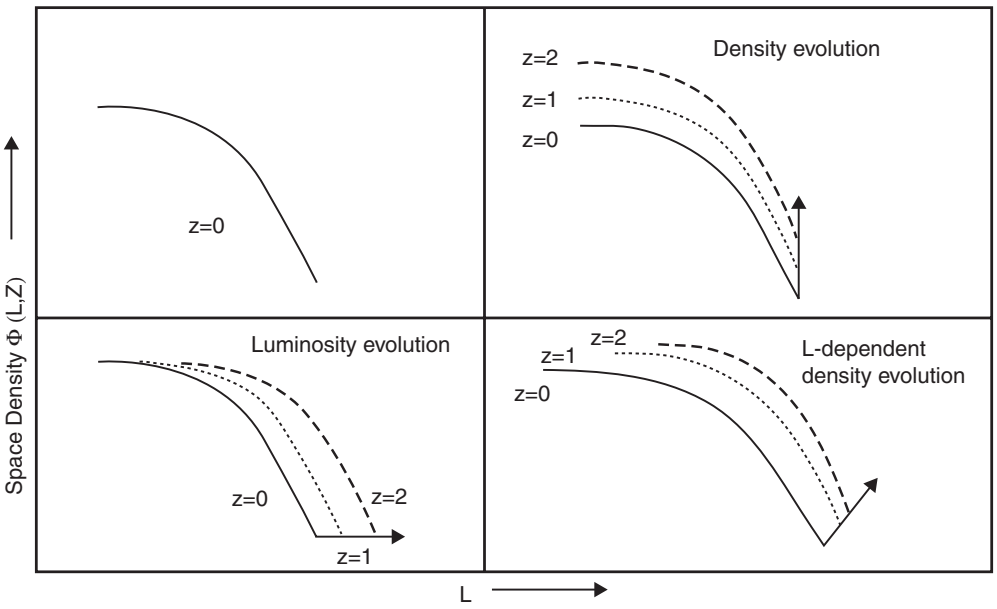

Figure 1.11 *Sketch of QLF, with different functional forms, demonstrating the change to these model QLF with redshift given the evolutionary dependency on source Luminosity and/or Space Density of the model's form. Figure reproduced from Netzer (2013).*

applied a Pure Luminosity Evolution (PLE) model to their data. However, studies performed over larger survey areas found a Pure Density Evolution (PDE) model was favoured (e.g. Schmidt, 1968). In order to account for X-ray background emissions, Gilli et al. (2007) proposed a form of the XLF that included Luminosity Dependent Density Evolution as well as incorporating an exponential component at high-luminosities that has been found by other studies to fit well to the observed population (e.g. Kalfountzou et al., 2014). In general the XLF is typically found to evolve substantially in both luminosity and density from $z \sim 0$ to the peak in AGN space density at $z \sim 2$ (e.g. Aird et al., 2015; Vito et al., 2014; Aird et al., 2010). Towards higher redshifts ($z \gtrsim 3$) the density of sources has been found to decrease (Vito et al., 2014; Brusa et al., 2009; Georgakakis et al., 2015) rapidly at all luminosities, a trend which is also found within Optical/UV data such as Shen et al. (2020). However, beyond $z \gtrsim 5$ there are few X-ray samples large enough to obtain a suitable fit to the form of the XLF, with the very recent study of Pouliasis et al. (2024) only beginning to attempt to fit a model to the XLF up to $z \sim 6$.

At high redshifts ($z \gtrsim 5$) there are typically too few AGN within a survey sample for a parametric XLF to be properly fitted. Within the Chandra Deep Field Survey, Luo et al. (2017) found only two $z > 5$ AGN, whilst Marchesi et al. (2016)

found only four $z > 6$ sources within the Chandra COSMOS-Legacy survey[5]. These samples of high redshift AGN have remained small due to both the observed decline in the number of AGN with redshift (seen in X-ray, Radio and Optical/IR studies, e.g. Lusso & Risaliti, 2016) and the depth of imaging required in order to find even intrinsically luminous AGN within the early Universe. As a result of the lack of high-redshift AGN samples the XLF at $z \gtrsim 5$, where early AGN growth is expected to occur, has remained poorly constrained.

1.9 This Thesis Layout

Despite the expected importance of Super Massive Black Holes (SMBHs), which reside in all galaxies, the formation and subsequent growth of these sources remains the subject of much debate. Mass measurements of SMBHs at redshifts around $z \sim 5-6$ find them to be comparable to the masses measured for SMBHs within the local Universe, and several orders of magnitude larger than the possible seed masses that have been theorised. Thus, these early SMBHs must have undergone very rapid growth within the first few 100 Myrs of the Universe. The X-ray Luminosity Function (XLF) could provide a tracer of this early growth, however at these high redshifts it has remained poorly constrained.

Using both large area and deep X-ray surveys, in order to find the brightest sources and the moderate luminosity sources where the majority of the population growth will be occuring, this Thesis aims to constrain the high redshift XLF. Investigating the obscuration within these populations I will further improve my constraints. Finally, with these obscuration corrected constraints on the XLF population at $z = 4-10$, I will perform preliminary predictions for the surveys possible with ESA's next X-ray Observatory NewAthena.

In chapter 2 I will introduce X-ray telescopes, outlining how they work as well as key observatories and the surveys that will be used in this work. Looking first at XLF estimations using the large sky area survey ExSeSS, chapter 3 details my initial constraints on the bright end of the $z = 5.7-6.4$ XLF. In chapter 4 I detail the process of obtaining measurements of the XLF at redshifts of $z = 4-10$, using *Chandra* and the COSMOS2020 sample of Weaver et al. (2022), and investigation of the effects of photometric redshift uncertainties and obscuration corrections on these measurements. Using these XLF measurements I will perform survey

[5]New IR data has allowed this number to be greatly increased, detailed in chapter 4

predictions for ESA's NewAthena Observatory, as detailed in chapter 5. Finally, in chapter 6, I will summarise my findings within this Thesis. Throughout this thesis I assume Flat ΛCDM cosmology with $H_0 = 70\,\mathrm{km\,s^{-1}Mpc^{-1}}$, $\Omega_M = 0.3$ and $\Omega_\Lambda = 0.7$, and all errors given are the 1σ uncertainties on the values.

Chapter 2

X-ray Telescopes

Observing Active Galactic Nuclei (AGN) at X-ray wavelengths provides information about the accretion occurring right at the heart of the system, near the Supermassive Black Hole itself (see chapter 1 for details). Unlike rest-frame optical and Ultra Violet (UV) observations, for which the AGN must be bright enough to be seen above the host galaxy, X-ray surveys of AGN do not suffer from strong biasing towards the brightest sources and are relatively uncontaminated by emissions from other processes in their host galaxy. As such, X-ray imaging provides some of the most important datasets available for AGN studies, as well as other areas of high-energy astronomy.

Observing at X-ray wavelengths can prove a challenge, thanks to the high energies of X-ray photons (defined as the energy range of 0.2-200 keV in Hickox & Alexander, 2018). The atmosphere of the Earth is also opaque to X-ray photons, even at the altitude of aircraft, thus telescopes specifically designed to be able to observe at X-ray wavelengths must be launched into space. The first X-ray telescope, *Uhuru*, was launched in the 1970s (Giacconi et al., 1971). Since then there have been multiple X-ray telescopes designed and launched, placing us now within the era of large X-ray observatories.

X-ray surveys form the basis of the work I have done in this thesis, using both large survey area instruments and high spatial-resolution observatories. In this chapter I will present an overview of how X-ray telescopes focus and detect X-ray photons, in section 2.1, detailing key characteristics of these telescopes. In section 2.2 I will then introduce the X-ray observatories and surveys used in this thesis.

2.1 How X-ray Telescopes Work

The underlying principle of all telescopes is essentially the same; virtually parallel beams of light enter the aperture of the telescope where it is then focused onto a detector which records the photons incident upon it in order to produce an image (Freedman, 2014). However, due to the high energies of X-ray photons, the design of an X-ray telescope's optics are very different to those of a UV or optical telescope.

X-ray telescopes focus incident photons through reflection. This requires very shallow grazing angles between the incident ray and the mirror otherwise the X-ray photons will simply pass through, and if it is dense enough they will be absorbed (Arnaud et al., 2011). The angle at which an incident X-ray meets the mirror is also important, as the higher the photon energy the smaller the critical angle (the maximum grazing angle for incident photons to be reflected). However, using denser mirror materials the grazing angle required for reflection to occur will be larger and more photons will be reflected. By layering materials, typically a high-density material and a low atomic number material (in order to provide a phase shift without absorbing the photon, and allow for additional reflections), the probability of an incident X-ray photon being reflected by the mirror, rather than penetrating it until it is absorbed, is increased (Seward & Charles, 2010). Thus, the mirrors in X-ray telescopes are typically made from gold, platinum or iridium (Seward & Charles, 2010), in order to be able to focus a larger range of X-ray photon energies.

The simplest configuration of mirrors for focusing X-rays is that of a single parabolic mirror, as shown in the left-hand diagram of figure 2.1, which focuses all incident photons (which are parallel to the axis of the parabola) to a single point, thanks to the nature of a parabola (see Arnaud et al., 2011, for details). In order to increase the area over which the telescope can collect and focus photons, known as the Field of View (FOV), multiple mirrors can be placed in a nested configuration. Although the parabolic mirror configuration can successfully focus incident X-rays to a single focal point, they cannot be used alone if a focal plane at which an image may be recorded is required. Wolter (1952) devised a number of more complex mirror configurations for X-ray instruments (initially with the intention of being used for X-ray microscopes) the most commonly used of which is the Wolter Type I configuration of a paraboloid mirror and a hyperboloid mirror, as shown in the right-hand diagram of figure 2.1. This configuration provides

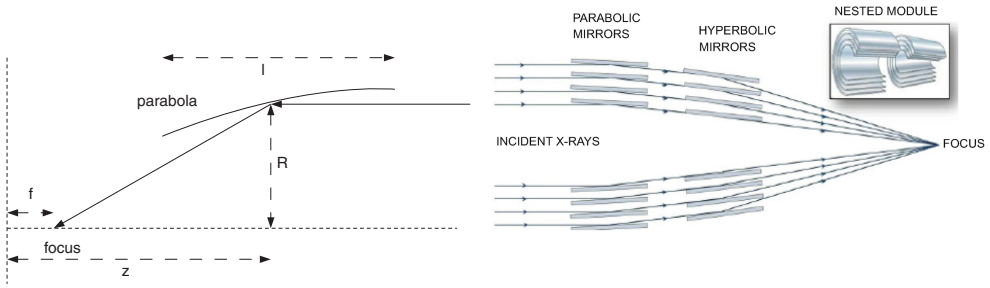

Figure 2.1 *(**Left**) Diagram showing the reflection of incident X-ray photons by a parabolic mirror. The incident X-rays strike the mirror at a shallow grazing angle and, being parallel to the axis of the parabola, are reflected down to the focal point of the mirror (shown here as "focus"). Figure reproduced from Arnaud et al. (2011). (**Right**) Diagram showing the focusing of X-ray photons using the Wolter (1952) Parabola and Hyperbola configuration of nested mirrors, as is typically used in telescopes such as Chandra. Figure reproduced from Christensen & Ramsey (2022).*

a large aperture-to-focal length ratio, thus telescopes utilising it do not have to be built as large as with other mirror configurations, in order to place the focal plane at the detector and within the telescope. Many telescopes are constructed from nested circles of a parabolic and then a hyperbolic mirror, made of layers of high-density and low-density materials. Another form of mirror, that makes use of the Wolter Type I configuration, is Silicon Pore Optics, which will be discussed later (in section 2.2.3).

In reality, refection within an X-ray telescope is not perfect. Contaminants within the mirror layers or on its surface can cause incident photons to be scattered, resulting in a halo of photons around what would be a point source and contributing to the Point Spread Function (PSF) of the telescope (Seward & Charles, 2010). In addition the structure of the telescope itself can block some photons from reaching the detector, an effect known as vignetting (Arnaud et al., 2011). Photons entering the telescope from sky positions further from the central axis of the telescope's line of sight (i.e. off-axis) have larger grazing angles when incident upon the outer mirrors in the nested configuration, which both reduces the effective area and contributes to vignetting. With knowledge of the internal structure of the telescope the vignetting can be modelled and through observations of known point sources the effect of contaminants (in addition to other properties of the mirror and detector) can be quantified, thus allowing for these imperfections to be taken into account when processing X-ray data.

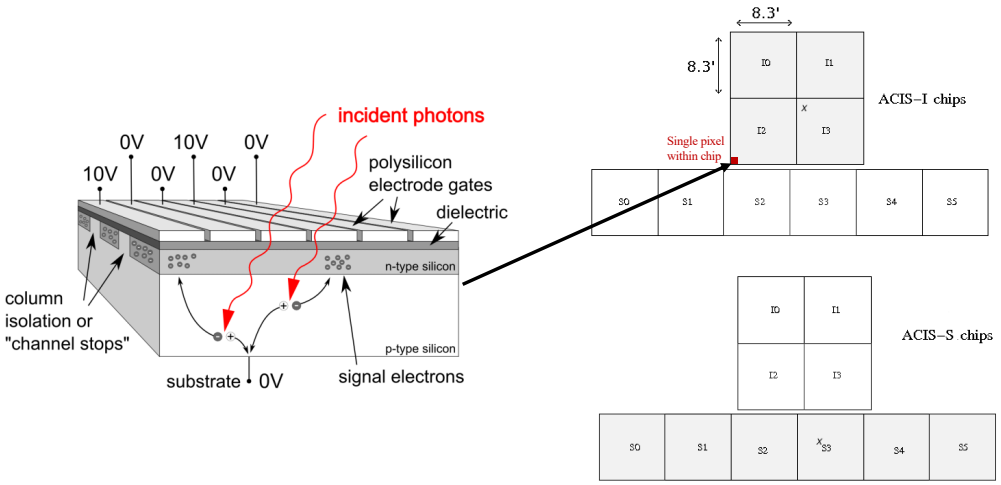

Figure 2.2 *Schematic of a CCD pixel (left) showing the release of electrons by an incident photon. Many of individual pixel units are set into an array to form a CCD chip, which are then place with other chips in order to form the detector plane (as shown on the right, for the ACIS detector within Chandra). Figure reproduced from Robbins (2014) and* `https://cxc.harvard.edu/cal/Acis/`.

Once the X-ray photons entering the telescope have been focused, their energy, arrival time, number and location within the focal plane, need to be recorded so that an image may be formed. A focused X-ray photon reaches the focal plane and enters the detector, and interacts with the material of the detector to produce a measurable response, such as the release of electrons due to the photoelectric effect (Arnaud et al., 2011). The detector is also protected from stray Optical/UV photons and high-energy particles, that would otherwise contaminate the X-ray detections, by an optical filter of material that is opaque to these longer wavelength photons and particles. Modern telescopes typically contain semi-conductor detectors, most common of which is the Charge-Coupled Device (CCD) formed of an array of linked capacitors (Seward & Charles, 2010). Incident X-ray photons produce an electron-hole pair within the semi-conductor material (see e.g. for an explanation of relevant semi-conductor physics Simon, 2013), the resulting free electron produces a measurable current through the detector array from which the energy and location within the CCD array of the incident X-ray photon is recorded. Higher energy photons will thus produce a higher current as more electron-hole pairs are created by the energy transferred. Through this process the energy of the X-ray photon can be recorded, given the measured

current, and thus all X-ray detectors are technically spectrometers. It should be noted that the time it takes for a detection to be recorded can result in multiple photons interacting with the detector material before the initial photon event has been read off, thus increasing the photon energy identified. Placing multiple individual detector units (i.e. pixels) within a grid (array) allows the location of an incident photon on the focal plane to also be recorded. The minimum difference in photon energy that a detector unit can discern between is it's energy resolution, which can depend on the material properties and detector design.

The size of a single CCD array is limited by the semi-conductor properties of the material. In order to achieve large scale CCD detectors single arrays, referred to as chips, are typically placed together on the detector plane, as shown in figure 2.2. However this results in narrow gaps between the individual chips, known as chip gaps. In order to image the areas of sky that the photons from which would otherwise fall into these chip gaps, and thus not be imaged, telescopes "wobble" in a pre-defined pattern as an observation is being performed, in a process known as dithering. This dithering also allows the CCD to image a larger area of sky than the telescopes FOV would otherwise allow.

When a photon has been detected there is a short delay before the charge has been read off and the pixel that detected it can detect another photon, referred to as the dead time. For detectors such as gas tubes this is the time it takes for the gas within to de-excite and return to neutral, whilst CCDs can be reset much faster through the application of a current to remove the electron-hole pair from the pixel location.

The response of a telescope, accounting for the mirrors and detectors, is typically defined by its response to a point source of photons. All photons from a single point source (i.e. any distant small object) will not reach the focal plane at a single infinitesimally small point, as a result of the optical design and the detector characteristics. The Point Spread Function (PSF) describes how spread out these photons become, and thus how much sky the point source appears to cover. The PSF is characterised by the resulting size of a point source such as the Full Width Half Maximum (FWHM), the diameter at which the brightness of a point source has dropped to 50%, or the Half Energy Width (HEW), the diameter over which half the total energy of the point source is spread. Imperfections and contaminants in the mirror surfaces can scatter photons whilst the size of pixels within the detector, and their sensitivity, all affect the PSF.

The PSF is amongst the most important properties by which to characterise an X-ray telescope, giving the smallest separation between point sources at which the telescope can resolve the individual sources. However, all properties defined here are important in characterising the capabilities of an X-ray telescope. These key properties are summarised in table 2.1.

2.1.1 The X-ray Background

In addition to the photons from sources being imaged, other photons from other sources within the effective FOV and high energy particles can be detected. This results in an X-ray background associated with each image. In order to successfully detect a desired source, the number of photons (counts) received by the telescope must be significantly above this background.

The X-ray background is comprised of the Cosmic X-ray Background (CXB) and the Particle Background. X-ray photons from unresolved sources such as galaxy clusters and AGN, as well as emissions from hot gas within the Galaxy or the intergalactic medium, all contribute to the overall background level of X-ray Photons that forms the CXB. The Particle Background stems from cosmic rays and solar flares, which can vary on short time scales or dominate the particle background during periods of high solar activity (Grant et al., 2002). Due to the high energies X-ray detectors must be sensitive to, the charged particles of the Particle Background which strike the detector can also be detected. The Earth's magnetic field is often used to protect X-ray telescopes from the particle background and thus they are place in low Earth Orbits, with the exception of *Chandra* and *XMM-Newton* which pass in and out of the Earth's magnetosphere (Arnaud et al., 2011).

The X-ray background must always be accounted for, with the amount contaminating an X-ray image depending on the telescope itself, as well as the length of time observed for. By observing a region of sky for longer, i.e. increasing the exposure time, sources that would otherwise be too faint to produce sufficient photons at the position of the source to be detected over the otherwise uniform background can be found. However, simply increasing the exposure time is not always the most efficient method for detecting more X-ray sources. Increasing the area of sky imaged at a given photon energy (effective area) or considering the photons detected within a given energy range may also aid in finding more sources.

Property	Description
PSF	The spread of photons from a point source due to the telescope's optics, imperfections and contaminants in the mirrors, and the detector properties.
HEW	The diameter of an aperture over which half of the total energy of the point source it is centred on, is contained.
FWHM	The diameter about which the brightness of a point source has dropped to 50%.
FOV	The area sky observable to the telescope, typically measured in terms of angle on the sky.
Energy Resolution	The minimum difference in the energy of two photons which can be measured by the detector.
Energy range	All photon energies for which the telescope can focus and detect.
Vignetting	Blocking and diffraction of light due to structures within the telescope.
Dithering	Motion of the telescope performed to prevent loss of imaged area due to gaps between detector chips or broken pixels.
Effective Area	The area of sky observable at a given photon energy, and the dither motion of the telescope during observation.
Dead time	The time during which a pixel within the detector cannot record an incident photon due to a previous photon event.
Exposure time	The length of time for which the telescope is observing and recording photons for a single image.
Background	X-ray photons not associated with a resolvable source.
Eddington Bias	Random Poisson fluctuations within the emission of photons (up or down) which results in more faint sources being detected due to the rising number density of sources towards fainter fluxes.

Table 2.1 *A summary of the key characteristics of X-ray telescopes and imaging.*

2.1.2 Eddington Bias

Within a given duration of time the emission of photons from a source is ultimately random, following a Poisson distribution of photon energy and number. As such, within a given exposure time, it is possible for a random fluctuation in the number photons received from a source to result in a higher (or lower) photon count than its true flux.

This effect can result in a number of sources that would otherwise be too faint to be detected appearing above the background, or sources that should be observable falling below the photon count of the background and thus being undetected. As the number density of fainter sources is higher than that of brighter sources, this random fluctuation in the measured source counts will result in more fainter sources fluctuating upwards, and thus being detected, than brighter sources fluctuating downwards. This effect is know as the Eddington bias.

2.2 X-ray Telescopes and this Thesis

The work carried out in this thesis uses X-ray survey imaging from a large sky area survey telescope, the X-ray Telescope on the *Neil Gehrels Swift Observatory* (*Swift,* Gehrels et al., 2004), and high resolution survey imaging from the *Chandra* X-ray Observatory (Weisskopf et al., 2002). In this section I will give a brief introduction to design of *Swift* (section 2.2.1) and *Chandra* (section 2.2.2), before looking to the future of X-ray astronomy in section 2.2.3.

2.2.1 Swift and ExSeSS

The *Neil Gehrels Swift Observatory* (hereafter *Swift,* Gehrels et al., 2004), shown in figure 2.3, is a multi-wavelength rapid-response telescope, designed for gamma-ray burst (GRB) astronomy (see van Paradijs et al., 2000, for a review on GRBs). Swift is comprised of three instruments; the Burst Alert Telescope (*Swift*-BAT; Barthelmy, 2005) which detects GRBs, a UV/Optical telescope (*Swift*-UVOT; Roming et al., 2005) to provide low resolution spectra of bright GRBs, and crucially the X-ray Telescope (*Swift*-XRT; Burrows et al., 2005) capable of performing targeted and survey imaging across an energy range of 0.2-10 keV.

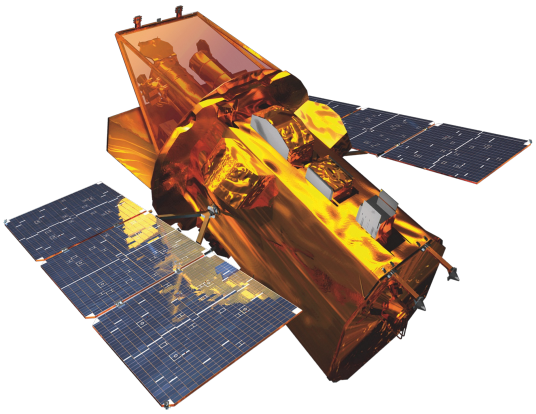

Figure 2.3 *Artist's impression of the Neil Gehrels Swift Observatory. Image source:* https://imagine.gsfc.nasa.gov/observatories/learning/swift/multimedia/spacecraft_art_gallery.html

Comprised of nickel and gold coated mirrors (see e.g. Wells et al., 1992) in the type I Wolter configuration (see above) and focal plane CCD detector, *Swift*-XRT has a 23.6 arcmin FOV and a PSF of 18 arcsec HEW, and maximum effective area of $\sim 110\,\mathrm{cm}^2$ when imaging at an energy of 1.5 keV. Set into a low-Earth orbit, it also has a low Particle background, improving the sensitivity (other survey telescopes such as eROSITA do not benefit from such a reduced particle background). Within a few minutes of receiving an alert, from *Swift*-BAT or gravitational wave alerts, *Swift* rapidly re-orients itself to image the region of sky that the alert originated from, with the *Swift*-XRT. The XRT is also used to perform targeted imaging of known X-ray sources. As a result the *Swift*-XRT has observed almost 4000 degrees^2 of sky over its lifetime.

Using the catalogue of all *Swift*-XRT observations performed from 2005 and 2008 (the 2SXPS catalouge of Evans et al., 2020), Delaney et al. (2023) constructed a catalogue of only extragalactic X-ray sources which had been serendipitously imaged (i.e. were not targeted observations) by *Swift*-XRT, known as the Extragalactic Serendipitous Swift Survey (ExSeSS). This was done by removing all observations which covered the galactic plane, the Large and Small Magellanic Clouds, M31 and M33, as well as a region around all sources that were specifically targeted by *Swift* (see Delaney et al., 2023, and section 3.1 for details of the sample creation). The resulting ExSeSS catalogue of 79 152 serendipitous X-ray sources covers 2086.6 degrees^2 and will be used in chapter 3, in order to study the bright-end of the high-redshift AGN population.

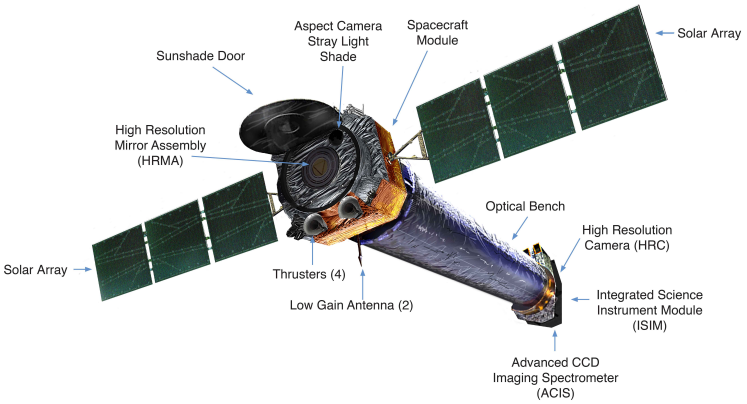

Figure 2.4 *Illustration of the Chandra X-ray Observatory, with key components labelled. Image credit: NASA/CXC.*

2.2.2 Chandra

Launched in 1999, the *Chandra* X-ray Observatory has long been one of the most sensitive X-ray telescopes available, and a flagship mission of NASA (see Weisskopf et al., 2002, for a summary). The High Resolution Mirror Assembly (HRMA), which provides *Chandra*'s unprecedented 0.5 arcsec angular resolution, consists of eight precision-polished iridium-coated mirrors set in a nested type I Wolter configuration (as shown on the right in figure 2.1). *Chandra* hosts both a high-resolution camera and Advanced CCD Image Spectrometer (ACIS, Garmire et al., 2003), with which it performs observations across 31 arcmin and 17 arcmin FOVs, respectively (Weisskopf et al., 2002). ACIS is one of the largest CCD detectors currently in operation (Arnaud et al., 2011), and has an energy range of 0.2-10 keV. Figure 2.4 shows a diagram of Chandra and its key components.

During its lifetime, *Chandra* has performed many deep surveys (see Brandt & Alexander, 2015; Xue, 2017, for reviews), although the total area of sky imaged remains relatively small. The deepest survey performed by Chandra, to date, is the Chandra Deep Field South (CDF-S, Luo et al., 2017), comprised of 102 individual observations (pointings) and covering a total of 484.2 arcmin^2 of sky to reach a combined maximum exposure time of $\sim$ 7 Ms. In this thesis I will use the Chandra-Legacy survey of Civano et al. (2016) which, although it only reaches a maximum exposure time of $\sim$ 160 ks, covers $\sim$ 2 degrees^2 of sky across the COSMOS field for which there is a wealth of multi-wavelength imaging from many other observatories (see section 4.1 for details). The sensitivity provided by Chandra allows studies of moderate luminosity AGN to be performed.

2.2.3 The Future of X-ray Telescopes

All telescopes are designed with a nominal mission duration, which is often exceeded. Although observatories such as *Chandra* and *Swift* are now well beyond their originally designed lifetimes, 5 years and 8 years, respectively (see Weisskopf et al., 2002; Gehrels et al., 2004), the future of X-ray astronomy is far from over.

Amongst the next generation of X-ray observatories are the X-ray imaging and spectroscopy mission (XRISM; Tashiro, 2022), launched in September of 2023, and the extended ROentgen Survey with an Imaging Telescope Array (eROSITA; Predehl et al., 2021), launched in July of 2019 (although not currently operating[1]). Also under development are telescopes such as NewAthena (see Nandra et al., 2013, and chapter 5) and concepts such as the Advanced X-ray Imaging Satellite (AXIS; Reynolds et al., 2023), to be launched in the first half of 2032 if selected by NASA.

The development of Silicon Pore Optics (SPO, Willingale et al., 2013; Beijersbergen et al., 2004) will likely be at the forefront of the development of future X-ray observatories. Previously proposed in the designs ESA's XEUS mission (Kraft et al., 2005) and IXO (Collon et al., 2010), SPO utilises wafers of silicon into which fine grooves are cut (as shown in figure 2.5) and coated with a thin layer of highly dense material to form a surface from which X-ray will reflect. These wafers are then stacked together into multiple mirror shells, and thus mirrors with a large effective area are achieved. As with most X-ray telescopes, the internal geometry of the silicon grooves, or "pores", follow the parabolic and hyperbolic configuration of Wolter (1952).

Most notably for the work presented in this thesis, given it's potential to image large sky areas to high depths (as required for fitting the XLF, see section 1.8), is the next flagship X-ray mission of ESA, the NewAthena X-ray Observatory (Nandra et al., 2013). Although still under development, and not due to launch until the late 2030s, NewAthena will be comprised of a SPO mirror as well as hosting both a Wide Field Imager (WFI; Rau et al., 2013) and X-ray Integral Field Unit (X-IFU; Barret et al., 2023). I will discuss NewAthena and the prospects for its survey capabilities further in chapter 5.

[1] https://www.mpg.de/21468451

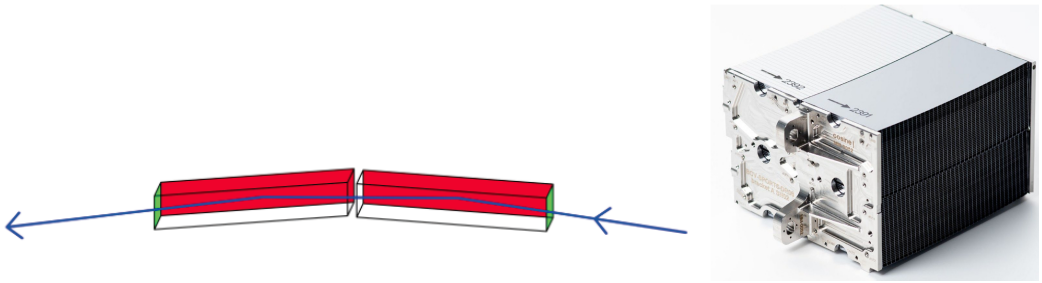

Figure 2.5 *(Left) Sketch of the geometry of a single pore within a silicon pore optics module. Following the Wolter Type I configuration, the pore has one section with a parabolic surface and a second with a hyperbolic surface. The principle plane of the mirror lies within the small gap between the two sections. Figure reproduced from Willingale et al. (2013) (Right) Image of a silicon pore module, comprised of many individual pore sections, as under development for the NewAthena X-ray Observatory. Reproduced from Bavdaz et al. (2023)*

Chapter 3

Constraints on the X-ray Luminosity Function of AGN at $z = 5.7 - 6.4$ with the Extragalactic Serendipitous Swift Survey

Supermassive Black Holes (SMBHs) play a crucial role within the Universe, impacting the growth of galaxies across cosmic time (see chapter 1.1). However, the formation and subsequent growth of these sources within the early Universe remains poorly constrained.

As discussed in chapter 1, the growth of AGN populations across cosmic time and the evolution of AGN accretion rate is traced by the X-ray Luminosity Function (XLF). Due to the strong decline in AGN space density and depths required in order to detect even intrinsically luminous AGN at the earliest times, the samples of X-ray selected AGN at $z \gtrsim 5$ have remain extremely small: 2 with photometric redshifts in the $\approx$ 7 Ms Chandra Deep Field South (Luo et al., 2017), 2 with spectroscopic redshift (the highest at $z = 5.3$) and 7 with photometric redshifts (4 of which are at $z > 6$ with the highest at $z = 6.85$) in the Chandra COSMOS-Legacy survey (Marchesi et al., 2016). Yet even with samples of just a few AGN at these very high redshifts, we can begin to place important constraints on the XLF.

In this chapter, I present the observational constraints on the XLF at $z > 6$

given by sources within the Extragalactic Serendipitous Swift Survey (ExSeSS) catalogue (Delaney et al., 2023). ExSeSS covers a total sky area of ∼2000 deg^2 and reaches ultimate flux limits of $f_{0.3-10\mathrm{keV}} \sim 10^{-15}$ erg s^{-1} cm^{-2} for $\sim 0.1\%$ of the area, which are considerably deeper than the current *eROSITA* all-sky coverage. I identify only one $z > 6$ X-ray source within ExSeSS, the source being associated with a previously known quasar with a spectroscopic redshift of $z = 6.31$. Given the serendipitous nature of ExSeSS both the sensitivity and, consequently, the survey volume can be well-defined, allowing us to place direct observational constraints on the space density of luminous X-ray AGN at $z > 6$. We then compare the estimated XLF and limits to extrapolated model XLFs from previous studies.

The source catalogue used in this study, ExSeSS, is introduced in §3.1, while the process to identify high-redshift sources is outlined in §3.2. In §3.3.1 I compare predicted source yields based on extrapolations of current XLF models to the observed sample, while in §3.3.2 I use this data to place constraints on the XLF. I also compare the constraints from my X-ray observations to existing estimates of the bolometric Quasar Luminosity Function from rest-frame optical/UV samples (§3.3.3). I summarise my findings and present the conclusions in §3.4. Throughout this chapter I assume a flat ΛCDM cosmology, with $H_0 = 70.0\,\mathrm{km\,s^{-1}Mpc^{-1}}$, $\Omega_\gamma = 0.7$ and $\Omega_m = 0.3$, and all errors given are the 1σ uncertainties on the values.

3.1 The ExSeSS catalogue

The studies performed in this paper make use of the sample of X-ray sources from the Extragalactic Serendipitous Swift Survey (ExSeSS), as defined by Delaney et al. (2023). Here, we give a brief overview of the sample construction and the vital step to define the area coverage and sensitivity of the survey that enables our measurements of the X-ray Luminosity Function (XLF).

The X-ray Telescope on the *Neil Gehrels Swift Observatory* (hereafter the *Swift*-XRT; Burrows et al., 2005) has performed both targeted observations of X-ray sources and searches for unknown X-ray counterparts to transient sources, often following the detection of Gamma-ray bursts by *Swift*'s own Burst Alert Telescope (*Swift*-BAT). Thus, *Swift*-XRT has obtained imaging of nearly 4000 degrees^2 of sky throughout its observing life (as of August 2018; Evans et al., 2020). The

ExSeSS sample was formed using the second *Swift*-XRT Point Source (2SXPS) catalogue of Evans et al. (2020) that identified all point sources in the full data set provided by *Swift*-XRT observations between 2005 January 01 and 2018 August 01. The effect of contamination by Galactic sources and nearby, individually resolved sources in nearby galaxies was reduced by removing the areas of sky corresponding to the Galactic plane (Galactic latitudes $|b| < 20°$), the Large and Small Magellanic Clouds, M31 and M33, ensuring the sample is dominated by extragalactic sources. In addition, only fields identified as *ultra-clean* (field flag=0) in 2SXPS are included in the ExSeSS datasets and only sources with a *good* detection flag are included in the sample.

In order to create a truly serendipitous sample and remove any sources that may bias the sample due to association with the target, all target objects were removed along with any associated X-ray detections using regions of the radius of the source (where an extended counterpart could be identified, e.g. a host galaxy) and adopting a minimum radius of 2 arcmin. Medium (1-2 keV), hard (2-10 keV) and total (0.3-10 keV) energy band detections by *Swift*-XRT were taken, and wherever there are multiple observations of sky only the stacked images are used in order to maximise the exposure time. This process to create the ExSeSS sample is detailed in Delaney et al. (2023).

A key feature of ExSeSS is that that the survey volume can be defined, enabling our goals to place constraints on the XLF. The area of sky surveyed by *Swift* to different exposure times is carefully tracked and well defined, enabling an accurate quantification of the "area curve", giving the area of sky covered by ExSeSS to different X-ray flux limits (see figure 5 of Delaney et al., 2023). Delaney et al. (2023) use simulations (from Evans et al., 2020) to determine the area curves in the soft, hard and total energy bands. They are calculated using the sky area coverage of the survey, excluding the areas within the specified radius of target sources and areas corresponding to the Galactic plane and nearby galaxies, thus matching the sample definition described above (see Delaney et al., 2023, for details).

It is these area curves, and the serendipitous nature of the survey, that enable us to perform measurements of the X-ray Luminosity Function based on the ExSeSS sample.

The resulting ExSeSS catalogue is comprised of 79 152 X-ray sources and covers 2086.6 degrees^2 of sky

3.2 Identifying X-ray Luminous High-Redshift Sources

In order to apply constraints to the high redshift X-ray Luminosity Function (XLF) with ExSeSS, I searched for all $z > 5.7$ sources in ExSeSS.

While a full statistical cross-matching between ExSeSS sources and multi-wavelength surveys, to identify robust counterparts, will be presented in a future work, here I adopt a simple cross-matching to existing redshifts in the SIMBAD Database (Wenger et al., 2000). I use a maximum separation on the sky of 9 arcsec, given by the half-energy width of the point spread function of the *Swift*-XRT (corresponding to the 2σ median positional uncertainty) with $> 90\%$ of all ExSeSS sources having a positional uncertainty of less than this value. 18 363 potential counterparts to the ExSeSS sources with pre-existing redshifts in SIMBAD were identified.

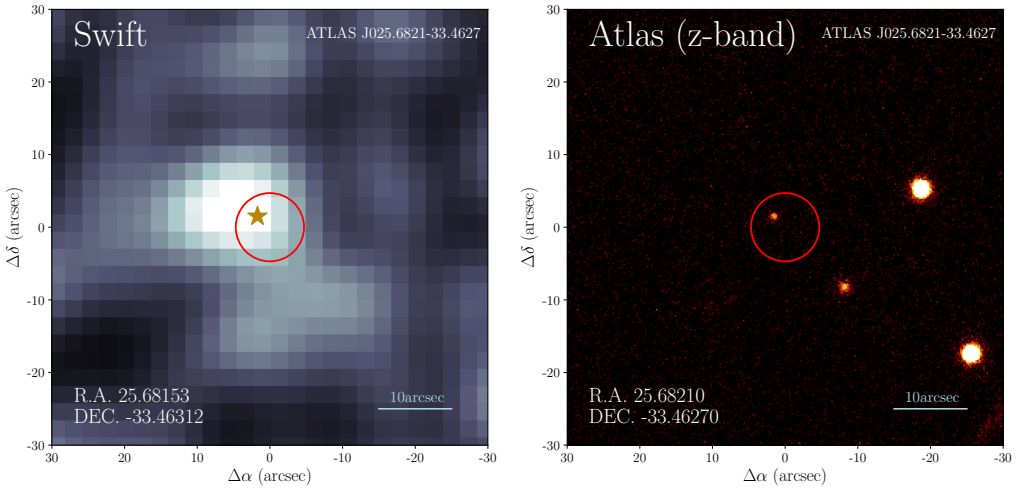

Figure 3.1 *The high redshift AGN ATLAS J025.6821-33.4627, identified in ExSeSS. The stacked 0.3–10 keV X-ray image from Swift (left), smoothed by a Gaussian of $\sigma \sim 2$ pixels corresponding to the half-energy width of the PSF of Swift (9 arcsec), and the z-band Atlas image (right) are shown. The optical position of the source is shown on the Swift image by the gold star. The radius of the solid red circles correspond to the 4.7 arcsec positional uncertainty of the source in Swift, centred on the observed soft-band position. It is clear from these images that no additional z-band sources lie within the positional uncertainty of the X-ray source, indicating that the association between ATLAS J025.6821-33.4627 and the Swift X-ray detection is reliable. The sky coordinates of the optical and X-ray sources are given in the corresponding image.*

I note that the majority of ExSeSS sources do not have pre-existing counterparts or redshift measurements. Nevertheless, following this initial cross-matching I identified one high-redshift ($z > 6$) counterpart to the ExSeSS X-ray sources, that of 2SXPS J014243.7-332742, corresponding to the previously optical/IR detected quasar ATLAS J025.6821-33.4627. This source was then visually checked to ensure there are no other potential counterparts to the X-ray source. At near-infrared wavelengths ATLAS J025.6821-33.4627 appears as a point source, as can be seen in Figure 3.1, with a separation of 2.3 arcsec between the ExSeSS source and the counterpart and no other sources within the 4.7 arcsec uncertainty of its X-ray position. I assessed the probability of a spurious alignment using the number of sources in the Ross & Cross (2020) catalogue over the total area covered by their sample to estimate the sky density of high-z AGN. This sky density is then multiplied by our search area, corresponding to a 9 arcsec radius around all 79 152 ExSeSS sources, to obtain the estimated probability of a spurious alignment. I find the probability of spurious alignment between an ExSeSS source and a known high-z AGN to be only 0.03, indicating that the ExSeSS source and the counterpart identified are most likely the same source.[1]

ATLAS J025.6821-33.4627 is detected in a stacked dataset, comprised of 18 separate *Swift*-XRT observations with a total exposure time of 189 ks (see Evans et al., 2020; Delaney et al., 2023, for details). The total (0.3–10 keV) band X-ray flux of this source was estimated from the measured total-band count rate, observed by the *Swift*-XRT, using a conversion factor of 3.256×10^{-11} erg s^{-1} cm^{-2}/(counts s^{-1}) [2], following the process in Delaney et al. (2023). The rest-frame 2–10 keV X-ray luminosity was then determined from the observed 0.3–10 keV flux, assuming a power-law of photon index $\Gamma = 1.9$. I note that the estimated X-ray luminosity of this source does not change significantly (compared to the quoted uncertainty based on the Poisson errors in the observed X-ray count rate) when assuming $\Gamma = 1.6$ to 2.2 and thus this assumption is reasonable. Given the high redshift of the source, the observed 0.3–10 keV band probes high rest-frame energies (~2.2–73.1 keV) and thus the observed flux would only be significantly suppressed by intrinsic column densities of $N_{\rm H} \gtrsim 10^{23}$ cm^{-2}. Given that the source exhibits broad optical emission lines, it is unlikely to be

[1] Evans et al. (2020) estimate that $\lesssim 0.3\%$ of the "good" X-ray detections in 2SXPS, used to construct ExSeSS, are spurious X-ray detections. Thus the chance of a spurious X-ray detection *and* spurious alignment with a known high-z quasar is extremely low ($\lesssim 0.009\%$).

[2] I adopt a fixed flux conversion that assumes a Galactic absorption with a column density of $N_{\rm H} = 2.50 \times 10^{20}$erg s^{-1} cm^{-2} (HI4PI Collaboration et al., 2016) and a photon index of $\Gamma = 1.9$ (e.g. Kalfountzou et al., 2014) calculated using *WebPIMMS*, which matches the assumptions used to calculate the ExSeSS area curves.

Table 3.1 *The Swift X-ray position and observed X-ray properties of the high-redshift ExSeSS source, along with the ATLAS z-band AB magnitude, spectroscopic redshift (z_{spec}), the rest-frame 2–10 keV luminosity calculated from the total-band flux, monochromatic luminosities at X-ray and optical wavelengths and the optical–to–X-ray slope, $\alpha_{\rm OX}$ (see Equation 3.1).*

Object	ATLAS J025.6821-33.4627
RA (deg)	$25.68211^{+0.00081}_{-0.00073}$
Dec (deg)	$-33.46189^{+0.00057}_{-0.00056}$
Total 0.3–10 keV counts	63
Net 0.3–10 keV counts	19.31
0.3–10 keV count rate (cts s^{-1})	$1.4^{+0.6}_{-0.5} \times 10^{-4}$
$f_{0.3-10\rm keV}$ (erg s^{-1} cm^{-2})	$4.59^{+1.84}_{-1.69} \times 10^{-15}$
z_{ABmag}	19.63 ± 0.06
z_{spec}	6.31 ± 0.03
$L_{\rm X_{2-10keV}}$ (erg s^{-1})	$8.47^{+3.40}_{-3.12} \times 10^{44}$
$L_{\rm 2keV}$ (erg s^{-1} Hz^{-1})	$2.01^{+0.80}_{-0.74} \times 10^{27}$
$L_{\rm 2500Å}$ (erg s^{-1} Hz^{-1})	$3.90^{+0.23}_{-0.21} \times 10^{31}$
$\alpha_{\rm OX}$	$-1.65^{+0.06}_{-0.09}$

heavily obscured at X-ray wavelengths and thus I have not applied any additional correction for intrinsic absorption when estimating the rest-frame 2–10 keV luminosity. The source is only detected in the total 0.3–10 keV energy band, with 19.31 net counts, and thus we do not have sufficient constraints to make a direct estimate of photon index or absorption column. The 0.3–10 keV band observed flux and rest-frame 2–10 keV band luminosity, with the sky coordinates of this high redshift X-ray source and spectroscopic redshift of the counterpart, are given in Table 3.1.

ATLAS J025.6821-33.4627 was originally identified as a candidate high-redshift quasar by Carnall et al. (2015), based on its combined WISE and VST ATLAS colours, indicative of a $z = 5.7 - 6.4$ source. Follow-up spectroscopy was obtained, by Carnall et al. (2015), using the Low Dispersion Survey Spectrograph 3 on the Magellan-II telescope from which a redshift of $z = 6.31 \pm 0.03$ was calculated based on the broad Lyman-α line in the source's spectrum. The X-ray properties of ATLAS J025.6821-33.4627 from 2SXPS are included in the compilation of known high-redshift quasars by Vito et al. (2019) but I now identify this source as a serendipitous X-ray detection with ExSeSS: I stress that ATLAS J025.6821-33.4627 was *not* the target of the *Swift* observation. Comparing to known X-ray detected high-redshift AGN (see Khorunzhev et al., 2021, and references there in), as shown in figure 3.2, ATLAS J025.6821-33.4627 can be seen to lie just above

the limit of the deepest sensitivity expected with eROSITA (that obtained at the Polar regions after 4 years of the survey; eRASS:8). Whilst X-ray detections of many $z > 5$ AGN have been reported, most are the result of targeted X-ray observations; very few X-ray detections have been obtained *serendipitously* or within dedicated survey fields (see figure 3.2), either of which is required to have a well-defined survey area that can be translated into a survey volume, enabling measurements of space densities and the XLF. With a rest-frame 2–10 keV X-ray luminosity of $L_{\rm X} = 8.47^{+3.40}_{-3.13} \times 10^{44} {\rm erg\,s^{-1}}$, in ExSeSS, ATLAS J025.6821-33.4627 is likely the highest redshift, spectroscopically confirmed, serendipitously X-ray detected quasar known to date.[3]

During the cross-matching of sources within ExSeSS a second bright X-ray source was matched to the previously identified Quasar 5C 2.183, with an spectroscopic redshift from the SDSS database of $z = 6.16892 \pm 0.00060$ (Pâris et al., 2017). However, as this source was detected in u, g, r, i, and z-bands of SDSS as well as the G-band of Gaia, not possible in a $z \gtrsim 5$ source, closer inspection of the SDSS spectrum of the source was performed. From this spectrum it can be seen that the redshift of the source is in fact $z = 0.714$ as identified by other studies (Machalski, 1998; Pâris et al., 2018; Chen et al., 2018) and thus this is not an additional high redshift AGN within ExSeSS.

With this contaminant removed, and no other high-redshift sources identified in ExSeSS, I can give a tentative number of high redshift sources with X-ray luminosities high enough to be detectable by Swift-XRT at $z \gtrsim 6$, which I can compare to predictions based on model extrapolations and use to place constraints on the XLF (see § 3.3 below). However, I first examine the X-ray and optical properties of ATLAS J025.6821-33.4627 in more detail.

3.2.1 Optical to X-ray Properties of ATLAS J025.6821-33.4627

High-redshift AGN are often selected based on their optical and UV properties. Whilst ATLAS J025.6821-33.4627 is a highly luminous source at optical wavelengths, I have shown that it is identified serendipitously based on X-ray selection as part of ExSeSS. In order to investigate its nature and the

[3]Since completion of this work and submission as a paper, Wolf et al. (2022) have reported a low-significance X-ray detection of a quasar with a spectroscopic redshift of $z = 6.56$ in the 140 deg^2 eFEDS field.

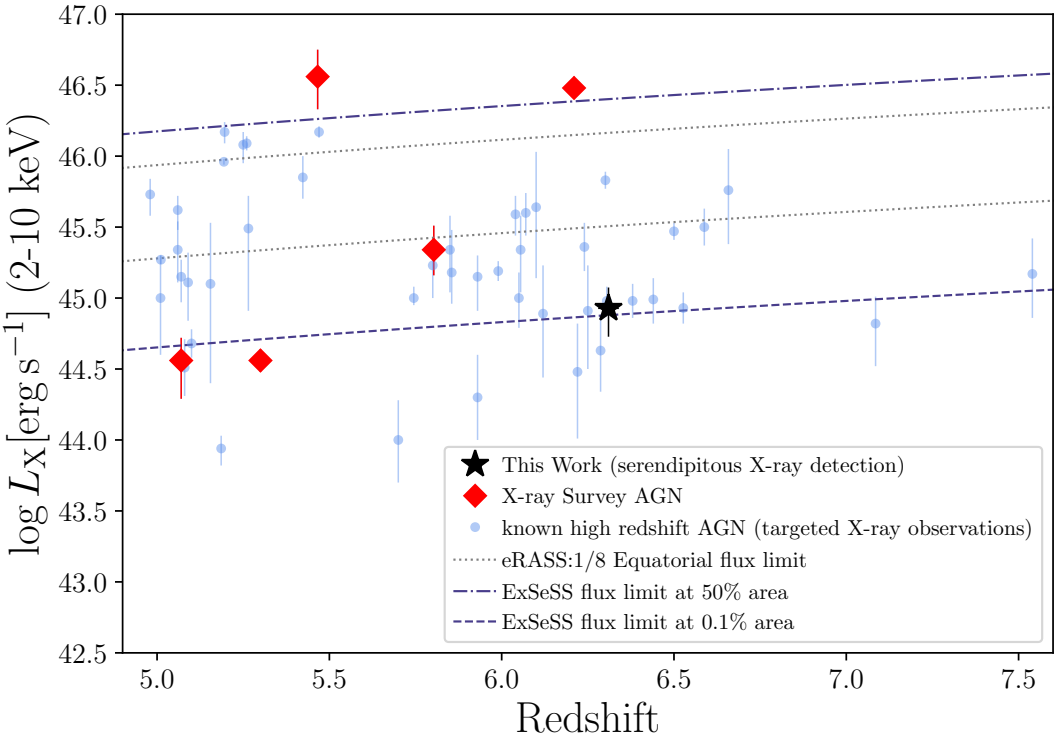

Figure 3.2 *The X-ray luminosity of the $z > 6$ ExSeSS source with respect to redshift (black star). Known high-redshift AGN with spectroscopic redshifts, detected using targeted X-ray observations (see Khorunzhev et al., 2021, and references therein), are shown by the light blue points. The few high-redshift sources that are detected in the dedicated eROSITA and COSMOS X-ray survey fields are shown for comparison (red diamonds). This source, which was serendipitously detected within ExSeSS, is the highest redshift source identified by X-ray surveys with a well-defined area coverage from which an XLF can be determined. The sensitivity limits of ExSeSS, for 50% and 0.1% (the flux limit of ExSeSS) of the total area, are show by the dot-dashed and dashed purple lines respectively. For comparison, the eROSITA sensitivity limits are shown by the dotted grey lines, the upper line showing after 6 months (eRASS:1) and the lower showing the limit after 4 years (eRASS:8), in the equatorial region (Predehl et al., 2021; Sunyaev et al., 2021). My ExSeSS $z > 6$ quasar can be seen to lie close to the sensitivity limit achieved by ExSeSS, below the eRASS limits, and is the highest redshift, serendipitously X-ray detected AGN to date.*

relation between the emissions of its accretion disk and X-ray corona, I determine the optical-to-X-ray relation of the source, as in Vito et al. (2019) (see also Tananbaum et al., 1979), given by

$$\alpha_{\rm OX} = 0.3838 \log \left(\frac{L_{\rm 2keV}}{L_{\rm 2500\mathring{A}}} \right) \tag{3.1}$$

where the optical-to-X-ray slope, $\alpha_{\rm OX}$, is given by the ratio of the monochromatic X-ray luminosity of the source at a rest-frame energy of 2 keV, $L_{2\ \rm keV}$, and the optical luminosity of the source at a rest-frame wavelength of 2500 Å, $L_{2500\mathring{A}}$. I determine the optical luminosity using the observed z-band luminosity and assuming a power-law continuum of $f_\nu \propto \nu^{\alpha_\nu}$, with $\alpha_\nu = -0.3$ (see Bañados et al., 2016; Pons et al., 2020, and references therein), as detailed in appendix A. The 2 keV luminosity is determined from the 2–10 keV band luminosity assuming a photon index of $\Gamma = 1.9$ (see equation A.3 in the appendix). The values used are given in table 3.1.

I find that the optical-to-X-ray slope of ATLAS J025.6821-33.4627 is $-1.65^{+0.06}_{-0.09}$, which lies within the 1σ scatter of the $\alpha_{\rm OX} - L_{2500\mathring{A}}$ relation of Nanni et al. (2017) (as shown in figure 3.3). Thus, although this is a relatively optically bright source, such an optical luminosity is consistent with that expected, given its X-ray luminosity. This indicates that the accretion mechanism in this high-redshift source is likely the same as seen in lower redshift AGN, as it follows the same optical-to-X-ray slope, and the source detection in ExSeSS is not a consequence of being relatively X-ray luminous.

Despite being X-ray selected and optically bright, I find that ATLAS J025.6821-33.4627 is typical of the AGN population observed at high redshift. Thus, the observed XLF constraints calculated including this source (see §3.3) are expected to be indicative of the typical AGN population at high-z.

3.3 Observational constraints on the high-redshift XLF

Using the sample of serendipitously detected high-redshift X-ray sources identified in ExSeSS, I calculate limits on the AGN space density and place constraints on the bright end of the high-redshift XLF. In §3.3.1 we compare the number

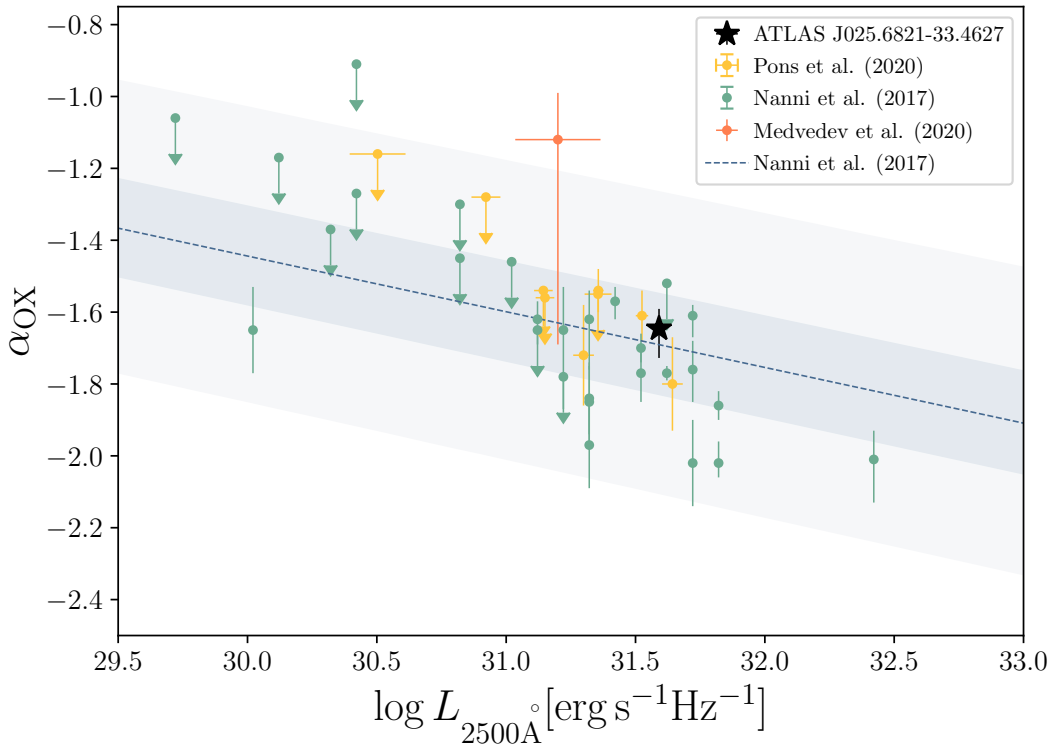

Figure 3.3 *The optical-to-X-ray slope, α_{OX}, and 2500Å monochromatic luminosity of the serendipitously detected ExSeSS source ATLAS J025.6821-33.4627 (black star). For comparison, measurements of α_{OX} for X-ray-targeted samples of high-redshift AGN from Pons et al. (2020), Medvedev et al. (2020) and Nanni et al. (2017) are shown by the yellow, pink and turquoise points, respectively. The standard relation for the optical-to-X-ray slope, as a function of the 2500Å monochromatic luminosity, determined by Nanni et al. (2017), is shown by the dashed line with shaded regions showing the 1σ (grey) and 3σ (light grey) scatter in the relation. My high redshift ExSeSS source can be seen to lie within the 1σ scatter of the expected relation.*

of sources observed with the number predicted by extrapolations of parametric XLF models. In §3.3.2, I present the constraints on the XLF that are obtained from the ExSeSS sample. I then compare my X-ray based constraints at $z > 6$ to prior measurements of the bolometric QLF, primarily based on optical samples at these redshifts, in §3.3.3.

As not all ExSeSS sources have counterparts there may be additional unidentified high-redshift sources in ExSeSS, for which I do not have redshift information. Even if there is a significant population of unidentified AGN at high redshift, I am still able to place *lower* limits on the XLF based on the ExSeSS survey. However, if I assume that any high-luminosity X-ray AGN would also be bright at rest-frame

UV wavelengths (as predicted by the optical-to-X-ray relation see, e.g. Nanni et al., 2017; Pons et al., 2020) and that they are unobscured then such such sources can be expected to have been identified in the numerous UV/optical searches for high-z quasars (that have now covered the majority of the extragalactic sky in both hemispheres, e.g. Bañados et al., 2016; Wang et al., 2019; Reed et al., 2019) and as such would have entered the redshift sample, if they exist in ExSeSS. Thus, I do *not* expect there to be significant additional high-redshift AGN within the ExSeSS X-ray selected sample that has not been yet identified. Nevertheless, it should be noted that the constraints obtained here are formally *lower* limits only.

3.3.1 Predicted numbers of z $\gtrsim$ 6 AGN

The number of AGN X-ray sources at different luminosities and redshifts that are expected to be observed in an X-ray survey can be predicted using XLF models and the area curve of the survey. As the area curve of the ExSeSS survey has been calculated I can perform such predictions of the expected number of AGN in ExSeSS.

Using the parametrised XLF models of Pure Luminosity Evolution (PLE), Pure Density Evolution (PDE), Luminosity And Density Evolution (LADE) and Luminosity Dependent Density Evolution (LDDE) from Georgakakis et al. (2015), I calculate the expected number of sources in ExSeSS. The XLF models are extrapolated out to high redshifts, then the predicted number obtained using the integral

$$N_{model} = \int_{z_1}^{z_2} \int_{\log L_{X_1}}^{\log L_{X_2}} \phi(L_X, z) A(f(L_X, z)) \frac{dV_{\rm co}}{dz} d\log L_X dz \tag{3.2}$$

where the XLF, $\phi(L_X, z)$, is the parametrised model (PLE, PDE, LADE or LDDE from Georgakakis et al., 2015), $\frac{dV_{\rm co}}{dz}$ is the differential comoving volume and $A(f(L_X, z))$ is the sky area covered by ExSeSS to an observed flux, $f(L_X, z)$, corresponding to a given 2–10 keV rest-frame luminosity, L_X, and redshift, z. I fix the redshift limits to $z_1 = 5.7$ and $z_2 = 6.4$, corresponding to the selection window of the Carnall et al. (2015) study (based on i-band drop-out selection). The 1σ uncertainties in these predicted numbers are obtained through Monte Carlo simulations using the model parameter uncertainties of Georgakakis et al.

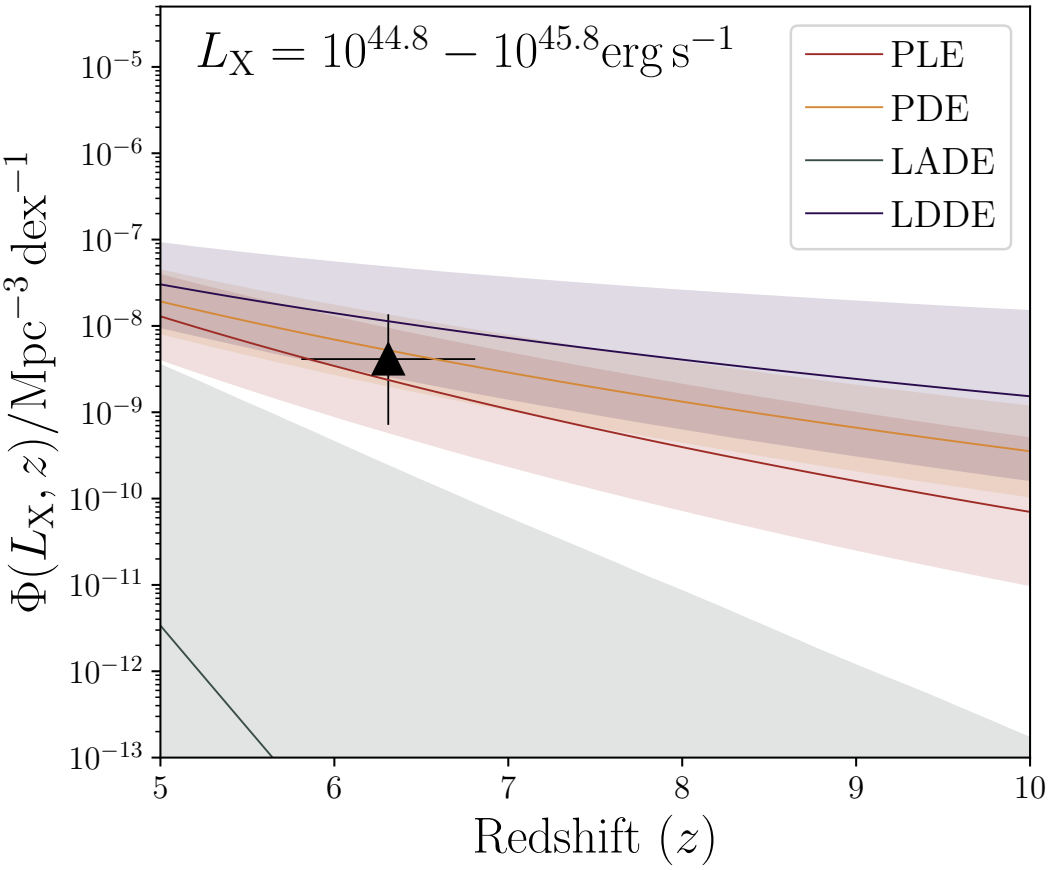

Figure 3.4 *Measurement of the space density of AGN in the* $\log L_X = 44.8 - 45.8$ *luminosity bin, based on the identification of a single high-redshift source in ExSeSS source and assuming no other high-redshift sources exist within ExSeSS (formally a lower limit; black triangle). The space densities predicted by the Georgakakis et al. (2015) models as a function of redshift are also shown, with the shaded regions showing the* 1σ *uncertainties in the predictions, and are generally consistent the observational constraints.*

(2015). I choose not to perform a global correction to the area curve for the spectroscopic completeness of the ExSeSS sample as the completeness is likely to vary substantially with redshift in a poorly constrained manner.

The predicted numbers of sources in the ExSeSS survey, based on the Georgakakis et al. (2015) models, are given in Table 3.2 and compared to my observed source numbers. I adopt 1 dex wide luminosity bins, with the minimum luminosity corresponding to the flux (for a source at $z > 5.7$) where the area curve drops to 0.1% of the total area of ExSeSS, assuming a spectral index of $\Gamma = 1.9$, in order to avoid the uncertainties inherent in the area curve at fainter fluxes. This results in the lowest luminosity bin being $\log L_X = 44.8 - 45.8$, in which the

source, ATLAS J025.6821-33.4627, identified in ExSeSS falls. However, I find no sources in the 1 dex higher luminosity bin, $\log L_{\rm X} = 45.8 - 46.8$, or at even higher luminosities, which would expect to be optically brighter (given the optical-to-X-ray slope at high redshift; Nanni et al., 2017) and thus would have been easier to identify in prior UV/optical searches for high-z quasars (assuming such high-luminosity sources are not obscured) and hence fall into the high-z population sample. Thus, I take an upper limit on the observed number of sources, N_{obs}, in this higher luminosity bin given by the upper 1σ equivalent Poisson limit for a sample size of $N = 0$ from Gehrels (1986).

Table 3.2 *The predicted number of sources, at $z = 5.7 - 6.4$, based on the four XLF models from Georgakakis et al. (2015) in the two luminosity bins where we place constraints on the number of high-redshift sources using ExSeSS. The 1σ uncertainties on the model predictions are obtained through Monte Carlo error propagation (for the LADE model we give the 1σ upper limit only given the large range). The N_{obs}/N_{model} binned XLF estimates obtained from the observed ExSeSS sources, $\phi(L_{\rm X}, z)$, and the observed number of AGN in each luminosity bin are also given, with 1σ limits based on the Poisson errors from Gehrels (1986) (see §3.3.2 for details).*

Model	$\log L_{\rm X} = 44.8 - 45.8$ erg s^{-1}	$\log L_{\rm X} = 45.8 - 46.8$ erg s^{-1}
PLE	$0.62^{+1.60}_{-0.48}$	$0.30^{+1.07}_{-0.25}$
PDE	$1.05^{+1.48}_{-0.67}$	$0.31^{+0.66}_{-0.22}$
LADE	< 0.051	< 0.015
LDDE	$2.76^{+10.8}_{-2.25}$	$1.80^{+16.8}_{-1.63}$
$\phi(L_{\rm X}, z)$	$2.98^{+6.86}_{-2.47} \times 10^{-9}$	$< 2.22 \times 10^{-10}$
$1/V_{\rm max}$	$3.27^{+7.52}_{-2.70} \times 10^{-8}$	No Data
N_{obs}	$1^{+2.300}_{-0.827}$	< 1.814

In general, I find good agreement between our predicted and observed source numbers given in Table 3.2, indicating that the XLF model extrapolations give reasonable predictions for the number of AGN at these luminosities and redshifts. The PLE and PDE models generally predict ~ 1 source in ExSeSS at $\log L_{\rm X} = 44.8 - 45.8$ and < 1 in the higher luminosity bin, consistent with the observed sample. The LDDE model predicts slightly higher numbers but remains consistent with the observed numbers. However, the LADE model under-predicts the number of observed sources, albeit with a very large uncertainty. Nonetheless, the 1σ upper limit based on the extrapolated uncertainty in the LADE model remains below the 1σ limit from my observed number; the LADE model, while not formally ruled out, is thus disfavoured based on my measurements.

3.3.2 AGN space densities and measurements of the XLF

Extrapolating parametrised models of the AGN XLF, such as those of Georgakakis et al. (2015); Aird et al. (2015); Ueda et al. (2014), out to high-redshift, provides insights into the AGN population in the very early Universe. However, due to the lack of observational data at redshifts of $z > 6$, these models are not constrained at high-redshifts. Thus the predictions are based on extrapolating a given parametric form (determined by the lower-z data). Even with just one high-redshift AGN found in ExSeSS, we can place new *observational* constraints on the space density of the high-z AGN population and compare with these models.

I use the N_{obs}/N_{model} method of Miyaji et al. (2001) to convert the observed number of sources in the luminosity bins of $\log L_{\rm X} = 44.8 - 45.8$ into a measurement of the AGN space density. My estimate of the space density, $\Phi_{est}(L_{\rm X}, z_i)$, is calculated by scaling the predicted space density based on a given model of the XLF, $\Phi_{model}\left(L_{{\rm X}_i}, z_i\right)$, by the ratio of the observed number of sources to the predicted number of sources, N_{obs}/N_{model}. Thus,

$$\Phi_{est}\left(L_{{\rm X}_i}, z_i\right) = \Phi_{model}\left(L_{{\rm X}_i}, z_i\right) \frac{N_{obs}}{N_{model}} \tag{3.3}$$

where the predicted number, N_{model} is estimated using the LDDE model (from Georgakakis et al., 2015), using eq.3.2, for a redshift range of $z = 5.7 - 6.4$ and in the luminosity bins given in Table 3.2, and the model space density, $\Phi_{model}\left(L_{{\rm X}_i}, z_i\right)$, is given by the integral of the LDDE model over the luminosity bin. The 1σ uncertainties on $\Phi_{est}\left(L_{{\rm X}_i}, z_i\right)$ are based on the Poisson uncertainties in the observed source number, as given by Gehrels (1986).

My measurement of the space density of AGN with $\log L_{\rm X} = 44.8{-}45.8$ is shown in figure 3.4 and compared to the space densities predicted by the four Georgakakis et al. (2015) XLF models. The measured space density is generally in good agreement with the extrapolated XLF models. The PLE and PDE models and the lower limit on the LDDE model agree with the observed space density, within the 1σ uncertainties, whilst the upper bound of the LADE model only agrees with the observed space density within the 3σ uncertainties (not shown). Thus, this observed space density can be seen to show the expected decline in space density of AGN, based on lower redshift data, towards higher redshift, as seen in in the PLE, PDE and LDDE models, but this decline is may not be as rapid as predicted by the some models, such as LADE.

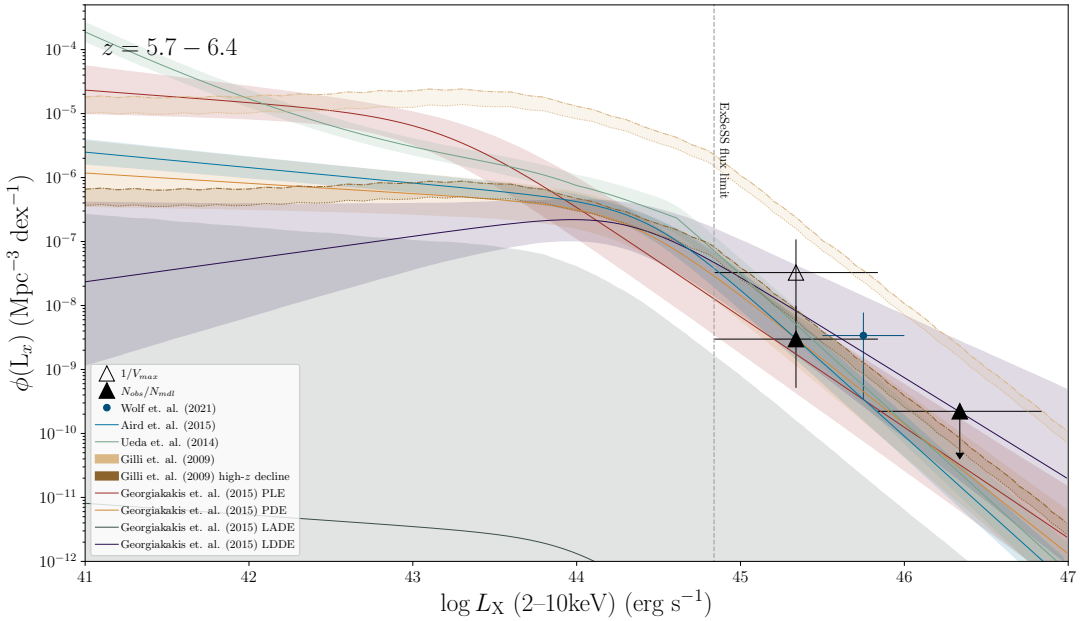

Figure 3.5 *Measurements of the XLF at $z \sim 6$ compared to extrapolations of the various different parametrised models from Georgakakis et al. (2015) and a number of other recent XLF models. My binned XLF measurements, given by the N_{obs}/N_{model} method (solid triangle), are plotted at the centre of the luminosity bins in which they were calculated with the width of the luminosity bins shown by the horizontal error bars. Vertical error bars give the 1σ uncertainties on the XLF estimates. I also show a binned measurement using the $1/V_{max}$ method in the lower luminosity bin (hollow triangle) for comparison. The observed XLF found by Wolf et al. (2021) is shown by the blue circle, and can be seen to agree with my constraints to within 1σ. I note that these binned XLF estimates are calculated assuming no other $z > 5.7$ sources exist within ExSeSS and thus are formally lower limits. The detection limit of ExSeSS, given by the 0.1% of the total observed area (as in §3.3.1), is shown by the vertical dotted line. XLF models fitted by previous studies, extrapolated to the redshift range here, are plotted with 1σ uncertainties shown by a shaded region. The PLE (red), PDE (yellow), LDDE (purple) models of Georgakakis et al. (2015), Ueda et al. (2014) LDDE model (green), Aird et al. (2015) Flexible Double Power-Law (FDPL; blue) model, and Gilli et al. (2007) LDDE with high L_X decline model (dark brown) are consistent with the binned measurements. In contrast, the Georgakakis et al. (2015) LADE model and Gilli et al. (2007) model without the high L_X decline (light brown) predict lower and higher space densities, respectfully, than has been observed with ExSeSS and are thus disfavoured. Both Gilli et al. (2007) models are shown with (dot-dashed) and without (dotted) Compton Thick AGN.*

Following a similar process, I also determine binned measurements of the XLF, given by

$$\phi_{est}\left(L_{\mathrm{X}_i}, z_i\right) = \frac{d\Phi_{est}\left(L_{\mathrm{X}_i}, z_i\right)}{d\log L_{\mathrm{X}}} = \frac{d\Phi_{model}\left(L_{\mathrm{X}_i}, z_i\right)}{d\log L_{\mathrm{X}}}\frac{N_{obs}}{N_{model}} \tag{3.4}$$

where the predicted number, N_{model} is given by the LDDE model as in equation 3.3, N_{obs} is the observed number of AGN and $\phi_{model}\left(L_{\mathrm{X}_i}, z_i\right)$ is taken to be the value of the LDDE model at the centre of the adopted redshift and luminosity bins. Figure 3.5 presents these binned measurements in both the $\log L_{\mathrm{X}} = 44.8 - 45.8$ bin where our single high-redshift detection lies. The 1σ uncertainties are based on the Poisson uncertainties in the observed source numbers, as given by Gehrels (1986). I also show an upper limit in the higher $\log L_{\mathrm{X}} = 45.8 - 46.8$ bin where no sources are found, based on the 1σ upper limit (given zero detected sources) from Gehrels (1986). This constraint relies on the assumption that any sources with such high X-ray luminosities at these redshifts would also be optically bright and thus would have been identified in existing optical/IR quasar searches, but it should not be considered a stringent upper limit given the potential for obscured or optically weak sources within ExSeSS that remain unidentified.

For comparison I also provide an XLF measurement in the lower luminosity bin based on the more commonly used $1/V_{max}$ method (Schmidt, 1968). The $1/V_{max}$ method does not assume an underlying parametric model but is more biased than the N_{obs}/N_{model} method as it does not account for a change in the XLF across a broad luminosity range or with redshift and is thus more strongly affected by source luminosity, in particular for low sample sizes. However, it is found that the N_{obs}/N_{model} estimate shows negligible change depending on the assumed XLF model and agrees well (within 1σ) with the $1/V_{max}$ estimate.

As can be expected from figure 3.4, the binned XLF measurements are found to be consistent with the fiducial values of the XLF models (see figure 3.5). The PLE, PDE and LDDE models from Georgakakis et al. (2015) agree with the observations within the 1σ Poisson uncertainty, whilst the LADE model in particular falls much lower than the binned XLF estimate (see §3.5). In addition to the Georgakakis et al. (2015) models, I also compare with the model XLFs of Aird et al. (2015) and Ueda et al. (2014), which agree to within 1σ of the $\log L_{\mathrm{X}} = 44.8 - 45.8$ binned XLF estimates, and Gilli et al. (2007) which lies more than 3σ above the binned XLF estimates, as shown in figure 3.5. The gradient of the bright-end of these XLF models is consistent with the gradient indicated

by the binned XLF estimates, with a value of $\gamma \gtrsim 0.367$, consistent with the relatively steep bright-end slope of the XLF at $z \gtrsim 6$.

In Figure 3.5, I also compare with the result obtained from eFEDs data by Wolf et al. (2021). It can be seen that my measurements are consistent to within 1σ of the XLF value based on the single $z = 5.81$ source found in the ~140 deg^2 eFEDS survey.

As noted above, there may be other $z \gtrsim 6$ AGN within ExSeSS that have not been identified as they do not currently have redshift estimates. There may also be a significant population of obscured AGN, which would result in a higher space density than observed here. However, given the agreement between my observed XLF and the model extrapolations, additional as yet unidentified AGN are not expected. Regardless, from the results presented here it can be seen that the ExSeSS sample provides important constraints on the bright-end of the high-redshift XLF. Further, significantly deeper observations would be needed to probe the faint-end of the high-z XLF, where the model extrapolations can be seen to diverge, and constrain the form of the XLF at high z.

3.3.3 The Bolometric QLF

More high-redshift AGN have been identified through rest-frame UV selection than X-ray selection, due to the limited survey areas covered with current X-ray telescopes compared to the efficiency and availability of large-scale optical/near-infrared imaging campaigns. In order to determine how well the observed XLF estimate compares to the luminosity functions given by the more biased Optical/UV selected AGN samples, I compare the X-ray binned XLF estimates to models of the bolometric QLF.

I convert the X-ray luminosity bins and binned XLF estimates into bolometric terms using a bolometric correction factor, adopting the luminosity-dependent corrections determined by Shen et al. (2020), where $L_{\rm bol} = k_{\rm bol}(L_{\rm bol}) \times L_{\rm X-ray}$ and $k_{\rm bol}(L_{\rm bol})$ is the luminosity-dependent X-ray-to-bolometric correction factor.

The binned XLF estimate from the single source detection at $\log L_{\rm X} = 44.8{-}45.8$ is converted to a bolometric QLF value and shown in figure 3.6 compared to the Shen et al. (2020) bolometric QLF model, which was based on a fit to a combination of bolometrically corrected UV/optical, IR and X-ray luminosity functions spanning

Table 3.3 *Estimates of the bolometric luminosity for my source, calculated from the X-ray and 1450 Å luminosities. The optical luminosity at 1450 Å is derived from the z-band luminosities, assuming a constant power-law relation of slope $\alpha_\nu = -0.3$, the bolometric luminosities are then calculated, from the 2-10 keV band and 1450 Å wavelength luminosities, using the conversion method of Shen et al. (2020).*

Object	$L_{\text{bol from 2–10keV}}$ erg s^{-1}	$L_{1450\text{Å}}$ erg s^{-1} Å^{-1}	$L_{\text{bol from 1450Å}}$ erg s^{-1}
ATLAS J025.6821-33.4627	$1.54^{+0.91}_{-0.72} \times 10^{47}$	$2.52^{+0.15}_{-0.14} \times 10^{45}$	$2.29^{+0.13}_{-0.12} \times 10^{46}$

a wide range of redshifts. At $z \sim 6$, the Shen et al. (2020) model is primarily constrained by rest-frame UV selected data; the original measurements, compiled from the literature, are shown by the purple points in figure 3.6 (see Shen et al., 2020, and references therein).

From figure 3.6 it can be seen that the X-ray based estimates of the bolometric QLF are consistent to within 2σ of the Shen et al. (2020) model and the prior UV/optical measurements. Similarly, the number of AGN within ExSeSS predicted by the Shen et al. (2020) QLF model (converted to an XLF and using equation 3.2) is $0.049^{+0.095}_{-0.0086}$, which is consistent to within 2σ with the observed number of sources in this bin, $N_{obs} = 1^{+2.300}_{-0.827}$.

While the X-ray–based estimate of the bolometric QLF is consistent with the Shen et al. (2020) QLF model, I have adopted large X-ray–to–bolometric corrections at these luminosities (as suggested by Shen et al., 2020). As discussed in §3.2.1, the serendipitously detected AGN lies on the fiducial $\alpha_{\text{OX}} - L_{2500\text{Å}}$ relation (see Figure 3.3) and thus appears typical in terms of its X-ray to optical properties for sources of such luminosity. However, at such high optical luminosities, the typical AGN is relatively X-ray weak due to the steep dependence of α_{OX} on optical luminosity (i.e. a large fraction of their power is emitted at optical wavelengths), which indicates that a large X-ray–to–bolometric correction factor is required.

At such high redshifts, inverse Compton scattering of cosmic microwave background photons from a jet, if present, can boost the X-ray emission from AGN (see e.g. Medvedev et al., 2020), which would then lead to an over-estimate of the bolometric luminosity from the observed X-ray luminosity. However, the source has not been detected at radio wavelengths (including with recent, deeper coverage from the Rapid ASKAP continuum survey: Hale et al., 2021) and thus there is no evidence that a jet is present or that the X-ray emission is being boosted by non-coronal processes.

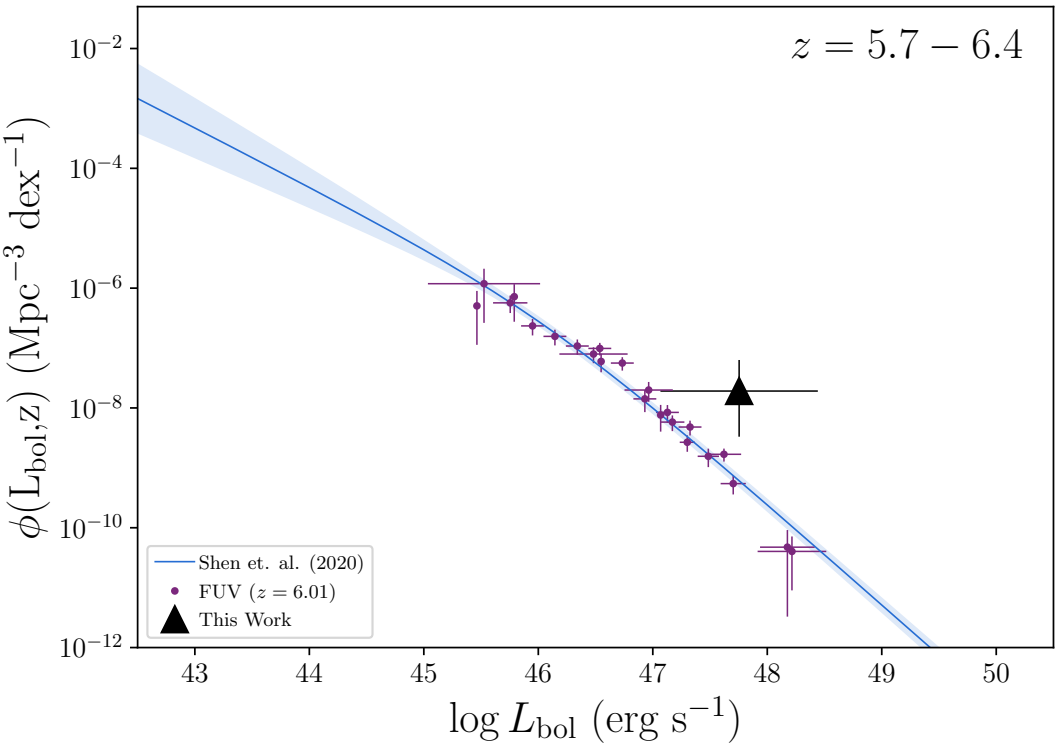

Figure 3.6 *Binned estimate of the bolometric QLF (black triangle), converted from the binned XLF estimate found in §3.3.2 based on the single source detection at* $\log L_X = 44.8 - 45.8$ *and assuming that there are no other high redshift sources in ExSeSS. The estimate is calculated using the bolometric conversion factor of Shen et al. (2020). While my estimate lies above the Shen et al. (2020) QLF model (blue), it is consistent at the 2σ level (1σ error bar is shown). Violet points show measurements at* $z \sim 6$ *based on rest-frame UV data, converted to bolometric values, which were used to constrain the QLF model (see Shen et al., 2020, and references therein).*

To further check whether such large X-ray–to–bolometric corrections are warranted in this luminosity–redshift regime, I also directly compare estimates of the bolometric luminosity of our source, ATLAS J025.6821-33.4627, based on the observed X-ray and rest-frame UV luminosities. I estimate the 1450Å luminosity (based on the z-band magnitude of the source and assuming a power-law UV spectrum, as in §3.2.1), which I use to estimate the bolometric luminosity of our source and compare with the bolometric luminosity derived from the observed X-ray luminosity (adopting the relevant luminosity-dependent bolometric corrections from Shen et al., 2020, in both cases). The various luminosity estimates are provided in table 3.3. The bolometric luminosity inferred from the rest-frame UV light is $L_{1450\text{Å to bol}} = 2.29^{+0.13}_{-0.12} \times 10^{46}$ erg s^{-1}, which is consistent to within 2σ of the bolometric luminosity inferred from the

X-ray, $L_{\mathrm{X-ray\ to\ bol}} = 1.54^{+0.91}_{-0.72} \times 10^{47}$ erg s^{-1} obtained using the large X-ray bolometric correction factor of $k_{\mathrm{bol}} = 182.4$. Thus, the large X-ray–to–bolometric corrections that I have adopted to convert the XLF estimates and compare with the bolometric QLF are warranted, given the properties of the single high-z source in the ExSeSS sample.

3.4 Conclusions

Luminosity functions provide a tracer of the AGN population across cosmic time. However, at high redshift these luminosity functions remain poorly constrained. In this chapter, I present observational constraints on the X-ray Luminosity Function (XLF) from the new Extragalactic Serendipitous Swift Survey (ExSeSS; Delaney et al., 2023).

I identified one X-ray selected AGN at $z > 6$ within the carefully constructed sample of serendipitous X-ray sources from Swift-XRT observations that form ExSeSS (Delaney et al., 2023). The serendipitous X-ray source, 2SXPS J014243.7-332742, is matched with the optically bright $z = 6.31 \pm 0.03$ quasar ATLAS J025.6821-33.4627, making it the highest redshift serendipitously X-ray detected quasar to date. With this detection, I am able to determine the space density of AGN and place constraints on the X-ray luminosity function at $z \sim 6$, under the assumption there are no other high redshift sources within ExSeSS. My conclusions are as follows:

- The space density of AGN given by the high-redshift ExSeSS source shows the steep decline of AGN with increasing redshift. This observed decline is consistent with the expected exponential decline in the space density of luminous AGN with increasing redshift. However, it should be noted that any additional sources at these luminosities and redshifts that remain unidentified within ExSeSS, such as a significant population of obscured AGN, would result in a higher space density.

- I place constraints on the shape of the $z \sim 6$ XLF, assuming no other $z > 5.7$ sources exist within ExSeSS, using the single detection and an upper limit on the number of sources at higher luminosities. Combined, these constraints are consistent with a relatively steep bright-end slope of the XLF, with $\gamma \gtrsim 0.367$, as found at lower redshifts. My binned XLF estimates are

broadly consistent with the extrapolation of parametric XLF models, based on fits to lower redshift data. However the constraints I have obtained here rule out the most extreme declines in the bright-end of the XLF indicated by some model extrapolations (e.g. the LADE model of Georgakakis et al., 2015). Furthermore, as there may be other high-z sources in ExSeSS these constraints are formally lower limits, strengthening this conclusion.

- The XLF constraints are consistent (within $\sim 1\sigma$) with the prior measurements by Wolf et al. (2021), which were based on the identification of a single $z = 5.81$ X-ray selected AGN in the 140 deg^2 eFEDS field observed by eROSITA.

- Applying a bolometric correction to my XLF measurement, I find a good agreement with the parametric QLF model of Shen et al. (2020). The estimate of the bolometric QLF is consistent, to within 2σ, with the QLF derived from rest-frame UV selected quasars at $z \sim 6$.

- I find that the optical-to-X-ray slope, $\alpha_{\rm OX}$, of our serendipitously detected source is consistent to within 1σ of the expected $\alpha_{\rm OX}$-$L_{2500\text{Å}}$ relation, indicating the accretion process in this high redshift source operates in a similar manner to AGN at lower redshift. Thus, despite being X-ray selected and optically bright, this source is typical of the population at this redshift. In addition, as this source is optically bright, a high correction factor is required to converting its X-ray luminosity to a bolometric estimate.

The measurements presented in this chapter provide important constraints on the extent of supermassive black hole growth within the early Universe. These estimates, based on the 2086.6 degrees^2 covered by ExSeSS, indicate that the ongoing all-sky surveys being performed by eROSITA will identify a few tens to a few hundred high-luminosity AGN at $z > 6$, once sufficient depth is achieved (i.e. by eRASS:8 all-sky depth), enabling further investigation of the growth of SMBHs within the early Universe. However, much deeper surveys will be required in order to constrain the faint-end of the XLF at high-z, which will become possible within the next decade with new telescopes such as the *NewAthena* X-ray Observatory.

Chapter 4

COSMOS Constraints on the $z = 4 - 10$ X-ray Luminosity Function of AGN, at Moderate Luminosities

As discussed in chapter 1, the X-ray Luminosity Function (XLF) of Active Galactic Nuclei (AGN) is very poorly constrained at high-redshifts, due to the low space density of AGN within the early Universe and the limited sensitivity of current survey telescopes. However, as shown in chapter 3, it is still possible to constrain the shape of the high-redshift XLF with only a small sample size.

Whilst the ExSeSS survey of Delaney et al. (2023, and see chapter 3) provides the large area needed to find the low number of high luminosity AGN within the very early Universe, in order to constrain the XLF at moderate luminosities much deeper X-ray imaging is required.

The *Chandra* X-ray Observatory (Weisskopf et al., 2002) is one of the most sensitive X-ray observatories to date, probing fluxes of $\leq 10^{-16}\,\mathrm{erg\,s^{-1}\,cm^{-2}}$ in the 0.5–2 keV energy band in the deepest observations, a factor of ≥ 100 deeper than achieved in ExSeSS. In order to obtain this depth of imaging, *Chandra* has observed a much smaller area of sky compared to *Swift* and other less sensitive survey telescopes. However, the depth achieved by *Chandra* is crucial to probing moderate luminosity AGN at high redshifts. For this chapter I use the Chandra legacy imaging of the COSMOS field from Civano et al. (2016), and the most recent photometric catalogue of this field (COSMOS2020: Weaver et al., 2022).

The form of the COSMOS2020 catalogue and the X-ray data used are detailed in section 4.1. The cross-matching of COSMOS2020 and X-ray sources performed in order to obtain the blind source sample is outlined in section 4.1.3, and section 4.1.4 details the creation of the blind and extracted sample through the direct extraction of X-ray counts for all COSMOS2020 sources. I then detail the measurement of the XLF using these X-ray AGN samples in section 4.2, and test the extremes of these measured constraints arising from the redshift spectral fits from COSMOS2020 in section 4.2.4. The impact of obscuration in early galaxies on the high redshift XLF is then investigated in section 4.3. Finally, the implications of these new constraints on the XLF are discussed in section 4.4 and I summarise the science in this chapter in section 4.5.

4.1 The COSMOS Field Data Sets

The COSMOS field, centred at $10^{\mathrm{h}}00^{\mathrm{m}}27^{\mathrm{s}}.92 + 02°12'03''.50$ (J2000), was originally defined by Scoville et al. (2007) for large-area deep (0.05 arcsec) Hubble Space Telescope (HST) imaging in order to address a number of science goals; from large dark matter distributions and galaxy assembly to early galaxies and the evolution of AGN. This $\sim 2\,\mathrm{degree}^2$ equatorial field was chosen as its location ensured it was visible to all astronomical instruments, at the time, thus allowing for detailed multi-wavelength studies of the sources within the field. The COSMOS field also benefits from having a relatively low and uniform Galactic extinction, compared to other equatorial fields, whilst being devoid of bright X-ray, UV and radio sources and thus reducing the contamination of the signals of faint sources within the field.

Following its definition, the COSMOS field has been surveyed using a wide range of facilities spanning the full wavelength range (including *HST*, *Spitzer*, GALEX, *XMM-Newton*, *Chandra*, Subaru, ALMA, VLA, VISTA, ESO-VLT, UKIRT, NOAO, CFHT, and more), with deep observations performed by almost all major astronomical facilities (see e.g. Sanders et al., 2007; Capak et al., 2007; Taniguchi et al., 2015; Le Fèvre et al., 2020). The wealth of data available within the COSMOS field makes it incredibly important to extragalactic astronomy. Crucially for the identification of galaxies out to very high redshifts, the COSMOS field has very deep imaging at Near and Mid-Infrared wavelengths from the VISTA telescope (McCracken et al., 2012; Moneti et al., 2023; Ashby et al., 2018). Recent

Near-Infrared (NIR) measurements of the galaxy luminosity function (such as Bowler et al., 2020; Finkelstein et al., 2022; Donnan et al., 2023b, 2024) have been shown to find an excess of high-redshift galaxies only visible in NIR observations, with Donnan et al. (2023a) finding 47 $z > 7.5$ previously undiscovered galaxies using *JWST* and UltraVISTA Near IR imaging, thus this deep Near and Mid-Infrared is vital to this work. However, JWST data would limit this study to sources selected within the small area of available imaging, as such I instead perform this work independent of JWST and thus I am not relying on unavailable multi-band data and can incorporate AGN redshift fits in this work. Figure 4.1 shows the extent of the *Chandra* imaging and UltraVISTA area of the COSMOS field.

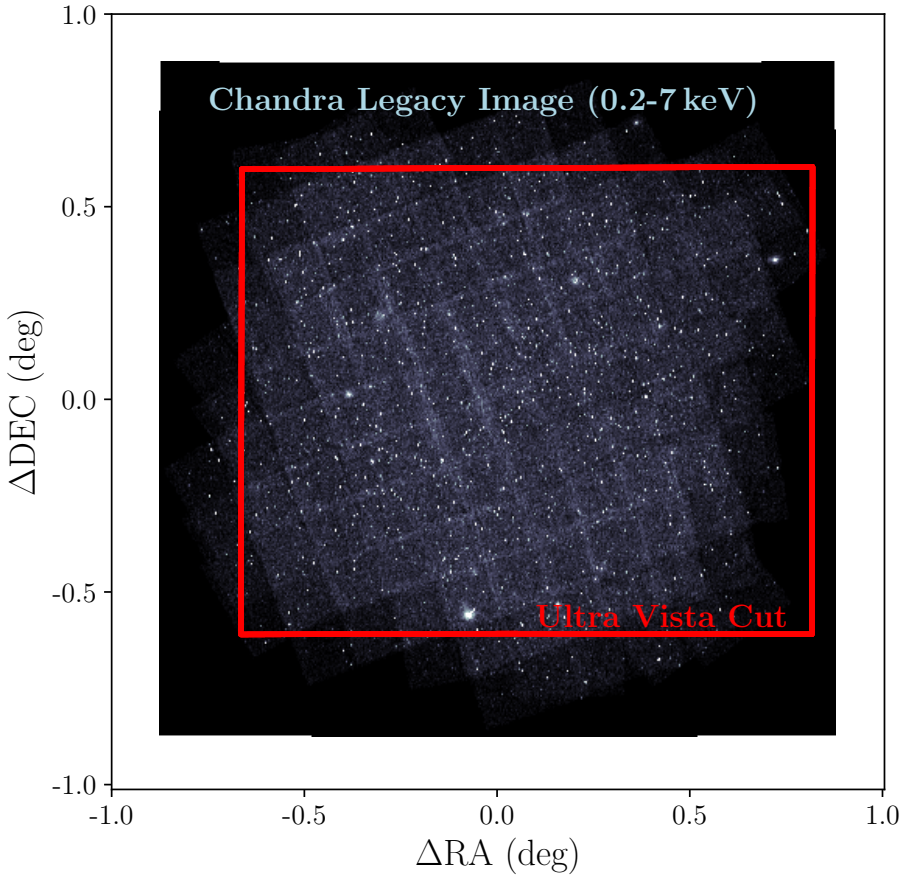

Figure 4.1 *The COSMOS Chandra Legacy Full-Band (0.7-2 keV) imaging from which the X-ray sample is obtained, centred on the Chandra image centre. The UltraVISTA area to which the COSMOS2020 catalogue version I use in this work is limited to, is shown by the red rectangle. The axes shown the relative change in Right Ascension (RA) and Declination (DEC) for comparison, to a maximum of* ±1 degree *corresponding to* 2 degree^2.

4.1.1 COSMOS2020

Since COSMOS was first defined several photometric catalogues of this field have been publicly released, as deeper data becomes available (Capak et al., 2007; Ilbert et al., 2009, 2013; Muzzin et al., 2013; Laigle et al., 2016). The COSMOS2020 catalogue of Weaver et al. (2022) is the most up to date release of the COSMOS catalogue, including deep UV (Sawicki et al., 2019) and ultra deep optical imaging (Aihara et al., 2019) as well as Near IR data from the UltraVISTA survey DR4 (Moneti et al., 2023; McCracken et al., 2012). For COSMOS2020, all legacy datasets used in previous iterations of the COSMOS catalogue (e.g. COSMOS2015 Laigle et al., 2016) have also been reprocessed to the newly available Gaia Astrometry, using the previously unavailable Gaia DR1 (Gaia Collaboration et al., 2016). The legacy imaging is resampled to a pixel scaling of 0.15 arcsec and stacked images aligned to the COSMOS Tangent point ($10^{\rm h}00^{\rm m}27.92^{\rm s} + 02°12'03''.50$), such that the COSMOS2020 data can be used for detailed stacking analysis.

Weaver et al. (2022) identified sources within the wealth of deep COSMOS data using two different detection methods; implementing SExtractor (Bertin & Arnouts, 1996) as in Laigle et al. (2016) for COSMOS2015, and THE FARMER software (Using the SEP code, Barbary, 2016) of Weaver et al. (2023) which utilises THE TRACTOR photometry modelling code (see Lang et al., 2016, for details). These two versions of the COSMOS catalogue are referred to as the CLASSIC Catalogue and THE FARMER Catalogue, respectively.

To create the CLASSIC catalogue Weaver et al. (2022) generate a χ^2 detection image using the SWarp package (Szalay et al., 1999). With i-band imaging being included in the COSMOS2020 source detection process, a larger number of small blue galaxies at intermediate redshifts are found than in the COSMOS2015 catalogue. SExtractor is then applied to the images, as was done for COSMOS2015, but with the minimum detection area set to half that used for the COSMOS2015 source detection (5 pix instead of the previous 10 pix) thanks to the improvements in the data reducing the number of spurious sources in COSMOS2020. The Point Spread Function is then homogenised, and the photometric fluxes at each wavelength, for which there is imaging, measured at each source position within circular apertures of 2 arcsec and 3 arcsec diameter. For both apertures, separately, the error in the photometric measurements is re-scaled for each wavelength band.

Although the source detection performed for the creation of THE FARMER catalogue is equivalent to that of SExtractor, THE FARMER catalogue is created using parametric models of source shape to direct the photometry measurements. As these models cannot be applied to saturated bright stars or sources contaminated by stellar halos, Weaver et al. (2022) adopt the HSC-SSP PDR2 (Coupon et al., 2018) bright-star masks in order to mask out all stars with a G-band magnitude of 18 or less, in the Gaia DR2 star catalogue. In order to prevent the introduction of inhomogeneities to the constraints on the models for photometric extraction, THE FARMER catalogue is also limited to the UltraVISTA region such that there is coverage in all wavelength bands used. THE FARMER software then measures the photometric fluxes at each wavelength through the scaling of one of five parametric models (Point Source, Simple Galaxy, ExpGalaxy, DevGalaxy and Composite Galaxy[1]) assigned to each source (see Weaver et al., 2023, for details). Thus, this alternative method of measuring the photometry does not require correct apertures or PSF homogenisation to be performed, as such the best quality photometry is not degraded to the lowest quality resolution achieved, and the photometry obtained is self-consistent.

Whilst THE FARMER catalogue suffers from PSF variability in the SuprimCam measurements, due to the lack of PSF homogenisation, and may fail to converge to a scaling solution when measuring the photometry in highly crowded regions or near bright sources (see e.g. Shuntov et al., 2022), Weaver et al. (2022) determined that all sources within THE FARMER catalogue can be considered to be reliable detections.

The two photometric catalogues of COSMOS sources, CLASSIC and THE FARMER, obtained by Weaver et al. (2022) contain 1 720 700 and 964 506 sources, covering 2.75 degrees^2 or 1.792 degrees^2, respectively (see table 4.1 for comparison of the source numbers within CLASSIC and THE FARMER). For this work I use THE FARMER catalogue, as it has been found to have a higher completeness than the Classic Catalogue (e.g. Shuntov et al., 2022). It also provides more accurate photometry for the faint sources (which will comprise the majority of the high redshift sample I will use in this chapter), is more robust against source blending and is able to identify a higher density of $z > 6$ sources (see e.g. Brinch et al., 2023; Sillassen et al., 2022).

[1]Point source models use the PSF directly, SimpleGalaxy uses a fixed exponential light profile and ExpGalaxy uses an exponential light profile parametrised by the source's image properties. The DevGalaxy model is similar to the ExpGalaxy, but uses the de Vaucouleurs light profile, whilst the CompositeGalaxy model combines both the ExpGalaxy and DevGalaxy models.

catalogue	full	bright star masked	UltraVista Region only
CLASSIC	1720700	1414142	790579
THE FARMER	964506	958926	816944

Table 4.1 *Number of sources within the CLASSIC and THE FARMER versions of the COSMOS2020 catalogue (Weaver et al., 2022), without any masking applied (full), with the bright star mask of (Coupon et al., 2018) applied, and then cut to only the UltraVista Region.*

For both THE FARMER and CLASSIC forms of the COSMOS2020 catalogue, Weaver et al. (2022) determine the photometric redshifts of their sources using the EAzY (Brammer et al., 2008) and LePhare[2] (Arnouts et al., 2002; Ilbert et al., 2006) photometric redshift codes, with the photometric measurements corrected for galactic extinction following the dust maps of Schlafly & Finkbeiner (2011).

EAzY fits a linear non-negative combination of 17 possible galaxy Spectral Energy Distribution (SED) templates, derived from the Flexible Stellar Population Synthesis models of Conroy et al. (2009); Conroy & Gunn (2010), to the available source photometry in order to determine photometric redshifts, along with a number of physical parameters, for each source. A number of Stellar SED templates from Allard et al. (2012) are also fitted, with the resulting χ^2 and effective temperature of the fits allowing for the separation of stars from galaxies within the catalogue. Similarly, LePhare determines the photometric redshift and physical parameters of each source through fits of 19 galaxy templates from elliptical and spiral galaxy models (Polletta et al., 2007), 12 from models of blue Star Forming Galaxies and 2 galaxy templates containing an exponentially declining Star Formation Rate (Bruzual & Charlot, 2003; Onodera et al., 2012). LePhare is also used to perform fits using the AGN templates of Salvato et al. (2009) and Salvato et al. (2011), formed from standard galaxy templates combined with QSO type 1 and 2 templates to varying AGN dominance, and Stellar templates (including G-K type Dwarf stars, giant stars and non-solar abundances) from Pickles (1998).

I take the LePhare photometric redshift measurements as the redshifts of my final galaxy catalogue, as LePhare accounts for a possible AGN component in the photometric redshift determination, whereas the EAzY process used in the COSMOS2020 catalogues assumes such a component is negligible with the resulting measurements appearing less reliable at first glance. LePhare is also found to have a lower outlier percentage (Weaver et al., 2022). However, for

[2]http://www.cfht.hawaii.edu/ arnouts/lephare.html

sources at redshifts of $z = 10$ the observed wavelength of the Lyman-break[3] will cause these extremely high-redshift sources to be undetectable within the $\sim 1526 - 79\,958$ Å wavelength photometry of the COSMOS2020 catalogue. As such, the redshift grid used by LePhare and thus my sample is limited to a maximum redshift of $z = 10$.

Finally, I restrict my catalogue to only include sources that lie within the footprint of the *Chandra* X-ray imaging, as deep X-ray data is not available for sources outside this region. The final, filtered catalogue consists of 816 944 optical/IR selected sources (see also table 4.1).

4.1.2 Chandra Imaging

The Chandra X-ray Observatory is the highest angular resolution X-ray telescope to date. With an on-axis resolution of 0.5 arcsec, Chandra is the best instrument available for finding moderate luminosity high-redshift X-ray sources, despite it's relatively small field of view compared to other current X-ray telescopes. It is these moderate luminosities at which I aim to measure and constrain the X-ray Luminosity Function (XLF) of Active Galactic Nuclei (AGN) in the early Universe, within this chapter.

The Chandra-COSMOS (C-COSMOS) program of Elvis et al. (2009) was the first contiguous survey of the COSMOS field performed, providing an unprecedented area and depth of X-ray imaging at the time. Utilising a strategy of overlapping pointings, with offsets of 8 arcmin around the survey centre at $10^{\mathrm{h}}00^{\mathrm{m}}24^{\mathrm{s}} + 02°10'55''$, provided a near uniform sensitivity across the centre of the COSMOS field. The final C-COSMOS survey covered $\sim 0.9\,\mathrm{deg}^2$ with a total effective exposure of 160 ks over the central $\sim 0.5\,\mathrm{deg}^2$ and 80 ks over the remaining $\sim 0.4\,\mathrm{deg}^2$. Later, Civano et al. (2016) combined the C-COSMOS survey with 2.8 Ms of additional Chandra imaging of the COSMOS field from Garmire et al. (2003). Uniformly covering the $1.7\,\mathrm{deg}^2$ COSMOS/HST field to an effective exposure of 160ks, the Chandra-Legacy Survey covers a total area of $\sim 2.2\,\mathrm{deg}^2$ over the full $2\,\mathrm{deg}^2$ COSMOS field. The 56 additional Chandra pointings were performed over a series of four periods (Nov 2012-Jan 2013, Mar 2013-July2013, Oct 2013-Jan2014 and Mar 2014), totalling 4.6 Ms of exposure with the C-COSMOS imaging, 80% of which has a resolution of 2-4 arcsec.

[3] Rest-frame UV wavelength of 1215 Å gets redshifted to $\geq 13\,365$ Å wavelengths beyond $z = 10$.

For this study I use deep Chandra imaging provided by the Chandra-Legacy survey (Civano et al., 2016). I adopt the custom reanalysis of this Chandra data following the data reduction and source detection process detailed in (Laird et al., 2009; Nandra et al., 2015; Kocevski et al., 2018), to produce the clean images and blind source catalogue used in this study and in the previous work of Aird et al. (2017, 2018, 2019); Laloux et al. (2023, 2024). Performing this reanalysis provides access to all resulting data products, required for this work, and better control of the sensitivity of the Chandra imaging, producing the source catalogues.

The actual data reduction of the Chandra-legacy data, used in this work, was performed by Georgakakis et al. (2017), using the pipeline described in Kocevski et al. (2018). Here I will briefly summarise the reduction of the Chandra-Legacy imaging (section 4.1.2) and the subsequent source identification (section 4.1.2), the products of which are used throughout this chapter.

Data Reduction

The raw data from Chandra is cleaned and processed using the CIAO (Chandra Interactive Analysis of Observations) suite v.4.8 (Fruscione et al., 2009). The event file is first corrected for the telescope dithering (outlined in section 2.1) such that the event positions have consistent sky co-ordinates. The event files are then cleaned by removing any Hot Pixels, caused by background X-ray events (such as stray photons, charged particles or neutral particles incident upon the detector), image streaking and Cosmic-Ray afterglows. High energy particles within solar winds also cause peaks in the observed X-ray background on short time-scales (Grant et al., 2002). These peaks must be removed before the generation of the final images, due to their poor signal to noise ratio and anomalous nature. A light curve of the measured background with respect to time is generated and background flares identified as peaks in this light curve of ≥ 1.4 times the quiescent background (as given by the count rate limit required for a variance excess, in the light curve, of 0), which are subsequently cut from the event file.

With all anomalous pixels and events removed, the cleaned event files are converted into the final Image file. This is done by summing the number of events (photon detections) of each pixel over the total observing time, with a measured energy corresponding to the energy band of the image being created (0.5-7 keV, 0.5-2 keV, 2-7 keV and 4-7 keV for Full, Soft, Hard and Ultra Hard images respectively). An effective exposure map is also generated for each energy band,

and weighted by energy assuming a power-law spectrum of photon index $\Gamma = 1.4$. The resulting exposure map accounts for the exposure time of the observation, quantum efficiency of the detector and the evolving effective area of the telescope across the multiple epochs of imaging performed (thus the degradation of the Chandra effective area across all observation epochs contributing to this work is accounted for by this exposure map; see Appendix C for a summary of the impact of the degradation of Chandra to this chapter), as well as bad pixels, chip gaps and edges, and the dithering motion of the telescope as a whole.

The Point Spread Function (PSF) of Chandra, which describes the distribution of counts from a point source due to scattering of photons and telescope properties (see section 2.1 for details), has significant changes across an image and increases with off-axis angle. In order to measure the PSF across the image the response of Chandra's High Resolution Mirror Assembly (HRMA) is simulated, using the MARX Simulator of Wise (1997). The passage of photons through the HRMA, including the effect of dither motion during imaging, is simulated and the PSF at each pixel position of the Chandra Image is defined. The PSF at each pixel position is then weighted by the effective exposure of the final image and a PSF map generate.

Creation of the Blind Source X-ray Catalogue

Once the raw data is processed a source detection method is applied to the resulting image, in order to produce a blind[4] catalogue of X-ray sources.

Initial source detections are performed on the full resolution images, using the WAVDETECT source detection code from the CIAO suite (Fruscione et al., 2009). This initial detection is done with a very low significance threshold, given by a False Probability Threshold of 10^{-4}, and limited to the image region where the exposure is $\geq 10\%$ of the maximum exposure. The low significance threshold prevents more real sources from being missed by the initial source detection, however there will be a number of spurious sources also introduced. Spurious sources occur when random fluctuations of the background fall above the significance threshold and result in the detection method falsely identifying a candidate source.

[4] i.e. based only on the X-ray data and without using any a priori knowledge of source positions from other wavelengths.

For all candidate sources the total counts is measured in an aperture of radius given by the 70% enclosed energy fraction (EEF) PSF. The estimated local background of the source is similarly measured in a 100 pixel wide annulus of inner radius 1.5× the 95% EEF PSF, at the source position, then re-scaled to the source detection area. The false probability ($P(\geq N|b)$), a measure of the probability the source is a spurious detection, is then calculated using the equation,

$$P(\geq N|b) = 1 - P(< N|b) = 1 - \sum_{i=0}^{N-1} \frac{b^i}{i!} e^{-b} \tag{4.1}$$

where N is the total number counts measured and b is background counts. A threshold false probability value of $\lesssim 4 \times 10^{-6}$ is then applied to the candidate sources, in order to remove those believed to be spurious detections and leave only the reliable source sample.

In order to search for potentially missed sources, all reliable detections are masked out and a second pass of this detection method is performed. The background and false probability of each candidate source are subsequently recalculated, and the same false probability threshold is applied once more. As there is negligible difference in the detections list following this second detection stage, the process is not run again. For sources within 5 pixels of one another only the source with the highest measured counts is kept, in order to prevent duplicated sources within the final catalogue. Once the source list is found, the background map is created by removing all source counts from the image.

This source detection process is carried out on the images from all four energy bands (Full, Soft, Hard and Ultra Hard). The resulting reliable source lists are then merged and for any sources that are not independently detected in all bands the missing detections counts, background and exposure values are extracted from the corresponding imaging and maps at the source position.

In this work I use the catalogue resulting from this source extraction process, containing a total of 3 627 X-ray sources, referred to as the blind source catalogue. The images, background maps, exposure maps and PSF maps generated through the above reduction process are also used in §4.1.4 for the extraction of X-ray information at the positions of all sources in my reduced COSMOS2020 catalogue.

The Chandra Sensitivity across the COSMOS field

The X-ray Luminosity Function (XLF) determination requires the sensitivity of the X-ray survey to be known and quantified. I do this by generating a sensitivity map (following the process detailed in Georgakakis et al., 2008), identifying the number counts required to produce a significant detection, i.e. a detection above the specified false probability threshold given the expected background count rate, at each pixel position in the image. From the sensitivity map, I then determine the area curve; the total area of sky where the available Chandra imaging is sensitive to sources above a given X-ray flux threshold.

For any given pixel position in an image there is small probability that a random fluctuation of the background emissions or in a source will result in sufficient counts for a spuriously detected source or result in a faint source appearing brighter and thus being detected when otherwise it would not be. Source counts at a given pixel position are given by the flux of the source ($f_{\rm X}$), the exposure time (t_{exp}) and EEF at the pixel position (p), and a spectral dependent conversion factor (k) for flux to count rate. The sum of the background (b) and expected source counts ($S(f_{\rm X})$, when present) gives the total observed counts, in each pixel. The probability that this sum exceeds the given detection threshold (L counts, determined for a given false probability threshold using equation 4.1) thus is described by the cumulative probability,

$$P(\geq L|S(f_{\rm X}),b) = 1 - P(< L|\lambda) = \frac{1}{\Gamma(L)}\int_0^{\lambda} e^{-t}t^{L-1}dt \tag{4.2}$$

where $\Gamma(L)$ is the incomplete gamma function and $\lambda = b + S(f_{\rm X})$, with expected source counts $S(f_{\rm X}) = k f_{\rm X} t_{exp} p$. Thus the area curve is the sum of the cumulative probability distributions across all pixels in the image, determined for a given source flux ($f_{\rm X}$) and spectral shape. The spectral shape is taken to be a power law with photon index $\Gamma = 1.4$ for the conversion of flux to counts when determining the area curve here, the resulting flux values are then simply converted back to counts when applying the area curve to the XLF determination, removing the effect of the selected spectral shape on my final XLF.

Any masking applied to the Chandra imaging will reduce the area that is actually observed by the survey. Thus, prior to the area curve calculation, any masking

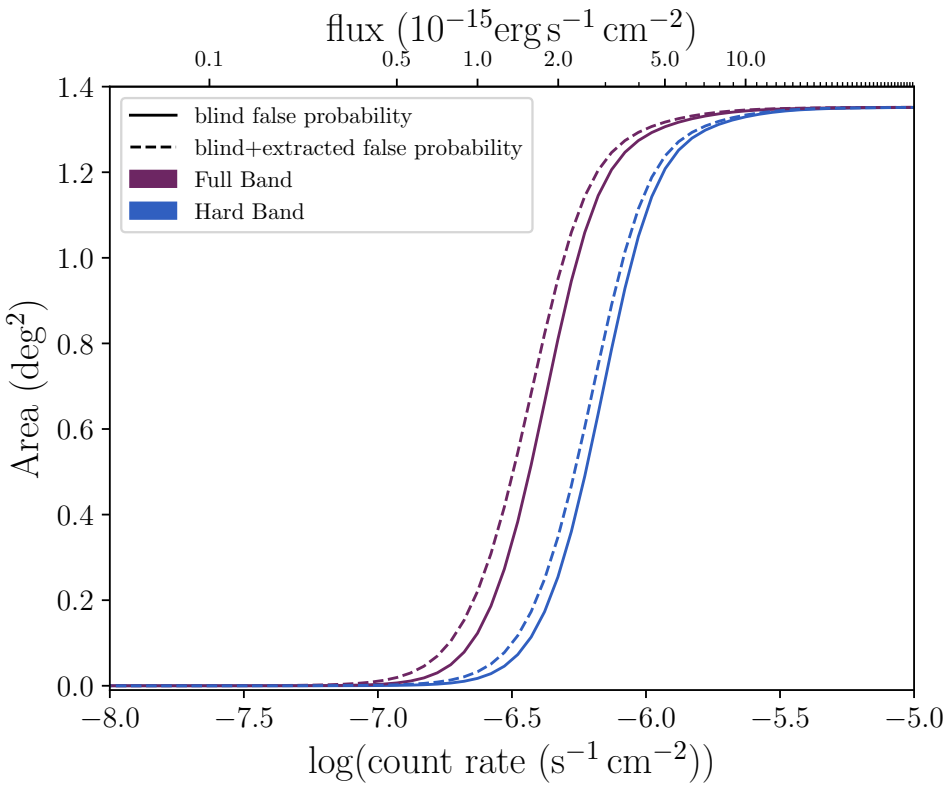

Figure 4.2 *Hard (blue) and Full band (purple) area curves determined with the blind sample false probability threshold of* 4×10^{-6} *(solid line) and the blind+extracted sample threshold of* 3.38×10^{-5} *(dashed line). All use of these area curves is with the area with respect to count rate.*

applied to the Chandra imaging must be similarly applied to the sensitivity map, such that the resulting area curve will be representative of the actual survey area. In this work I apply the bright-star mask and limit the survey area to the UltraVISTA region (see §4.1.2) to my source samples, and as such I apply the corresponding masks to the sensitivity map following its initial generation.

Sensitivity maps, and corresponding area curves, are calculated for the Full and Hard band imaging for both a false probability threshold of 4×10^{-6}, corresponding to the blind source catalogue detailed above, and for the less stringent threshold adopted when considering the X-ray data at known COSMOS2020 source positions (see §4.1.1). Figure 4.2 shows the resulting area curves, as given by a false probability threshold of 4×10^{-6}, for the Full and Hard energy bands used for the XLF determination (§4.2 and §4.3). From these area curves, the full survey area of my X-ray catalogue is $1.35\,\mathrm{deg}^{-2}$, with a 10% area coverage at a count rate of $2.41 \times 10^{-7}\,\mathrm{s}^{-1}\,\mathrm{cm}^{-2}$ and $3.89 \times 10^{-7}\,\mathrm{s}^{-1}\,\mathrm{cm}^{-2}$ for the Full and Hard band imaging respectively.

4.1.3 X-ray and redshift catalogue cross-matching

In order to perform redshift dependent studies of the X-ray AGN population, I identify counterparts in the filtered COSMOS2020 sample (see §4.1.1) to sources within my blind X-ray catalogue (detailed in §4.1.2), producing a sample of X-ray sources with optical/IR photometry. The counterparts to my blind catalogue are determined using the Bayesian Cross-Matching code NWay (Buchner et al., 2021).

Identifying the counterpart to an X-ray source detection through positional only cross-matching has a high risk false matches for faint sources, due to the large positional uncertainties in faint X-ray sources. As detailed in Salvato et al. (2018), NWay was developed to identify multi-wavelength counterparts to X-ray sources without this bias, through a Bayesian framework, building on the work of Budavári & Szalay (2008).

Using the distance between the counterpart and the X-ray source, as well as their positional uncertainties and the total area of sky covered by the samples, Nway determines the probability (p_i) of each multi-wavelength source being the true counterpart to the X-ray detection and the probability that the true counterpart of each X-ray source is in the multi-wavelength sample (p_{any}). Weighting is then applied to these probabilities, given specified magnitude and colour priors for the cross-match.

Prior to identifying counterparts to my blind X-ray sample, any sources within the X-ray positional uncertainty of the bright-star masks applied to the COSMOS2020 catalogues (HSC-SSP PDR2 Coupon et al., 2018) are masked from the sample, in order to ensure the final cross-matched sample contains only X-ray sources for which, with reasonable confidence, the optical/IR counterparts do not lie within the masked regions of the COSMOS2020 sample. Apertures of radius $r = 0.82$ arcsec, given by the mean positional uncertainty of all blind X-ray sources, are placed at the X-ray source positions, and all sources for which this aperture intersects the bright star mask regions are removed from the X-ray sample producing a sample of 2792 X-ray sources. In addition, as the COSMOS2020 sample used in this study is limited to the UltraVISTA sky area, I similarly limit the blind X-ray source sample to this area. Thus the resulting area of both our masked COSMOS2020 and blind X-ray source samples is 1.35 degrees^2, containing 816 944 and 2 408 sources respectively.

I consider potential COSMOS2020 counterparts, to the blind X-ray sources, within a 10 arcsec search radius of each X-ray position, assuming all X-ray sources have a counterpart within the COSMOS2020 sample. This search radius exceeds 3 times the maximum X-ray positional uncertainty of the sample and thus ensures that $> 99\%$ of the true counterparts are included (I note that the typical offset between an X-ray source position and the final, best counterpart is typically ~ 0.47 arcsec, i.e. much lower than this initial search radius).

I experiment with adopting a number of possible internally generated priors. These priors are based on the magnitudes in the UltraVISTA Ks-band, IRAC channel 1 and IRAC channel 2, chosen as they are good tracers of AGN activity at high redshifts (see e.g. Reines & Comastri, 2016) as well as the IRAC channel 1-channel 2 colour. Those cross-matches which are identified as the best matches (i.e. those with the largest p_i value) are taken to be the sample of cross-matched sources.

In order to assess the fraction of incorrect associations from a given Nway run, I perform the same cross-matching process with Nway using a catalogue of fake X-ray sources. The resulting catalogue of fake sources assigned COSMOS2020 counterparts provides a measure of the incorrect associations that will be present in the sample of cross-matched blind X-ray sources. The fake sample is generated by applying a random positional shift, of $20 - 120$ arcsec, to the positions of all sources in the unmasked blind X-ray sample. The same sample masking as is applied to the real sample of blind X-ray sources is then applied to this fake sample, in order to remove any fake sources that fall within the masked regions of the COSMOS2020 sample, where the photometry is unreliable. Following the same assumptions as for the real blind X-ray sample, I assign counterparts to the fake blind X-ray sample with the magnitude priors generated, by Nway, during the cross-matching of the real blind X-ray sample to COSMOS2020. The resulting sample is then, similarly, limited to only the potential counterparts with the largest p_i value, reducing the sample to only the best cross-matches identified for each fake blind X-ray source.

Using the real and fake cross-matched samples, I assess the quality of the resulting sample of counterparts to my blind X-ray sources. For the two cross-matched samples I determine the completeness (the fraction of the real sample have a correctly matched counterpart) The completeness of the sample of counterparts to the sample of real X-ray sources is calculated as,

$$\text{Completeness} = \frac{N_{p\_\text{any,threshold}}}{N_{total}} \tag{4.3}$$

where N_{total} is the total number of x-ray sources in the sample, and $N_{p\_\text{any,threshold}}$ is the number of matched sources with p_any (the probability of the correct galactic counterpart existing within the galaxy sample) greater than a given threshold value ($p\_\text{any}, \text{threshold}$). The fraction of matched sources that are likely to be incorrectly matched, known as the false positive fraction, is similarly calculated from the fake match sample by taking the ratio of the number of matches to the fake sample with $p_$any exceeding the same $p\_\text{any}, \text{threshold}$ to the total number of X-ray sources.

The completeness and false positive fraction are calculated for a range of $p\_\text{any}, \text{threshold}$ values, for each of the matched samples resulting from the different combinations of magnitude and colour based priors used. Plotting the Completeness and False Positive Fraction against $p\_\text{any}, \text{threshold}$, given by the different combinations of priors, I find that the completeness remains above 0.9 until a $p\_\text{any}, \text{threshold}$ of ~ 0.7 and the false positive fraction drops rapidly to below 20% by a $p\_\text{any}, \text{threshold}$ of ~ 0.4, for all but the spatial-only and IRAC colour magnitude only cross-matches (see figure 4.3). Comparing the Completeness and False Positive Fraction (right hand plot in figure 4.3), it can be seen that the cross-match performed with the Ks-band and IRAC colour magnitude priors remains at the lowest False Positive Fraction of all tested combination of magnitude priors, as the Completeness increases to over 0.9. Thus, I select the cross-match performed with the combination of a Ks-band magnitude and IRAC channel1-channel2 colour magnitude priors for the final cross-matched sample.

For this study I choose a false positive fraction of 10%, as an acceptable failure rate of the cross-matching. This corresponds to a sample completeness of 0.97 and threshold p_any value of 0.388. When considering the high-redshift samples only, given by the best fit photometric redshift values (as defined in §4.2.1 below), this $p\_\text{any}, \text{threshold}$ corresponds to a False Positive fraction of $1.0{\times}10^{-3}$%, $3.3{\times}10^{-4}$% and 1.1×10^{-4}% for the samples with photometric redshifts of $z \geq 4$, $z \geq 5$ and $z \geq 6$ respectively. These very small False Positive Fractions in the high-redshift samples are due to both a much lower surface density of high-redshift sources compared to the full COSMOS2020 sample and that higher redshift sources tend

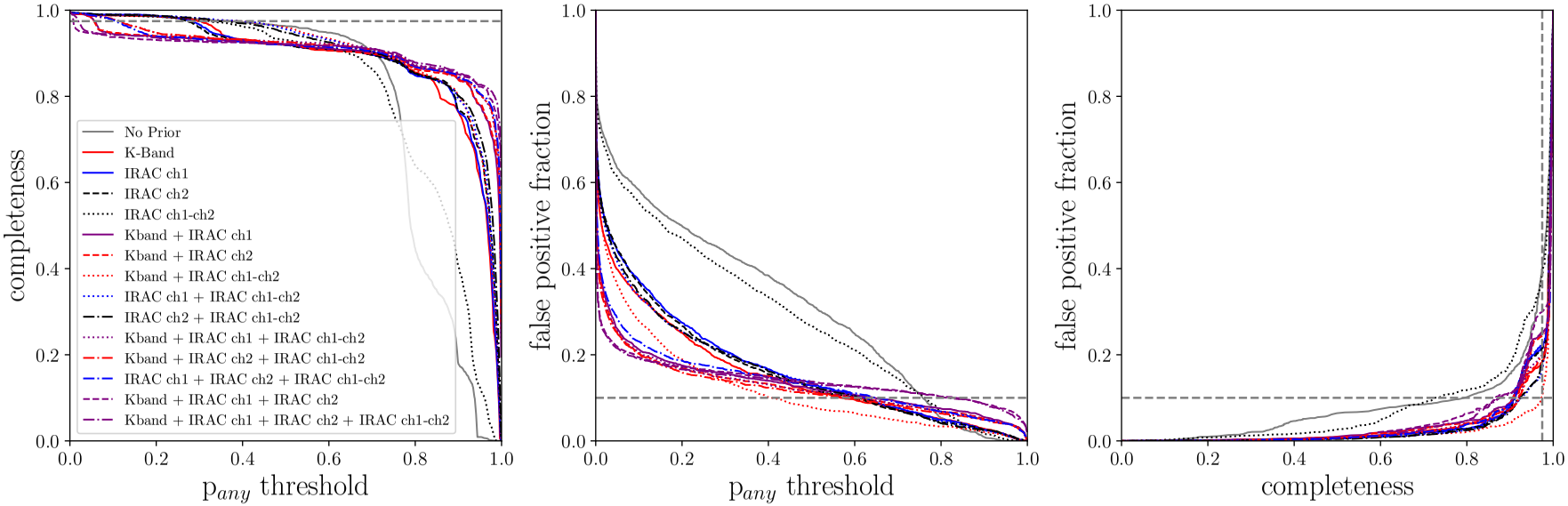

Figure 4.3 *Plots of the completeness and false positive fraction for all possible p_any thresholds applied to the Nway matched samples, as performed for different combinations of internally generate magnitude priors (based on the magnitudes in the UltraVISTA K-band, IRAC channel 1 and IRAC channel 2, and the IRAC channel 1-channel 2 colour). Left: The change in sample completeness with p_any threshold apply to the sample. Centre: The change in the false positive fraction of the sample with p_any threshold chosen. Right: Comparison between the completeness and false positive fraction in the sample, with changing p_any threshold applied.*

to have fainter magnitudes. As such, a random alignment between an X-ray source position and a high-redshift galaxy, which is subsequently falsely identified as the best counterpart to the X-ray source, is very unlikely to occur.

4.1.4 X-ray counts extraction at galaxy positions

High-redshift AGN appear observationally very faint (see §1.5 for details) thus there are likely to be fainter X-ray AGN within my high-redshift galaxy sample that fall just below the X-ray detection thresholds adopted in the creation of the blind sample. As such these very faint AGN will not be present within the blind source catalogue. In order to further exploit the available X-ray data of high-redshift AGN, and push the limits of this study to the fainter X-ray regime, I extract X-ray counts directly from the cleaned Chandra imaging (detailed in §4.1.2) at the positions of the COSMOS2020 sources within my sample.

Prior to extracting X-ray counts at the COSMOS2020 positions, any COSMOS2020 sources in my sample that lie within 2 times the 90% EEF radius for the Chandra PSF of a bright X-ray source position (where the blind X-ray source sample is taken to be the bright source list) are removed from the sample of sources for which X-ray counts will be directly extracted from the Chandra imaging. This ensures that no counts due to the emissions of a source, identified through the blind X-ray detection, are erroneously included when attempting to identify additional, fainter X-ray sources.

For all sources within my COSMOS2020 sample, with those near bright X-ray sources removed, the 70% EEF radius for the Chandra PSF at each source position is identified from the PSF maps generated in §4.1.2 (with the value taken to be the mean measurement of the Chandra PSF within 1 pixel of the exact source position from COSMOS2020). At the position of each COSMOS2020 source in my sample I place apertures of radius, given by the 70% EEF radius, and measure the total counts and total background within these apertures from the Chandra image and background map respectively[5]. Similarly, the average exposure time within the aperture, for each source, is determined from the exposure map. The net count rates (c) of each source are then calculated using the total measured counts ($\boldsymbol{C}_{total}$), background counts ($\boldsymbol{B}_{aper}$) and exposure time (t_{exp}),

[5]The value of pixels within the source aperture are only counted if their centre lies within the source aperture. No additional weighting to the pixel values is applied.

$$c = \frac{C_{total} - B_{aper}}{p_{70} t_{exp}} \tag{4.4}$$

where the factor of $p_{70} = 0.7$ is applied in order to correct for the choice of an aperture extraction radius corresponding to the 70% EEF at the source position.

For each extracted count rate of the COSMOS2020 sources, the false probability is calculated using equation 4.1. As can be seen by the pink histograms in figure 4.4, the frequency of sources increases exponentially towards a false probability of 1, i.e the majority of the extracted count rates for my COSMOS2020 sources are consistent with being produced by random fluctuations in the background.

In order to identify those sources for which the extracted count rates are unlikely to be due purely to a random background fluctuation, and thus obtain the sample of X-ray detections, I apply a false probability threshold to the extracted sample, as was done for the blind X-ray catalogue. However, as only positions of known COSMOS2020 sources are considered, and thus where a galaxy or AGN was known to be a priori, a less stringent threshold than was used in the formation of the blind catalogue can be applied. This enables fainter X-ray sources to be identified within the Chandra imaging, and increases the size of the sample of high-redshift, X-ray detected AGN without introducing a significant number of additional false X-ray sources.

The threshold false probability is determined iteratively. For a range of false probability thresholds, the fraction of the X-ray detected sample which have been falsely detected (the False Fraction) is calculated, using the following relation,

$$FalseFraction = \frac{\lambda_{false}}{N_{f_{prob} < f_{prob,threshold}}} \tag{4.5}$$

where $N_{f_{prob} < f_{prob,threshold}}$ is the number of X-ray detected sources in the sample, at a given f_{prob} threshold ($f_{prob,threshold}$) and λ_{false} is the corresponding expected number of false detections, given by,

$$\lambda_{false} = N_{gal} f_{prob} \tag{4.6}$$

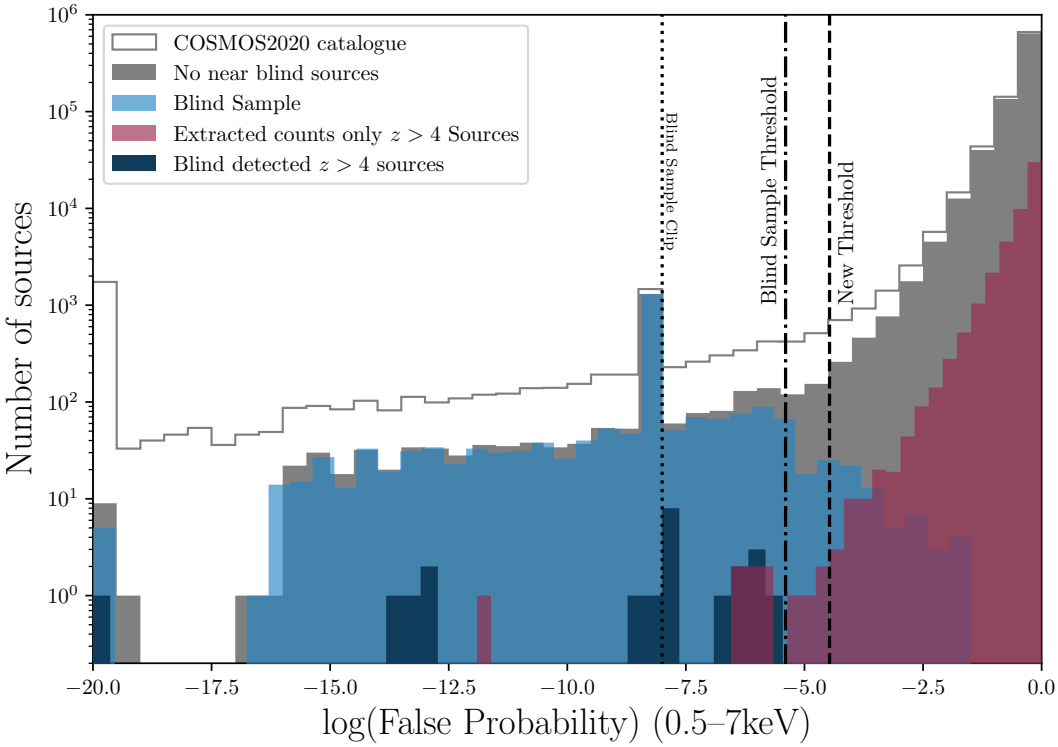

Figure 4.4 *Histograms of the false probabilities of sources from the full-band Chandra-COSMOS data, showing values directly extracted from the Chandra imaging or the blind detections where available. The full sample of COSMOS2020 sources is shown by the grey outline, with those remaining once sources around the blind x-ray detected sources are removed shown in solid grey. The blind only sample, obtained using the false probability threshold of* 4×10^{-6}*, is shown in blue. The source numbers above the* 4×10^{-6} *threshold are due to the detection of sources in the soft, hard or ultrahard bands, but not in the full band. The high redshift sources within this sample, for both the blind only sources (navy) and the newly extracted sources only (pink) are shown. The updated threshold applied to the extracted sample is indicated by the dashed line, with the threshold of* 4×10^{-6} *shown by the dot-dashed line, for comparison. For this histogram, I set a minimum false probability of* 10^{-20}*, resulting in a peak of sources where all those with a false probability below this are set to a value of* 10^{-20}*. Similarly any sources with extremely low (but non-zero) false probabilities within the blind detected source catalogue are set to a false probability of* 1×10^{-8} *(as indicated by the thin dotted line) in order to distinguish them from a false probability of 0, this results in an artificial peak in source numbers at this false probability.*

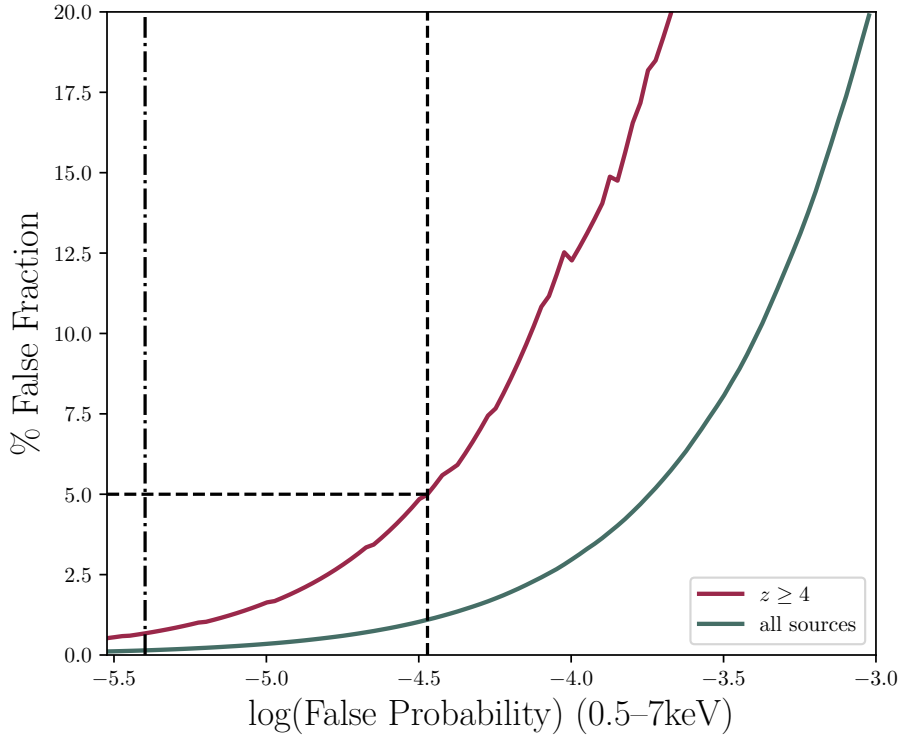

Figure 4.5 *The change in false fraction with increasing false probability threshold, shown for all sources (sage) and $z \geq 4$ sources only (pink) in the full-band blind+extracted sample. The blind catalogue false probability fraction of 4×10^{-6} is shown by the dot-dashed line, with the new threshold false probability for the blind+extracted sample (3.38×10^{-5}) shown by the dashed line, corresponding to a False Fraction of 5% with respect to the $z \geq 4$ sources only (shown by the horizontal dashed line for reference).*

where N_{gal} is the total number of sources in the sample X-ray data was extracted for. This is done for both the full sample of extracted sources and the sample of sources with a best fit photometric redshift of $z \geq 4$ (see section 4.2.1 for details on the redshift values). The resulting relation between the False Fraction and the False Probability Threshold of my samples (shown in figure 4.5) can be seen to rise at lower threshold values for the $z \geq 4$ sample (shown in blue) compared to the full sample (shown in red). This is due to the smaller sample size of $z \geq 4$ sources and lower X-ray count rate of all sources at higher redshifts.

The threshold false probability of my sample is taken to be that corresponding to a False Fraction of 5% in the $z \geq 4$ sample, giving a threshold of 3.38×10^{-5}. This threshold is then applied to my combined sample of 882856 extracted and blind X-ray sources, removing all sources with a full-band false probability of more than this threshold value I obtain my final sample of 2591 X-ray AGN.

4.2 Measurements of the XLF

4.2.1 The High-Redshift sample and X-ray Luminosities

In order to measure the X-ray Luminosity Function (XLF) of Active Galactic nuclei (AGN) within the early Universe, a survey sample of X-ray sources with corresponding redshifts and a defined sensitivity is required. Following the processes detailed in section 4.1, I have obtained a sample of 2591 *Chandra* X-ray sources with counterparts in the FARMER version of the COSMOS2020 photometric redshift catalogue. Here I will summarise the high-redshift X-ray sample and properties used in the following sections.

My sample of X-ray sources is comprised of 2265 detections from the blind search of *Chandra* Legacy Imaging and an additional 326 sources obtained through direct extraction of X-ray counts from the *Chandra* Images. For all of these sources I use the LePhare photometric redshift fits performed by Weaver et al. (2022). However, due to poor imaging or faint sources, there is a lack of photometeric measurements for a few of the sources within this sample. For these sources LePhare was unable to obtain a secure fit to the existing photometry (these sources are marked as failed fits by LePhare). In order to ensure only sources with reliable photometric redshift measurements are included, the 261 sources for which LePhare was unable to reliably fit a photometric redshift measurement (due to a lack of photometric measurements, contamination by nearby sources or edge effects in the imaging) are removed from my sample[6]. Following this my X-ray source sample is comprised of 2035 blind X-ray detected sources and 295 directly extracted sources, for a total sample size of 2330.

As detailed above (in §4.1.1), the LePhare code performs redshift fits using galaxy templates and again using templates with an AGN spectral component. For sources with multiple redshift measurements from LePhare the better fit photometric redshift (that with the smaller χ^2), either using galaxy or AGN spectral energy distribution templates, is taken to be the best estimate of the source redshift and used in the subsequent AGN space density investigations. As

[6]This corresponds to a failed fraction of 0.1. Whilst it would be unphysical for all 261 failed fits to correspond to high redshift sources ($\sim 8\times$ more sources than my final sample), this failed fraction suggest there may be ~ 3 sources missed from my final $z \geq 4$ sample. If so my final measurements of the space density would be higher than currently, and thus further indicative of a larger space density than predicted by model extrapolations (see also section 4.4).

such 1239 of my sample sources have best fit photometric redshifts from galaxy spectral models and 1091 sources have photometric redshifts given by the fits of AGN templates. Applying a redshift cut of $z_{best} \geq 4.0$ to this sample I obtain my high-redshift X-ray sample of 32 sources, with which I will perform my initial calculations of the observed X-ray Luminosity Function.

For all sources within the high-redshift sample, I convert directly from the measured net count rate in a given band (i.e. the full 0.5–7 keV and hard 2–7 keV bands) into a rest-frame 2-10 keV luminosity (denoted as $L_{\rm X}$). I assume an X-ray spectral model consisting of a power-law with a photon index $\Gamma = 1.9$, a reflection component modelled using the pexrav model (Magdziarz & Zdziarski, 1995, assumes an infinite plane reflector) of relative strength 1.0 and take the galactic absorption ($N_{\rm H,Gal}$) to be that of the COSMOS field (average of $10^{20.25}{\rm cm}^{-2}$ (HI4PI Collaboration et al., 2016)). This model is then folded through the response function of Chandra as given for the middle of the observing period of the imaging used (cycle 16, see Appendix C for details), to determine the conversion between the observed counts measured by Chandra (c in equation 4.7) and the rest-frame 2-10keV luminosity ($L_{\rm X}$) of each source.

$$L_{\rm X} = c \times \kappa(z, N_{\rm H,Gal} = 10^{20.25}, \Gamma = 1.9), \tag{4.7}$$

where $\kappa(z, N_{\rm H,Gal}, \Gamma = 1.9)$ is the redshift dependent conversion factor determined. By converting the measured count rates directly into luminosities I avoid the need to make multiple spectral assumptions, as would be required to convert counts to flux and then to luminosity.

For my initial XLF measurements I use $L_{\rm X}$ as given by the full band count rate and the best fit redshift, assuming the standard spectral model of Aird et al. (2015). My resulting high-redshift sample, with respect to their $L_{\rm X}$, are shown in figure 4.6, as given by both the galaxy fit and AGN fit photometric redshifts.

With the redshift of a source significantly affecting it's estimated luminosity, I will later determine the luminosity of sources using both the redshift from their galaxy redshift fits and their AGN redshift fits. As can be seen in figure 4.6, sources can move in and out of my high-redshift sample, depending on the choice of photometric redshift fit, as well as change in rest-frame luminosity (however, the change in number of sources with photometric redshift fit chosen will have

a more significant effect on and XLF measurements). In §4.2.4 I will investigate the impact of this uncertainty in the true redshift of my sources on the measured XLF.

The spectral model used here is relatively simple and does not correctly model the more obscured X-ray sources. As such, in order to investigate the impact of obscuration on my XLF measurements (see section 4.3), I also use a more complex spectral model from Baloković et al. (2018) which includes a dusty "torus" around the accretion disk, modelling the effect of Compton scattering of high energy photons which comes into play in obscured sources.

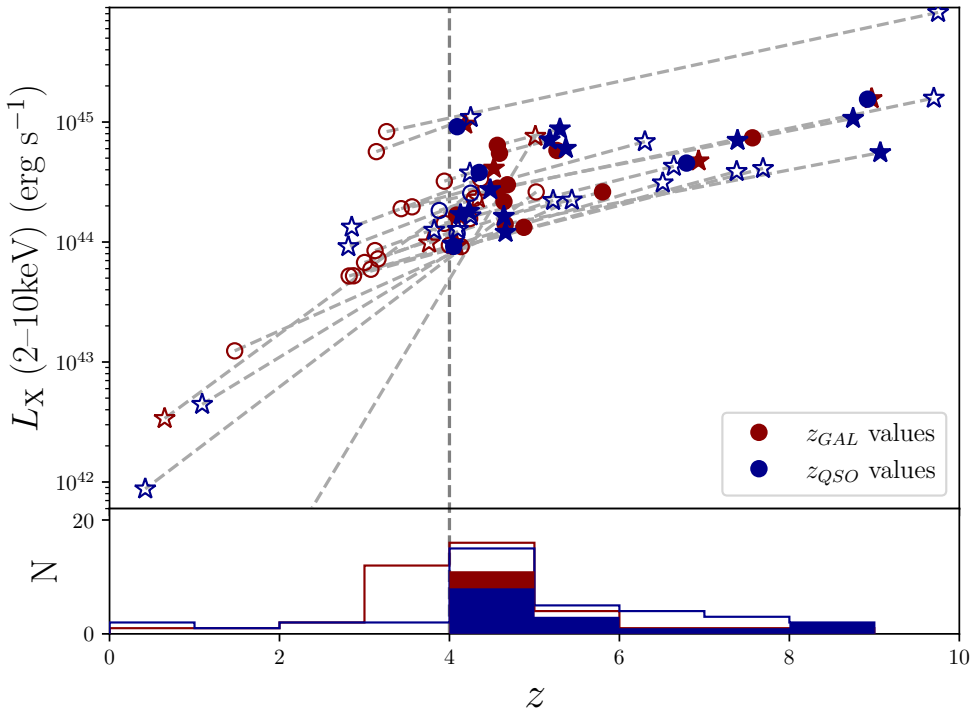

Figure 4.6 *Plot of the rest-frame 2-10 keV X-ray luminosity against redshift, obtained from the full band count rate, for all sources within my high redshift sample. Sources are shown with both their galaxy fit (z_{GAL}) and the AGN fit (z_{QSO}) photometric redshifts (red and blue respectively), with sources that would leave the high redshift sample given either their galaxy or AGN redshift fit indicated by empty points. For each source the best fit photometric redshift, used to determine the XLF, is shown as a star.*

4.2.2 XLF measurements from the blind source catalogue

The X-ray luminosity function describes the population of active galactic nuclei, at a given redshift and AGN luminosity, however it is poorly constrained at

high redshifts (see chapter 1 for details). Although my sample of $z \geq 4$ sources summarised above (§4.2.1) is too small to perform a secure fit of a parametric XLF model, it can still be used to obtain measurements of the XLF through the deep Chandra imaging of the COSMOS field.

In order to determine measurements of the observed XLF I first use only the more secure (lower false probability threshold) blind X-ray detected sources in my sample. These 21 $z \geq 4$ sources are divided into redshift bins of $z = 4-5$, $5-7$ and $7-10$, corresponding to the highest redshift where commonly accepted parametric XLF models have been constrained in prior studies, the epoch of cosmic reionisation and extremely high redshifts, respectively. The sources within each of these redshift ranges are then split into 0.5 dex wide luminosity bins from $\log L_{\mathrm{X(2-10keV)}}\,\mathrm{erg\,s^{-1}} = 43-46$, which allows the detailed shape of the X-ray Luminosity Function to be seen across each redshift range.

The observed space density of AGN, in the form of the XLF ($\phi_{obs}(L_{X_i}, z_j)$), is then determined in each redshift (z) and luminosity (L_{X}) bin, following the N_{obs}/N_{model} method of Miyaji et al. (2001). As this method accounts for changes in the X-ray sensitivity and AGN space density within each bin, it provides a more robust estimate of the XLF for the low source numbers within my sample.

In order to obtain the XLF estimates in each redshift and luminosity interval the predicted value of the XLF, as given by a parametric model at the centre of each bin, is scaled by the ratio of the number of observed sources in that bin to the number of sources predicted by the model;

$$\phi_{obs}(L_{\mathrm{X}_i}, z_j) = \phi_{model}(L_{\mathrm{X}_i}, z_j)\frac{N_{obs}}{N_{model}} \tag{4.8}$$

where N_{obs} is the observed number of sources in each bin. The parameterised XLF model, $\phi_{model}(L_{\mathrm{X}_i}, z_j)$, is taken to be the value of the Luminosity Dependent Density Evolution (LDDE) XLF model of Georgakakis et al. (2015) at the centre of the $z - L_X$ bin (at L_{X_i} and z_j). Despite requiring a parametric model, from previous XLF studies (e.g. Georgakakis et al., 2015; Ueda et al., 2014; Pouliasis et al., 2024), the N_{obs}/N_{model} method is only slightly sensitive to the specific choice of model with the large uncertainty in source numbers used here. Finally the predicted number of sources in the bin, N_{model}, is given by;

$$N_{model} = \int_{z_1}^{z_2} \int_{\log L_{X_1}}^{\log L_{X_2}} \phi(L_X, z) A(f(L_X, z)) \frac{dV_{\rm co}}{dz} d\log L_X dz, \tag{4.9}$$

where $\phi(L_X, z)$ is the parametrised LDDE XLF model of Georgakakis et al. (2015), $\frac{dV_{\rm co}}{dz}$ is the differential comoving volume at a given redshift, z, and $A(f(L_X, z))$ is the sky area imaged by Chandra at an observed flux, $f(L_X, z)$, corresponding to a given 2–10 keV rest-frame luminosity, L_X, and redshift, as determined in §4.1.2 with a false probability threshold of 4×10^{-6} (as used in the sample creation). resulting observed, binned XLF measurements are shown in figure 4.7.

For each redshift and luminosity interval, the 1σ uncertainty on the number of sources is given by the Gehrels (1986) Poisson uncertainties, and folded through the calculation of the observed XLF in order to to determine the uncertainties on these values. Where there are no observed sources in a bin (i.e. $N_{obs} = 0$) the XLF measurement is taken to be an upper limit on the XLF as given by the upper 1σ uncertainty given a sample size of 0.

For comparison I plot the parametric models of Georgakakis et al. (2015) (LDDE model), Ueda et al. (2014) and Pouliasis et al. (2024) (fit to data at redshifts of $z = 3 - 5$, $z = 0.002 - 5$ and $z = 3 - 6$ respectively), extrapolated to the redshift at the centre of each bin. The uncertainty in these models are obtained through Monte Carlo simulations using the XLF model parameter values and their uncertainties, as given in Georgakakis et al. (2015), Ueda et al. (2014) and Pouliasis et al. (2024).

At $z = 4 - 5$ my observed XLF measurements are consistent with the parametric models, which were fit to data including this redshift range. However, as the redshift increases the observed XLF can be seen to remain at high space densities, with only a slight decrease from the values at $z = 4 - 5$ towards $z = 7 - 10$, whilst the extrapolated models would predict a clear drop in the space density. As the redshift increases the observed XLF remains consistent with the models at $z = 4 - 5$, around the break luminosity, with a flattening of the bright-end slope observed towards higher redshift bins. These results indicate a less steep evolution in the space density of AGN in the early Universe than was predicted from parametric models, with more sources found at higher redshifts than previously expected.

Despite the obvious trends in my observed measurements, however, there remain

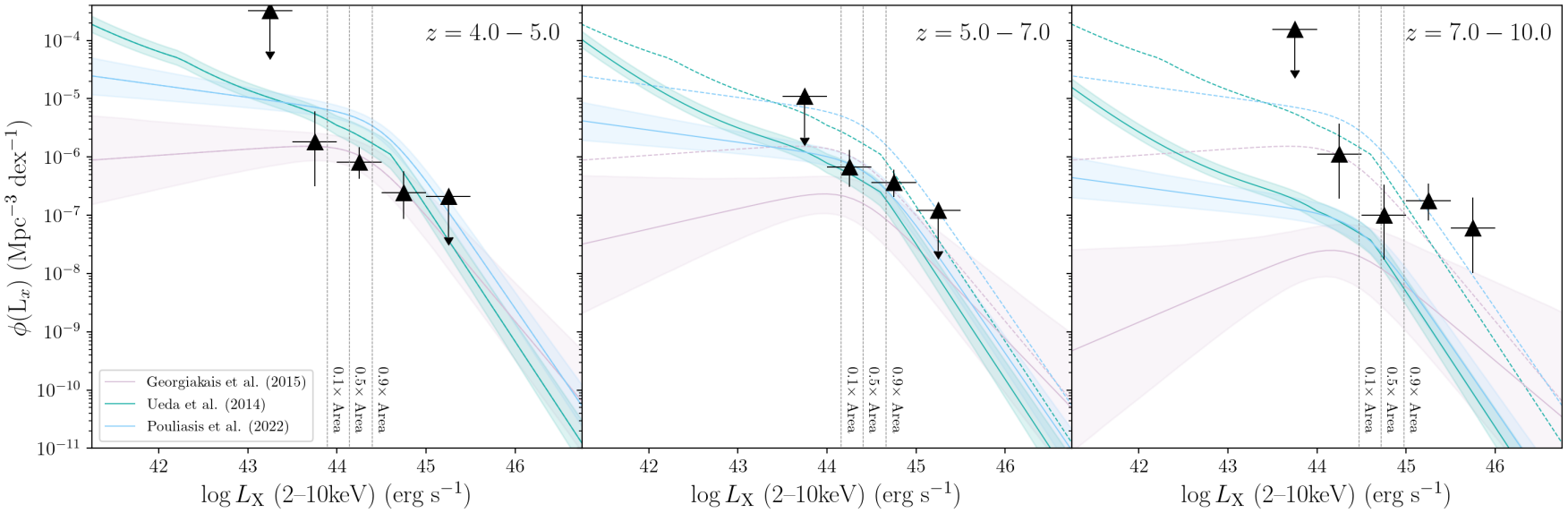

Figure 4.7 *Observed binned measurements of the high redshift XLF of AGN, as given by the cross-matched blind source sample (black triangles) for Luminosity intervals of 0.5 dex. At $z = 4 - 5$ (left hand panel) my measurements are consistent with the model XLF of Georgakakis et al. (2015) (pink), Ueda et al. (2014) (green) and Pouliasis et al. (2024) (blue), as fit to data within the same redshift range, whilst indicating a higher space density than predicted by the model extrapolations at $z = 7 - 10$ (right hand panel). For comparison the model XLF at $z = 4 - 5$ are shown on the plots of $z = 5 - 7$ and $7 - 10$ by the dashed lines. The luminosity at which 10%, 50% and 90% of the survey area is visible by Chandra are indicated by the vertical grey lines. Upper limits are provided by the upper Poisson uncertainty on 0 sources, as given by Gehrels (1986).*

large uncertainties due to the small number of sources. In order to improve the constraints further I now move onto using the full sample of Blind detections and Directly Extracted sources.

4.2.3 Blind and Extracted AGN XLF Measurements

In order to fully exploit the deep X-ray data available from the Chandra Legacy survey, and improve the statistics of my measurements of the high-redshift AGN X-ray Luminosity Function, I extracted X-ray counts for all COSMOS2020 sources. I then determined a sample of X-ray AGN from the combination of the blind X-ray detected sources and the directly extracted X-ray measurements (see §4.1.4 for details of the sample creation). Following the process detailed above (in section 4.2.2), I obtain the blind+extracted sample measurements of the XLF.

The rest-frame 2-10 keV luminosity (L_X) of each source within this combined catalogue is taken to be that given by the blind source X-ray counts where available, and for all COSMOS2020 sources without blind detections the directly extracted X-ray measurements are used. The observed XLF given by this full sample of $z \geq 4$ X-ray detected sources is determined, as for the blind X-ray detected source sample only (see section 4.2.2), with redshift bins of $z = 4-5$, $5-7$ and $7-10$, and 0.5 dex bins of luminosity from $\log L_{X(2-10keV)} = 43 - 46\,\mathrm{erg\,s^{-1}}$. As a less stringent false probability threshold was used in the creation of the blind and extracted X-ray sample, a false probability of 3.38×10^{-5}, the sky area imaged by Chandra is recalculated for this threshold (see §4.1.2 for details of the calculation). This new area curve is used to determine the predicted number of sources (equation 4.9). The resulting measurements of the high-redshift XLF are shown in figure 4.8.

With the less stringent false probability threshold possible for this combined sample, I have improved the sensitivity of my observations and increased the area of sky visible by Chandra at lower luminosities. This new sensitivity has reduced the upper limits on the space density at the faint-end of my observed XLF measurements, allowing for tighter constraints on the faint-end of the high-redshift XLF.

Due to the larger sample size used here, I have increased the number of sources at each redshift interval, and thus reduced the uncertainty in my observed XLF measurements. As can be seen in figure 4.8, the space density at $z = 4 - 5$

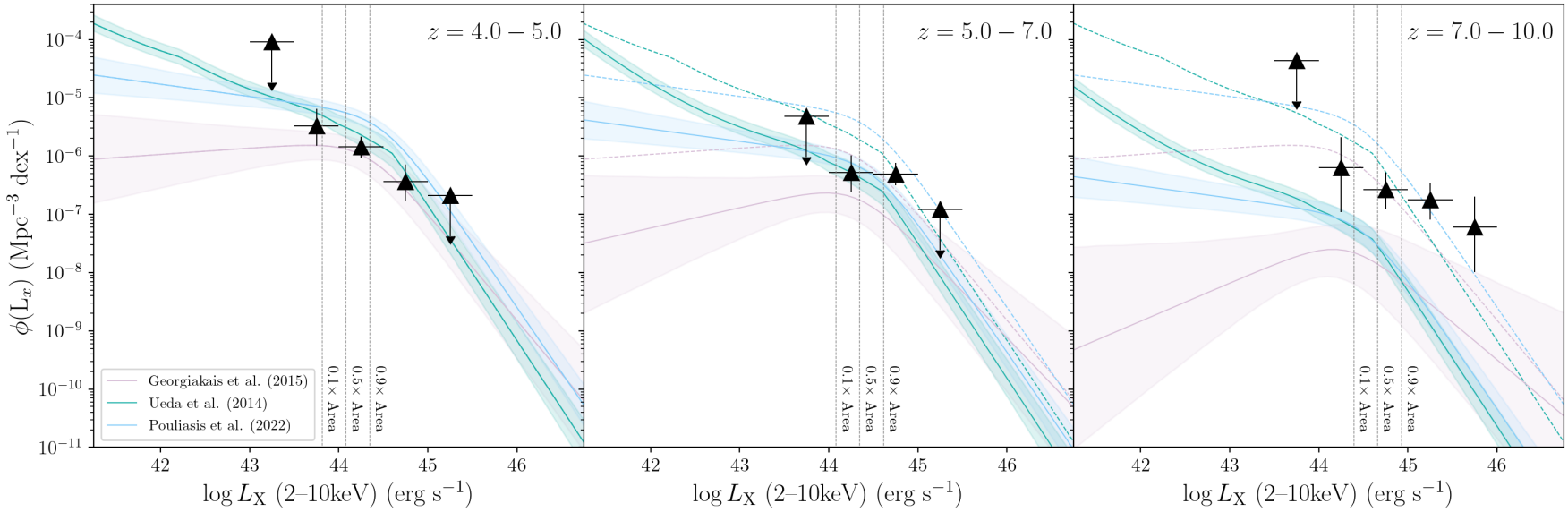

Figure 4.8 *As for Figure 4.7, with sources from both the blind source detection and directly extracted counts. Consistent with models at $z = 4 - 5$, my binned XLF measurements begin to hint at a higher than predicted space density at $z = 5 - 7$ whilst clearly indicating the space density of AGN is higher than predicted, by parametric models, for the redshift interval of $z = 7 - 10$.*

increases slightly from that in figure 4.7, to be above that of Georgakakis et al. (2015), whilst remaining consistent with all extrapolated models shown. The decline in space density with increasing luminosity, at $z = 7 - 10$, is less steep than the blind only measurements and continues to show a more flattened trend than the model predictions. My improved observed XLF measurements remain significantly higher than the model predictions at $z = 7 - 10$ and continue to indicate a higher space density at $z = 5 - 7$ than previously predicted.

4.2.4 Photometric Redshifts; the Uncertainty in XLF Measurements

Photometric redshifts are obtained through the fitting of combinations of template Spectral Energy Distributions (SEDs) to the measured photometry. The choice of templates and fitting process can impact the measured redshift, in particular the inclusion of an AGN component to the SED can drastically alter the resulting redshift measurement. The LePhare photometry code determines a redshift for each source in the COSMOS2020 catalogue both with and without an AGN component in the templates used (these redshift fits are shown in Appendix B). As such, all sources within my blind+extracted X-ray sample have two possible photometric redshifts, with the choice of SED fit having the potential to dramatically alter the measured XLF.

As can be seen in figure 4.6, the photometric redshift of a source when found with AGN templates can alter whether that source falls within my high-redshift sample, compared to its photometric redshift as given by galaxy only templates. For the previous measurements of the XLF, in §4.2.2 and §4.2.3, the redshift of each source was taken to be that given by the best template fit (as determined in section 4.2.1). However, as source numbers are considered based on their redshifts and their rest-frame luminosity (which depends on source redshift), the contribution of an AGN component to the templates fit will impact the number of sources that goes into the measurements of the XLF. Here I investigate this, in order to obtain the most conservative and most optimistic values for the XLF measurements that can be found from my X-ray sample.

Considering both forms of the photometric redshift, from the galaxy only templates and the AGN templates, I generate four different high-redshift samples. The creation of these samples is summarised in figure 4.9. Some of the sources

within my X-ray sample only fall into the range of $z = 4-10$ with one their galaxy or their AGN photometric redshift fits, but not the other. Thus, I form samples for the case where for each source for which only one redshift measurement would place them in my high redshift range, the redshift is taken to be that which places such sources within the $z = 4-10$ redshift range, hereafter referred to as the "with" samples and for the case where their redshift is taken to be that which places them outside this redshift range, hereafter referred to the "without" samples. Of the sources for which both their galaxy and AGN photometric redshifts place them within the redshift range of $z = 4-10$, for both with and without samples I consider the cases where the redshift of each source is taken to be the smallest of the two redshift values and the case where it is taken to be the largest value, hereafter referred to as the "low" and "high" samples respectively. The resulting distribution of source numbers for the four samples (with+low, with+high, without+low, without+high) are shown in figure 4.9.

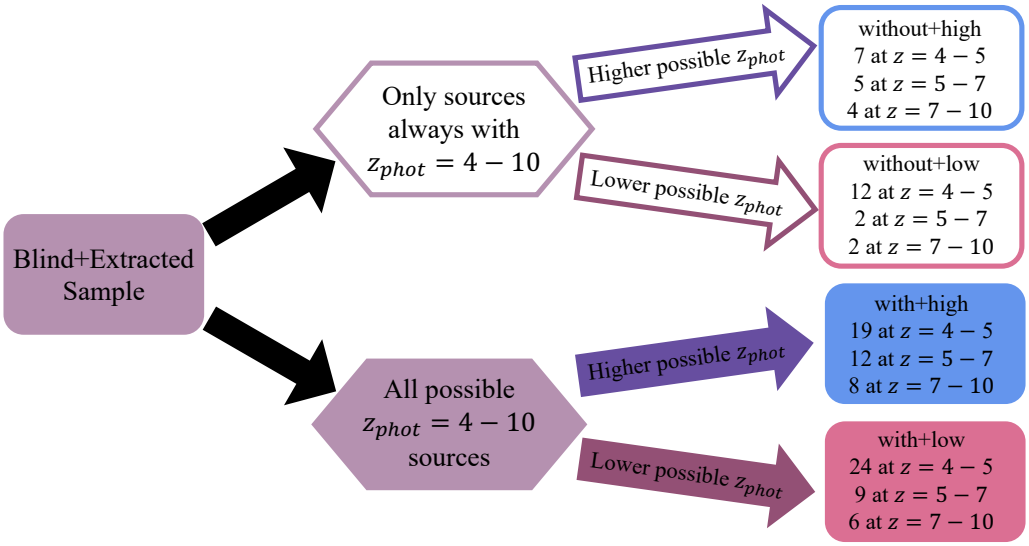

Figure 4.9 *Flow chart illustrating the creation of the four photometric-redshift version dependant high-redshift samples, from my blind+extracted sample, with+low (solid pink), with+high (solid blue), without+low (empty pink) and without+high (empty blue). The number of sources in each redshift interval are shown for the four sample variants .*

The observed XLF measurements are determined for all four redshift samples following the process detailed in §4.2.2. The without sample can be expected to produce the most conservative XLF measurements; the without+high sample producing the lowest XLF measurements in the $z = 4-5$ range and the without+low giving the smallest measurements in the $z = 7-10$ redshift range.

Conversely, there will be a maximum XLF measurement in the $z = 4 - 5$ and $z = 7 - 10$ ranges when determined from the with+low and with+high samples respectively. The four forms of the XLF measurements are shown in figure 4.10.

At $z = 4 - 5$ the different XLF measurements all remain consistent with the models, whilst the most optimistic values suggest the XLF tends to higher space densities at the faint end. Towards higher redshifts, however, even the most conservative measurement indicates a higher space density of AGN than predicted by the extrapolations of models. Taking the lowest and highest measured values of my XLF, in each redshift and luminosity interval, I convert these measurements into an uncertainty region on my observed XLF. From these constraints, shown in figure 4.11, we can see the bounds of the observed XLF given the most conservative and most optimistic values, for which the high redshift space density can be seen to fall above the extrapolated predictions.

4.3 Hardness Ratio and Obscuration in the XLF

Obscuring gas and dust in both the host galaxy and torus of a SMBH absorbs softer (lower energy) X-rays, causing the source to have a stronger signal at harder X-rays relative to its observed emissions in softer bands. The effect of obscuration on AGN emissions is detailed in §1.5. In the early Universe, as fewer stars have formed galaxies are expected to have a higher gas content (see e.g. Carilli & Walter, 2013, for review), thus early SMBHs are likely to be more heavily obscured.

The X-ray Luminosity Function is notably affected by obscuration. A decrease in observed counts at Soft and Full band energies, due to obscuring material around the AGN, results in the intrinsic luminosity of sources being under estimated and can result in an AGN not being observed above the X-ray background. Thus increasing obscuration both reduces the measured space density of AGN and shifts it to lower luminosities. In this section I investigate the effect of obscuration in my high-redshift blind+extracted sample on my measurements of the X-ray Luminosity Function. I will then perform a simple correction to my measurements, to account for any obscuration present in my sample (see §4.3).

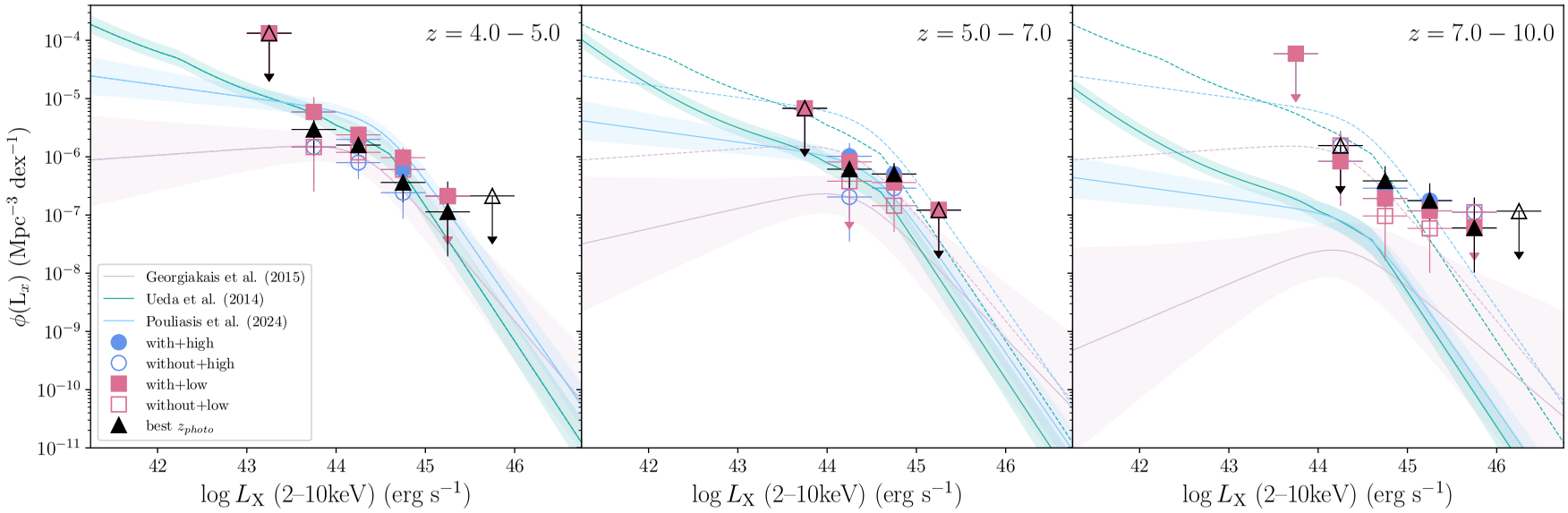

Figure 4.10 *Observed binned XLF measurements at $z \geq 4$ determined from the blind and extracted sample using either the lowest (pink) or the highest (blue) possible photometric redshift, with (full) and without (empty) sources for which only one photometric redshift measurement, given by the galaxy or AGN redshift fits, is $z \geq 4$. For comparison, the measured XLF from the best redshift values (as found in §4.1.4) is shown by the black points, and the parametric models from Ueda et al. (2014), Georgakakis et al. (2015) and Pouliasis et al. (2024) (green, pink and blue lines respectively) extrapolated out to the centre of the redshift ranges for which the binned measurements were determined. Even for the lowest measured XLF, providing the most conservative result, indicates a higher space density than predicted by the parametric models.*

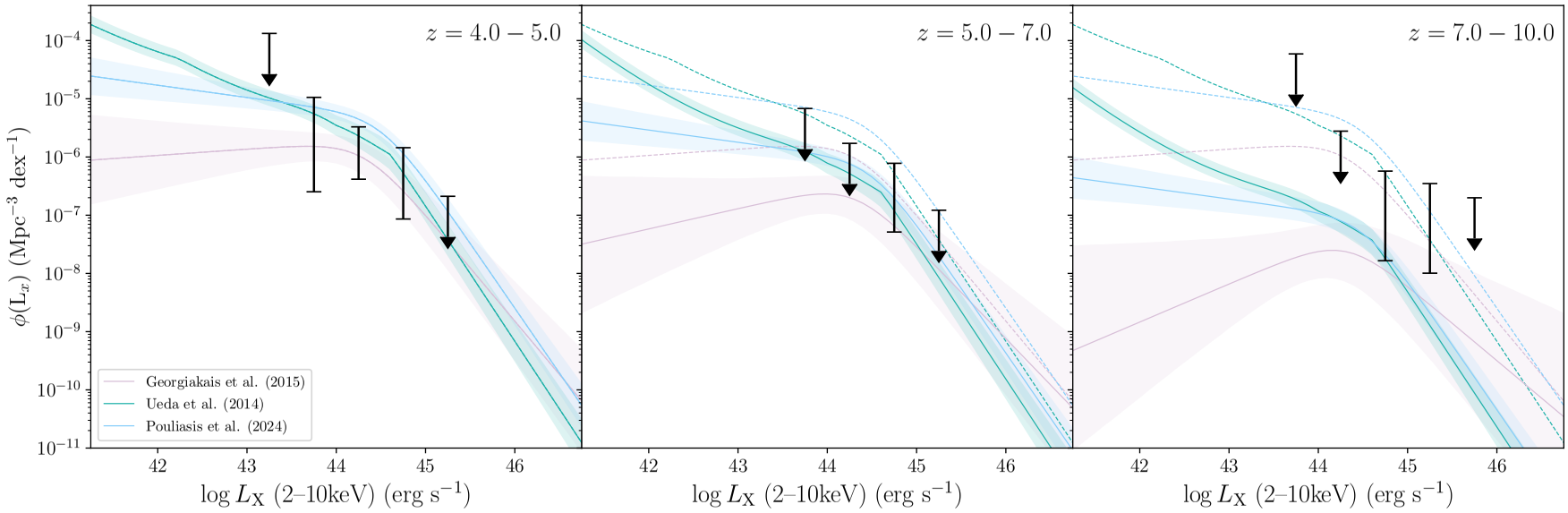

Figure 4.11 *As for 4.10, with the maximum upper uncertainties and the minimum lower uncertainties from the four forms of the variable redshift XLF shown as single uncertainty ranges on the measured value of the XLF in each redshift and luminosity bin. At* $z = 4 - 5$ *(left hand panel) the XLF uncertainty is consistent with the model extrapolations. However, even the lowest bound of the measured XLF at* $z = 7 - 10$ *(right hand panel) indicates a potentially higher space density than the models.*

4.3.1 The Hard-Band XLF

Obscuration reduces source counts at softer energies, resulting in obscured sources being more easily detected at hard-band energies than in the soft-band. However, the measurements of the XLF I performed above were done using the full-band only. Thus, in order to determine if obscuration in my high-redshift sources has a significant effect upon the observed XLF measurements, I calculate the observed XLF from source detections made in the hard-band.

Using the sample of blind detected and hard-band extracted sources, obtained in §4.1.4 with a false probability threshold of 1.74×10^{-5} corresponding to a 5% False Fraction in the $z \geq 4$ sources, I calculate the observed XLF measurements given by the hard-band count rates. The measured hard-band count rates of my sources are converted directly to an X-ray 2-10 keV Luminosity (L_X, as in §4.2.1) and the measured XLF given by these hard-band observations is determined following the process detailed in §4.2.2. For these measurements, the sensitivity in the hard-band is calculated using the false probability threshold of 1.74×10^{-5} (see §4.1.2 for the calculation of the sensitivity of my Chandra observations).

The resulting measurements of the hard-band XLF are shown in figure 4.12, with the full-band measurements for comparison. The hard-band XLF measurements indicate a higher space density of AGN, in the early Universe, than is seen with the full-band measurements. This disparity between the full and hard band measurements can be seen to increase with redshift. This is consistent with a higher obscuring gas content in early galaxies and is indicative of a highly obscured population, as is found by Ni et al. (2020) and is beginning to be found by JWST (Yang et al., 2023; Maiolino et al., 2023; Greene et al., 2023).

With my hard-band XLF measurements indicating significant obscuration within my high-redshift sample, my full-band measurements of the XLF can be expected to be significantly affected by this obscuration. However, obscuration may vary between sources rather than affecting the sample in a uniform manner. As such, in order to further analyse the obscuration within my sample and the impact on my XLF measurements, I first determine the hardness ratios of each source in the full-band sample (see §4.3.2). With the hardness ratios determined, I will then obtain corrections for the XLF based on the observed hardness ratio of individual sources within my high-redshift sample (see §4.3.3).

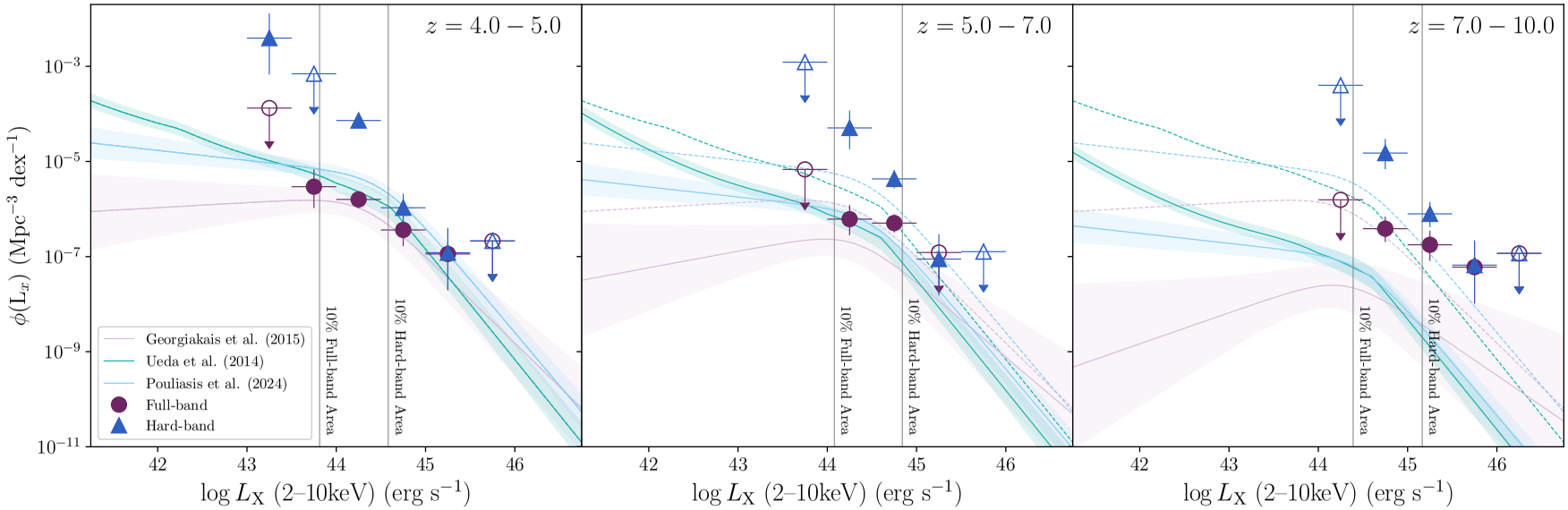

Figure 4.12 *The observed binned XLF, as given by the hard-band measurements of my blind and extracted sample (blue triangles). For comparison the models of Georgakakis et al. (2015), Ueda et al. (2014) and Pouliasis et al. (2024) extrapolated out to the centre of these redshift ranges are plotted, and the XLF calculated using the full-band measurements (in section 4.2.3) is shown (purple points). For both the hard and full band measurements, the luminosity at which the area observed by Chandra is 10% of the total imaged area, is indicated. The hard-band measurements can be seen to lie at consistently higher space-densities than the full-band measurements, whilst maintaining the trend seen in section 4.2.*

4.3.2 The Bayesian Estimation of Hardness Ratio

A good indication of the amount of obscuration there is in an AGN, by material surrounding the black hole and accretion disk, is given by the ratio of the measured soft and hard counts of the source, known as the hardness ratio (see also chapter 1). Obscuring material absorbs lower energy, soft photons preventing them from escaping the system and thus reducing the observed soft-band counts of the source. As such, a more heavily obscured AGN will appear to produce relatively more counts in the hard-band than in the soft-band, as more low energy photons are absorbed, and hence it will have a more positive hardness ratio than a less obscured AGN of the same intrinsic spectrum.

For all sources within my high-redshift blind+extracted sample (summarised in section 4.2.1) I determine the Bayesian Estimation of the Hardness Ratio (BEHR), following the method detailed in Park et al. (2006). As detailed in §4.1.4, the total hard and soft-band counts of each source are taken to be the 70% PSF measurements obtained in the blind catalogue creation, where available, or extracted directly from the Chandra imaging at the position of the COSMOS2020 source. The posterior distribution of possible values of the Hardness Ratio, for each source in my sample, is then determined by combining prior knowledge of the source with the likelihood of a particular observation (see Park et al., 2006, for details). As such the Hardness Ratio of sources only detected in one energy band can still be determined and constraints can be placed on the level of obscuration of such a source. For this calculation I take the form of the Hardness Ratio (HR) to be,

$$HR = \frac{H - S}{H + S}, \tag{4.10}$$

where H and S are the total number of source counts measured in the hard and soft-bands, respectively. The Hardness Ratio for each source within my high redshift sample is thus calculated from the measured total counts in the hard and soft bands, with the corresponding background and exposure, using a Gaussian quadrature algorithm (as detailed in Appendix A.2 of Park et al., 2006). The resulting BEHRs for all $z \geq 4$ sources within my Chandra-COSMOS sample can be seen in figure 4.13.

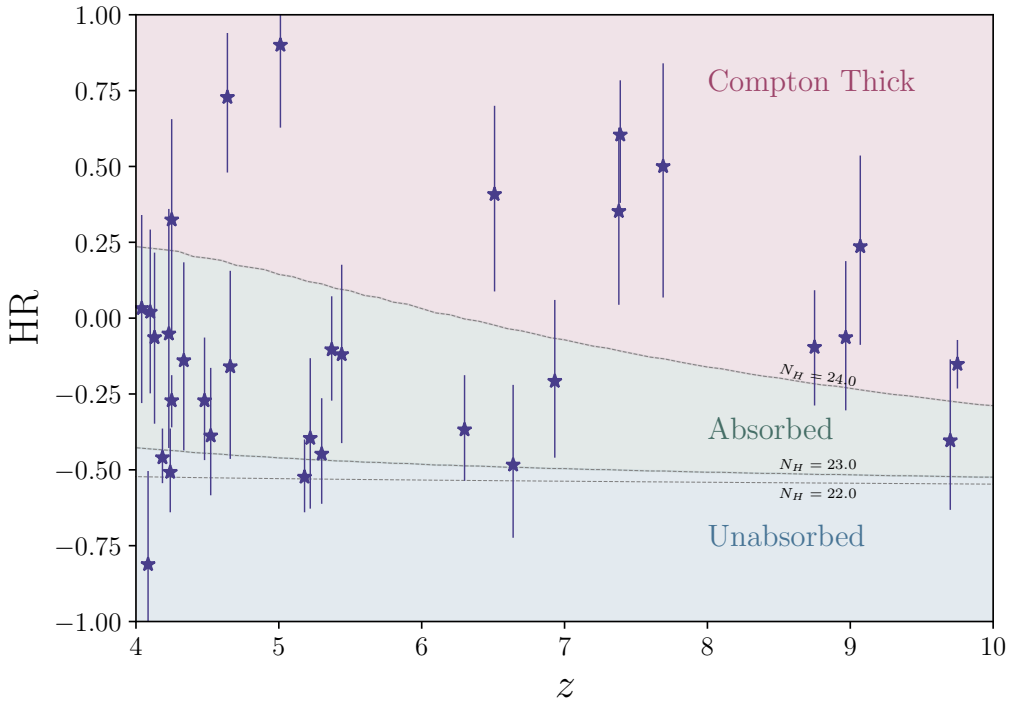

Figure 4.13 *The Bayesian Estimation of the Hardness Ratio (BEHR) with respect to the best fit redshift of all sources within my blind+extracted sample. Lines of* $N_H = 10^{22}cm^{-2}$, $10^{23}cm^{-2}$ *and* $10^{24}cm^{-2}$, *given by the Borus spectral model (Baloković et al., 2018) are shown with the corresponding unabsorbed, absorbed and Compton Thick regions. It can be see that there is no clear trend in the BEHR with redshift for the sample.*

Plotting the Bayesian Estimation of the Hardness Ratio of all $z \geq 4$ blind and extracted sources within my sample, I find little trend in the overall hardness of the population. As can be seen in figure 4.13, there is scatter across the redshift range of this study, indicating that a single obscuration correction applied to the XLF measurements would be inaccurate. However, it should be noted that the conversion between Hardness ratio and the obscuration, N_H, of a source is dependent upon the redshift. This is due to the shift in the X-ray spectrum towards lower energies with redshift (see section 1.8), and as such two sources of the same N_H but different redshifts, will have different HR values.

Previously my spectral model assumed a negligible obscuration component, using the model of Aird et al. (2015). Here, in order to account for the effect of obscuration on our observed source counts we employ a the Borus spectral model of Baloković et al. (2018), which includes an obscuring torus component. Using this Borus model (folded through the Chandra response at approximately the

middle of the survey period[7] as in section 4.2.1 to convert count rates into 2-10keV luminosities), I determine the Hardness Ratio across the redshift range of $z = 4 - 10$ corresponding to constant obscuration (i.e. constant values of N_H). With increasing redshift, the hardness ratio along lines of constant N_H decrease, with a more rapid drop at higher N_H values (see figure 4.13). For obscuration below $N_H = 10^{23}cm^{-2}$ the Hardness ratio remains roughly constant, with the track of $N_H = 10^{22}cm^{-2}$ showing no redshift evolution, due to the low-energy limit of Chandra (0.3 keV, corresponding to a rest-frame energy of 1.5–3.3 keV for $z = 4 - 10$) resulting in little observable change in HR for $N_H < 10^{23}cm^{-2}$. As such I take unabsorbed[8] sources to be those of $N_H < 10^{23}cm^{-2}$ (given by their measured BEHR), with absorbed and compton-thick sources those with BEHR corresponding to $10^{23}cm^{-2} \leq N_H \leq 10^{24}cm^{-2}$ and $N_H > 10^{24}cm^{-2}$ respectively.

With BEHRs determined for all sources in the blind+extracted sample I split the sample, based on their measured BEHR, into unabsorbed, absorbed and Compton-thick. As can be seen in figure 4.13, there are fewer unabsorbed sources (those that lie below the $\log N_H = 23$ line on the HR-z plot) with increasing redshift, which is consistent with a more obscured population of AGN at higher redshifts. The resulting fraction of the total $z = 4 - 10$ sample within each obscuration range (unabsorbed, absorbed and Compton-thick), at redshifts of $z = 4 - 5$, $z = 5 - 7$ and $z = 7 - 10$, are shown in figure 4.14. The majority of my sources can be seen to fall within the absorbed and Compton Thick N_H ranges, with the larger fraction of sources found to be absorbed. This is consistent with the results of Vito et al. (2014) which found the obscuration of AGN increases with redshift (see also e.g. Hickox & Alexander, 2018, for a review of obscured AGN), as such most $z \gtrsim 4$ sources can be expected to be absorbed.

For comparison I determine the predicted number of sources in each redshift and obscuration bin given the PDE XLF model from Pouliasis et al. (2024), assuming all sources given by this model have the given obscuration of the bin. This is done using spectral models for $N_H = 10^{21.5}\,cm^{-2}$, $10^{23.5}\,cm^{-2}$ and $10^{24.5}\,cm^{-2}$, corresponding to the approximate centre of each obscuration interval ($N_H < 10^{23}$, $10^{23}\,cm^{-2} \leq N_H \leq 10^{24}\,cm^{-2}$ and $N_H > 10^{24}\,cm^{-2}$ respectively) to convert between count rate and luminosity when determining area in equation 4.9. The

[7] The telescope response of Chandra has evolved over it's life time. As such I use the response at the approximate centre of the observing period for consistency. The effect of these different responses is shown in Appendix C

[8] This interval will potentially contain some sources with a low level of absorption, however for the purpose of this work they shall all be assumed to be unabsorbed, as in Vito et al. (2018).

predicted number of sources is thus calculated across each redshift interval and summed across all possible luminosities[9], given equation 4.9. The resulting N_H dependent model predictions are shown in figure 4.14, by the coloured histograms.

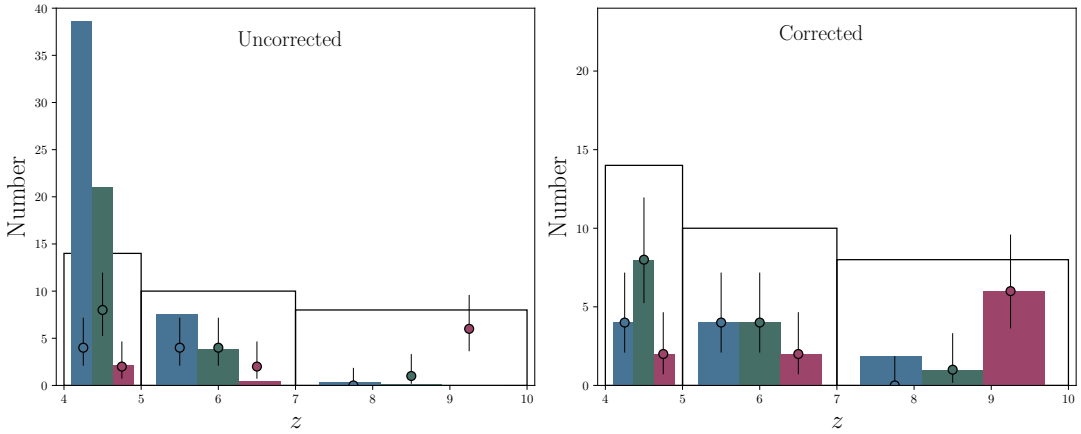

Figure 4.14 *Histograms of model predicted source numbers (left) and corrected source numbers (right; see section 4.3.3) for unabsorbed (blue), absorbed (green) and Compton-thick (red) samples, with the observed number of sources shown by the points. Open histograms show full sample of observed sources before* N_H *binning, within each redshift interval. It should be noted that within the highest redshift bin* ($z = 4 - 10$) *the unabsorbed source number is corrected to the upper limit on 0 sources, as given by Gehrels (1986), and as such is above the observed number of sources.*

The number of sources observed overall decreases with redshift, as sources appear fainter at higher redshifts and thus are less likely to be detected. When the obscuration of sources is considered, I find that the number of unabsorbed sources decreased with redshift, with the absorbed sample experiencing an increase at $z = 5 - 7$ before dropping again. In the very high-redshift range there are no unabsorbed sources observed, and the majority of sources are heavily obscured (Compton-thick). The model, however, can be seen to over predict the number of unabsorbed sources at all redshifts, and under predict the number of obscured sources (absorbed and Compton-thick).

The hardness ratios measured for my sample, and the comparison of predicted to observed sources at different levels of obscuration, clearly indicates the need for a correction to be applied to the XLF calculation, with both a N_H and redshift dependence.

[9]The X-ray luminosity range used goes from a minimum luminosity, as given by the count rate observable at 0.1% of the total survey area, in order to prevent contamination by Eddington Bias effects within the area curve.

4.3.3 Obscuration Corrections on the XLF

The study of the obscuration in my blind and extracted sample of high-redshift AGN, described above, indicates a significant redshift-dependent population of obscured sources, which is not accounted for in the model XLF. Thus, a correction to account for the disparity between the observed fraction of obscured sources and the predicted numbers (shown in the left hand plot of figure 4.14) needs to be applied.

With no clear redshift trend in BEHR of my sample, a correction factor that depends on both redshift and N_H is required. I determine the scale factor ($\gamma(N_H, \mathrm{bin}, z)$) given the observed number of unabsorbed, absorbed and Compton Thick sources and the number of sources predicted by the Pouliasis et al. (2024) PDE model using rest-frame 2–10 keV Luminosity ($L_X(N_H)$) given by the Borus spectral models (Baloković et al., 2018) of $N_H = 10^{21.5}\,\mathrm{cm}^{-2}$, $N_H = 10^{23.5}\,\mathrm{cm}^{-2}$ and $N_H = 10^{24.5}\,\mathrm{cm}^{-2}$ (corresponding to unabsorbed, absorbed and Compton Thick respectively, as calculated above and in the left-hand panel of figure 4.14).

$$\gamma(N_{H,\mathrm{bin}}, z) = \frac{N_{obs}(N_{H,\mathrm{bin}})}{N_{model}(N_H, bin|\phi_{fiducial})}, \tag{4.11}$$

where $N_{obs}(N_H, \mathrm{bin})$ is the number of sources observed within a given obscuration range ($N_{H,bin}$), and $N_{model}(N_H, bin|\phi_{fiducial})$ is given by,

$$N_{model}(N_H, bin|\phi_{fiducial}) = \int d\log L_X \int \frac{dV_{co}}{dz}\phi_{fiducial}(L_X, z)A(f(L_X(N_H), z))dz, \tag{4.12}$$

as in equation 4.9, with sky area $A(f(L_X(N_H), z))$ at an observed flux ($f(L_X(N_H), z)$) given by the redshift (z) rest-frame 2–10 keV Luminosity ($L_X(N_H)$) with $N_H = 10^{21.5}$, $N_H = 10^{23.5}$ and $N_H = 10^{24.5}$, for unabsorbed, absorbed and Compton-thick sources, respectively. In the case of no observed sources, I take the Poisson upper limit from Gehrels (1986) on 0 sources to be the observed number.

Applying the resulting redshift and obscuration dependent correction factors ($\gamma(N_H, \mathrm{bin}, z)$) to the predicted numbers scales them to the observed number

of sources in each redshift and obscuration interval, as can be seen in the right hand plot of figure 4.14. I then apply these correction factors to the model XLF ($\phi_{fiducial}$) in order to obtain the obscuration corrected model XLF $\phi_{model,corr}$,

$$\phi_{model,corr} = \gamma(\mathrm{N_H}, \mathrm{bin}, z)\phi_{fiducial}, \tag{4.13}$$

for a given redshift and obscuration ($\mathrm{N_H}$, bin) in the unabsorbed, absorbed and Compton-thick bins, assuming the shape and redshift evolution of the XLF remains that of the fiducial model. Figure 4.15 shows the fiducial and corrected XLF models at $z = 4-5$, $5-7$ and $7-10$, for unabsorbed, absorbed and Compton-thick sources.

With the correction applied the extrapolated XLF model can be seen to match the observed XLF more closely across all three redshift ranges and in the different levels of obscuration. With increasing obscuration, an increasingly positive shift in the models is required to better represent the observations, whilst the model XLF overpredict the number of unabsorbed sources. At $z = 7-10$ I have no unabsorbed sources within my sample, and as such the model can only be corrected to the upper limit on the binned XLF, as given by the Poission uncertainty of Gehrels (1986), the shape of which depends predominantly on the Chandra sensitivity.

Having obtained the correction factors and confirmed they suitably adjust the model XLF for the obscuration I have observed, the obscuration corrected XLF measurements across all N_{H} are calculated using the full-band count rates of my blind and extracted sample (following the process in 4.2.3),

$$\phi_{obs,corr}(L_{\mathrm{X}}, z) = (\gamma_{unabs}+\gamma_{abs}+\gamma_{ctk})\phi_{mdl}(L_{\mathrm{X}}, z)\frac{N_{obs}}{N_{mdl,unabs} + N_{mdl,abs} + N_{mdl,ctk}}, \tag{4.14}$$

where γ_{unabs}, γ_{abs} and γ_{ctk} are the obscuration correction factors at z, for the bins of unabsorbed, absorbed and Compton-thick respectively (see table 4.2 for values). The predicted number of unabsorbed ($N_{mdl,unabs}$), absorbed ($N_{mdl,abs}$) and Compton-thick ($N_{mdl,ctk}$) sources are given by equation 4.12. The resulting

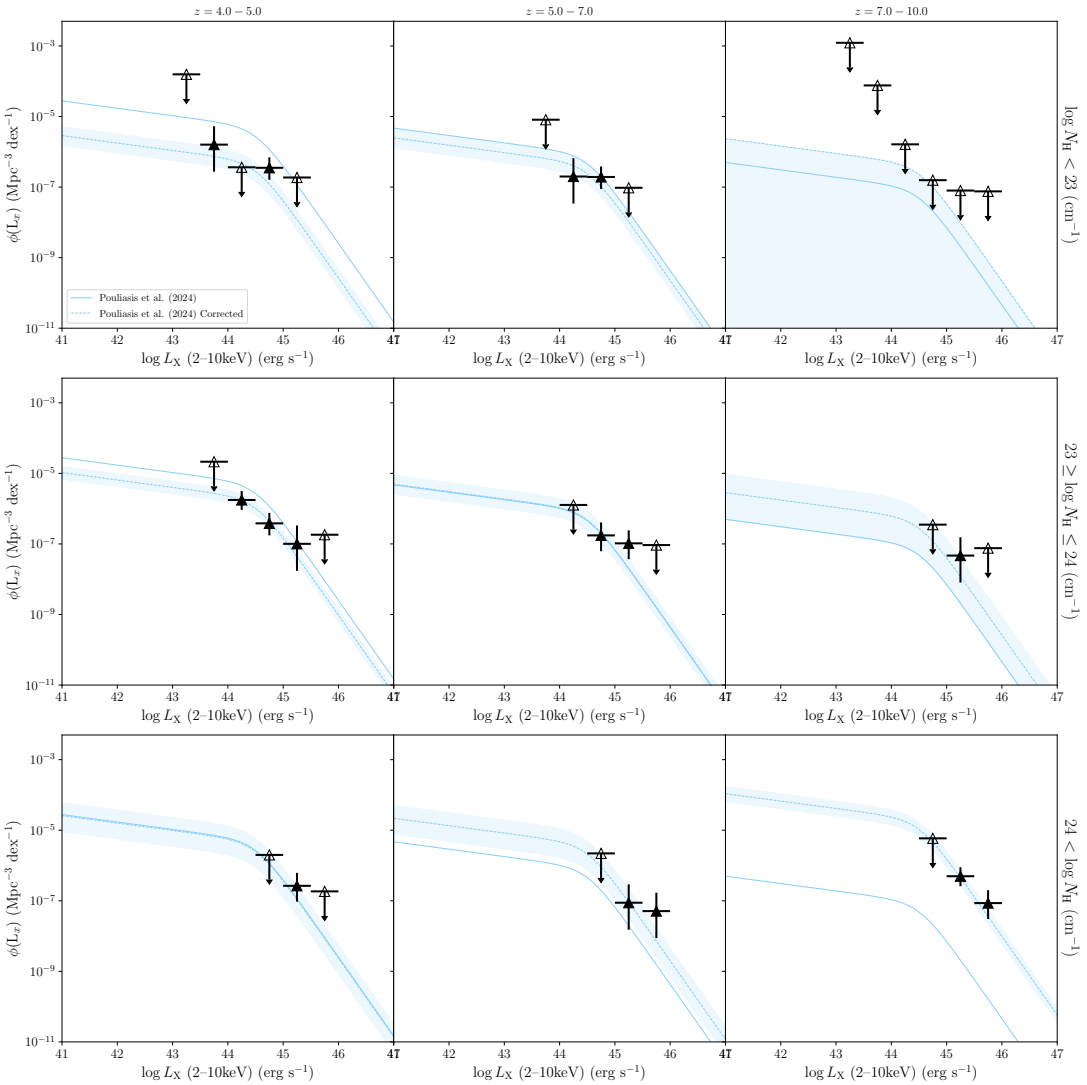

Figure 4.15 *The Pouliasis et al. (2024) XLF model before (solid line) and after (dashed line) correction to my obscuration binned measurements, for* $N_H < 10^{23}$ *(top row),* $10^{23}cm^{-2} \leq N_H \leq 10^{24}cm^{-2}$ *(middle row) and* $N_H > 10^{24}cm^{-2}$ *(bottom row). My measured XLF are shown for comparison by the black triangles, with limits given by Gehrels (1986) where no sources exist within my sample (open triangles). The Obscuration correction can be seen to reproduce the shape of the XLF well, as seen with my blind+extracted measurements. For the case of* $N_H < 10^{23}$ *at* $z = 7 - 10$ *my blind+extracted sample contains no sources, thus the obscuration correction can only provide an upper limit on the number of sources, based on the survey area of the sample.*

z	γ_{unabs}	γ_{abs}	γ_{ctk}
4–5	0.104	0.379	0.933
5–7	0.529	1.05	4.63
7–10	4.73	5.69	218

Table 4.2 *Obscuration corrections to the Pouliasis et al. (2024) PDE XLF model for unabsorbed (γ_{unabs}), absorbed (γ_{abs}) and Compton-thick (γ_{ctk}) sources determined here.*

observed XLF measurements are shown in figure 4.16, with the full band blind and extracted XLF (from §4.2.3) and the hard band blind XLF (from §4.3.1) plotted for comparison.

With the obscuration correction, my full-band measurements more closely follow those of the Hard-band measurements, showing a higher space density across all redshift ranges than the full-band uncorrected measurements. At $z = 4-5$ these corrected measurements remain broadly consistent with the model predictions, as in section 4.2.3. However, even at $z = 5-7$ my measurements suggest a higher space density than the extrapolated models, with the models clearly under-predicting the sample observed at $z = 7-10$.

From the obscuration within my blind+extracted sample, I determine the fraction of unabsorbed, absorbed and compton-thick AGN across the full redshift range of my sample ($z = 4-10$) and within each redshift bin ($z = 4-5$, $5-7$ and $7-10$) given,

$$f_{bin} = \frac{\gamma_{bin}}{\gamma_{unabs} + \gamma_{abs} + \gamma_{ctk}} \tag{4.15}$$

where γ_{bin} is the correction factor for a given obscuration bin (***unabs***, ***abs*** or ***ctk***). Uncertainties are determined through random posterior draws of possible "true" values of the fraction. From this the fraction of unabsorbed, absorbed and Compton-thick AGN across the redshift range of $z = 4-10$ is $0.007^{+0.004}_{-0.003}$, $0.06^{+0.03}_{-0.02}$ and $0.93^{+0.02}_{-0.03}$ respectively.

Across the three redshift bins ($z = 4-5$, $5-7$ and $7-10$) used in this chapter I find the fraction of absorbed sources declines with increasing redshift, whilst remaining above that of the unabsorbed sources. The absorbed fraction declines from $0.17^{+0.10}_{-0.09}$ at $z = 5-7$ to $0.025^{+0.05}_{-0.01}$ at $z = 7-10$. The fraction of Compton Thick sources follows an opposite trend, increasing from $0.75^{+0.12}_{-0.14}$ at $z = 5-7$ to

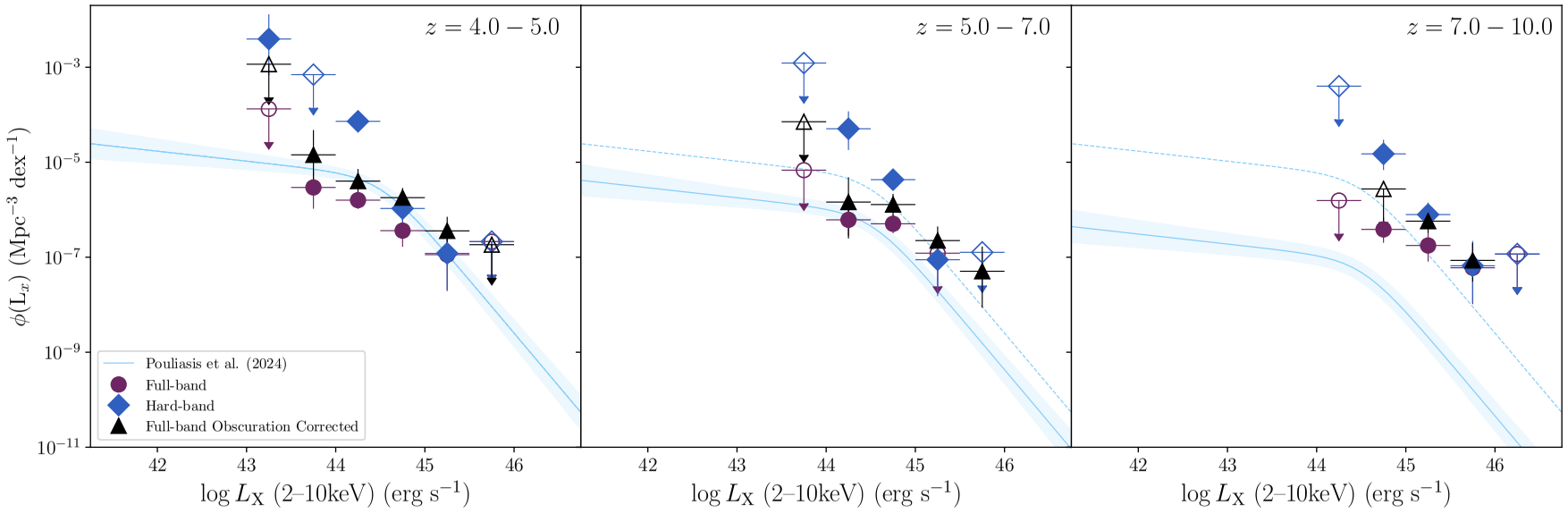

Figure 4.16 *Full band obscuration corrected XLF measurements (black triangles) for the redshift bins of $z = 4-5$, $5-7$ and $7-10$. The uncorrected full band (purple circles; from figure 4.8), hard band (blue diamonds; from figure 4.12) and Pouliasis et al. (2024) model extrapolations are shown for comparison. My corrected measurements can be seen to be more consistent with the hard band measurements than the uncorrected case, indicating an even higher space density of AGN at these high-redshifts than is predicted by the model extrapolations.*

$0.95^{+0.02}_{-0.05}$ at $z = 7-10$. From these measured fractions the fraction of sources which are Compton Thick, given their hardness ratios, becomes increasingly dominant over the fraction of sources for which their obscuration is due only to absorption.

With the fraction of unabsorbed sources found to be very small, the majority of X-ray AGN at these high-redshifts are highly obscured. This is consistent with the work of Gilli et al. (2022) that suggests there is a high gas content in very early galaxies, fuelling both star formation and SMBH growth.

4.4 Discussion

4.4.1 Comparisons to previous XLF

As detailed in chapter 1, the AGN X-ray Luminosity Function (XLF) has only been parametrically modelled up to $z \sim 6$ (e.g. Georgakakis et al., 2015; Pouliasis et al., 2024; Vito et al., 2018) due to the limitations on high-redshift X-ray surveys (i.e. the small area observable to the required depth with current telescopes and the known decline in space density of AGN with increasing redshifts) and the XLF beyond $z = 6$ has remained poorly constrained. With new deep IR imaging from UltraVISTA, within the COSMOS2020 catalogue, it is possible to measure redshifts for sources at $z > 6$. Through the work detailed above, I have obtained measurements of the XLF, at moderate luminosities, out to $z = 10$.

The work I have performed in this chapter relies on photometric redshift measurements. As investigated in section 4.2.4, the choice of redshift photometric fitting can add an additional uncertainty to the XLF measurements. As such I determined the uncertainty range in my XLF measurements, shown in figure 4.11. In addition to the adjustments for photometry fitting giving a broader uncertainty on the measured XLF, the obscuration corrections to my full-band XLF measurements performed in section 4.3 increase the observed space density of AGN further. I now combine my obscuration corrected XLF and photometric redshift uncertainties, in order to determine the most optimistic and most conservative measurements of the XLF given by my blind+extracted X-ray sample.

From the photometric uncertainty range on the XLF, I take the lower bounds of the uncertainty range (as shown in figure 4.11) to be the minimum value of the

observed XLF uncertainty. I then take the upper uncertainty on the obscuration corrected measurements to be the maximum value of my XLF uncertainty. The resulting uncertainty range in my observed XLF measurements, at the redshifts of $z = 4-5$, $5-7$ and $7-10$, are shown in figure 4.17.

I note that applying the obscuration corrections (as in section 4.3.3) whilst also considering the range of possible redshifts for each source (as in section 4.2.4) would provide a more comprehensive uncertainty range of my XLF measurements. However, as there is significant obscuration across the full redshift range of my sample, this would increase the disparity between the model predictions and the most optimistic space densities at $z = 7-10$, whilst the most conservative measurements of the XLF would remain the value of the lower uncertainties found in section 4.2.4 for the uncorrected XLF. As such, with the obscuration corrections only applied to the best redshift measurements the results shown in figure 4.17 may still be relatively conservative, rather than showing strict upper limits on the high-redshift AGN space density.

Within the redshift range of $z = 4-5$, at which previous XLF models have been fitted to survey data, I find my measurements of the XLF to be consistent with the parametric models (as is to be expected) and thus suitably representative of the AGN population at the end of cosmic reionisation (see left hand plot of figure 4.17). Although consistent with the model predictions, the upper limits on my measurements, which account for the obscuration within my sample, suggest a higher space density of fainter AGN than would be predicted based on prior model extrapolations. This is likely due to the (potentially substantial) effects of absorption at these high-redshifts not accounted for in prior studies of the XLF, as well some limitation in the sensitivity achieved with current telescopes.

At higher redshifts, as can be seen in the centre plot of figure 4.17, my measurements remain broadly consistent with the parametric model extrapolations at $z = 5-7$. Whilst the most conservative measurements are clearly consistent with the model predictions, at the most optimistic values my measured XLF indicates that the true space density of AGN may be higher than predicted by the parametric models. Comparing to my bright-end XLF constraints from chapter 3 and the XLF observed with eROSITA eFEDs by Wolf et al. (2021) (determined for a narrower redshift interval of $z = 5.7-6.4$), I find they are only broadly consistent with the lower bounds of my new constraints, using deep Chandra legacy data. The results found here suggest the space density of high-redshift AGN is much higher than that measured by Wolf et al. (2021) and in chapter 3.

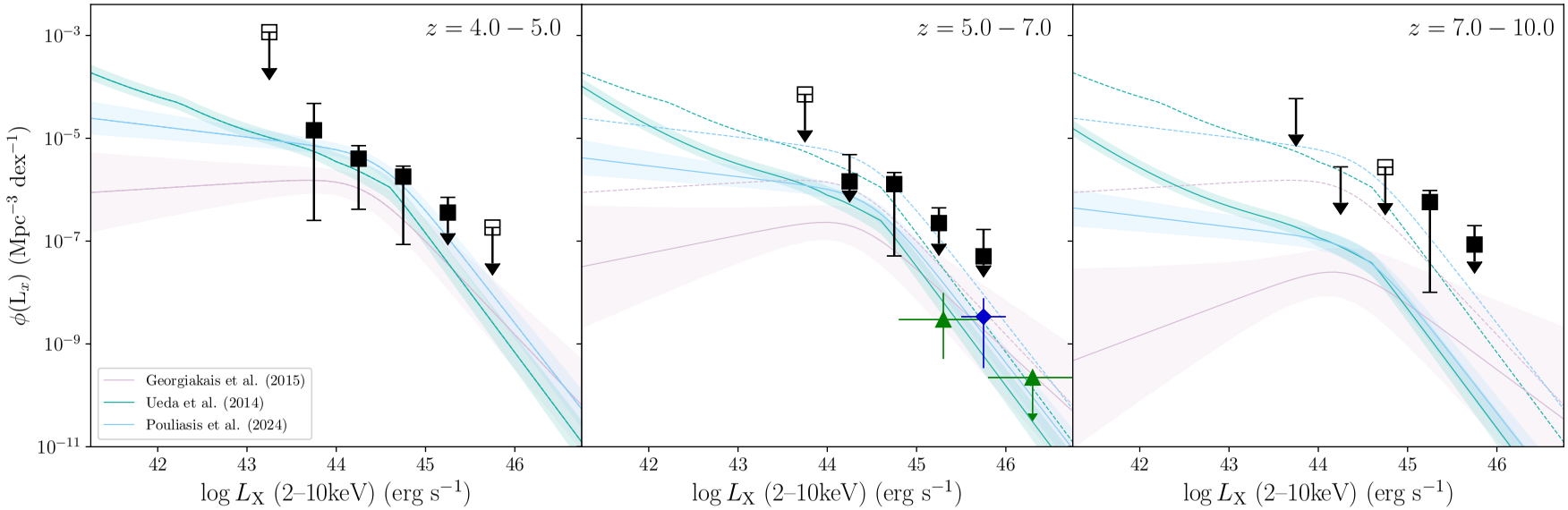

Figure 4.17 *The bounds of the XLF measured in this chapter, with lower bounds given by the lower bounds of the photometry dependent XLF determined in section 4.2.4 and the upper bounds given by the upper uncertainty on the obscuration corrected XLF measurements (see section 4.3.3). Extrapolated models of XLF fit to redshift $z \sim 3-6$ data are plotted for comparison at the centre of each redshift bin, with the dotted lines indicating the space density given by the models at $z = 4-5$. The bright-end XLF measurements given by ExSeSS (see chapter 3) are shown by the green triangles, and similarly the result of Wolf et al. (2021) is shown by the blue diamond.*

It should be noted that my ExSeSS measurement of the XLF is formally a lower limit and thus may be incomplete, for obscured AGN in particular, resulting in the lower space density than my deeper Chandra measurements.

Despite the agreement between my blind+extracted measurements and the extrapolations of parametric models out to $z = 7$, the extrapolated models can be seen to under-predict the observed XLF at $z = 7 - 10$ (see right hand plot of 4.17). Although the most conservative measurements of the observed XLF at this very high redshift is within 1σ of the Georgakakis et al. (2015) LDDE model predictions, the AGN space-density in the very early universe is likely much higher than previously expected. Although previous studies (e.g Gilli et al., 2007) suggest the need for a high-redshift decline in the AGN space density, the results I have presented here indicate that there is no such decline in the AGN space density at $z \gtrsim 7$.

The space density of AGN I have determined here indicates a large number of actively accreting supermassive black holes within the very early universe, which are observable even with current X-ray telescope capabilities, and indicates significant black hole growth may be occurring at early times. This early AGN population within the first galaxies would likely have a significant impact upon the evolution of galaxies in the early Universe.

4.4.2 The QLF and JWST

Following the recent launch of the JWST, populations of moderate to low-luminosity AGN at redshifts above $z \sim 4$ are being revealed (e.g. Greene et al., 2023; Matthee et al., 2024; Kokorev et al., 2024; Larson et al., 2023), with some studies claiming to have found early AGN out to $z \sim 10$ (Kovács et al., 2024). These early JWST results indicate a relatively high AGN occupation fraction within the first galaxies, with the majority of JWST studies pointing towards unexpectedly high AGN space-densities within the early Universe (see e.g. Greene et al., 2023; Maiolino et al., 2023).

In order to compare my X-ray measurements of the $z \gtrsim 4$ AGN space density to the UV measurements from JWST, I convert all measurements into those of the bolometric Quasar Luminoisty Function (QLF). As in section 3.3.3, I adopt the luminosity dependent bolometric correction of Shen et al. (2020). Applying a bolometric correction to the full-band, obscuration corrected XLF measurements

obtained above (see section 4.3.3), I compare my new QLF estimates at $z = 5 - 7$ to those of Maiolino et al. (2023) (from UV luminosity function measurements at $z \sim 4{-}6$) and Greene et al. (2023) (see figure 4.18). Greene et al. (2023) performed their measurements of the QLF on the space density of Little Red Dots, based on photometric selection of Red Compact sources and spectroscopic broad lines, and thus may not capture all low-luminosity AGN. In contrast, Maiolino et al. (2023) use a less stringent selection of AGN, based simply on the identification of a broad Hα or Hβ line, and thus measure a higher space density than Greene et al. (2023) at low-luminosities. In addition to the JWST measurements, I also show the bright-end QLF constraints obtained in section 3.3.3 and from a bolometric conversion of the Wolf et al. (2021) observation, both determined using the method of Shen et al. (2020).

As can be seen in figure 4.18, my obscuration-corrected measurements of the AGN space density follow a consistent trend between the early JWST results and X-ray observations at the bright-end of the luminosity function. As referenced in Scholtz et al. (2023), the majority of AGN detected by JWST are found to have no visible X-ray emissions, with stacking of X-ray imaging of the sources finding no clear X-ray signal (R. Hickox; private communication). This lack of X-ray detection indicates a very high obscuration fraction (of the order of 100× the fraction of unobscured sources), as is consistent with the obscuration found in my blind+extracted sample ($\sim$ 230×, given by the obscuration correction to the model XLF). Pouliasis et al. (2024) similarly argue that the X-ray population is likely to miss a small fraction of heavily obscured AGN; those being found by JWST. With my blind+extracted sample pushing the limit of current X-ray imaging, and probing higher luminosity AGN than the JWST imaging of studies such as Maiolino et al. (2023); Greene et al. (2023), it is likely that the AGN found by JWST are simply the less active AGN, within the same population as my blind+extracted high redshift sample. In order to investigate this further, spectra and JWST imaging of my high redshift sample are required to determine their physical nature and compare to the observations of the compact AGN (known as Little Red Dots, e.g. Kocevski et al., 2024) found by JWST.

The moderate luminosity measurements of the AGN space density I have obtained in this chapter, clearly point towards a reconciliation of the JWST AGN population and those identified through X-ray surveys. With improved redshift measurements from the mid-IR imaging of JWST, even fainter X-ray sources could be identified within the Chandra Deep Fields (following the method detailed

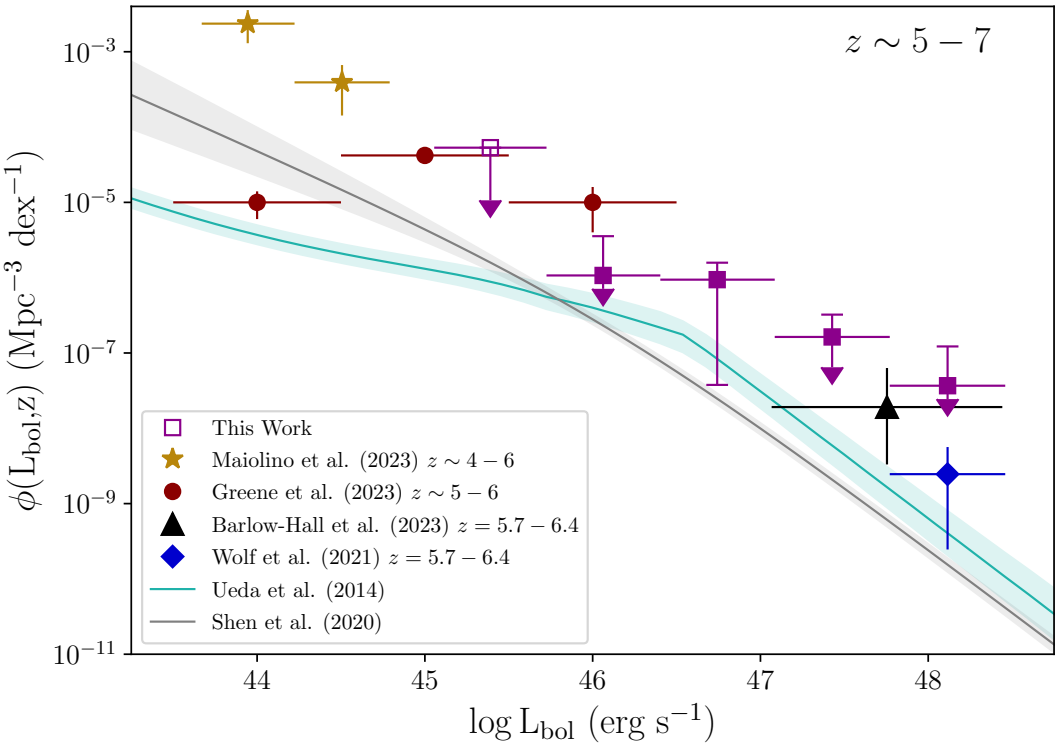

Figure 4.18 *The bolometric QLF given by the Shen et al. (2020) corrections to my final XLF measurements at $z = 5-7$ (purple squares), with uncertainties from the maximum obscuration corrected measurement and minimum unobscured redshift measurements (as shown in figure 4.17). Bright-end $z = 5.7-6.4$ X-ray measurements are shown from the results of Chapter 3 (black triangle) and Wolf et al. (2021) (blue diamond). The JWST measurements at $z = 5-6$ from Greene et al. (2023) are shown by the green circles, and the $z = 4-6$ UVLF measurements of Maiolino et al. (2023), similarly converted to bolometric luminosities using the conversions of Shen et al. (2020), are shown by the red stars. For comparison, the bolometric QLF model of Shen et al. (2020) and bolometric converted XLF model of Ueda et al. (2014) are plotted at $z = 5.7-6.4$ (grey and turquoise respectively). My constraints on the QLF can be seen to bridge the gap between the latest JWST observations and the bright-end X-ray measurements, with the extrapolated models all slightly underpredicting the space density of AGN in the early Universe. However, I note that for a more detailed analysis precise matching of the redshift ranges for all measurements of the QLF is required.*

in section 4.1.4) and thus probe the very-faint-end of the XLF, where the majority of the AGN population resided. In order to truly reconcile these measurements a combination of deep X-ray observations and JWST imaging is required.

As contamination of galaxy observations by AGN will significantly impact any measurements of galaxy properties, the presence of the high-redshift AGN population observed here should be accounted for in studies of galaxy properties at $z \gtrsim 4$ (as in e.g. de Graaff et al., 2024; Trinca et al., 2024; Bowler et al., 2020).

4.4.3 The Implications on Early Black Hole Growth

Galaxies within the early Universe are expected to undergo significant stellar mass build up. An actively accreting Super Massive Black Hole (SMBH) within a galaxy is expected to play a role in its evolution (see chapter 1), in some cases enhancing star formation and in others quenching it. Thus, the presence of a significant population of Active Galactic Nuclei (AGN) within the early Universe, as has been demonstrated by my XLF measurements, is likely to have a significant impact upon the growth of the first galaxies.

Previous studies out to redshifts of $z \sim 6$, such as those of Vito et al. (2014); Aird et al. (2015), found a decrease in the space density of AGN with increasing redshift, suggesting that the build-up of stellar mass within galaxies occurred before the central SMBH of the galaxy underwent significant mass build-up. However, the results I have presented in this chapter point to a more simultaneous growth in galaxy stellar mass and SMBH mass, or even significant Black Hole mass assembly prior to stellar mass build up. As such, AGN can be expected to undergo significant growth at earlier times than previously thought, as has been postulated in the work of Guetzoyan et al. (2024).

From my measurements of the obscuration within my high-redshift sample (see section 4.3.3, above) I found the majority of sources to be obscured, consistent with the predictions of Gilli et al. (2022) from models of both the Interstellar Medium of galaxies and an obscuring torus associated with the AGN itself. With the high fraction of Compton Thick sources found for my sample, $0.91^{+0.03}_{-0.03}$ for $z = 4 - 10$, this points towards an abundance of gas within the early Universe, in agreement with the gas mass fraction expected within high redshift galaxies (see review of Carilli & Walter, 2013). Thus, feedback processes due to an AGN may impact the growth of the first galaxies.

The high space density and obscuration fraction I have measured here points towards a build up of SMBHs within heavily obscured environments, indicative of an abundance of gas that may fuel both AGN and star formation within the first galaxies, with early AGN activity potentially impacting the evolution of their host galaxies. Whilst the mechanisms driving this early SMBH growth and co-evolution with their host galaxies is beyond the scope of this thesis, this presents an exciting prospect for the future of our understanding of galaxy formation within the early Universe.

4.5 Conclusions

Detecting the high-redshift X-ray population of moderate luminosity Active Galactic Nuclei (AGN), where the majority of growth within the population occurs, is limited by the sensitivity of current X-ray observatories. As such, the X-ray Luminosity Function (XLF) is poorly constrained at high redshifts, with only a few studies fitting a parametric XLF model to $z = 3 - 6$ (e.g. Georgakakis et al., 2015; Pouliasis et al., 2024). In this chapter I have presented observational measurements of the XLF at $z = 4-10$ using Chandra legacy imaging from Civano et al. (2016) and the COSMOS2020 photometric catalogue of Weaver et al. (2022).

In order to measure the high-redshift XLF I have obtained a sample of $z \geq 4$ X-ray detected sources within the COSMOS field, with photometric redshifts from THE FARMER version of the COSMOS2020 catalogue. I first performed a cross-match of blind X-ray detections from the Chandra Legacy data, to the COSMOS2020 catalogue, producing the blind sample. I then pushed the limits of the Chandra Legacy imaging through direct extractions of X-ray counts at the positions of sources within the COSMOS2020 catalogue, allowing greater completeness of my sample with a higher false probability threshold on the X-ray detections.

Through this process I obtained a sample of 21 blind detected and 32 blind+extracted $z \geq 4$ X-ray AGN, with which I then determined the XLF following the N_{obs}/N_{mdl} method of Miyaji et al. (2001). The XLF was measured for the blind only sample and then the blind and extracted sample using the best fit photometric redshifts of each source and subsequently testing the upper and lower bounds on the XLF measurements given the possible z_{photo} of my sources. I then investigated the effect of obscuration within my AGN sample, on the measured XLF, and applied an N_H correction to my XLF measurements.

These new, improved XLF measurements at moderate luminosities place constraints on the space-density of AGN where previously only extrapolated predictions from XLF models at lower redshifts were available. My conclusions are as follows:

1. Through cross-matching of blind X-ray detections within Chandra Legacy data and subsequent extraction of additional X-ray counts at the position of COSMOS2020 sources, I have developed a sample of 21 blind X-ray sources and 9 directly extracted X-ray sources, at $z_{photo} \geq 4$. The redshifts of these sources are taken to be the best fit photometric redshift, as given by model fits using either galaxy only or galaxy and AGN component redshift spectral templates.

2. I have measured the XLF at redshifts of $z = 4-5$, $z = 5-7$ and $z = 7-10$, assuming no additional X-ray sources to my sample of blind and extracted sources exist within the Chandra Legacy data, across 0.5 dex luminosity bins between $\log L_{\rm X} = 43-46$. The uncertainties on the number of sources at each redshift and luminosity interval are taken to be the Poisson uncertainties given by Gehrels (1986), with the upper uncertainty on 0 sources taken to be the upper limit for intervals with no sources. These XLF measurements, using the blind only sample or the blind+extracted sample, are consistent with the XLF models at $z = 4-5$ (where the models were fit to data). However, my measurements indicate a higher space density, with increasing redshift, than previously predicted by the model extrapolations. At $z = 7-10$ my measurements clearly show a space density closer to that of the models at $= 4-5$, suggesting the expected high redshift decline in the number of AGN is far shallower than lower redshift measurements previously indicated.

3. Determining the maximum and minimum number of AGN at each redshift and luminosity interval, given by the possible photometric redshifts of each source, I have calculated the range of XLF measurements that could be given by my sample. The resulting measurements provide a more conservative uncertainty on my measured XLF, and remain consistent with the model predictions at $z = 4-5$ and $z = 5-7$. However, the upper bound of these photometry limits indicates a potentially higher space density of AGN than previously expected at $z = 5-7$ and $z = 7-10$, with the lower bound of the photometry measurements also hinting at a higher space-density of AGN at the highest redshift interval investigated here.

4. Performing measurements of the XLF using detections from the hard-band legacy imaging, I have found that obscuration likely has a significant impact on the Full-band XLF measurements. The hard-band observations indicate a much higher space density of AGN than the full-band observations. The hardness ratios of my X-ray sample, determined through a Bayesian estimation method in order to account for the low photon counts, indicate a significant fraction of obscured and likely Compton Thick AGN.

5. Dividing my X-ray sample into unabsorbed, absorbed and compton-thick AGN, based on their observed hardness ratios, I have determined N_H and redshift dependent corrections to the XLF measurements. I find that the obscuration corrected XLF, given by the full-band observations, provides a higher space density than the uncorrected measurements and thus the model predictions.

6. From the obscuration corrections I calculate the fraction of absorbed ($N_{\rm H} > 10^{23}{\rm cm}^2$) and Compton Thick ($N_{\rm H} > 10^{24}{\rm cm}^2$) AGN within my blind+extracted sample. I find the absorbed and Compton Thick fractions to be $0.17^{+0.10}_{-0.09}$ and $0.75^{+0.12}_{-0.14}$ at $z = 5-7$, respectively, the absorbed fraction dropping to $0.025^{+0.05}_{-0.01}$ as the Compton Thick fraction rises to $0.95^{+0.02}_{-0.05}$ at $z = 7-10$. I find the fraction of obscured sources increasingly dominates over the fraction of unobscured sources ($N_{\rm H} \leq 10^{23}{\rm cm}^2$), with increasing redshift.

7. Considering the full range of uncertainty in the XLF I have measured, whilst my measurements remain within 1σ of the model extrapolations, I find that the space density of AGN in the early Universe *could* be significantly higher than previously expected. This larger population of early AGN could be expected to have a significant effect on the growth of the first galaxies.

8. I find that my obscuration corrected XLF measurements indicate a rising space density towrds lower luminosities, which appears to be consistent with the high space densities of low luminosity AGN being discovered within deep JWST fields. Thus, my measurements point towards a reconciliation between the X-ray and rest-frame UV measurements at $z \geq 6$.

Through the work presented in this chapter I have obtained important constraints on the moderate-luminosity XLF from $z = 4$ out to a redshift of $z = 10$. These measurements, performed using the $\sim 2{\rm deg}^2$ COSMOS field clearly indicate a

significant population of AGN at high redshifts, with the space density observed higher than that predicted by extrapolations of XLF models fit at lower redshifts (even when fit to AGN samples across a redshift range of $z = 3-6$). This observed high-redshift space density suggest that AGN growth occurred at earlier times, with the growth of SMBHs hosted in early galaxies likely to impact their initial stellar mass build up. Care should thus be taken when determining the properties of galaxies at $z \gtrsim 6$, as AGN emissions are likely to contaminate rest-frame UV observations.

Whilst the results obtained here point towards a reconciliation between the new JWST AGN observations and bright-end X-ray measurements, further studies using larger area X-ray surveys and redshift measurements possible with both the mid-IR imaging of JWST and the large sky area that will be afforded by Euclid are required to constrain the space density of AGN at fainter luminosities and to improve the constraints found here. However, this observed XLF presents exciting possibilities for the population studies that will be possible with the launch of deep, large scale survey telescopes, such as ESA's NewAthena X-ray Observatory mission.

Chapter 5

NewAthena High-redshift Survey Predictions

Current X-ray telescopes are unable to probe large areas of sky down to the faint fluxes needed to probe low luminosity sources within the early Universe. As such, studies of Active Galactic Nuclei (AGN) within the early Universe are limited by the currently available X-ray instruments (see chapter 1 for details). However, ESA's new X-ray observatory, NewAthena, will be able to provide deep survey data over larger areas than possible with current X-ray observatories, allowing us to better constrain the nature of AGN populations across cosmic time.

In 2014 the European Space Agency (ESA) selected the Athena telescope to be the second largest mission within its Cosmic Vision Program[1], alongside the gravitational wave instrument Laser Interferometer Space Antenna (LISA; see e.g. Amaro-Seoane et al., 2017, for details of LISA). In 2023 Athena has subsequently undergone redefinition into NewAthena, involving a redesigned mission in order to save costs, whilst maintaining its status as a flagship of ESA's next generation of observatories.

Able to perform deep survey imaging over an unprecedented area, NewAthena will provide a wealth of survey data with which the the growth of Supermassive Black Holes (SMBHs) in the early Universe can be better understood. In order to be prepared for its launch in the late 2030s, and direct the science aims of the mission, preliminary predictions of the surveys possible with NewAthena are

[1] https://sci.esa.int/web/cosmic-vision/

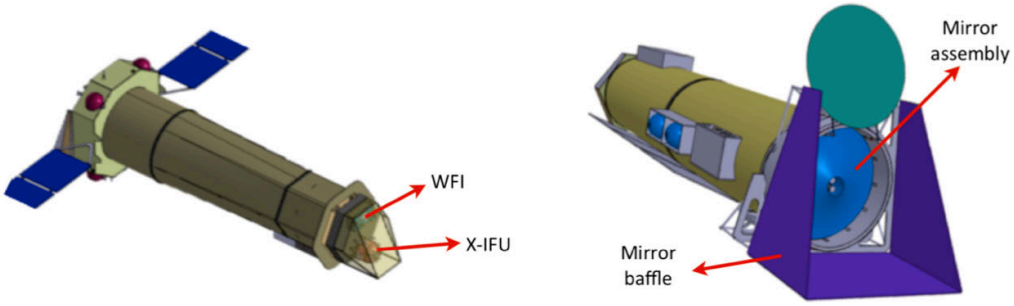

Figure 5.1 *Diagram of the spacecraft design specifications of Athena as of 2022, prior to redefinition. NewAthena retains the 3 key elements depicted here; a large collecting area mirror (utilising silicon pore optics), and both the Wide Field Imager (WFI) and X-ray Integral Field Unit (X-IFU). Image reproduced from Nandra et al. (2013)*

vital. In this chapter I will perform predictions for the yield of high-redshift X-ray AGN surveys with NewAthena, using the updated estimates of the XLF I have obtained in chapter 4.

The specifications of the NewAthena telescope (as of 2024) used to perform the predictions in this chapter are outlined in section 5.1. In section 5.2 I will detail the prediction of the survey sensitivity possible with NewAthena, given by simulated survey imaging (section 5.2.1) with which I will calibrate the analytic sensitivity determined in section 5.2.2. Using the analytic sensitivity determined, I will then predict the yields of high-redshift AGN possible with different survey strategies, using my XLF measurements in chapters 3 and 4, as detailed in section 5.3. The implications for NewAthena science are discussed in section 5.4, and I summarise the results of this chapter in section 5.5.

5.1 The NewAthena Telescope

One of the largest X-ray observatories ever conceived, Athena (Advanced Telescope for High-ENergy Astrophysics) was designed to explore "The Hot and Energetic Universe" (Nandra et al., 2013). Specifically, Athena was designed to address two key aspects within this science theme. "The Hot Universe" focuses on the chemical history of baryons above $10^5 - 10^6$ K as well as the formation and evolution of galaxy clusters and groups, cluster feedback and the underlying mechanisms driving the intergalactic medium. The growth and influence of black holes on the Universe forms the focus of the "Energetic Universe"; with the aim of understanding the formation and evolution of early SMBHs, the physics of

accretion and the galaxy scale feedback process of heating, shocks and outflows due to the activity and growth of SMBHs (Barcons et al., 2017).

In order to address the science goals of "The Hot and Energetic Universe" the Athena concept consisted of a large ($\gtrsim 1.4\text{m}^2$) mirror utilising silicon pore optics technology (Willingale et al., 2013; Beijersbergen et al., 2004, see also section 2.2.3) to provide an unprecedented effective area. Combined with this large mirror, and crucial to the science opportunities provided by Athena, was both a Wide Field Imager (WFI; Rau et al., 2016; Rau et al., 2013) and an X-ray Integral Field Unit (X-IFU; Barret et al., 2023), as shown in figure 5.1.

Originally selected in 2014 as a flagship L-class[2] mission, Athena has undergone significant redefinition in order for the mission's cost-at-completion to meet the allocated budget[3]. The resulting modified version of the Athena X-ray Observatory, NewAthena, was approved in November 2023[4].

Following its redefinition the main design of the observatory has been simplified in order to reduce the cost of construction, whilst maintaining many of the original features and overall science objectives. The main change to the design of the telescope is a simplification of the cooling chain of the X-IFU, to consist of a passive (radiative) cooling mode as the first stage, limiting the area of sky that can be observed relative to the Sun (to allow for effective radiative cooling of the X-IFU). As a result the Target of Opportunity response time will now be ~ 12 hours ($3\times$ slower than the original design). Further reducing development costs, as well as the weight of the mirror and telescope (and thus the cost to launch) the mirror area (at 1 keV) of the observatory has been reduced to $\sim 1\,\text{m}^2$ (corresponding to an on axis effective area of $\sim 0.86\,\text{m}^2$), and the previous planned on-axis angular resolution of 5 arcsec will now be only 9 arcsec. However a 40 arcmin field of view with the WFI will be maintained, as well as X-ray spectroscopic capabilities within a 4 arcmin field of view (only slightly smaller than the originally intended 5 arcmin) provided by the X-IFU. The key specifications set out for the WFI and X-IFU on the NewAthena observatory are summarised in table 5.1.

Despite these changes NewAthena will still provide large sky area surveys, greatly increasing the number of sources that will be identified in such surveys. The angular resolution, 0.3-12 keV energy range, survey speed and sensitivity to

[2]Large mission classification.

[3]https://www.the-athena-x-ray-observatory.eu/en/mission/status-and-milestones

[4]https://www.the-athena-x-ray-observatory.eu/en/node/801

Parameter	WFI	X-IFU
Effective Area at 1 keV (m^2)	0.86	0.52
FOV (arcmin)	40×40	4 (effective diameter)
On Axis Angular Resolution (arcsec)	9	5
Energy Range (keV)	0.2–12	0.2–12
Spectral Resolution (eV)	176	4

Table 5.1 *Key parameters expected for the Wide Field Imager (WFI) and X-ray Integral Field Unit (X-IFU) on the NewAthena mission. Crucial to the predictions performed in this chapter are the effective area and angular resolution of the WFI.*

spectroscopic weak-lines, still provided following the redefinition, are some of the main enablers of Athena science (Nandra et al., 2013; Barcons et al., 2017). As such, NewAthena remains a flagship mission of the next generation of ESA's science observatories, with the final adoption goal of 2027 and expected launch in 2037.

5.2 Sensitivity Predictions

The quality of telescope imaging is dependent upon a number of factors (see §2.1). The focusing of incident light by the telescope mirrors, detector properties and their layout within detector chips with which the image is recorded, as well as a number of other instrument properties, all contribute to the final image produced and impact upon the sensitivity of the telescope.

In order to perform predictions of the X-ray source yields of possible NewAthena surveys a measure of the sensitivity is required. Prior to actual imaging by NewAthena, the sensitivity can be determined by performing analytical modelling of the imaging process or through simulation of incident photons passing through the instrument to detection. Whilst such an analytical sensitivity prediction can be obtained more quickly, and is easily applied to survey predictions, it must be calibrated using realistic survey simulations in order to correctly represent the source detection process. Here I will detail the process of obtaining the simulated survey sensitivity using the SIXTE package (see section 5.2.1) with which I then calibrate the analytic sensitivity prediction, calculated in section 5.2.2.

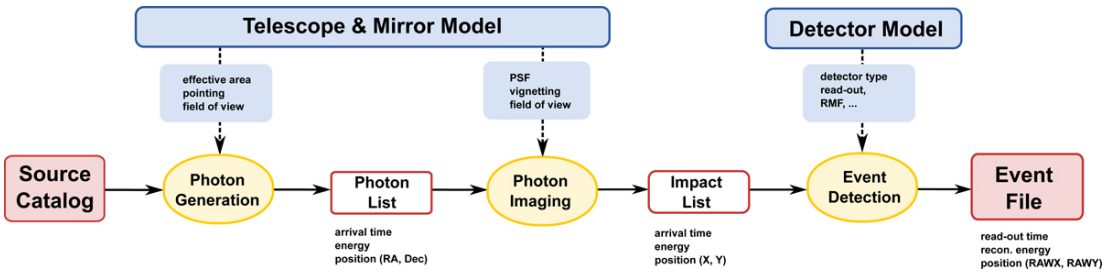

Figure 5.2 *Flow chart illustrating the process of SIXTE in simulating a telescope image, from the initial catalogue of mock sources to the final event file. The key functional processes carried out by SIXTE are shown in yellow, with the telescope specifications passed to the simulation shown in blue. Figure reproduced from Dauser et al. (2019)*

5.2.1 Simulated Survey Sensitivity, using SIXTE

Through detailed simulation of imaging by a telescope, a numerical measure of the expected sensitivity can be determined. In order to obtain a numerical measure of the expected sensitivity of a NewAthena survey image, I perform a detailed simulation of a NewAthena wide field image using the multi-mission SImulation of X-ray TElescopes (SIXTE) software package (Dauser et al., 2019) for exposure times of 5 ks and 150 ks, chosen to represent the case of low source confusion (as only the brightest sources are detected)[5] and confusion-limited imaging respectfully.

Unlike simulation tools designed for specific X-ray instruments (e.g. Wise, 1997; Gabriel et al., 2005; Madsen et al., 2011; Zoglauer et al., 2011), SIXTE is designed to simulate telescope detector characteristics for multiple X-ray instruments. The optics of the X-ray instrument under investigation are described within the simulation using calibration data, such as the point spread function (PSF), detector response matrices and vignetting effects. Applying a Monte Carlo framework of individual photons, produced by simulated astrophysical sources, SIXTE propagates photons through this model of the telescope optics. By modelling the path of incident photons from simulated sources and their effects on the detector, through to the generation of events file as obtained when performing actual observations with the telescope, SIXTE creates predictions for the instrument capabilities. This process is outlined in figure 5.2.

Prior to the simulation of photon collection at the detector the astrophysical

[5] Although 3 ks would be the case of no source confusion, 5 ks is chosen in order to prevent low number statistics impacting the resulting sensitivity.

sources of these photons are simulated from three mock catalogues of sources of X-rays (AGN, galaxies and clusters), as an initial step within SIXTE. For this NewAthena simulation I use a mock AGN catalogue of sources obtained through the simulation of AGN using the Cosmic X-ray Background synthesis model of Gilli et al. (2007) and the Vito et al. (2018) model for the high-redshift AGN, in the redshift ranges of $z = 0 - 10$ and $z = 3 - 20$ respectively, with a minimum luminosity of $L_X \geq 10^{40} \mathrm{erg\,s^{-1}}$. The mock catalogue of X-ray emissions from non-active galaxies are derived through interpolation between the models of Ranalli et al. (2005), down to a 0.5–2 keV flux limit of $10^{-20} \mathrm{erg\,s^{-1}\,cm^{-2}}$ (assuming a power-law spectrum with $\Gamma = 2$). Finally, the mock galaxy cluster catalogue is generated from the dark matter halo masses of Tinker et al. (2008) and Despali et al. (2016), using a mass range of $10^{12} - 4 \times 10^{15} \mathrm{M_\odot}$ across a redshift range of $z = 0.03 - 6$.

Once the simulated sources are defined, photons due to the sources within a given angular separation from the optical axis, set to the typical value of 150% of the Field Of View (FOV), are generated. Dithering (see section 2.1) of the telescope is incorporated, given a predefined time-dependent motion of the telescope pointing, centred at RA 2.00° DEC 2.00° on the sky, generated by the attgen_dither SIXTE tool using a Lissajous-type pattern[6]. The rate at which photons are produced by the simulated sources is given by the energy flux of the source, with a time dependent component for variable sources, assuming the production of photons follows a Poisson distribution. Finally, photon energies are randomly assigned, according to the spectrum of the source, and for photons from extended sources a random direction of origin from the source is also assigned.

SIXTE propagates all generated photons through the given optical properties of the telescope, applying vignetting effects using the off-axis and azimuthal angle of the photon, to the detector plane where the location of impact on the detector is calculated through weighting of randomly drawn Point Spread Functions (PSF). The final detection of the photon impact depends upon the type of detector being simulated; for NewAthena Si-type detectors are used, for which a photon impact produces a charge cloud of electrons that may induce a small current in neighbouring detectors (see e.g. Arnaud et al., 2011). Pixels on each of the four detector chips are defined by their location, and the current produced by photon impacts continuously read off (Event-triggered read-out mode) with effects such as photon pile-up and the addition of random, exposure-dependent background

[6] http://www.sternwarte.uni-erlangen.de/~sixte/data/simulator_manual.pdf

signals, defined by a pre-generated flat field image and simple X-ray background spectrum.

As would be done with event files produced during an observation with the telescope, I perform processing of the event files produced by SIXTE using the FTOOLs package of Blackburn et al. (1999). I merge the event files for each of the four chips that form the NewAthena detector into a single event file, which is then cut to imaged energy ranges of 0.7–2.0 keV and 2.0–10.0 keV (soft and hard band respectively). The final simulated NewAthena image I obtain using SIXTE, covering a sky area[7] of 0.5deg^2, is shown in figure 5.3.

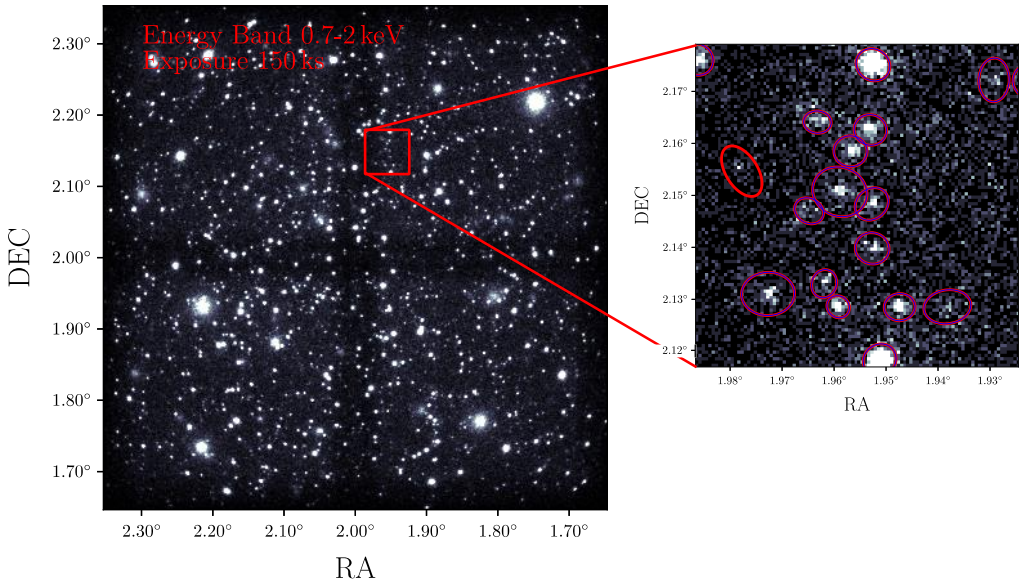

Figure 5.3 *SIXTE simulated soft band (0.7-2 keV) NewAthena WFI image, with Gaussian smoothing of σ = 2 pixels (corresponding to the 9 arcsec PSF of NewAthena) applied, obtained from processing of the event files produced for a 150ks exposure time. A 100×100 pixel zoom-in is shown with the sources detected by WAVDETECT with a false probability threshold of 1×10^{-5} and 1×10^{-6} indicated by the red and blue regions respectfully. As can be seen from the detected source regions, a false probability threshold of 1×10^{-5} results in a more complete detection of all apparent sources within the imaging.*

[7]The final sky area of the simulated image is larger than the NewAthena FOV area of 40arcmin × 40arcmin, due to the dithering motion shifting the FOV across this final imaged area.

Source Extraction on Simulated Images

In order to measure the sensitivity of the simulated NewAthena imaging to the mock X-ray sources, I run a source detection algorithm on the simulated images to identify sources and compare to the likely counterpart in the mock catalogue. This process is carried out using the simple source detection method, WAVDETECT, from the CIAO suite (Fruscione et al., 2009), as was done for the Chandra imaging in chapter 4.

In order to identify sources within the image, CIAO requires a measure of the variation in PSF and exposure across the final image. Given the dithering and expected vignetting of the telescope, I simulate the corresponding exposure map for the image using SIXTE and convert to effective exposure using a factor of $9042.83\,\mathrm{cm}^{-2}$ (as given by the on-axis effective area in the 0.7–2 keV band, weighted by an assumed power-law spectrum with photon index $\Gamma = 1.9$). The variation in PSF across the image is based on the NewAthena PSF and variation with off-axis angle, with the PSF at each pixel position determined for apertures corresponding to the 39% EEF[8]. The source detection is then performed on the more sensitive 0.7–2 keV imaging, using the WAVDETECT code, with the sigthresh parameter (from which WAVDETECT determines the significance threshold for source detections) set to 1×10^{-6} and 1×10^{-5} (Freeman et al., 2002). From visual inspection of the detected source regions and the simulated image, it can be seen that using a sigmathresh of 1×10^{-5} identifies more source-like fluctuations in the image counts (see figure 5.3). Thus the source list obtained with a false probability threshold of 1×10^{-5} is used for further investigation of the NewAthena sensitivity.

The resulting sample of NewAthena detected sources is cross-matched to the original (mock) source list based on source position and flux. All mock sources within a search radius of 5 arcsec around the detected source are identified and the highest flux mock source taken to be that detected by NewAthena.

For comparison between the detected flux and original source flux, I first convert the count rate extracted for each detected source into a soft band (0.7-2keV) flux, given the conversion factor 1.92275×10^{-9}. Figure 5.4 shows the comparison between the flux of the mock sources (f_{in}) and the flux of their detections as

[8]This EEF aperture has been found to maximise the source detection by WAVDETECT (G. Lanzuisi, private communication), and the resulting measurements are subsequently converted to the 100% EEF fluxes after detection.

measured by NewAthena (f_{out}). As can be seen, the imaging by NewAthena has reproduced the source fluxes with a close to one-to-one relation, indicating the success of the telescope in identifying X-ray sources. Towards very low fluxes a number of overly bright sources are detected within the NewAthena imaging; this is likely due to spurious source detections and the effects of Eddington bias that come in at these low fluxes as well as potentially source blending or failed cross-matches due to bad CIAO positions (as can occur in extended sources).

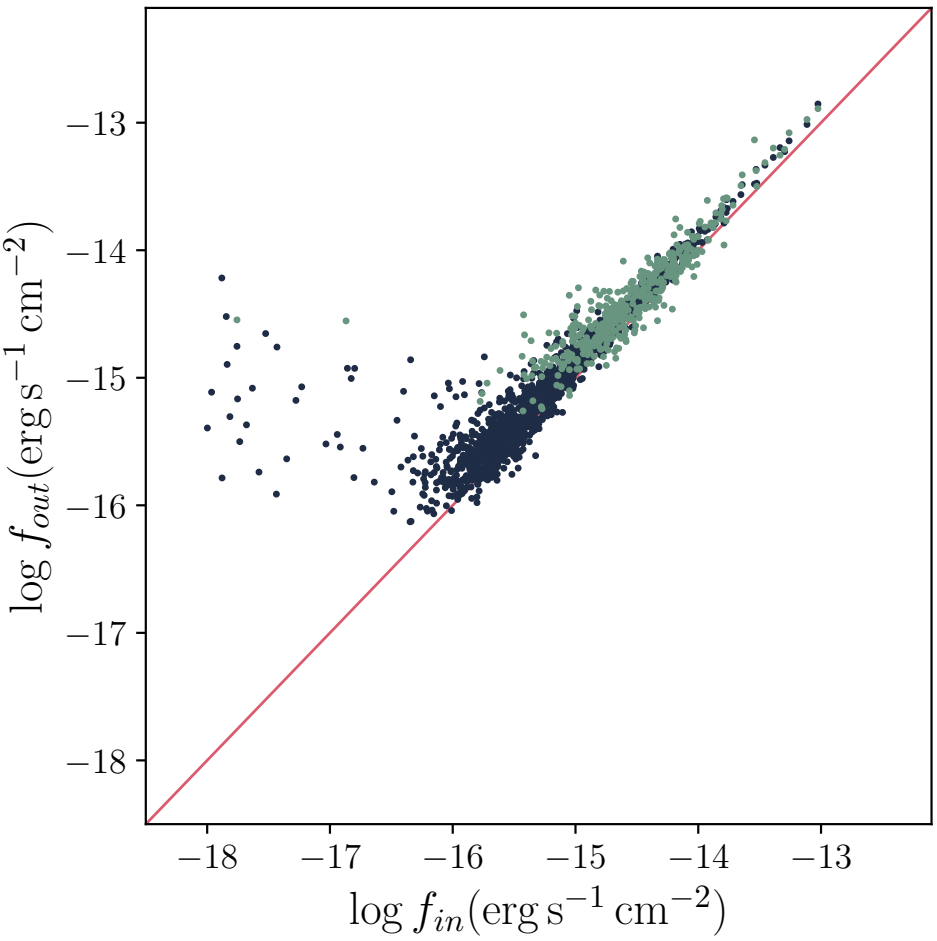

Figure 5.4 *Comparison of source flux passed to SIXTE (f_{in}), as given by the mock source catalogues, and corresponding source flux measured by NewAthena (f_{out}), for an exposure of 150 ks (black dots) and 5 ks (green dots). The one to one relation is shown by the red line. The measurements can be seen to closely follow the one-to-one trend, indicating the success of the WAVDETECT algorithm in identifying sources and accurately measuring their fluxes in simulated NewAthena WFI images. For both exposures there can be seen to be deviation from the one-to-one line at faint fluxes, as Eddington bias begins to significantly contribute to the measured fluxes.*

With my sample of detected sources and their corresponding input source properties the survey sensitivity of NewAthena, given the predicted properties of the telescope, can be determined. As the input catalogues of mock X-ray sources cover a much larger area of sky than the simulated imaging, the mock catalogue is first reduced to only those sources that fall within the footprint of the NewAthena $0.5\,\mathrm{deg}^2$ image. This reduces noise at the bright end, where the probability of detecting such sources depends on the total survey area, due to the low space density of the brightest X-ray sources.

The number of mock and detected sources, given the corresponding input flux, is determined for flux intervals of at least 0.1 dex between $f_\mathrm{X} = 10^{-18} - 10^{-9}\,\mathrm{erg\,s^{-1}\,cm^{-2}}$. The bins are of variable width, such that each bin contains at least 10 sources, in order to reduce noise at the highest fluxes where source numbers are low. The sensitivity of NewAthena is then given by the total area of sky imaged in the simulation, scaled by the ratio of the number of detected sources to the number of mock sources within each flux interval.

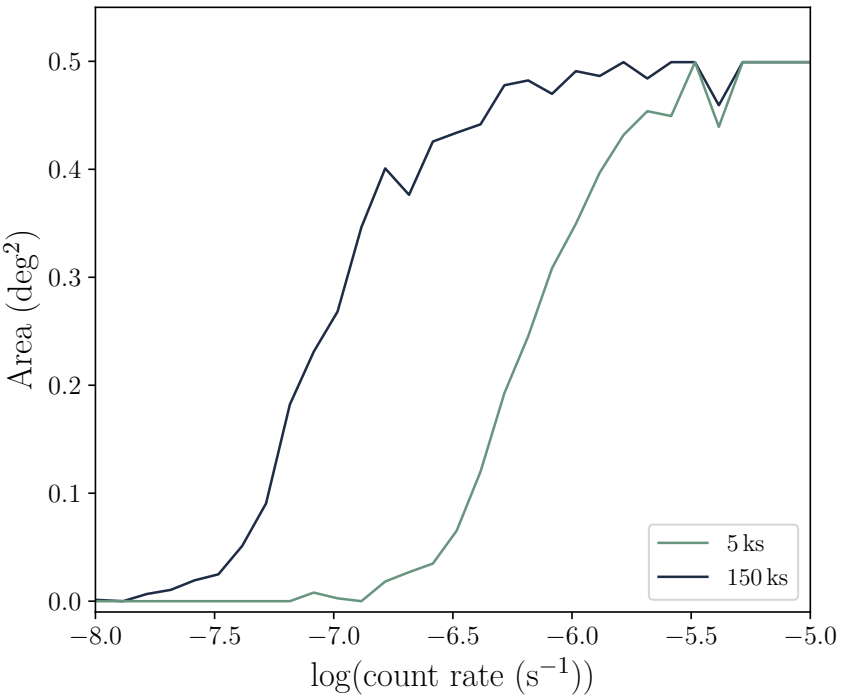

Figure 5.5 *NewAthena area curve produced by SIXTE simulations of imaging performed with 5 ks (green) and 150 ks (black) exposure times. Noise within the curves is the result of the small sample size from which the area curves are determined. The sensitivity achieved with 5 ks exposure is ∼ 3 orders of magnitude lower than that achieved with the 150 ks exposure, as can be seen in the delayed rise in area of the 5 ks curve.*

The resulting sensitivity curves produced by the SIXTE simulations are shown in figure 5.5. The small sample size results in random fluctuations in the area curve calculated, Most notably at high count rates where fewer mock sources will exist in the total sample area. This noise in the sensitivity measurements could be improved by performing a large number of simulated imaging with SIXTE however such a process would be highly time consuming. Thus, in order to quickly obtain a measure of the likely sensitivity of NewAthena across a large range of exposure times an analytical model, calibrated using the simulated measurements, is required. With such an analytical model further predictions of the surveys possible with NewAthena can be performed.

5.2.2 Analytic Modelling of Survey Sensitivity

The sensitivity of a survey corresponds to the probability of detecting a source of given flux f_X, across the detector. Performing an analytic calculation of this sensitivity will provide a detailed model with which further calculations of the survey properties can be determined.

In order to calculate the sensitivity the change in the point spread function and effective collecting area across the field of view, resulting from the properties of the telescope itself, must be determined. This FOV is given by the exposure map calculated above, using SIXTE, from the dithering and vignetting effects of the telescope[9] (see section 5.2.1). The effective exposure of the telescope is thus the exposure map, multiplied by the energy response of the WFI for a given energy band, across the FOV (determined from the on-axis response files for the NewAthena WFI[10]).

The change in PSF across the FOV is generated using the PSF Half Energy Width (HEW) with respect to off-axis viewing angle estimates[10], assuming a modified pseudo Voigt profile. The PSF is determined within apertures of diameter 0.83×HEW, corresponding to an Enclosed Energy Fraction (EEF) of 36%, across the FOV, in order to align with the detection process of WAVDETECT (used in section 5.2.1).

[9] Without accounting for the dithering motion of the telescope the FOV would very simply be that of the WFI (40×40 arcmin) minus the area lost in the 86 arcsec gaps between the 4 chips. However, with dithering effects a single pointing covers a somewhat larger area ($\sim 0.5\,\mathrm{deg}^2$), albeit with a reduced effective response around chip gaps and the edges of the FOV.

[10] https://www.cosmos.esa.int/web/athena/resources-by-esa

In addition, in order to calculate the probability of a given source flux being detected above the background, the total background counts across the FOV of the detector is determined. The total background is given by the sum of the constant particle background (assumed to be $8 \times 10^{-3} \mathrm{cts\,s^{-1} keV^{-1} cm^{-2}}$, as given by the NewAthena specification), the focused celestial background and a stray light background. The focused celestial background is calculated, on-axis, from the model of Hasinger et al. (2005), assuming 20% of the AGN are unresolved and thus contribute to the Cosmic X-ray Background, and rescaled across the FOV given the exposure map. The stray light background is calculated following a similar process, assuming 100% of AGN are unresolved. The resulting background map provides an estimate of the the total background in an aperture of diameter 0.83×HEW across the WFI field of view.

With the background, PSF and effective exposure across the full FOV of the NewAthena WFI calculated, the sensitivity can be determined, as in chapter 4. The minimum source counts, L, required to detect a source at each pixel position within the FOV is determined for a given false probability threshold, as described in Section 4.1.2. The sky area contributed by each pixel to the total area curve at a given flux, $S(f_X)$, is then given by the probability of a source of such flux producing accounts above the minimum count threshold, L, as given by equation 4.2. This calculation accounts for Poisson fluctuations in measured source counts which may result in a source of flux lower than the threshold producing counts above that limit. This is done using the method of Georgakakis et al. (2008), as in chapter 4.

The nominal area curve resulting from this calculation is shown in figure 5.6 for the soft band with an exposure time of 150 ks. However, this analytical model cannot independently characterise all aspects of the telescope and detector system, and perfectly model the true source detection process. As such, I use the simulated sensitivity from SIXTE (see above, section 5.2.1) in order to calibrate the analytical model and confirm whether it successfully characterises the full process of imaging and source detection with NewAthena. First I will calibrate the value of the false probability threshold within the analytical model, which corresponds to the sigthresh parameter within WAVDETECT, using a short simulated exposure time of 5 ks (for which there should be little confusion between imaged sources). Then I will calibrate the characterisation of source confusion within the analytical simulation, using an exposure time of 150 ks simulation.

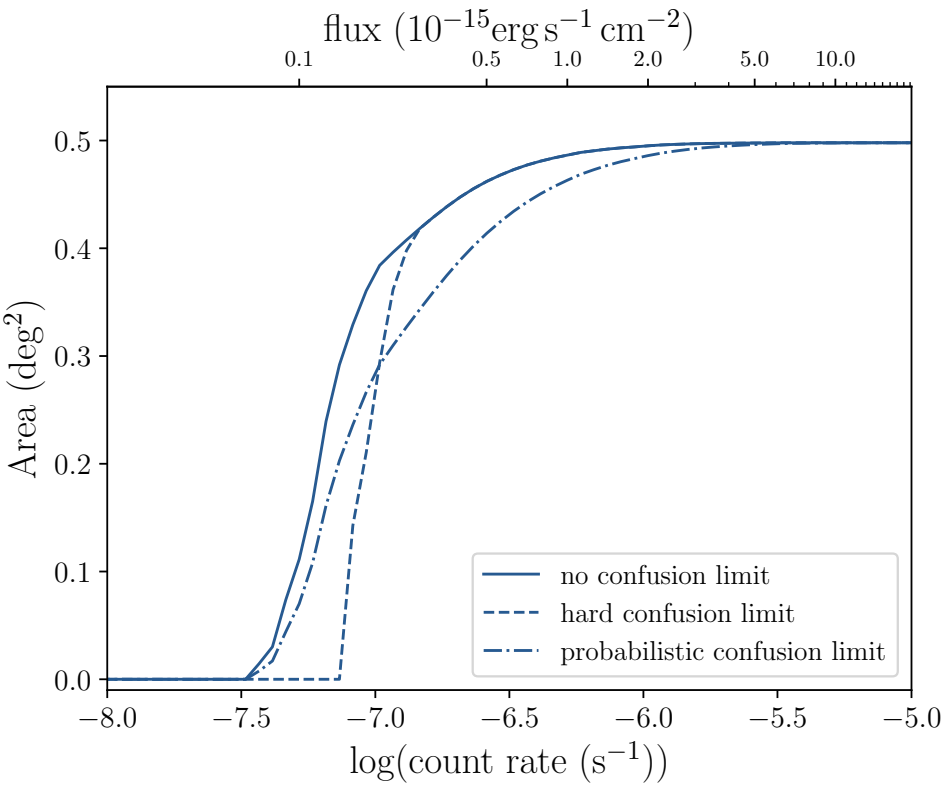

Figure 5.6 *NewAthena area curve produced by an analytical calculation of the sensitivity obtained with a single pointing of 150 ks exposure. The calculation has been performed here with an assumed 20 beams per source and false probability threshold of 1e-5 (see section 5.2.2). The sensitivity is shown in the case of no source confusion (solid), a hard source confusion limit (dashed) and probabilistic source confusion (dot-dashed) applied.*

False Probability Threshold Calibration

Unresolved sources contribute to the background noise within an image. Sources become confused within an image when this background is such that nearby sources can become blended (appearing as a single source) In general it can be assumed that once there is more than one source per 30 beams, where a beam is defined as one resolution element in the image, confusion between sources must be accounted for (Hogg, 2001). Here the area of a single beam is taken to be πHEW^2. The analytic sensitivity calculated depends on the choice of false probability threshold and the number of beams per source.

In order to determine an appropriate false probability for the analytic calculation, I perform the calibration within a regime of low source confusion (i.e. where few to no sources within the image are blended together). For low source confusion the

space density of detectable sources must be such that only one source occupies the total area of the number of beams (i.e. few faint sources observable and thus a lower space density of sources). Assuming the point source sky density is given by the $\log N - \log S$ of Georgakakis et al. (2008), this corresponds to fluxes of $5 \times 10^{-16}\,\mathrm{erg\,s^{-1}cm^{-2}}$ in the soft band, detectable with a $\sim 3\,\mathrm{ks}$ exposure by NewAthena. As this very short exposure time is likely to enter into the regime of low source count, I take the case of low source confusion to occur for an exposure time of 5 ks.

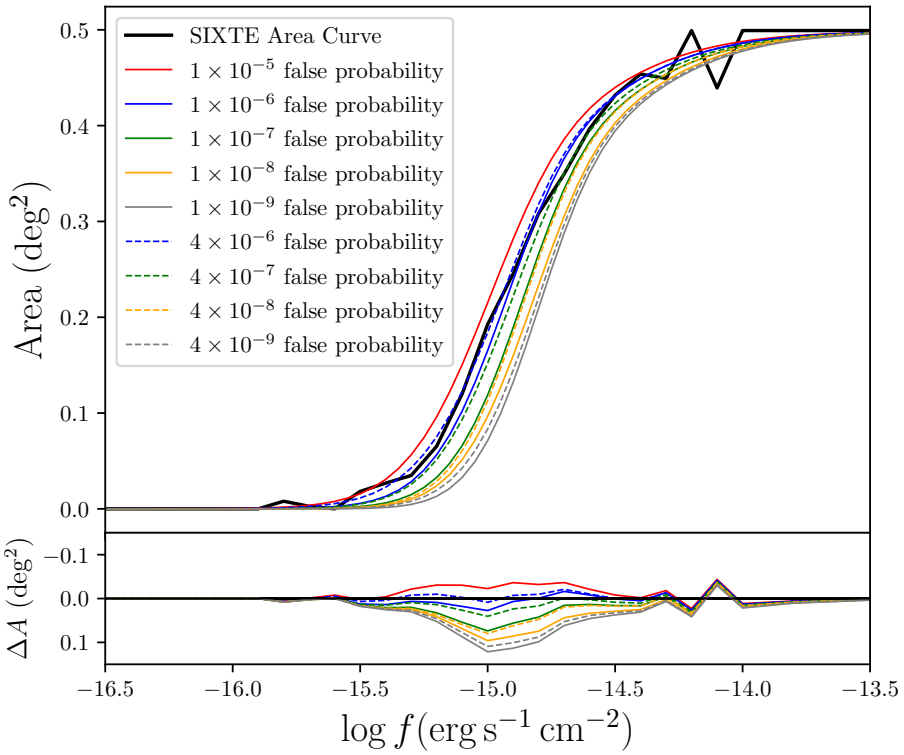

Figure 5.7 *Possible analytic sensitivities for the unconfused case of 5 ks imaging by NewAthena, determined with a fixed beam number of 20 and varying false probability threshold. The simulated sensitivity of NewAthena (black solid line) is closely traced by the different analytical curves, with the 4×10^{-9} measurement showing only slight deviation from the simulated curve.*

The analytic sensitivity is thus calculated in the case of no source confusion, for a survey performed with a 5 ks exposure, and with false probability thresholds of $1{\times}10^{-5}$, $1{\times}10^{-6}$, $1{\times}10^{-7}$, $1{\times}10^{-8}$, $1{\times}10^{-9}$, $4{\times}10^{-6}$, $4{\times}10^{-7}$, $4{\times}10^{-8}$ and $4{\times}10^{-9}$. Comparing the resulting sensitivity curves to the simulated sensitivity determined for an exposure of 5 ks (see section 5.2.1 above) the analytic measurement that best reproduces the simulated sensitivity is that determined with a false probability threshold of 4×10^{-6} (see figure 5.7).

Source Confusion Calibration

With the false probability threshold calibrated within my analytical model, I then account for the effect of source confusion on the sensitivity. Using the simulated sensitivity from the 150 ks SIXTE run, I determine the optimum number of beams per source within the analytic sensitivity calculation.

It can be assumed that sources cannot be reliably detected at the point where there are more than one source expected within the combined area of a given number of beams, i.e. when

$$\rho(> f_{\rm X}) N_{beam} A_{beam} > 1, \tag{5.1}$$

where $\rho(> f_{\rm X})$ is the sky density of sources above a given flux $f_{\rm X}$, N_{beam} is the number of beams and A_{beam} is the area of one beam. The values of N_{beam} and A_{beam} within the model are what must be calibrated within the analytical model, using the realistic simulations from SIXTE[11].

This simple confusion limit is referred to here as the "hard limit" (shown in figure 5.6 by the dashed line). However, a more realistic case of this source confusion can be applied to the sensitivity calculation through a probabilistic confusion limit, as it is still possible to observe some unconfused sources below the hard limit thanks to the random distribution of sources. This probabilistic confusion limit is thus given by the Poission probability of having more than one source within the total area of the beams ($A_{tot} = N_{beam} A_{beam}$),

$$P(n > 1 \text{ in } A_{tot}) = 1 - P(n \leq 1 \text{ in } A_{tot}) = 1 - P(n = 0) - P(n = 1) = 1 - e^{-n} - n e^{-n}, \tag{5.2}$$

where n is the expected number of sources within the area A_{tot} such that $n = \rho(> f_{\rm X}) N_{beam} A_{beam}$, with the area of a single beam fixed at $A_{beam} = \pi \text{HEW}^2$. The sensitivity is thus determined, as before, with the effective sky area of a single pixel at each flux reduced by the probability of no source confusion (i.e.

[11] There is a degeneracy between the number of beams and the area of a single beam as it is only possible to determine the total area given by the product of these values. As such, I fix the area of a single beam to be $A_{beam} = \pi \text{HEW}^2$, and thus determine N_{beam}.

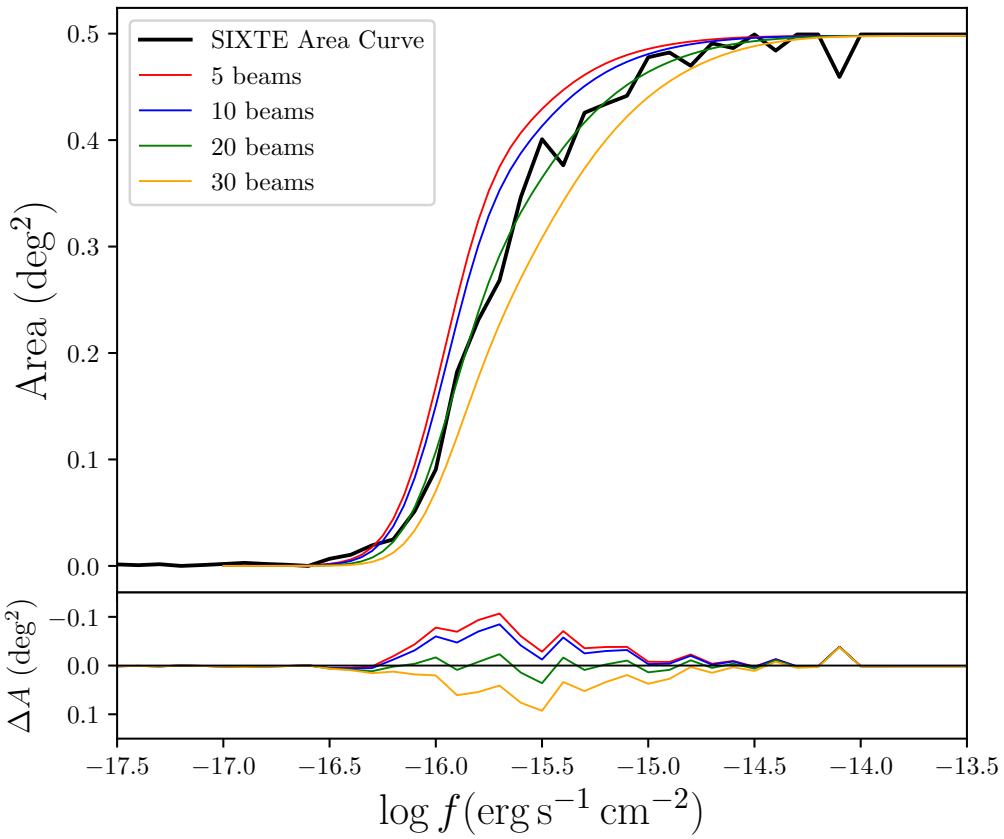

Figure 5.8 *Analytic NewAthena sensitives for 150 ks imaging, with source confusion, as given by a fixed* 4×10^{-6} *false probability threshold and variable beam number. The corresponding 150 ks SIXTE simulated sensitivity is shown by the black solid line. The 20 and 30 beam cases can be seen to closely follow the simulated sensitivity, with the 20 beam case showing the least deviation.*

$1 - P(n > 1 \text{ in } A_{tot})$) given the HEW at the pixel. The resulting probabilistic confusion limited sensitivity (shown by the dot-dashed line in figure 5.6) can be seen to allow for sensitivity to fluxes below the hard limit, however the sensitivity just above the hard limit is reduced as there is also a non-zero probability that 2 or more sources could fall within the total area of the beams.

For a survey of exposure time of 150 ks, where sources will likely be confusion limited, I thus calculate the probabilistic confusion-limited analytical sensitivity, given the false probability determined above and N_{beam} = 5, 10, 20 and 30. As can be seen in figure 5.8, from comparison between the analytic calculation of the sensitivity and the SIXTE 150 ks simulated sensitivity measurements, $N_{beam} = 20$ can be seen to provide a suitable model of the NewAthena sensitivity curve (with a fixed value of $A_{beam} = \pi \text{HEW}^2$).

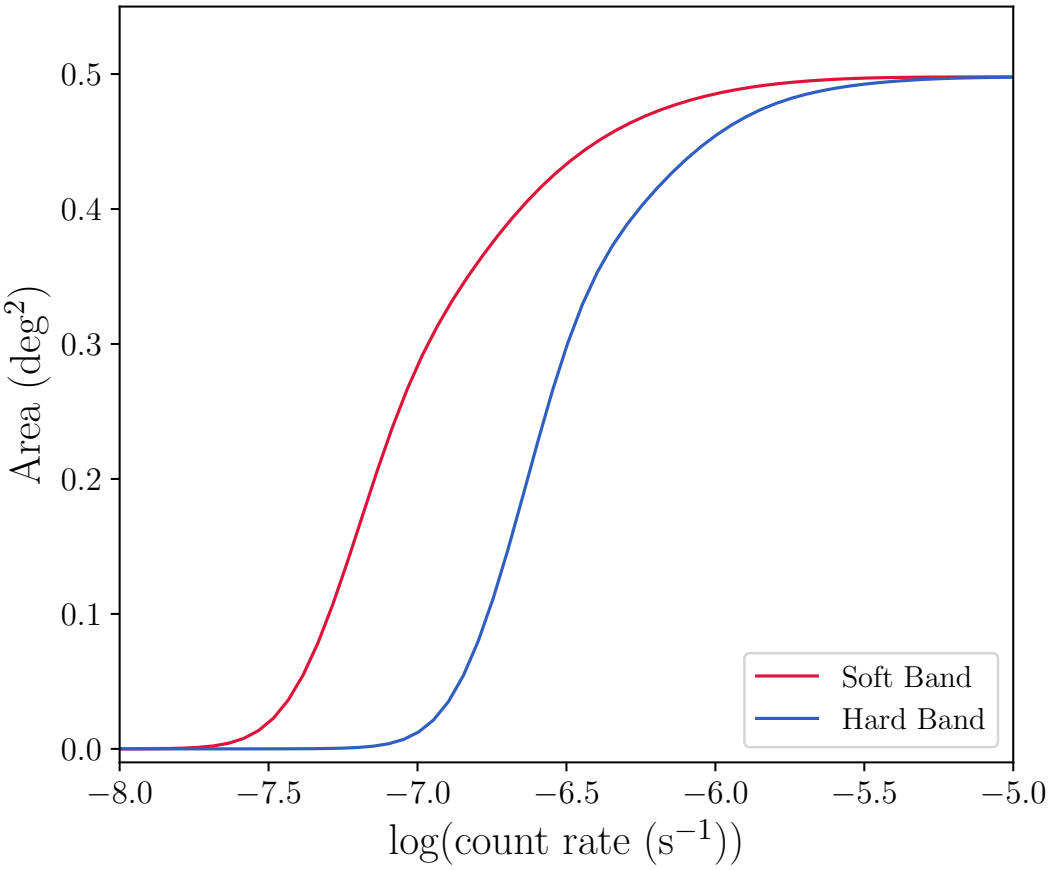

Figure 5.9 *The NewAthena hard and soft band analytic area curves, given by a false probability threshold of* 4×10^{-6} *and* $N_{beam} = 20$*, plotted for an exposure time of 150 ks. These area curves will be used throughout the rest of this chapter.*

As such the final analytic model of the survey sensitivity of the NewAthena WFI is given by a false probability threshold of 4×10^{-6} and 20 beams per source. This is shown in figure 5.9 for both soft and hard-band energies, calculated for a standard survey exposure time of 150 ks. The soft-band sensitivity of NewAthena is clearly more sensitive to faint fluxes than the hard-band, with the area probed at each flux rising sooner (albeit more gradually) than the hard-band area.

Using this simulation calibrated analytical model I can now generate smooth predicted area curves (without the noise produced in simulations) quickly for a wide range of exposure times. Thus further predictions for the surveys possible with the NewAthena WFI can be performed.

5.3 Predicting $z \gtrsim 4$ Survey Yields

As discussed in section 5.1, NewAthena is expected to provide deep survey imaging across larger sky areas than ever before. Quantifying the sensitivity of this imaging and the optimal survey strategy that should be possible with the current specifications of NewAthena is vital to directing the science aims of the telescope. With the predicted sensitivity of NewAthena analytically modelled (see section 5.2) I will now perform predictions for the source numbers likely within a NewAthena survey of varying survey duration.

5.3.1 Single Pointing Source Numbers

As discussed in chapter 1, the X-ray Luminosity Function (XLF) traces the space density of the AGN population, as a function of luminosity, across cosmic time. Thus, for a given telescope sensitivity, the XLF can provide a predicted number of sources that could be detected by that telescope depending on the redshift and luminosity of the sources to be detected. With my observed XLF measurements from chapter 4 indicating a higher space density of AGN than previously thought, I use the XLF model of Pouliasis et al. (2024) with my obscuration dependent corrections applied in order to calculate the number of sources that would be detected by NewAthena's WFI for a given pointing exposure.

For sources at redshifts of $z = 4-5$, $5-7$ and $7-10$, with luminosities in 1 dex bins from $L_{\rm X} = 10^{42} - 10^{46}\,{\rm erg\,s^{-1}}$, I calculate the predicted number of sources that would be detected at soft-band energies by the NewAthena WFI, using equation 4.9. In this case the XLF model is that of Pouliasis et al. (2024) corrected for unabsorbed, absorbed or Compton thick sources (defined as in section 4.3), and the sky area given by my analytical sensitivity for a range of possible pointing exposures (as calibrated above, in section 5.2.2). The resulting source numbers expected in a single NewAthena WFI pointing for a given exposure time are shown in figure 5.10, with uncertainties given by the upper and lower limits on the XLF correction factor.

The number of detected sources within a single NewAthena WFI pointing can be seen to increase gradually with exposure time, for the case of unabsorbed, absorbed and Compton thick sources alike. For the higher luminosity bins used here, the predicted number of sources within a single pointing can be seen to

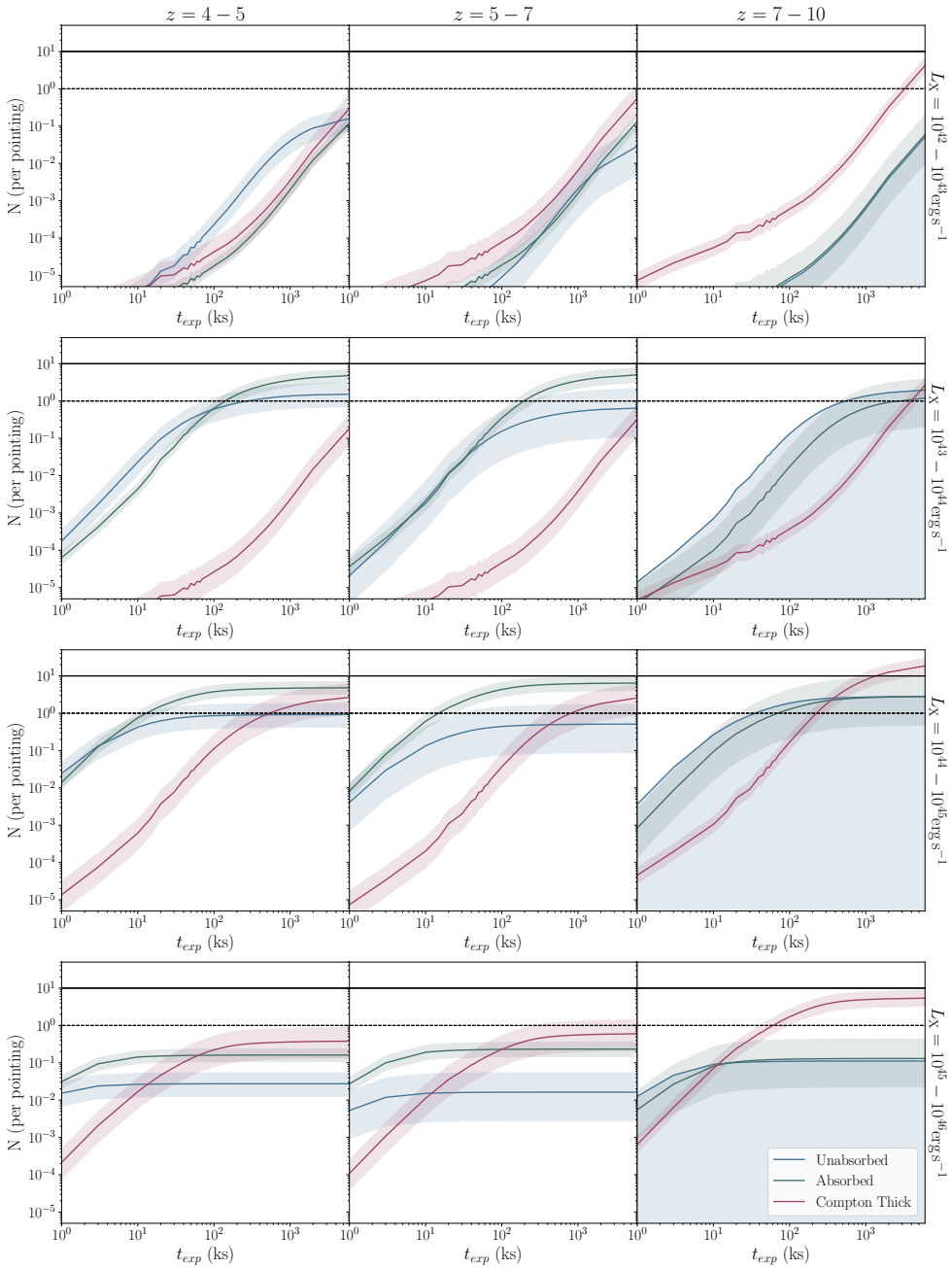

Figure 5.10 *Predicted number of soft-band detected unabsorbed ($N_{\mathrm{H}} < 10^{23}\mathrm{cm}^{-2}$; blue), absorbed ($10^{23}\mathrm{cm}^{-2} \geq N_{\mathrm{H}} < 10^{24}\mathrm{cm}^{-2}$; green) and Compton thick ($N_{\mathrm{H}} \geq 10^{24}\mathrm{cm}^{-2}$; red) AGN, within 1 dex luminosity bins from $L_{\mathrm{X}} = 10^{42} - 10^{46}\,\mathrm{erg\,s^{-1}}$, in a single pointing of a given exposure time, at redshifts of $z = 4 - 5$, $5 - 7$ and $7 - 10$. Uncertainties are given by the error in the obscuration correction factor, as found in chapter 4. A detection of 1 (dashed line) and 10 (solid line) AGN per pointing are shown. The number of Compton thick AGN rises more sharply with exposure time, from below to above the number of absorbed and unabsorbed AGN, with more heavily obscured sources at higher redshifts. Even with a single pointing by NewAthena a significant number of high-redshift AGN should be detected.*

level off as the exposure becomes deep enough to detect all sources within the given luminosity and redshift interval. This maximum number decreases with increasing luminosity, as the space density of these very bright sources is too low for them to definitely be found within a single pointing. At the faintest luminosity, $L_{\rm X} = 10^{42} - 10^{43}\,{\rm erg\,s^{-1}}$, at the highest-redshift interval it is only for the Compton thick sources that any detections can be expected, even with an exposure time of 6000 ks. From comparison between the different number of sources predicted in each obscuration bin, it can clearly be seen that the Compton thick sources require longer pointing exposures in order to be detected, however they begin to dominate over the absorbed sources at $z = 7 - 10$.

At long exposure times, longer than $\gtrsim$ 100ks, imaging is likely to be heavily confusion limited. As such, pushing to longer exposure times, of the order of several Ms, begins to provide little additional gain in source numbers from a single pointing. Instead, a survey comprised of multiple pointings performed for a short exposure time is likely to provide a larger sample of detected sources.

5.3.2 Survey Source Number Predictions

As shown in figure 5.10, for a given redshift and luminosity bin there is a maximum number of sources predicted to be detected within a single NewAthena WFI pointing. Given the predicted number of detected sources within a single pointing (N), calculated above, I divide by the corresponding pointing exposure. I determine the efficiency of detecting sources of each redshift interval and luminosity for a given pointing exposure, i.e. the source yield per 1 Ms of survey time. The resulting number of sources per 1 Ms of survey time is shown in figure 5.11, with uncertainties propagated from those on the number of sources within a single pointing.

From figure 5.11 it can be seen that the number of sources detected by NewAthena's WFI increases with the pointing exposure, before dropping again as the exposure time of a single pointing results in fewer overall pointings to reach a total survey time of 1 Ms. As such, for a given redshift and luminosity of sources to be detected, there exists an optimum pointing exposure at which the most sources can be detected per 1 Ms of the total survey time (as shown by the peak in N per 1 Ms). For higher luminosity sources this pointing exposure is lower than for fainter sources, as a larger sky area must be observed in order to find them. Whilst Compton thick sources typically requiring longer pointing exposures in

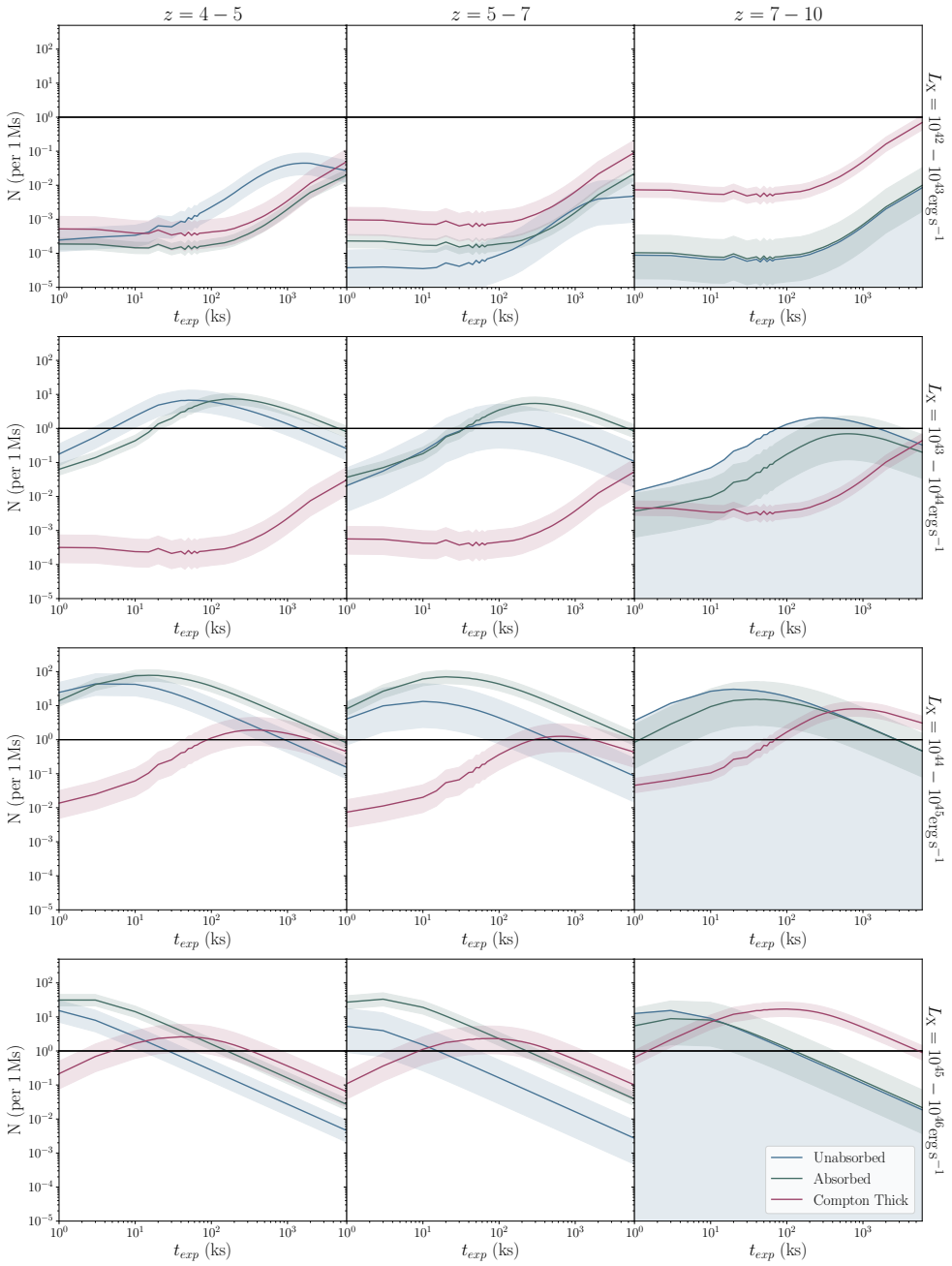

Figure 5.11 *Predicted number of AGN per 1 Ms of a survey by NewAthena, with respect to the pointing exposure used, for unabsorbed (blue), absorbed (green) and Compton thick (red) AGN within 1 dex luminoisty bins from* $L_X = 10^{42} - 10^{46}\,\mathrm{erg\,s^{-1}}$ *at redshifts of* $z = 4 - 5$, $5 - 7$ *and* $7 - 10$. *Uncertainties in the predicted number are given by the error in the obscuration correction factor found in chapter 4. The optimal detection efficiency of AGN within each bin can be seen as the peak in predicted number per Ms, with the majority of redshift and luminosity bins reaching a source yield of greater than the 1 source per Ms (solid black) line and thus could viably be probed by an appropriate NewAthena WFI survey.*

order to be detected with a survey. From these efficiencies it is clear that even at the highest redshifts ($z = 7 - 10$) it is possible to observe significant numbers of absorbed and Compton thick AGN of luminosity $L_X = 10^{44} - 10^{46}\,\mathrm{erg\,s^{-1}}$ within a total survey duration of $\sim$ 1Ms; the peak in the number per 1 Ms of these sources clearly exceeds the line of 1 source per 1 Ms.

5.3.3 Optimal Exposure Time to Yield Sources at different Redshifts and Luminosities

For a given luminosity and redshift range there is an optimum pointing exposure, at which the highest yield of sources per 1 Ms of survey time will be achieved. This is the point of optimal balance between the exposure required to detect sources within a given redshift and luminosity bin, and the area of sky needed in order to find significant numbers of such sources, given their intrinsic space density. In figure 5.11 this can be seen as the turn over point in the predicted number per 1 Ms.

At both soft and hard-band energies I calculate the peak source yield, and the corresponding exposure per pointing, as given by the the maximum of the ratio of number of sources to pointing exposure within 1 dex luminosity bins from $L_X = 10^{42} - 10^{46}\,\mathrm{erg\,s^{-1}}$), for redshift intervals of $z = 4 - 5$, $5 - 7$ and $7 - 10$. This is determined for unabsorbed ($N_H < 10^{23}\,\mathrm{cm^{-2}}$), absorbed ($10^{23}\,\mathrm{cm^{-2}} \geq N_H < 10^{24}\,\mathrm{cm^{-2}}$) and Compton thick ($N_H \geq 10^{24}\,\mathrm{cm^{-2}}$) sources, given the corrections to the Pouliasis et al. (2024) XLF found in chapter 4. The optimum predicted survey capabilities of NewAthena are thus shown in figures 5.12 and 5.13 for the soft and hard-bands respectively.

From the maximum survey yields it can be seen that, in both the hard and soft-bands, NewAthena is able to find significant numbers of high-redshift unabsorbed, absorbed and Compton thick AGN down to a minimum luminosity of around $L_X = 10^{43}\mathrm{erg\,s^{-1}}$. The number of AGN detected by a NewAthena WFI survey can be expected to increase with luminosity until the space density of sources limits the number available to be observed. Overall, the hard band predictions indicate fewer AGN will be found at hard-band energies, due to the lower hard-band sensitivity compared to the soft-band (see figure 5.9), however in the case of Compton thick sources the hard-band will yield a larger sample of sources than the soft-band.

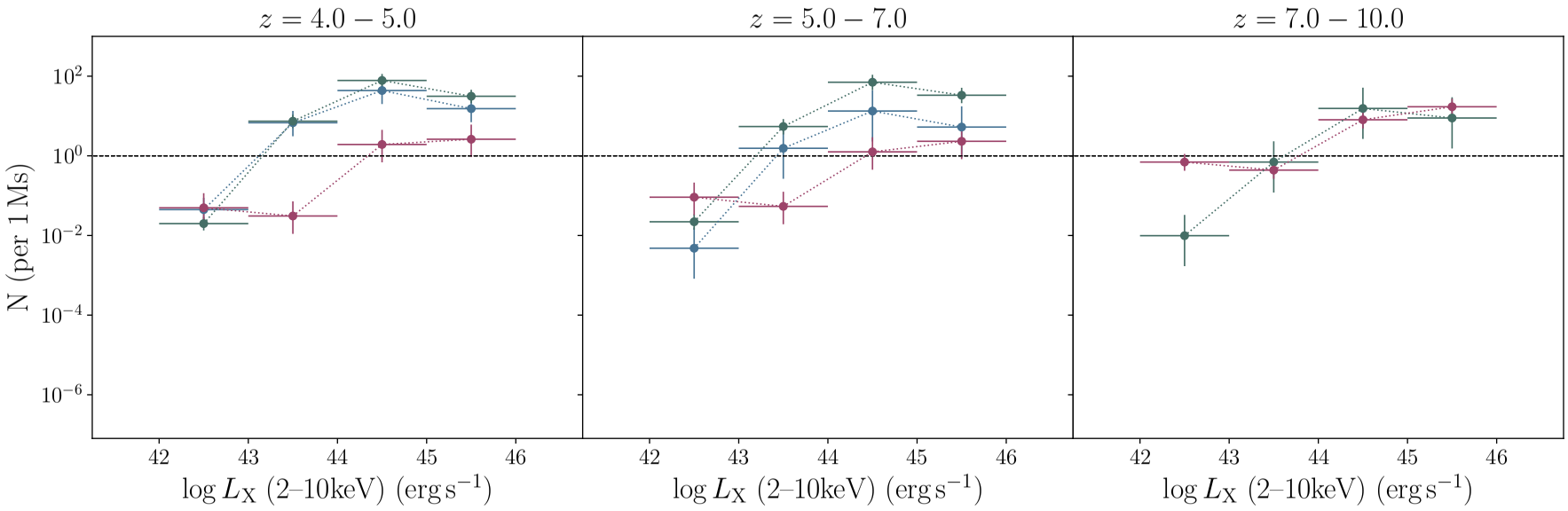

Figure 5.12 *Number of AGN detectable by NewAthena, per Ms survey time, when survey imaging is performed with the peak efficiency pointing exposure given by figure 5.11, for the soft (0.7–2 keV) band. Predicted numbers of unabsorbed, absorbed and Compton thick AGN are shown by the blue, green and red points respectively. The black line indicates the point of 1 source detected per Ms. Although requiring a large total observing time, NewAthena will be able to observe both absorbed and Compton Thick AGN at* $z = 7 - 10$.

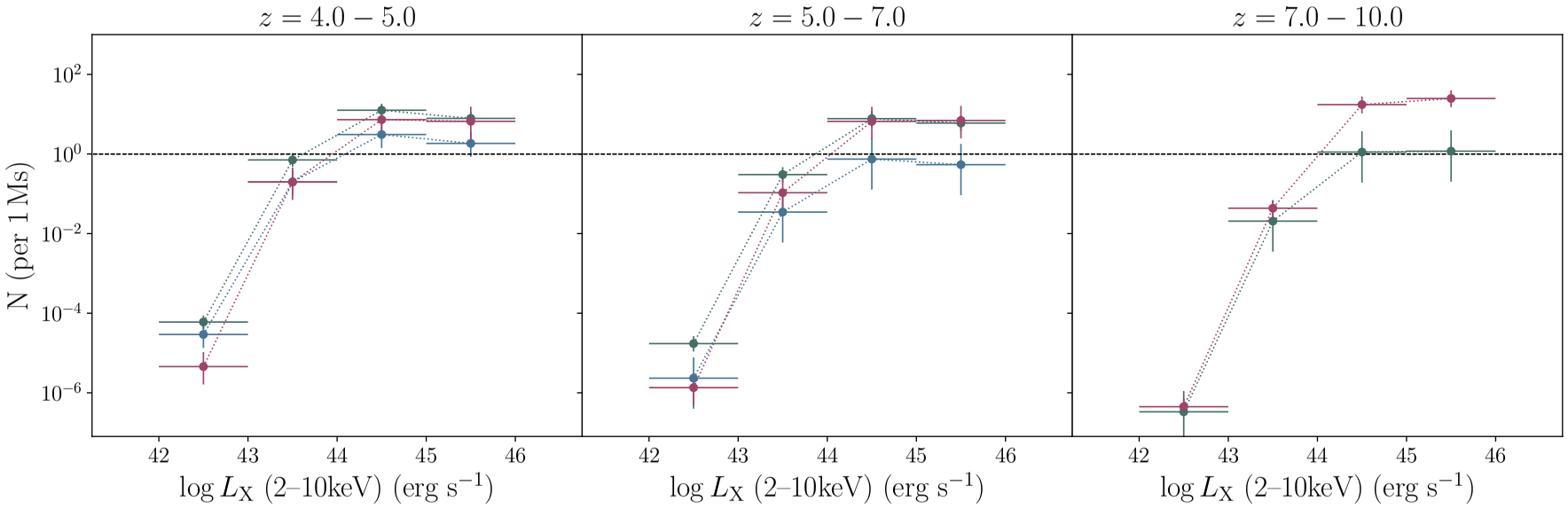

Figure 5.13 *As for figure 5.12, at the hard (2–10 keV) energy band. Although similar to the survey predictions for the soft-band overall there will be far fewer sources detectable due to the lower hard-band sensitivity. It can be seen that above a redshift of $z = 4 - 5$ NewAthena will not be able to detect any unobscured sources with a total hard band survey of 1 Ms. However, at the highest redshifts ($z = 7 - 10$) there is expected to be a similar number if not more Compton thick sources detected than at soft-band energies.*

NewAthena will be able to detect a significant number of sources up to redshifts of $z \sim 7$, even at the hard band energies. As such NewAthena will provide excellent data for the characterisation of absorption within early AGN, complimenting the latest observations from JWST. With soft band observations, NewAthena will also be able to push down to very low luminoisities and out to redshifts of $z \gtrsim 7$, allowing detailed observation of the very early growth of AGN within the Universe. From the pointing efficiencies for a given luminosity and redshift, determined in here, survey strategies for NewAthena can be identified prior to it's launch in the 2030s.

5.4 Implications for NewAthena WFI Surveys

How supermassive black holes, within the early Universe, grew rapidly from seed black holes to the observed masses at $z \sim 6$ remains an open question (see chapter 1). In order to constrain the population of high-redshift X-ray AGN and explore this early growth, deep survey imaging over large sky areas is required, to obtain the X-ray sensitivity needed to detect faint or obscured sources and the area of sky needed given the lower space density of brighter sources. Current X-ray observatories lack the combination of area and depth of imaging required. However, NewAthena's design will allow it to perform deep X-ray imaging over large areas of sky, with it's WFI.

From my estimates of survey yield above (see section 5.3), the optimal exposure time per pointing required to identify sources within different luminosity and redshift ranges can be determined, along with the corresponding source yield (per Ms). Thus, from these survey yields, a suitable survey strategy for constraining the early AGN population can be identified.

At very high redshifts ($z = 7-10$) it is only possible to obtain a viable source yield (i.e. > 1 source per Ms) for higher luminosity, heavily obscured sources. Such yields are obtained with ~100 ks exposures, detecting sources at both hard and soft-band energies. A survey consisting of 100 pointings at an exposure of 100 ks each (totalling 10 Ms) would thus be expected to yield ~ 200 obscured and sources. However, in order to detect a larger number of fainter ($L_{\rm X} = 10^{44-45}\,{\rm erg\,s^{-1}}$) Compton thick sources requires even deeper observations. From my estimated survey yields, 20 pointings with an exposure time of 500 ks is expected to detect ~ 300 Compton thick sources at $z = 7-10$. The combination of 100 ks and 500 ks

exposure pointings, to a total survey time of 20 Ms, would thus yield hundreds of sources within this important redshift range and place crucial constraints on the extent of rapid, heavily obscured, black hole growth within the very early Universe. Such a survey strategy would also provide a viable yield of ~ 120 faint ($L_X = 10^{43-44}\,\mathrm{erg\,s^{-1}}$) AGN at redshifts of $z = 4 - 7$, with which the faint (low growth rate) population of low-obscuration sources could be investigated.

In order to obtain a significant sample of sources within the redshift range of $z = 5 - 7$, around the epoch of cosmic ionisation, requires only relatively shallow individual pointings (~20 ks) which enables a large area of sky to be covered. Performing 500 pointings of 20 ks, for a total survey time of 10 Ms, would yield around 5000 moderate luminosity sources at $z = 5 - 7$, with which strong constraints could be placed on the early XLF. Such a survey yield would allow detailed study of the regime where the majority of growth within the early AGN population is likely occurring.

As such, a survey strategy that would allow for in-depth investigation of the AGN population at early times, probing the moderate luminosity population around cosmic reionisation as well as the faintest sources and heavily obscured $z = 7 - 10$ population, can be devised. Such a survey would be comprised of 20 pointings at an exposure of 500 ks, 80 pointings at an exposure of 100 ks (totalling 100 pointings of at least 100 ks) and 400 pointings at 20 ks exposure (totalling 500 pointings of at least 20 ks). Given the obscuration corrected XLF I found in chapter 4 such a survey would detect 1159 unabsorbed, 2748 absorbed and 1091 Compton thick AGN at $z > 4$ across all luminosities, with the predicted survey yields detailed in table 5.2. These observations would take approximately a year of observing time, finding 4998 total sources by completion of the survey. Although these predicted survey yields seem high given previous studies (e.g. Aird et al., 2015; Georgakakis et al., 2015; Ueda et al., 2014; Gilli et al., 2007), as was shown in chapter 4 the space density of AGN within the early Universe is likely higher than extrapolated model predictions suggest. If NewAthena does not find such extensive populations of AGN at $z > 4$, it would still place strong constraints on the high-redshift XLF.

Comparing the sensitivity probed by a NewAthena survey of such pointings to that achieved by current surveys, as shown in figure 5.14, it can be seen that NewAthena will push the reaches of our current survey capabilities into a new regime. Whilst not reaching the ultimate depth of the 4 Ms *Chandra* Deep Field South (CDF-S) survey (Luo et al., 2017) (given NewAthena's broader PSF

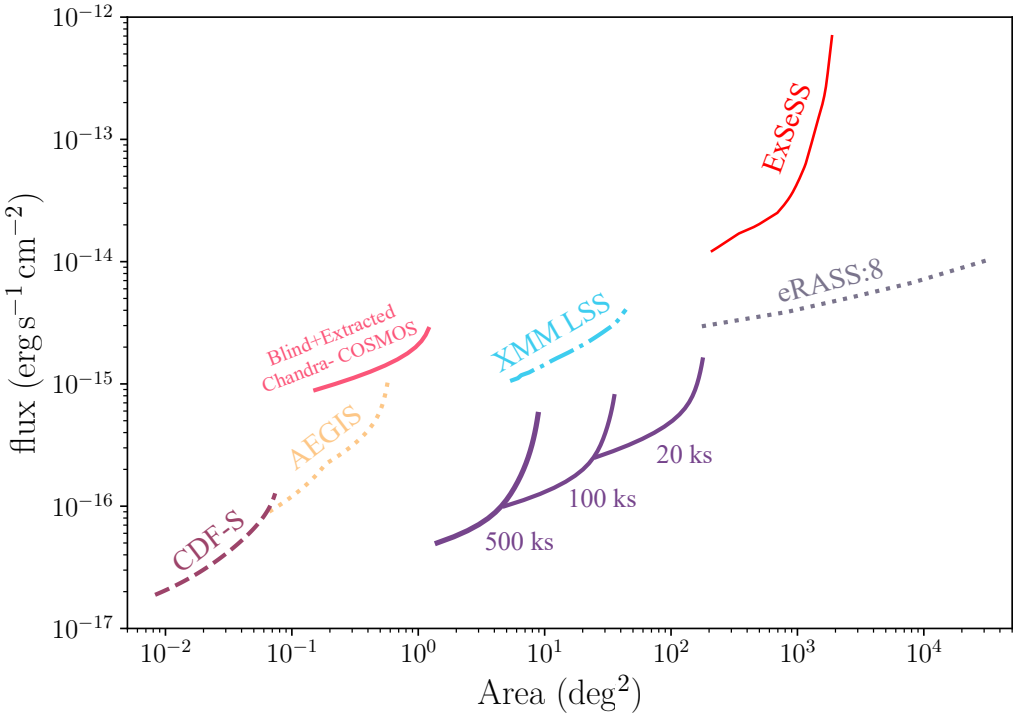

Figure 5.14 *Combined survey sensitivity of a NewAthena survey comprised of* 20×500 *ks,* 80×100 *ks and* 400×20 *ks pointings (purple). Shown for comparison are the sensitivities achieved in the Chandra surveys of CDF-S (dashed plum), AEGIS (dotted gold) and my COSMOS blind+extracted survey (crimson) detailed in chapter 4, as well as the XMMLSS survey performed by XMM-Newton(dot-dashed cyan) and ExSeSS (see chapter 3 and Delaney et al., 2023). The expected eRASS:8 sensitivity is also shown by the lilac dotted line, however it is unknown if this will be completed. It can be seen that NewAthena will probe in a new regime, surveying areas* ~ 3 *orders of magnitude larger than CDF-S or AEGIS, to comparable depths.*

compared to Chandra), it will reach fluxes fainter than the deep *Chandra* surveys of the All-Wavelength Extended Groth Strip International Survey (AEGIS; Davis et al., 2007) and COSMOS regions (given the sensitivity determined in chapter 4). Although my predictions and calibrated sensitivity for NewAthena indicates that surveys such as ExSeSS and eRASS:8 (once completed) will still surpass it in survey area, my suggested survey strategy is for only one year of observing time[12] whilst ExSeSS covers the full survey duration of *Swift*-XRT (from 2005 to 2008; Delaney et al., 2023) and eRASS:8 is planned for 4 years of dedicated survey time[13].

[12] Although the NewAthena mission is planned to last at least 5 years, it will not be a survey-only mission and as such no survey performed with NewAthena can be expected to last for the full mission duration.

[13] It should be noted that eROSITA has, to date, only completed 4 full scans of the sky, and

These results clearly show that NewAthena will expand the horizons of X-ray astronomy, with the WFI and mirror design allowing for an unprecedented area of sky to be imaged to depths that will probe even the early growth of SMBHs within the Universe.

5.5 Conclusions

ESA's new X-ray observatory, NewAthena, is designed to perform deep survey imaging across an unprecedented area of sky. Performing predictions of the surveys possible and the sensitivity of NewAthena is vital to directing the science aims of the mission. In this chapter I present the preliminary survey predictions for NewAthena, using the WFI.

Simulating imaging by NewAthena, using the SIXTE software, I have calibrated analytical models of the sensitivity. Combining the analytical sensitivities and the obscuration corrected XLF from chapter 4, I am able to perform predictions for the number of AGN at $z = 4-10$ that will be detected by NewAthena surveys. My conclusions are as follows:

1. Through calibration to sensitivity measurements from direct simulation of photon detection by the WFI, I have obtained an analytical model of the survey sensitivity which is representative of that possible with NewAthena. This analytical model, adopting a 4×10^{-6} false probability threshold and a prescription for source confusion using $N_{\rm beams} = 20$, will allow for further predictions of NewAthena's survey capabilities.

2. NewAthena is expected to find a significant number of obscured and Compton thick AGN at $z \geq 4$, which has been shown to be the majority of the population at these early times (see chapter 4 and e.g. Gilli et al., 2022). If such populations are not detected, NewAthena would strongly rule out the constraints found in chapter 4.

3. I have performed predictions for the survey yield of sources at redshifts of $z = 4-5$, $5-7$ and $7-10$, with luminosities of $L_{\rm X} = 10^{42}-10^{43}$, $10^{43}-10^{44}$, $10^{44}-10^{45}$ and $10^{45}-10^{46}\,{\rm erg\,s^{-1}}$. From these I find that NewAthena will be able to detect a significant number of sources up to redshifts of $z \sim 7$, even

it remains unclear if eRASS:8 will be completed.

at the hard-band (2-10 keV) energies with which absorption within early AGN can be characterised. NewAthena can be expected to reach redshifts of $z \geq 7$ at both soft (0.7-2 keV) and hard-band energies.

4. I have established a survey strategy, taking approximately 1 year of observing time, that can be expected to find 1159 unabsorbed, 2748 absorbed and 1091 Compton thick AGN at $z = 4-10$ alone. Such a survey by NewAthena would provide X-ray imaging comparable to the depths reached within the deepest *Chandra* surveys, but over $\gtrsim 100$ times the area of sky achieved by *Chandra*. The resulting high-redshift NewAthena survey would be comprised of a total of 4998 sources by completion.

The survey predictions and sensitivity presented here provide vital details for the development of NewAthena and preparation for the science achievable with this large X-ray observatory. Performing additional simulations of NewAthena observations would allow for further careful calibration of the expected sensitivity, reducing noise within the simulated area curve and exploring the possible spectral constraints of NewAthena (required to measure the obscuration of sources). More careful identification of counterparts between the input and output sources could also be performed, and alternative source detection algorithms tested.

Following it's launch in the late 2030s, NewAthena will probe the very early "Hot and Energetic Universe", providing a clearer picture of X-ray AGN growth within the high-redshift Universe than possible with current X-ray observatories.

$L_{\rm X}$ (erg s^{-1})	$z = 4-5$	$z = 5-7$	$z = 7-10$	Total
$10^{42}-10^{43}$	$0+0+0=$ **0**	$0+0+0=$ **0**	$0+0+0=$ **0**	$0+0+0=$ **0**
$10^{43}-10^{44}$	$111+117+0=$ **228**	$25+81+0=$ **106**	$31+8+0=$ **39**	$167+206+0=$ **373**
$10^{44}-10^{45}$	$337+1010+124=$ **1471**	$139+1031+101=$ **1271**	$445+264+197=$ **906**	$921+2305+422=$ **3648**
$10^{45}-10^{46}$	$13+76+93=$ **182**	$7+107+112=$ **226**	$51+54+464=$ **569**	$71+237+669=$ **977**
Total	$461+1203+217=$ **1881**	$171+1219+213=$ **1603**	$527+326+661=$ **1514**	**1159** + **2748** + **1091** = **4998**

Table 5.2 *The total number of unabsorbed ($N_{\rm H} < 10^{23}{\rm cm}^{-2}$; blue), absorbed ($10^{23}{\rm cm}^{-2} \geq N_{\rm H} < 10^{24}{\rm cm}^{-2}$; green) and Compton thick ($N_{\rm H} \geq 10^{24}{\rm cm}^{-2}$; red) AGN expected to be detected by a NewAthena WFI survey comprised of 20×500 ks, 80×100 ks and 400×20 ks pointings. The total source numbers are shown in bold. All yield predictions are for sources found at hard and/or soft-band energies.*

Chapter 6

Overall Conclusions and Future Directions

Supermassive Black Holes (SMBHs) are expected to reside at the centres of galaxies, and can have a crucial role in the build up of the host galaxy's stellar mass (Kormendy & Ho, 2013). How these esoteric objects formed and subsequently grew to the masses observed at $z \sim 6$, within the first few 100 Myr of the Universe, remains an open question. The X-ray Luminosity Function (XLF), which traces AGN population growth, can constrain the extent of this early growth. However, due to the limitations of current X-ray telescopes, the XLF has remained poorly constrained at high redshifts. Constraining the XLF at very high redshifts forms the focus of this Thesis.

Using both the large area survey of ExSeSS and deep X-ray data from the *Chandra* COSMOS Legacy Survey, I have obtained samples of high redshift AGN. Using these samples and the survey sensitivity, I have obtained constraints on the high redshift XLF at both high and moderate-luminosity.

Here I will summarise the results of this thesis, detailing the overall results of the work done using ExSeSS (section 6.1.1) and *Chandra* imaging and COSMOS2020 (section 6.1.2), before discussing the survey predictions for ESA's next X-ray mission, NewAthena (section 6.1.3). I will then detail future directions from the work performed in this thesis in section 6.2, and summarise the key conclusions of this work in section 6.3

6.1 Thesis Conclusions

6.1.1 Conclusions from Chapter 3

Previous studies, such as those of Brusa et al. (2009); Vito et al. (2014); Georgakakis et al. (2015), have shown the space density of AGN to decline with increasing redshift. At the high-luminosity end of the XLF the space density is also found to be lower than for more moderate luminosities. Thus, in order to find the rare high-redshift high-luminosity AGN and subsequently constrain the bright end of the XLF, large areas of sky must be surveyed. In chapter 3 I used the new Extragalactic Serendipitous Swift Survey (ExSeSS; Delaney et al., 2023) of X-ray AGN, which covers 2086.6 degrees^2 of sky, in order to place constraints on the bright end of the XLF. This is possible thanks to the serendipitous nature of ExSeSS and its well defined sensitivity.

Within ExSeSS I identified a sample of $z > 6$ AGN, consisting of a single serendipitous X-ray source that was previously identified in high redshift QSO searches, at $z = 6.31 \pm 0.03$. This source is optically bright, however, given the optical-to-X-ray slope determined for this source, it is typical of the expected AGN population at this redshift. Assuming no other very high-redshift sources exist within the ExSeSS sample, I placed constraints on the XLF at $z = 5.7-6.4$ as given by one source at $L_{\rm X} = 10^{44.8-45.8}\,{\rm erg\,s^{-1}}$ and no sources ($N_{obs} = 0$) detected at a higher luminosity (i.e. $L_{\rm X} = 10^{45.8-46.8}\,{\rm erg\,s^{-1}}$). This is detailed in full in chapter 3.

My resulting bright end constraints are consistent with the expected exponential decline in the space density of luminous AGN with increasing redshift, and the relatively steep bright end slope of extrapolations of parametric models of the XLF fit to data at lower redshifts. However they rule out the most extreme declines in the XLF at high luminosities, as is seen in extrapolations of the LADE model from Georgakakis et al. (2015). It is important to note that these constraints are formally **lower limits** as there may be additional sources within the redshift and luminosity ranges used in chapter 3, such as a heavily obscured population, which remains unidentified.

Converting the XLF constraint to bolometric luminosities, I also find that my ExSeSS high-redshift constraint on the AGN population agrees with the bright-end of the bolometric QLF model from Shen et al. (2020). I thus conclude

that current parametric models of the AGN population accurately describe a rapid decline in the space density of the most luminous AGN, towards very high redshifts, suggesting these observations are reaching the epoch of assembly for the most massive black holes.

6.1.2 Conclusions from Chapter 4

The majority of black hole growth occurs within the moderate-luminosity AGN population. At high redshifts, however, observations of these moderate luminosity AGN is limited by the sensitivity of current X-ray telescopes. In chapter 4 I obtained a sample of $z = 4 - 10$ AGN within the *Chandra* COSMOS Legacy survey through blind source detection and direct extraction of X-ray counts at the positions of COSMOS2020 sources. Using my samples of blind and extracted sources, with COSMOS2020 photometric redshifts, I calculated the high redshift XLF at $z = 4{-}5$, $z = 5{-}7$ and $z = 7{-}10$. I then determine the effect of obscuration on the measured XLF.

From my measurements of the high-redshift XLF at moderate luminosities I found the space density of AGN within the early Universe to be higher than predicted by the extrapolations of model predictions. Although consistent with the parametric models fit to data at $z = 4 - 5$, towards higher redshifts ($z > 5$) I find the space density does not show the rapid decline expected within these models out to $z = 7 - 10$. When considering the effect of errors in the photometric redshifts, I found a more conservative uncertainty on my XLF measurements which remains consistent with the model predictions from $z = 4 - 7$. However, the upper limits on my XLF measurements allow for a much higher space density and thus a much more extensive population of high-redshift AGN.

With the hard-band XLF measurements indicating a higher space density than the full-band measurements, I investigated the effect of obscuration on my XLF. Dividing the blind+extracted sample into unabsorbed, absorbed and Compton thick sources, defined as $N_H < 10^{23}$, $10^{23}cm^{-2} \leq N_H \leq 10^{24}cm^{-2}$ and $N_H > 10^{24}cm^{-2}$ respectively (based on their observed hardness ratios), I find a significant fraction of my sample is heavily obscured (i.e. absorbed or Compton Thick). The fraction of obscured sources can also be seen to increase with redshift. Correcting for the effect of this obscuration on the full-band XLF, I obtain even higher measurements of the space-density.

My final moderate luminosity XLF measurements clearly suggest the space density of actively accreting SMBHs within the early Universe could be far higher than previously thought, although the lower limits remain within 1σ of the extrapolated models. A high fraction of this population was also found to be heavily obscured, thus even with deep X-ray observations it will be difficult to identify them. Such an actively accreting population would likely have a significant effect on the growth of the first galaxies. This space density also points towards a reconciliation between JWST and X-ray observations, with recent JWST measurements of the AGN space density by Greene et al. (2023) and Maiolino et al. (2023) also indicating a larger population at faint luminosities than previously expected. Both my X-ray measurements and the recent JWST observations indicate the majority of the high redshift AGN population is likely very heavily obscured.

6.1.3 Conclusions from Chapter 5

Designed to be able to perform both deep and large area surveys, ESA's new X-ray Observatory, NewAthena, will survey an unprecedented area of sky to deep X-ray limits. Through SIXTE simulations of the imaging that will be possible with the NewAthena Wide Field Imager (WFI), I have calibrated analytical sensitivities. Combining the analytical sensitivity with an obscuration model, from chapter 4, I have predicted the number of $z = 4-10$ AGN that will be detected by NewAthena and designed a potential survey strategy.

An analytic prescription for the sensitivity of NewAthena can be used to rapidly estimate the sensitivity for a range of exposures. However, in order to fully represent the observation and detection process, a fully realistic simulation of a WFI observation and source detection procedure as provided by SIXTE, is required to calibrate the analytic model. Calibrating the model of the NewAthena WFI sensitivity I found the analytic model accurately characterises the performance of the WAVDETECT source detection algorithm, on shallow (5 ks) SIXTE simulations, with a false probability threshold of 4×10^{-6}. I then determined a suitable prescription for source confusion, which ultimately limits the sensitivity of deeper observations given the PSF of NewAthena, that applies a probabilistic approach to represent the reduced source detection capabilities due to source confusion. I have shown this probabilistic prescrition is able to characterise the limitations of source detection in deeper (150 ks) simulated

NewAthena fields. The resulting analytical model of the NewAthena WFI will allow for further predictions of its survey capabilities.

From my analytic model of the sensitivity and the resulting XLF measurements of chapter 4, I find that NewAthena can be expected to detect a significant number of high-redshift AGN (from $z = 4 - 10$), with the hard band detections likely to yield more detections of heavily obscured sources at $z = 7 - 10$ than the soft band. Devising a survey strategy to probe the high redshift obscured sources as well as constrain the moderate luminosity XLF, NewAthena can be an be expected to find 1159 unabsorbed, 2748 heavily absorbed and 1091 Compton thick AGN at $z = 4 - 10$.

Comparing to existing deep and large area X-ray surveys, NewAthena can be seen to provide X-ray imaging to an comparable depth to all but the deepest *Chandra* surveys, to ≥ 100 times the sky area.

6.2 Future Prospects

6.2.1 High Luminosity XLF Constraints from Large Area Surveys

As there may be additional $z > 6$ sources within ExSeSS for which redshifts had not been identified, the constraint I obtained in chapter 3 places a lower limit on the possible high-luminosity space density. The results of chapter 4 clearly indicate a very large fraction of the AGN population at high-redshift is heavily obscured, and thus would not have been identified in the prior QSO searches used to obtain the $z \sim 6$ sample of ExSeSS sources. However, as heavily obscured sources are more easily detected at hard-band energies (2-10 keV), where ExSeSS is especially powerful (accessing a unique parameter space, see Delaney et al., 2023), there are likely additional high-redshift sources within ExSeSS for which there was no redshift data.

Since I obtained constraints on the bright end of the XLF, Delaney et al. (in prep) has performed a more detailed search for photometric counterparts to sources within ExSeSS, using NWay cross-matching to optical-to-mid-IR survey data from the Legacy Survey as well as WISE. The corresponding ExSeSS source photometry enables the calculation of photometric redshifts and thus an

additional small number of $z \gtrsim 6$ candidates may be identified leading to an upwards revision of the XLF estimates presented in chapter 3. However, careful consideration of the accuracy and reliability of the photometric measurements would be required, ideally with spectroscopic follow up performed in order to confirm their redshifts. It should also be noted that spectroscopic follow-up of a sample of ExSeSS sources, which will provide further information on the nature of these sources and confirm their redshifts, is now underway within SDSS-V.

The results of my ExSeSS constraints suggest a significant number of high luminosity AGN, at high-redshift, will be observable with sufficiently large surveys. Crucially, the eROSITA all-sky survey can thus be expected to find a few 10s to a few 100 of these sources. As such, following a similar process to that used in chapter 3, the observations obtained by eROSITA in its all-sky survey mission could be used to obtain further constraints on the bright end of the XLF and enable further investigation of the population growth within the early Universe. However, the limited hard-band sensitivity of eROSITA will likely restrict the samples of high-redshift AGN it will find, as the large obscured population of high-redshift AGN can be expected to appear brighter at hard-band energies than soft-band energies, thus ExSeSS will remain the ideal large sky survey for finding the bright, heavily obscured early AGN population.

In addition to the use of larger sky surveys to constrain the bright end of the XLF, serendipitously detected samples of AGN from deeper imaging are required in order to constrain the fainter end of the XLF. This formed the basis for my work with *Chandra* imaging of the COSMOS field in chapter 4, and for which I now discuss the prospects of.

6.2.2 Moderate Luminosity XLF constraints from Deep Survey Data

Chandra imaging of the COSMOS field is by no means the deepest of image data obtained with this telescope. Following the same process as carried out on the COSMOS field in chapter 4, further measurements of the XLF at high redshifts could be obtained using deeper *Chandra* surveys such as the *Chandra* Deep Fields (7 Ms in CDF-S and 2 Ms in CDF-N; Luo et al., 2017; Xue, 2017, respectively) and AEGIS-X Deep (800 ks; Nandra et al., 2015). The addition of new near-IR imaging of these fields by JWST, CEERs covering the AEGIS field (Finkelstein

et al., 2017) and JADES in CDF-S (Eisenstein et al., 2023), will enable accurate photometric redshift measurements with which to find the high-redshift sources. Such measurements may begin to probe to even fainter luminosities, and into the regime of low luminosity AGN being discovered independently by JWST. However, as these fields cover smaller sky areas than the COSMOS field such deeper samples are likely to only contain a small number of sources.

In order to begin to properly reconcile AGN identified by JWST (through e.g. evidence of spectroscopic broad-lines) with the observations performed at X-ray wavelengths, X-ray information for these sources could be extracted. This could be done by following a similar process to that performed in chapter 4; first cross-matching JWST sources to known X-ray AGN and then for all high-redshift JWST galaxies within the sky area of deep X-ray imaging, extracting X-ray counts at these source positions directly from the X-ray images. Such studies would thus push the limit of the available X-ray data in order to find otherwise unidentifiable AGN.

Using IR tracers of obscuration within AGN, the level of obscuration of my blind+extracted sample could also be tested. For a small region at the centre of the COSMOS field, JWST imaging has been performed. Identifying the blind+extracted sources that fall within the area of COSMOS-Webb, the nature of these sources could be further investigated. This would allow for comparisons between the IR morphology of my X-ray selected sources and the morphologies identified in JWST AGN, and thus potential links could be found between these X-ray detected heavily obscured sources and the little red dots that have been found by JWST. Obtaining JWST spectra of my high-redshift sample could further provide details of the nature of these early AGN and their growth.

6.2.3 Future Preparations for NewAthena Surveys

Prior to its launch the predicted survey sensitivity of NewAthena WFI could be further improved, in preparation for high-redshift survey data that will allow further constraints to be placed on the population and early growth of AGN.

In order to improve the calibration of the analytical sensitivity model, performing multiple SIXTE simulations of imaging at a given exposure could improve the calibration of the analytical model. In addition, using the obscuration corrected XLF obtained in chapter 4 to simulate the input AGN sources at high redshifts

directly would provide further insight into the success of the source detection performed on NewAthena WFI imaging at recovering sources at $z > 4$.

The detection algorithm used in chapter 5 is relatively simple, and known to struggle with noise around the edges of images. Testing alternative source detection algorithms, an optimum detection method for NewAthena surveys could be devised, improving the detections, positions, and fluxes of faint sources, particulalrly when pushing into the regime of high source confusion. Finally, by testing alternative energy ranges for the detection, of sources within NewAthena imaging, an optimum detection band to use when searching for high-redshift AGN (which my work has shown are likely heavily obscured) could be identified, prior to launch.

6.3 Overall Conclusions

Utilising existing X-ray survey data, I have placed new constraints on the XLF at high redshifts. From these measurements I have found the space density of AGN at $z = 4 - 10$ to be higher than previously predicted by parametric model extrapolations. This larger population of AGN is also likely heavily obscured, as is consistent with studies such as Gilli et al. (2022), indicating there is likely a high gas content within early galaxies which may be fuelling both star formation and the growth of SMBHs.

With the need for ever larger area and deeper X-ray surveys in order to probe the very early SMBH growth, I look to the future of X-ray observatories with NewAthena. ESA's next flagship X-ray mission, NewAthena will open the door to a new regime of X-ray astronomy within the early Universe.

Appendix A

Derived Luminosity Calculations

Assuming the flux of the AGN follows a power law relation of $f_\nu \propto \nu^{\alpha_\nu}$ (see e.g. Pons et al., 2020; Bañados et al., 2016; Selsing et al., 2016), with $\alpha_\nu = -0.3$, the flux in the z-band can be converted to a different wavelength flux using

$$\frac{f_\nu}{f_{\mathrm{z-band}}} = \left(\frac{\nu_{\mathrm{obs}}}{\nu_{\mathrm{z-band}}}\right)^{\alpha_\nu} = \left(\frac{\lambda_{\mathrm{z-band}}}{\lambda_{\mathrm{rest}}(1+z)}\right)^{\alpha_\nu} \tag{A.1}$$

where f_ν is the monochromatic flux at a rest frame frequency ν and $f_{\mathrm{z-band}}$ is the flux in the z-band (in units of $\mathrm{erg\,s^{-1}\,cm^{-2}\,Hz^{-1}}$), given by the observed z-band apparent magnitude. The ratio of these fluxes is given by the frequency of the z-band, $\nu_{\mathrm{z-band}}$, and the observed frequency at which to determine the monochromatic flux, ν_{obs}, or by the wavelength of the z-band, $\lambda_{\mathrm{z-band}}$, and the rest frame wavelength at which to determine the monochromatic flux, λ_{rest}. For ATLAS the z-band central wavelength, used in this calculation, is 8780.0 Å.

From the monochromatic flux, found using equation A.1, the monochromatic luminosity (in units of $\mathrm{erg\,s^{-1}\,cm^{-2}\,\mathring{A}^{-1}}$) is given by the equation

$$L_{\lambda_{\mathrm{rest}}} = \frac{c}{\lambda_{\mathrm{rest}}^2}\frac{4\pi D_L^2}{(1+z)}\left(\frac{\lambda_{\mathrm{z-band}}}{\lambda_{\mathrm{rest}}\,(1+z)}\right)^{\alpha_\nu} f_{\mathrm{z-band}} \tag{A.2}$$

where the monochromatic luminosity, $L_{\lambda_{\mathrm{rest}}}$, at a rest frame wavelength of λ_{rest}

is related to the monochromatic flux observed in the z-band, $f_{\mathrm{z-band}}$, by the luminosity distance D_L, the rest-frame wavelength, the central wavelength of the z-band $\lambda_{\mathrm{z-band}}$ and the power α_ν. z is the redshift of the source and c is the speed of light.

The monochromatic luminosity at an energy of 2 keV, $L_{2\,\mathrm{keV}}$, is given by the equation

$$L_E = N(E)E = \frac{(2-\Gamma)L_{2-10\ \mathrm{keV}}}{(10.0\ \mathrm{keV}^{\ 2-\Gamma} - 2.0\ \mathrm{keV}^{\ 2-\Gamma})} E^{1-\Gamma} \tag{A.3}$$

where the X-ray spectrum is assumed to be given by a power-law $N(E) \propto E^{-\Gamma}$, with a photon index of $\Gamma = 1.9$, and the measured hard-band luminosity is given by the total (0.3-10 keV) band flux. The resulting monochromatic luminosity can then be converted from units of $\mathrm{erg\,s^{-1}\,keV^{-1}}$ to $\mathrm{erg\,s^{-1}\,Hz^{-1}}$ by multiplying the luminosity by a factor of h. For the calculation of α_{OX}, I calculate this monochromatic luminosity at an energy $E = 2$ keV

Appendix B

COSMOS2020 LePhare Redshift Fits of the $z \geq 4$ Blind+Extracted Sources

In this appendix I provide plots of the redshift photometric fits of my sample of 39 blind+extracted $z \geq 4$ sources as performed by Weaver et al. (2022) using LePhare with both galaxy only (red) and AGN (blue) Spectral Energy Density (SED) models (see figure B.1). The galaxy templates used by Weaver et al. (2022) are those of Polletta et al. (2007) Ilbert et al. (2009), Bruzual & Charlot (2003) and Onodera et al. (2012), and the AGN templates consist of a galaxy SED with a QSO component of varying dominance over the galaxy SED (see Salvato et al., 2009, for a detailed explanation of the creation of the AGN templates). For each source the probability distribution of the redshift with the galaxy template fits is shown in the inset plot with the redshift of the AGN fit shown by the blue line for comparison and the $z < 4$ region shaded. UltraVISTA Ks-band imaging for all of these sources is also shown, with the location of the source as given by the FARMER catalogue indicated by the orange cross, for which all sources can be seen to have a Ks-band detection as is required of my sample.

The shape of the SEDs of all my blind+extracted $z \geq 4$ X-ray sources are suitably reproduced by the LePhare fits performed by Weaver et al. (2022). For those sources which are within close proximity to a brighter object within the Ks-band image shown, the measured photometry at the blue end of the SEDs may be contaminated in certain filters resulting in the scatter of photometry in those

sources. It can be seen that, by eye, there are cases where the galaxy only model provides a better fit to the measured photometry, the majority of which have the galaxy redshift (z_{GAL}) around $z \sim 4$. For a number of my sources the measured photometry rises at IR wavelengths, as does the AGN sed model, above that predicted by the galaxy only models. This trend is indicative of high-redshift AGN appearing as red sources with rising power-law slope, as is being seen by JWST (e.g. see Matthee et al., 2024; Maiolino et al., 2024; Yue et al., 2024; Brooks et al., 2024).

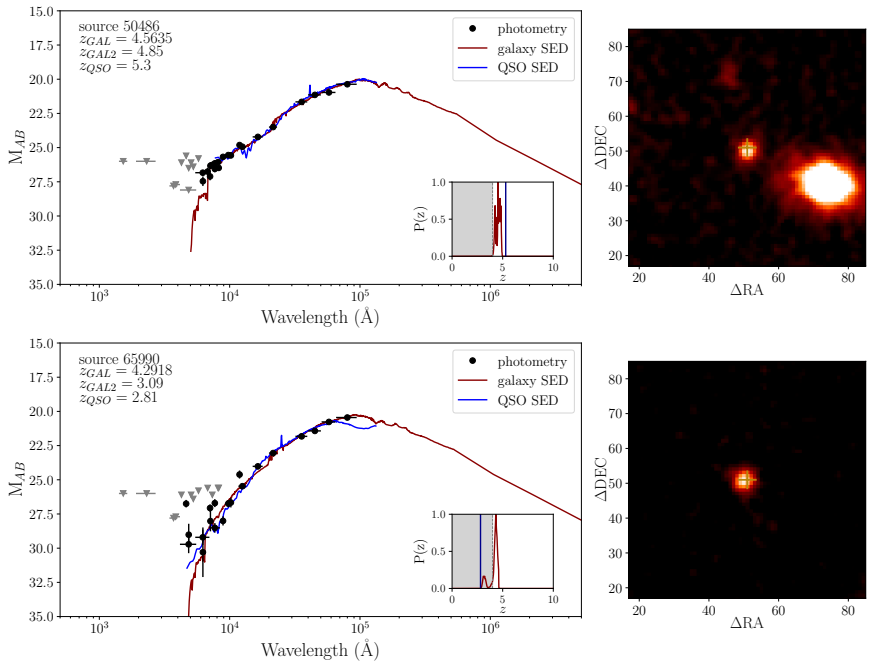

Figure B.1 *The LePhare photometric redshifts fits of all 39 potentially $z \geq 4$ sources in my blind+extracted sample, as given by galaxy templates (red) and AGN templates (blue). The photometric measurements of each source are shown by the black points, with the measurement in filters for which there are none detections plotted as an upper limit given by the filter depth (grey triangles). The spectral shape measured by the photometry of each source is reproduced by the fitted models. Some sources showing a slight rise in brightness at IR wavelengths above that predicted by the galaxy models, indicative of high redshift AGN being red sources with rising power-law slope (as has been found with JWST; Matthee et al., 2024; Maiolino et al., 2024) The probability distribution of possible redshifts based on the galaxy template fits is shown in the inset plot, with the best AGN redshift fit indicated by the blue line, and the region outside the redshift range of my blind+extracted sample shaded. The Ks-band UltraVISTA imaging of each source is shown, with the COSMOS2020 position indicated by the gold cross and a detection clearly seen in all sources which have been fit by both a galaxy and AGN template.*

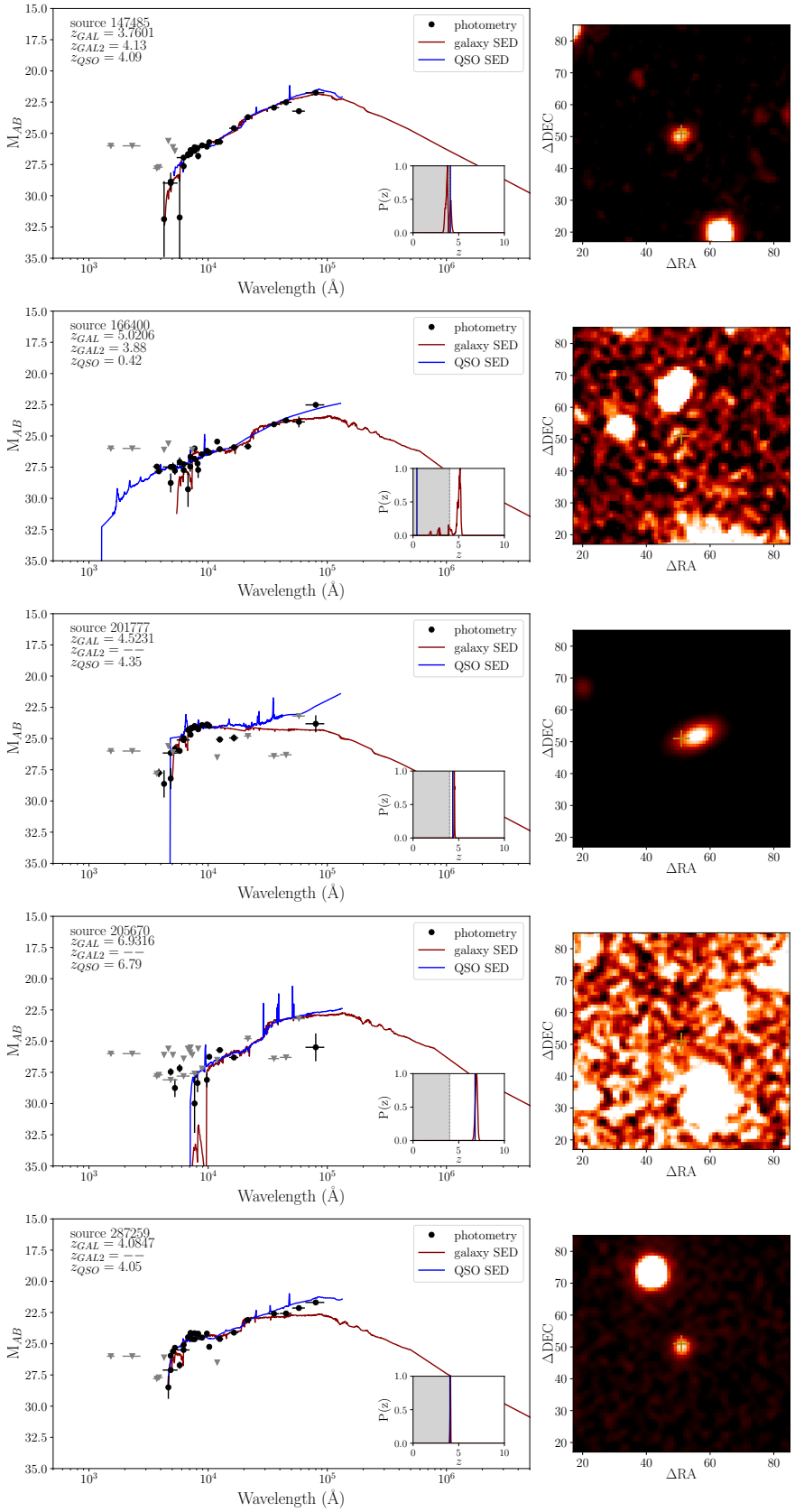

Figure B.1 *continued.*

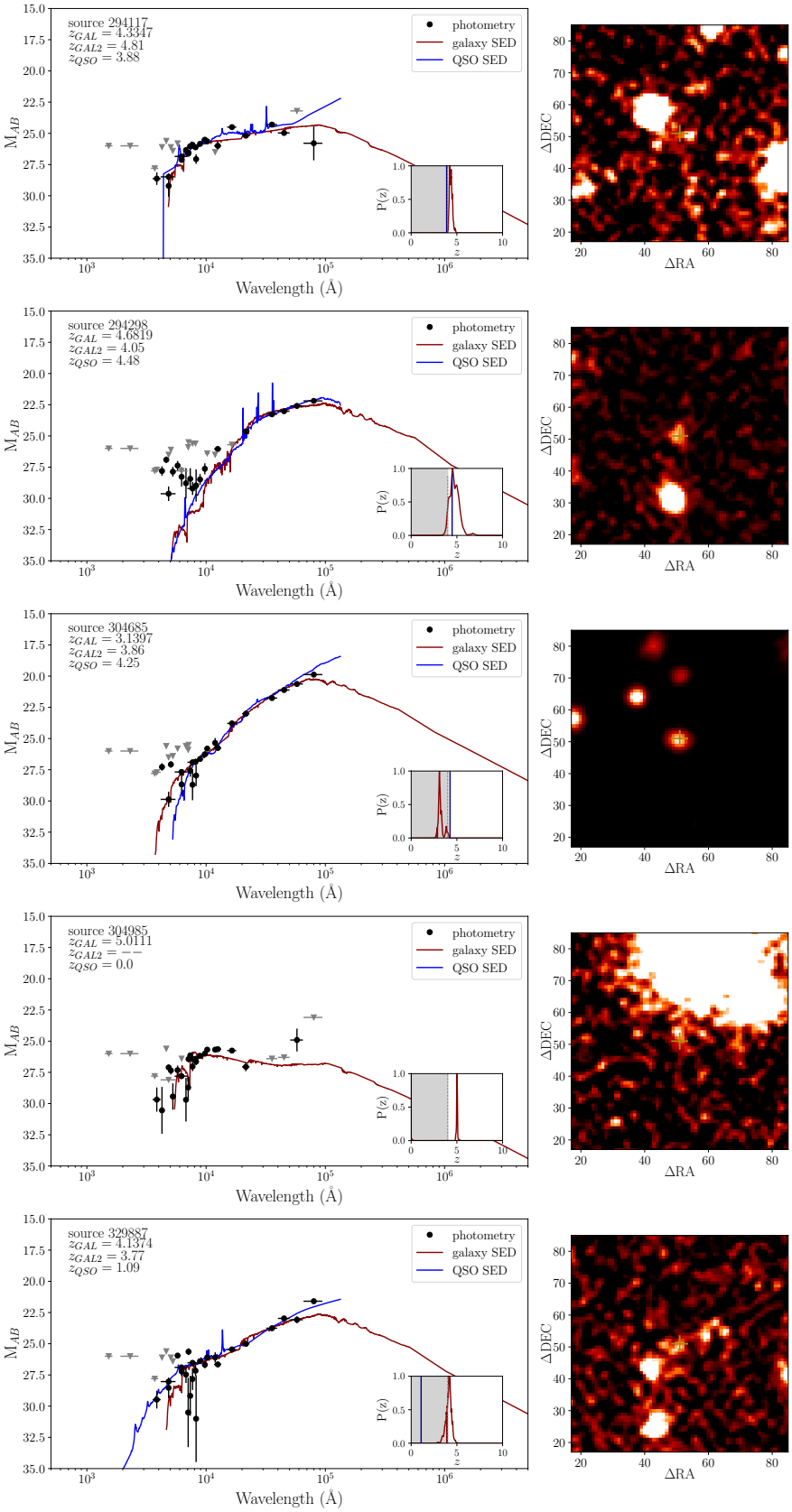

Figure B.1 *continued.*

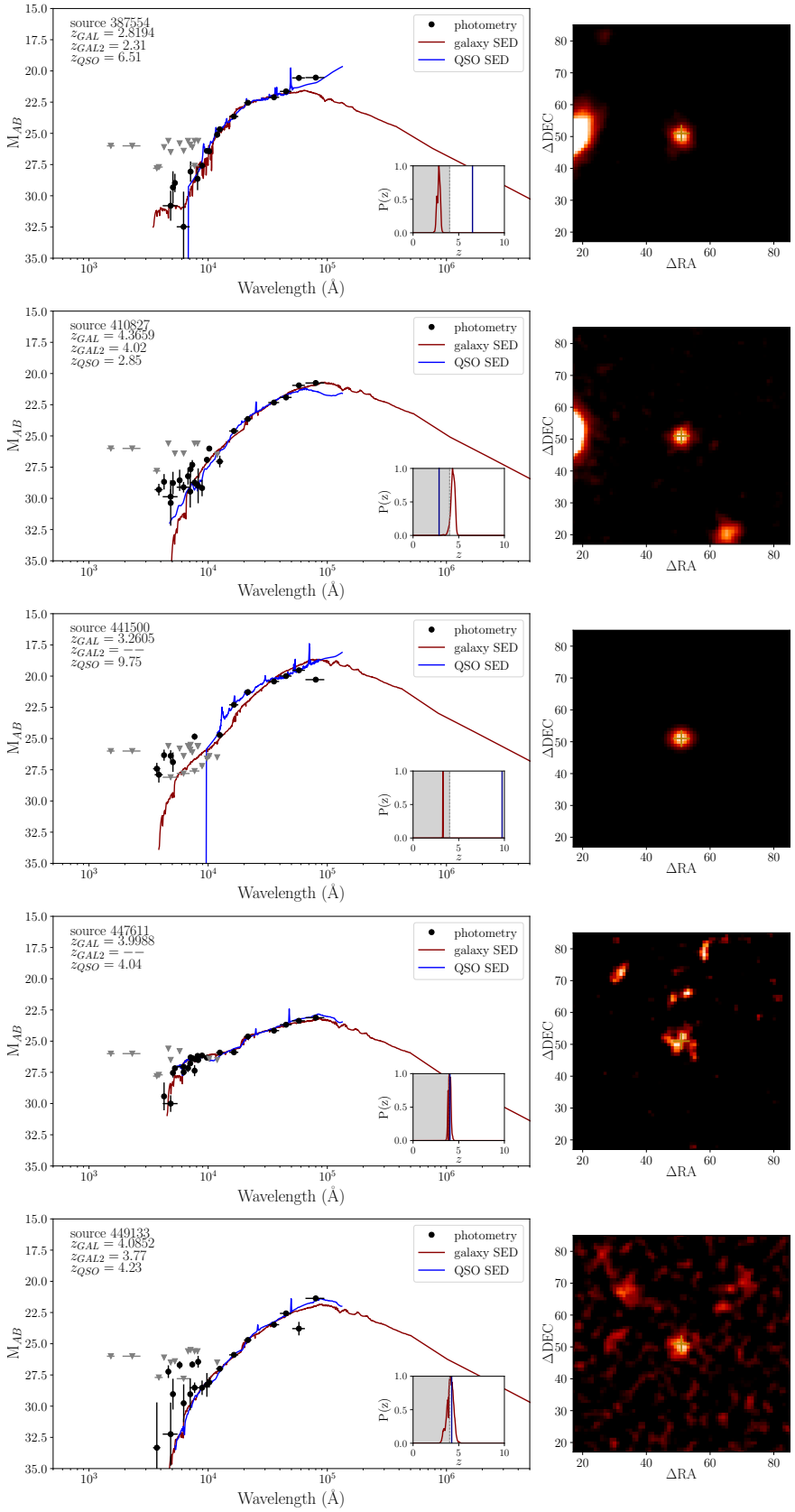

Figure B.1 *continued.*

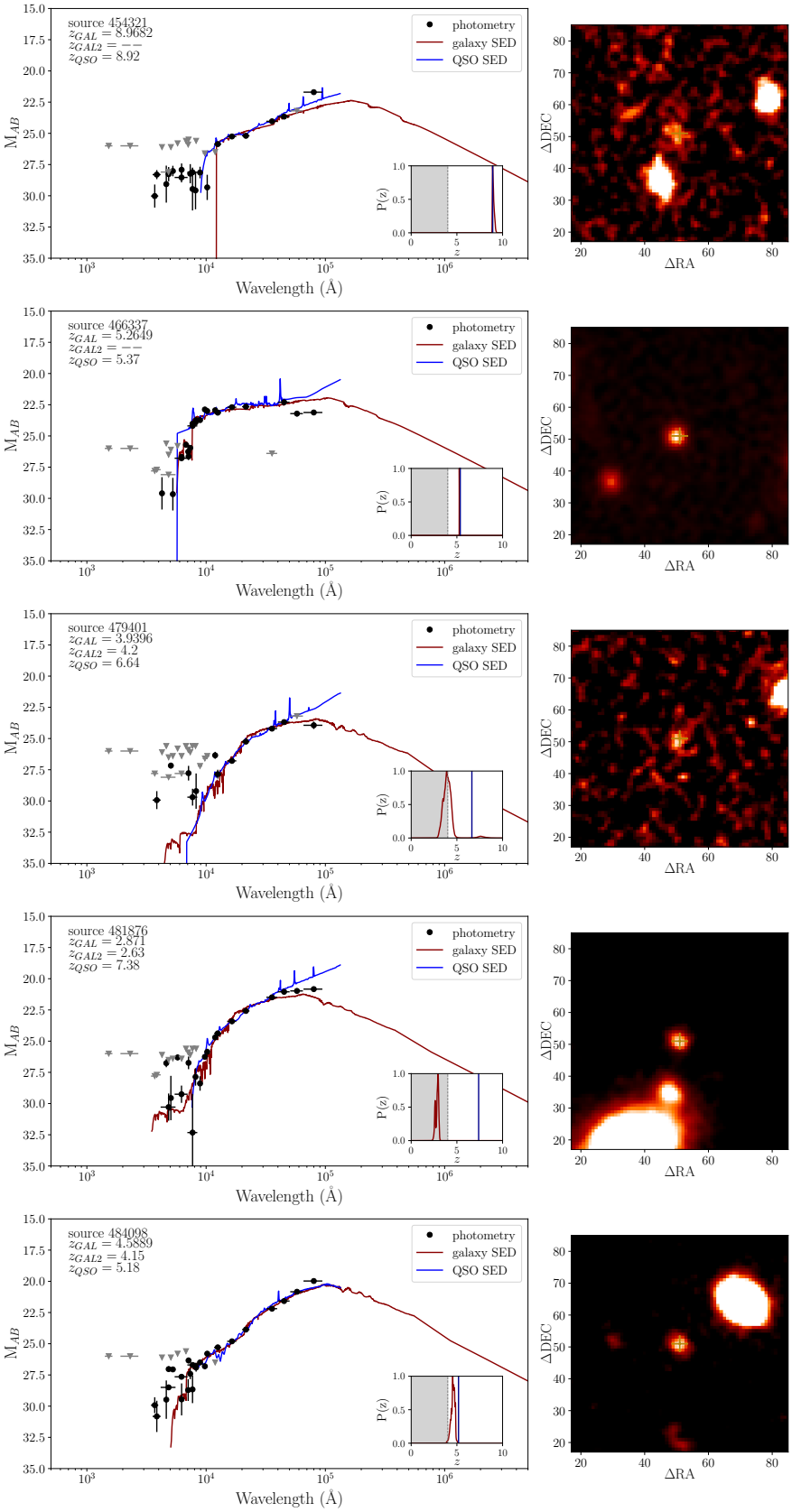

Figure B.1 *continued.*

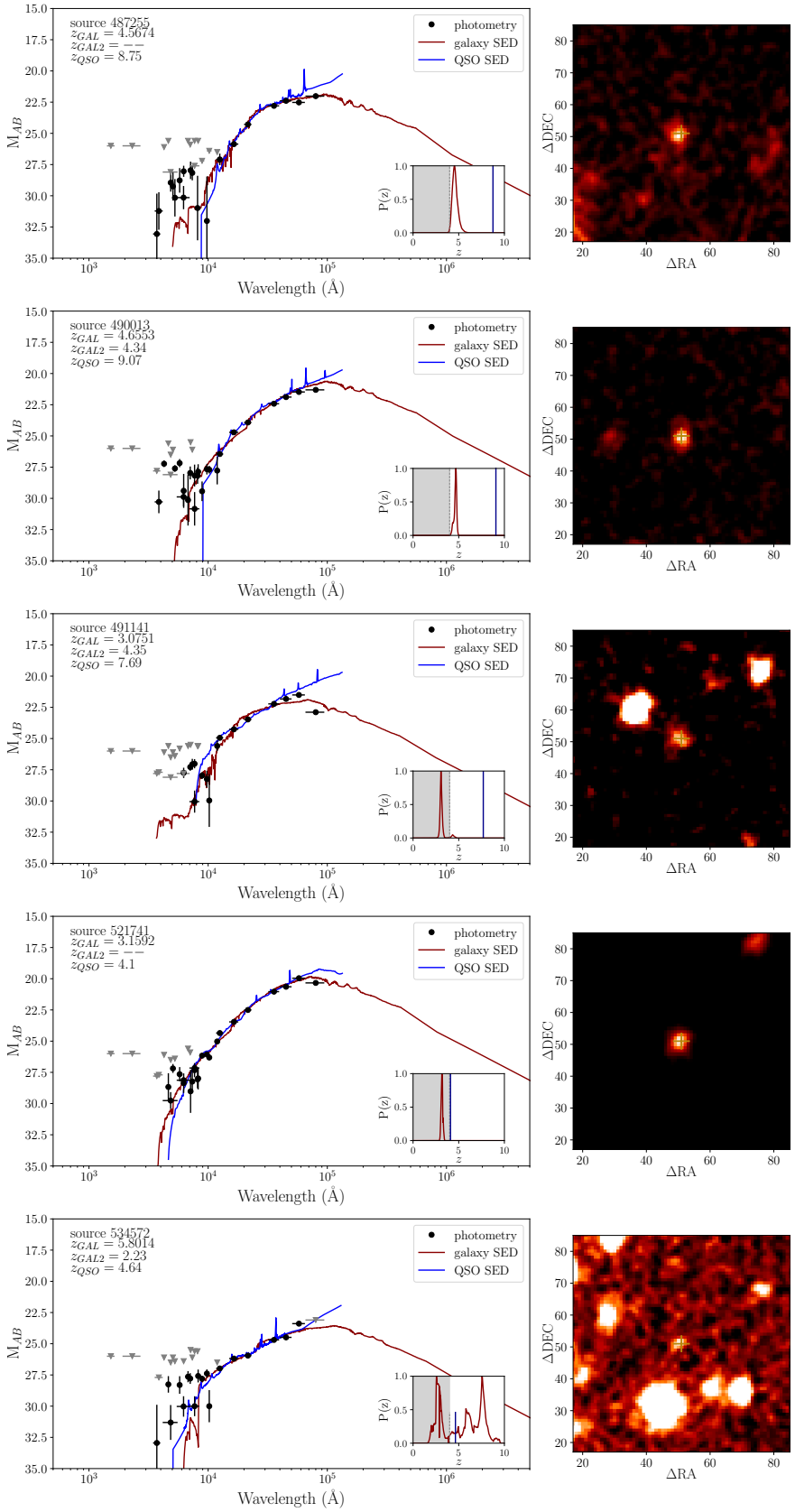

Figure B.1 *continued.*

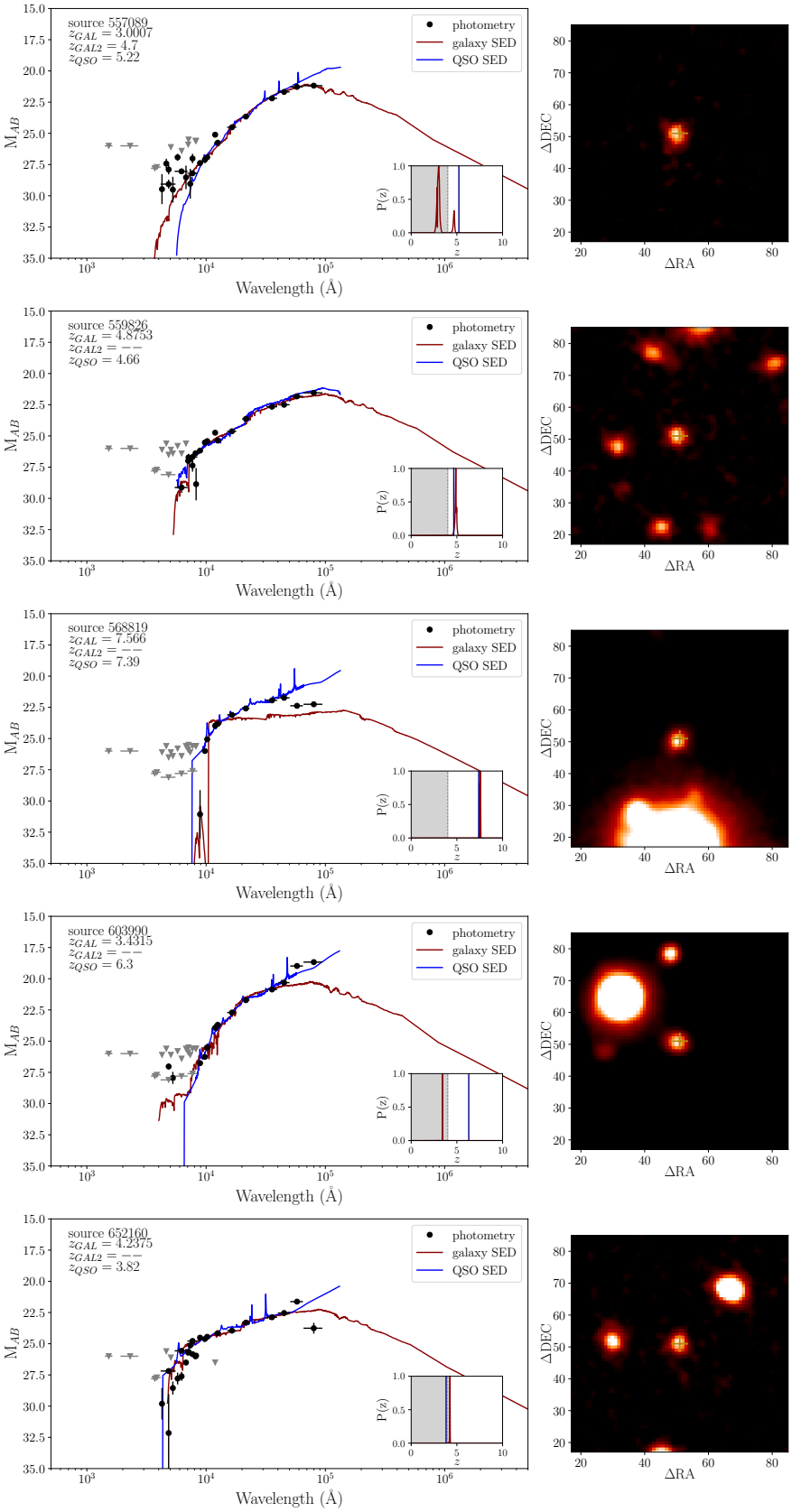

Figure B.1 *continued.*

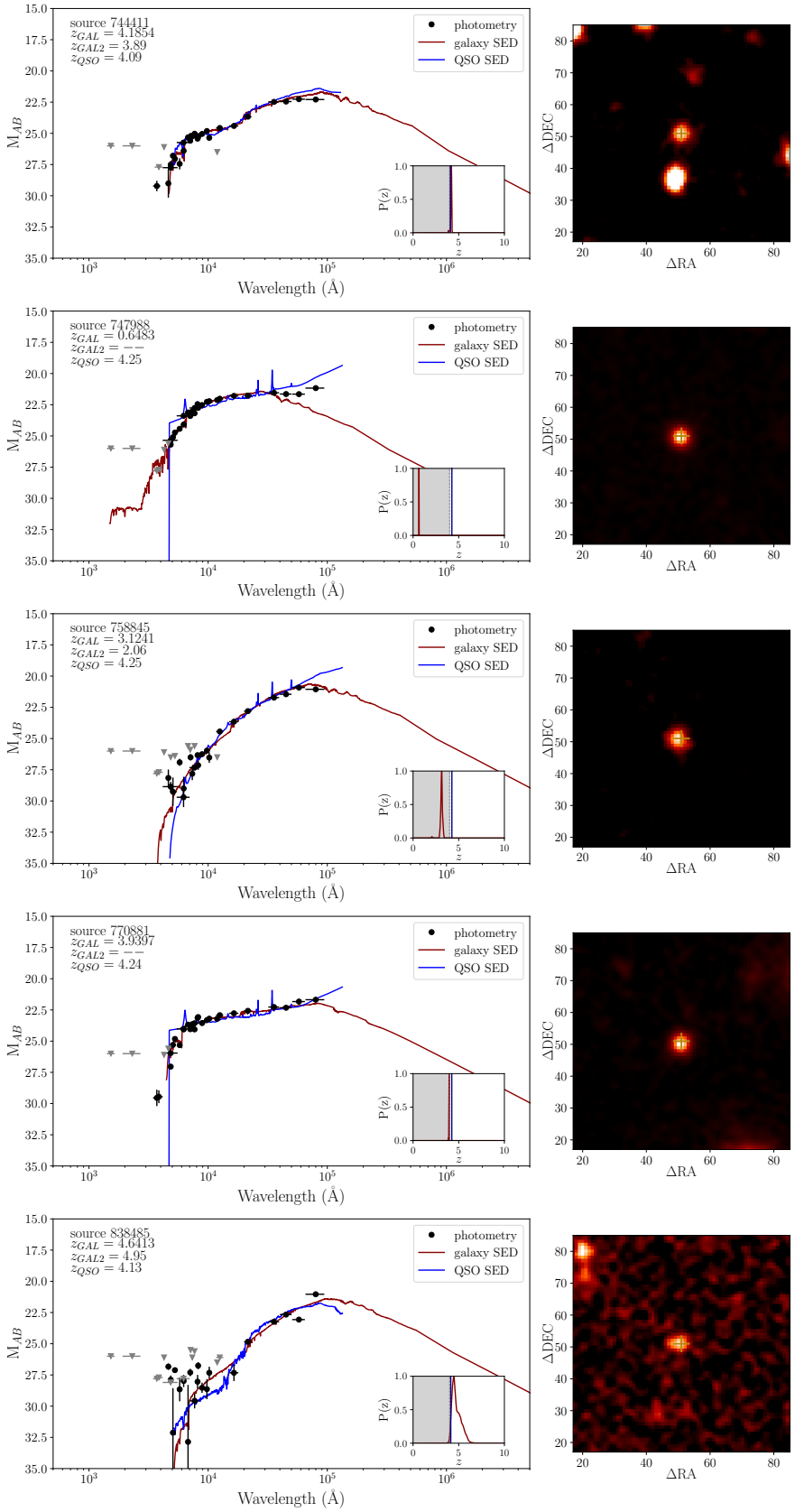

Figure B.1 *continued.*

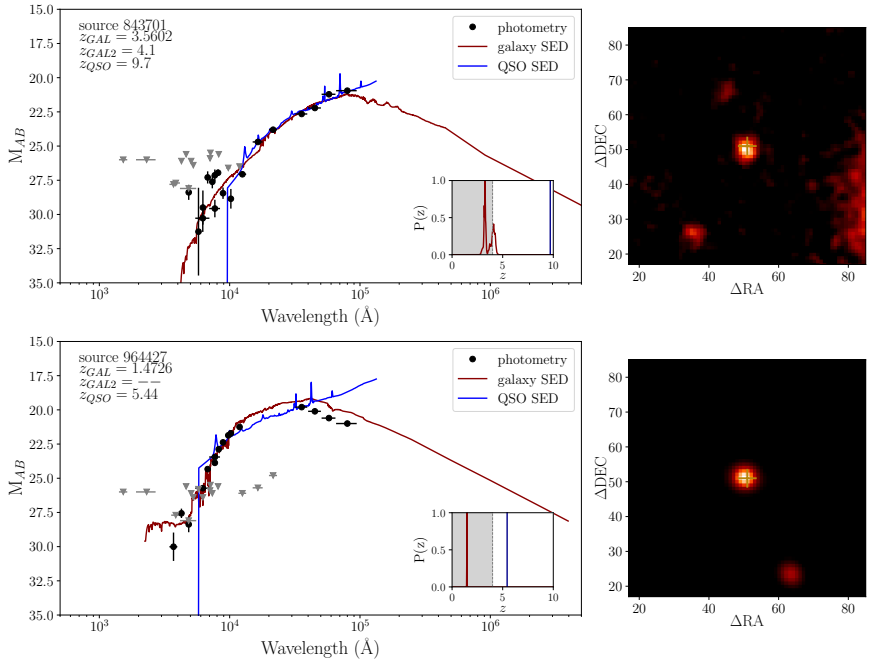

Figure B.1 *continued.*

Appendix C

Degradation of Chandra Response

The response of the Advanced CCD Imaging Spectrometer (ACIS) on the Chandra X-ray Observatory (see chapter 2) has evolved over the course of Chandra's ~25 years of operating; the effective area of the telescope decreasing most notably at softer energies (Grant et al., 2024). This loss of sensitivity is a consequence of a number of factors impacting the 10 CCDs (of which 8 are front lit and 2 are back lit) that comprise the ACIS and is most prominent around 1 keV before becoming negligible around 2 keV (see figure C.1). The causes of this degradation in sensitivity are detailed in O'Dell et al. (2007, 2005, 2003), and are summarised as follows:

Over time the insulation protecting the CCDs from the background heat of the telescope has slowly degraded, and as such it has become more difficult to maintain the spacecraft at a low temperature resulting in an increase in the background noise due to the telescope itself. Continued exposure to both high and low energy photons as Chandra operates gradually impacts the charge transfer inefficiency in the CCDs (Grant et al., 2006), causing it to increase. Most notably the front illuminated CCDs are preferentially impacted by low energy (soft) photons, to which they are strongly sensitive to the damaging effects of (Grant et al., 2024; O'Dell et al., 2000; Cameron et al., 2002). Finally, molecular contaminants have accumulated on the optical blocking filter, resulting in an excess of low energy photons being absorbed and thus a decrease in the number of soft X-ray counts that will be measured by Chandra from the same source over different periods of time (see the recent summary of Grant et al., 2024). The result of this ageing of Chandra is an increasing loss of effective area at soft

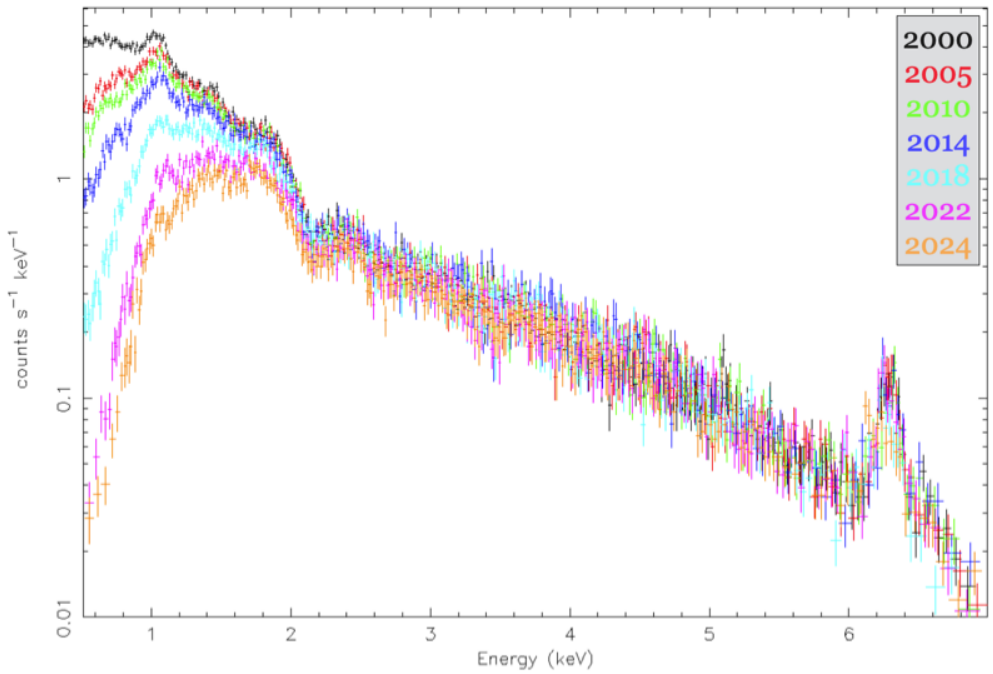

Figure C.1 *The spectrum of Abell 1795 as taken by the ACIS at seven different epochs during it's operating time to date (from 2000 to 2024), demonstrating the loss of soft band energy counts as a result of the degradation of the CCDs with time. The loss of effective area can be seen to have the greatest effect on the measured count rate at 0.277 keV, whilst becoming negligible around ~ 2 keV. Figure reproduced from The Chandra Proposers' Observatory Guide (Version 27.0 https://cxc.harvard.edu/proposer/POG/html/chap6.html)*

energies compared to the telescope at launch. This degradation in Chandra's response is accounted for in the source detection and photometry procedure via the effective exposure map, and thus are corrected for throughout chapter 4. Nonetheless, subtle changes in the response as a function of energy may alter the interpretation of source count rates, which require an assumed X-ray spectral model that differs from the assumption used in the generation of the exposure maps (a $\Gamma = 1.4$ power law). In this appendix, I thus explore in detail the extent of any differences on our estimated luminosities and interpretation of hardness ratios in chapter 4.

The degradation in the effective area of Chandra at soft energies means that the same number of detected counts (in a given exposure time) later in Chandra's observing lifetime will correspond to a higher intrinsic luminosity source. The bulk of this effect, however, is captured in our use of *effective exposure-corrected count rates* i.e. detected counts divided by the effective exposure map value.

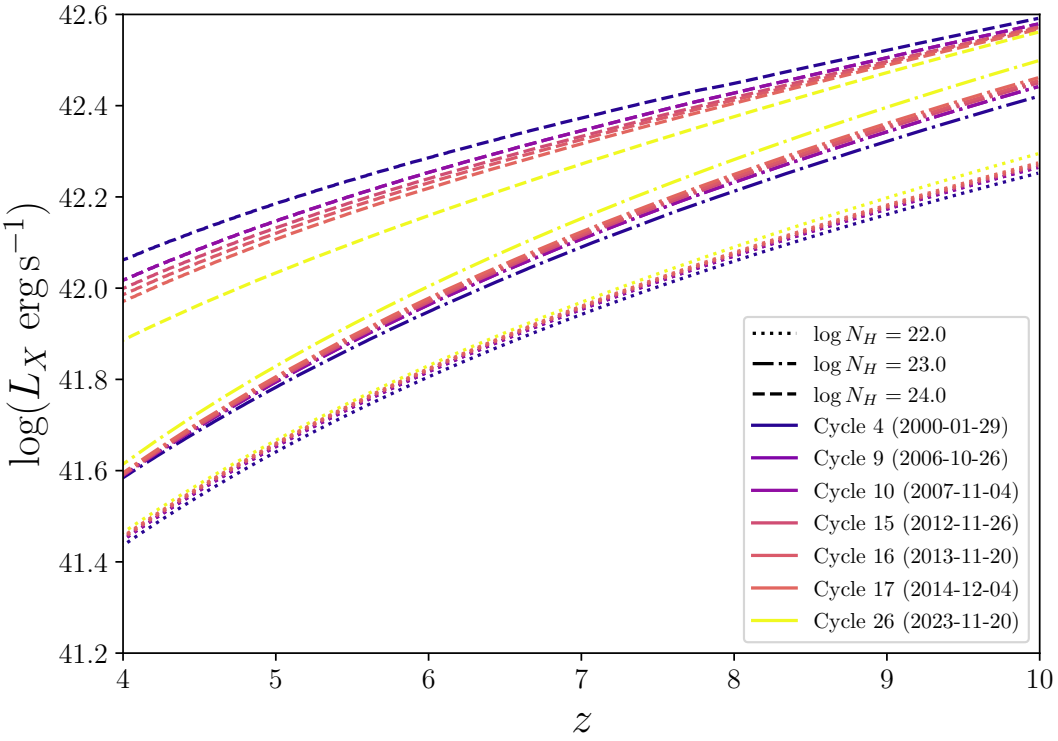

Figure C.2 *The luminosity of a source of* $N_{\rm H} = 10^{24}{\rm cm}^{-2}$ *(dashed),* $10^{23}{\rm cm}^{-2}$ *(dot-dashed)* $10^{22}{\rm cm}^{-2}$ *(dotted) and with an observed count rate of* 10^{-9} *cts* s^{-1} *cm*$^{-2}$*, for a given redshift. The conversion lines are plotted for different epochs of Chandra imaging (cycles) within the observing times of the C-COSMOS (cycles 9-10) and Chandra Legacy data (cycles 15-17) used in this thesis work as well as the instrument response shortly after launch (cycle 4) and as determined for the current observing epoch (cycle 26).*

Nonetheless, subtle differences may remain that depend on the precise shape of the X-ray spectrum of a source (compared the simple $\Gamma = 1.4$ adopted in the exposure map calculation); for our analysis we assume a source spectrum with $\Gamma = 1.9$ and an absorption turnover corresponding to different $N_{\rm H}$ values. As an absorbed power law drops off more steeply towards softer energies than the assumed $\Gamma = 1.4$—and it is at these soft energies that Chandra's response has degraded most substantially—the level of discrepancy may change over Chandra's lifetime. Figure C.2 shows the extent of the effect, indicating the intrinsic luminosity that would be inferred for a given (effective exposure-corrected) count rate for sources at different redshifts. Results are shown for a range of assumed intrinsic absorption columns: $N_{\rm H} = 10^{24}$ cm^{-2}, 10^{23} cm^{-2} and 10^{22} cm^{-2}. A fixed count rate corresponds to a higher intrinsic luminosity at higher redshift. Equally, assuming a larger intrinsic $N_{\rm H}$ means the same count rate indicates a higher

intrinsic L_X. In contrast, the change in the intrinsic luminosity corresponding to a fixed effective exposure-corrected count rate over different observing cycles is slight. For the less obscured spectral assumption (lower N_H) there is negligible change between epochs. For higher values of N_H the changes are more substantial as the loss of soft response has more of an impact. Nevertheless, over the period when the Chandra COSMOS observations were obtained (Cycle 9–17) the relative differences are minor.

The loss of soft band sensitivity will also affect Hardness Ratios as fewer soft band counts would be measured at a later observing epoch whilst the sensitivity to hard band counts suffers a negligible change. However, as my hardness ratios are based on *effective exposure-corrected* count rates the impact should be minimised. Figure C.3 shows how the predicted effective exposure-corrected HR values depend on redshift for different N_H (corresponding to the conditions for Unabsorbed, Absorbed and Compton Thick AGN) and for different Chandra cycles[1]. The change across the observing period of the imaging used in this work is minimal and will not result in a change to the number of source within each obscuration bin.

The Chandra imaging used in this work is comprised of C-COSMOS imaging (taken between December 2006 and June 2007) and Chandra Legacy imaging (taken between November 2012 and March 2014). As shown in figures C.2 and C.3, despite the loss of effective area at soft energies the change in the inferred L_X or N_H between epochs of the used Chandra imaging is minimal and the impact on my results is negligible. As the legacy imaging dominates the total Chandra survey time (2.8 Ms as compared to 1.8 Ms), I use the response at the epoch corresponding to the approximate middle of the legacy observing period (i.e. Cycle 16) throughout Chapter 4.

[1]See Chandra Proposers' Observatory Guide (Version 27.0 https://cxc.harvard.edu/proposer/POG/html/chap6.html)

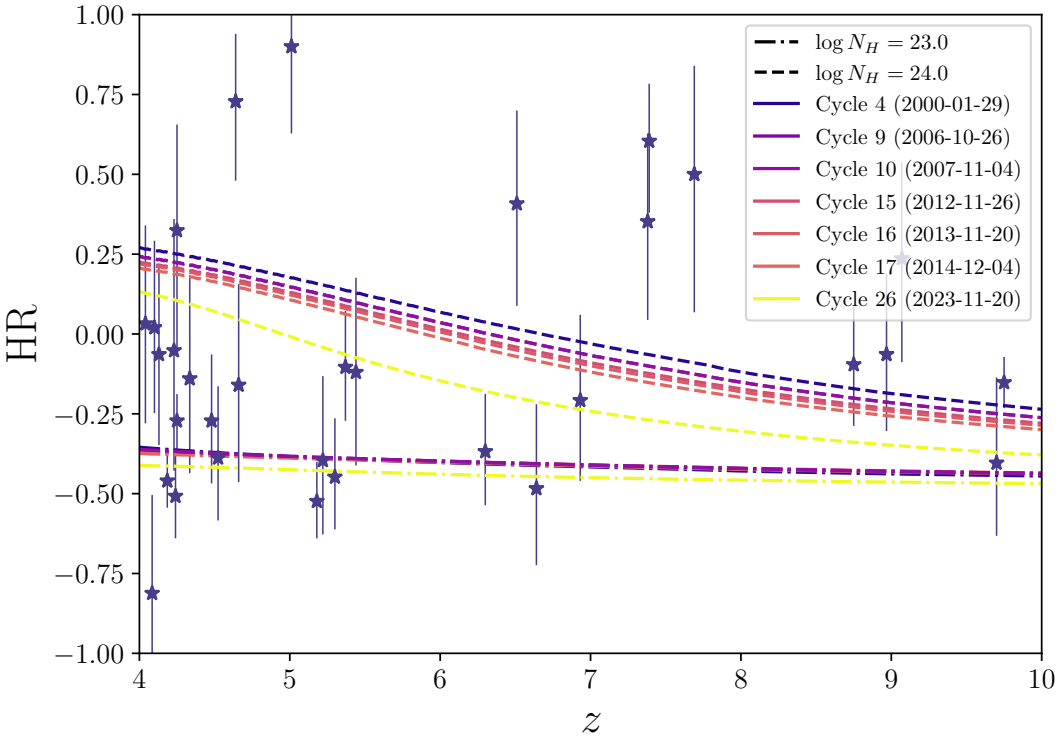

Figure C.3 *The BEHR-redshift plot, as in figure 4.13, with lines of constant* N_{H} *plotted for the Chandra responses at different epochs throughout the observing period of the C-COSMOS (cycles 9-10) and Chandra Legacy data (cycles 15-17) used in chapter 4 as well as the instrument response shortly after launch (cycle 4) and as determined for the current observing epoch (cycle 26). It can be seen that there is little change in the BEHR at a given redshift between the cycle responses of the imaging I use in this work, with the resulting sample of Unabsorbed, Absorbed and Compton Thick AGN remaining constant. Only with the most recent Chandra response can a difference in the samples be seen. Therefore the choice of Chandra response across the period of the imaging used will have a negligible effect on my results.*

Bibliography

Abbott B. P., et al., 2016, Physical Review Letters, 116, 061102

Aihara H., et al., 2019, Publications of the Astronomical Society of Japan, 71, 114

Aird J., et al., 2010, Monthly Notices of the Royal Astronomical Society, 401, 2531

Aird J., Coil A. L., Georgakakis A., Nandra K., Barro G., Pérez-González P. G., 2015, Monthly Notices of the Royal Astronomical Society, 451, 1892

Aird J., Coil A. L., Georgakakis A., 2017, Monthly Notices of the Royal Astronomical Society, 465, 3390

Aird J., Coil A. L., Georgakakis A., 2018, Monthly Notices of the Royal Astronomical Society, 474, 1225

Aird J., Coil A. L., Georgakakis A., 2019, Monthly Notices of the Royal Astronomical Society, 484, 4360

Alexander D. M., Hickox R. C., 2012, New Astronomy Reviews, 56, 93

Allard F., Homeier D., Freytag B., 2012, Philosophical Transactions of the Royal Society of London Series A, 370, 2765

Amaro-Seoane P., et al., 2017, Laser Interferometer Space Antenna, doi:10.48550/arXiv.1702.00786, https://ui.adsabs.harvard.edu/abs/2017arXiv170200786A

Ananna T. T., et al., 2019, The Astrophysical Journal, 871, 240

Angione R. J., 1973, AJ, 78, 353

Antonucci R., 1993, ARA&A, 31, 473

Arnaud K., Smith R., Siemiginowska A., 2011, Handbook of X-ray Astronomy. https://ui.adsabs.harvard.edu/abs/2011hxra.book.....A

Arnouts S., et al., 2002, Monthly Notices of the Royal Astronomical Society, 329, 355

Ashby M. L. N., et al., 2018, The Astrophysical Journal Supplement Series, 237, 39

Bailey M. E., Clube S. V. M., 1978, Nature, 275, 278

Baloković M., et al., 2018, The Astrophysical Journal, 854, 42

Bañados E., et al., 2015, The Astrophysical Journal, 804, 118

Bañados E., et al., 2016, The Astrophysical Journal Supplement Series, 227, 11

Bañados E., et al., 2018a, The Astrophysical Journal, 856, L25

Bañados E., Carilli C., Walter F., Momjian E., Decarli R., Farina E. P., Mazzucchelli C., Venemans B. P., 2018b, The Astrophysical Journal, 861, L14

Barbary K., 2016, The Journal of Open Source Software, 1, 58

Barcons X., et al., 2017, Astronomische Nachrichten, 338, 153

Barret D., et al., 2023, Experimental Astronomy, 55, 373

Barrow K. S. S., Aykutalp A., Wise J. H., 2018, Nature Astronomy, 2, 987

Barthelmy S., 2005, in APS April Meeting Abstracts. APS Meeting Abstracts. p. M9.004

Barvainis R., 1987, The Astrophysical Journal, 320, 537

Bavdaz M., et al., 2023, in Optics for EUV, X-Ray, and Gamma-Ray Astronomy XI. SPIE, p. 1267902, doi:10.1117/12.2678522, https://www.spiedigitallibrary.org/conference-proceedings-of-spie/12679/1267902/NewATHENA-optics-technology/10.1117/12.2678522.full

Bean R., Magueijo J., 2002, Phys. Rev. D, 66, 063505

Begelman M. C., 2010, Monthly Notices of the Royal Astronomical Society, 402, 673

Begelman M. C., Blandford R. D., Rees M. J., 1984, Reviews of Modern Physics, 56, 255

Begelman M. C., Volonteri M., Rees M. J., 2006, Monthly Notices of the Royal Astronomical Society, 370, 289

Beijersbergen M., Kraft S., Gunther R., Mieremet A. L., Collon M., Bavdaz M., Lumb D. H., Peacock A. J., 2004, in Hasinger G., Turner M. J. L., eds, Society of Photo-Optical Instrumentation Engineers (SPIE) Conference Series Vol. 5488, UV and Gamma-Ray Space Telescope Systems. pp 868–874, doi:10.1117/12.585122

Berdina L. A., Tsvetkova V. S., Shulga V. M., 2021, A&A, 645, A78

Bertin E., Arnouts S., 1996, Astronomy and Astrophysics Supplement Series, 117, 393

Blackburn J. K., Shaw R. A., Payne H. E., Hayes J. J. E., Heasarc 1999, Astrophysics Source Code Library, p. ascl:9912.002

Blandford R. D., McKee C. F., 1982, ApJ, 255, 419

Bogdan A., et al., 2023, Evidence for Heavy Seed Origin of Early Supermassive Black Holes from a Z˜10 X-ray Quasar, doi:10.48550/arXiv.2305.15458, https://ui.adsabs.harvard.edu/abs/2023arXiv230515458B

Bondi H., Hoyle F., 1944, Monthly Notices of the Royal Astronomical Society, 104, 273

Booth C. M., Schaye J., 2009, Monthly Notices of the Royal Astronomical Society, 398, 53

Bowler R. A. A., Jarvis M. J., Dunlop J. S., McLure R. J., McLeod D. J., Adams N. J., Milvang-Jensen B., McCracken H. J., 2020, Monthly Notices of the Royal Astronomical Society, 493, 2059

Boyle B. J., Terlevich R. J., 1998, Monthly Notices of the Royal Astronomical Society, 293, L49

Boyle B. J., Shanks T., Croom S. M., Smith R. J., Miller L., Loaring N., Heymans C., 2000, Monthly Notices of the Royal Astronomical Society, 317, 1014

Brammer G. B., van Dokkum P. G., Coppi P., 2008, The Astrophysical Journal, 686, 1503

Brandt W. N., Alexander D. M., 2015, Astronomy and Astrophysics Review, 23, 1

Brandt W. N., et al., 2002, The Astrophysical Journal, 569, L5

Brinch M., et al., 2023, The Astrophysical Journal, 943, 153

Brooks M., et al., 2024, Here There Be (Dusty) Monsters: High Redshift AGN are Dustier Than Their Hosts (arXiv:2410.07340), https://arxiv.org/abs/2410.07340

Brusa M., et al., 2009, The Astrophysical Journal, 693, 8

Bruzual G., Charlot S., 2003, Monthly Notices of the Royal Astronomical Society, 344, 1000

Buchner J., Salvato M., Budavári T., Fotopoulou S., 2021, Astrophysics Source Code Library, p. ascl:2102.014

Budavári T., Szalay A. S., 2008, The Astrophysical Journal, 679, 301

Burrows D. N., et al., 2005, Space Science Reviews, 120, 165

Cackett E. M., Bentz M. C., Kara E., 2021, iScience, 24, 102557

Camenzind M., 2007, Compact Objects in Astrophysics White Dwarfs, Neutron Stars, and Black Holes / Max Camenzind.. Astronomy and Astrophysics Library, Springer, Berlin ;

Cameron R. A., Morris D. C., Virani S. N., Wolk S. J., Blackwell W. C., Minow J. I., O'Dell S. L., 2002, in Bohlender D. A., Durand D., Handley T. H., eds, Astronomical Society of the Pacific Conference Series Vol. 281, Astronomical Data Analysis Software and Systems XI. p. 132

Capak P., et al., 2007, The Astrophysical Journal Supplement Series, 172, 99

Carilli C. L., Walter F., 2013, Annual Review of Astronomy and Astrophysics, 51, 105

Carnall A. C., et al., 2015, Monthly Notices of the Royal Astronomical Society, 451, L16

Carroll B. W., 2013, Introduction to Modern Astrophysics, An., 2nd ed. edn. Pearson Education UK

Carroll B. W., Ostlie D. A., 2017, An Introduction to Modern Astrophysics:, 2 edn. Cambridge University Press, doi:10.1017/9781108380980, https://www.cambridge.org/highereducation/books/an-introduction-to-modern-astrophysics/140DDF8A480C3841DCCD76D66984D858#contents

Chen Z.-F., Pan D.-S., Pang T.-T., Huang Y., 2018, The Astrophysical Journal Supplement Series, 234, 16

Christensen F. E., Ramsey B. D., 2022, X-Ray Optics for Astrophysics: A Historical Review, doi:10.1007/978-981-16-4544-0_1-1. , https://ui.adsabs.harvard.edu/abs/2022hxga.book..112C

Ciotti L., Pellegrini S., 2018, Proc. IAU, 14, 5

Civano F., et al., 2016, The Astrophysical Journal, 819, 62

Clark P. C., Glover S. C. O., Smith R. J., Greif T. H., Klessen R. S., Bromm V., 2011, Science, 331, 1040

Cole S., Lacey C., 1996, MNRAS, 281, 716

Collon M. J., et al., 2010, in Arnaud M., Murray S. S., Takahashi T., eds, Society of Photo-Optical Instrumentation Engineers (SPIE) Conference Series Vol. 7732, Space Telescopes and Instrumentation 2010: Ultraviolet to Gamma Ray. p. 77321F, doi:10.1117/12.858166

Combes F., Boisse P., Mazure A., Blanchard A., Seymour M., 2002, Galaxies and cosmology

Conroy C., Gunn J. E., 2010, The Astrophysical Journal, 712, 833

Conroy C., Gunn J. E., White M., 2009, The Astrophysical Journal, 699, 486

Costa T., Pakmor R., Springel V., 2020, Monthly Notices of the Royal Astronomical Society, 497, 5229

Costa T., Arrigoni Battaia F., Farina E. P., Keating L. C., Rosdahl J., Kimm T., 2022, Monthly Notices of the Royal Astronomical Society, 517, 1767

Coupon J., Czakon N., Bosch J., Komiyama Y., Medezinski E., Miyazaki S., Oguri M., 2018, Publications of the Astronomical Society of Japan, 70, S7

Dauser T., et al., 2019, Astronomy and Astrophysics, 630, A66

Davies R. I., et al., 2006, The Astrophysical Journal, 646, 754

Davies M. B., Miller M. C., Bellovary J. M., 2011, The Astrophysical Journal, 740, L42

Davis M., et al., 2007, The Astrophysical Journal, 660, L1

Delaney J. N., Aird J., Evans P. A., Barlow-Hall C., Osborne J. P., Watson M. G., 2023, Monthly Notices of the Royal Astronomical Society, 521, 1620

Despali G., Giocoli C., Angulo R. E., Tormen G., Sheth R. K., Baso G., Moscardini L., 2016, Monthly Notices of the Royal Astronomical Society, 456, 2486

Do T., et al., 2019, Science, 365, 664

Dolgov A. D., 2018, Physics Uspekhi, 61, 115

Donnan C. T., et al., 2023a, Monthly Notices of the Royal Astronomical Society, 518, 6011

Donnan C. T., McLeod D. J., McLure R. J., Dunlop J. S., Carnall A. C., Cullen F., Magee D., 2023b, Monthly Notices of the Royal Astronomical Society, 520, 4554

Donnan C. T., et al., 2024, JWST PRIMER: A New Multi-Field Determination of the Evolving Galaxy UV Luminosity Function at Redshifts $\mathbf{z \simeq 9-15}$, doi:10.48550/arXiv.2403.03171, https://ui.adsabs.harvard.edu/abs/2024arXiv240303171D

Edgar R. G., 2004, New Astronomy Reviews, 48, 843

Einstein A., 1916, Annalen der Physik, 354, 769

Eisenstein D. J., et al., 2023, Overview of the JWST Advanced Deep Extragalactic Survey (JADES), doi:10.48550/arXiv.2306.02465, https://ui.adsabs.harvard.edu/abs/2023arXiv230602465E

Elvis M., Schreier E. J., Tonry J., Davis M., Huchra J. P., 1981, The Astrophysical Journal, 246, 20

Elvis M., et al., 2009, The Astrophysical Journal Supplement Series, 184, 158

Evans P. A., et al., 2020, The Astrophysical Journal Supplement Series, 247, 54

Event Horizon Telescope Collaboration et al., 2019a, ApJ, 875, L2

Event Horizon Telescope Collaboration et al., 2019b, ApJ, 875, L3

Event Horizon Telescope Collaboration et al., 2019c, ApJ, 875, L4

Event Horizon Telescope Collaboration et al., 2022, The Astrophysical Journal, 930, L16

Fabian A. C., 2012, Annual Review of Astronomy and Astrophysics, 50, 455

Fabian A. C., Lasenby A. N., 2019, Astrophysical Black Holes, doi:10.48550/arXiv.1911.04305, https://ui.adsabs.harvard.edu/abs/2019arXiv191104305F

Fabian A. C., Lohfink A., Kara E., Parker M. L., Vasudevan R., Reynolds C. S., 2015, Monthly Notices of the Royal Astronomical Society, 451, 4375

Finkelstein S. L., et al., 2017, JWST Proposal ID 1345. Cycle 0 Early Release Science, p. 1345

Finkelstein S. L., et al., 2022, The Astrophysical Journal, 940, L55

Freedman R. A., 2014, Universe, 10th ed. edn. W.H. Freeman and Company, New York

Freeman P. E., Kashyap V., Rosner R., Lamb D. Q., 2002, The Astrophysical Journal Supplement Series, 138, 185

Fruscione A., Burke D., Siemiginowska A., 2009, Chandra News, 16, 26

Fujimoto S., et al., 2023, UNCOVER: A NIRSpec Census of Lensed Galaxies at Z=8.50-13.08 Probing a High AGN Fraction and Ionized Bubbles in the Shadow, doi:10.48550/arXiv.2308.11609, https://ui.adsabs.harvard.edu/abs/2023arXiv230811609F

Gabriel C., Ibarra Ibaibarriaga A., Hoar J., 2005, in Siegmund O. H. W., ed., Society of Photo-Optical Instrumentation Engineers (SPIE) Conference Series Vol. 5898, UV, X-Ray, and Gamma-Ray Space Instrumentation for Astronomy XIV. pp 469–478, doi:10.1117/12.613895

Gaia Collaboration et al., 2016, Astronomy and Astrophysics, 595, A2

Garmire G. P., Bautz M. W., Ford P. G., Nousek J. A., Ricker George R. J., 2003, in Truemper J. E., Tananbaum H. D., eds, Society of Photo-Optical Instrumentation Engineers (SPIE) Conference Series Vol. 4851, X-Ray and Gamma-Ray Telescopes and Instruments for Astronomy.. pp 28–44, doi:10.1117/12.461599

Gehrels N., 1986, The Astrophysical Journal, 303, 336

Gehrels N., et al., 2004, The Astrophysical Journal, 611, 1005

Georgakakis A., Nandra K., Laird E. S., Aird J., Trichas M., 2008, Monthly Notices of the Royal Astronomical Society, 388, 1205

Georgakakis A., et al., 2015, Monthly Notices of the Royal Astronomical Society, 453, 1946

Georgakakis A., Aird J., Schulze A., Dwelly T., Salvato M., Nandra K., Merloni A., Schneider D. P., 2017, Monthly Notices of the Royal Astronomical Society, 471, 1976

Giacconi R., Kellogg E., Gorenstein P., Gursky H., Tananbaum H., 1971, The Astrophysical Journal, 165, L27

Gilli R., Comastri A., Hasinger G., 2007, Astronomy and Astrophysics, 463, 79

Gilli R., et al., 2022, Astronomy and Astrophysics, 666, A17

Grant C. E., Bautz M. W., Virani S. N., 2002, in Schlegel E. M., Vrtilek S. D., eds, Astronomical Society of the Pacific Conference Series Vol. 262, The High Energy Universe at Sharp Focus: Chandra Science. p. 401 (arXiv:astro-ph/0202086), doi:10.48550/arXiv.astro-ph/0202086

Grant C. E., Bautz M. W., Kissel S. E., LaMarr B., Prigozhin G. Y., 2006, in Dorn D. A., Holland A. D., eds, Society of Photo-Optical Instrumentation Engineers (SPIE) Conference Series Vol. 6276, High Energy, Optical, and Infrared Detectors for Astronomy II. p. 62761O (arXiv:astro-ph/0606178), doi:10.1117/12.672019

Grant C. E., Bautz M. W., Plucinsky P. P., Ford P. G., 2024, in den Herder J.-W. A., Nikzad S., Nakazawa K., eds, Society of Photo-Optical Instrumentation Engineers (SPIE) Conference Series Vol. 13093, Space Telescopes and Instrumentation 2024: Ultraviolet to Gamma Ray. p. 130931E (arXiv:2406.18395), doi:10.1117/12.3018498

Greene J., et al., 2019, Bulletin of the American Astronomical Society, 51, 83

Greene J. E., Strader J., Ho L. C., 2020, Annual Review of Astronomy and Astrophysics, 58, 257

Greene J. E., et al., 2023, UNCOVER Spectroscopy Confirms a Surprising Ubiquity of AGN in Red Galaxies at $z>5$, doi:10.48550/arXiv.2309.05714, https://ui.adsabs.harvard.edu/abs/2023arXiv230905714G

Greif T. H., 2015, Computational Astrophysics and Cosmology, 2, 3

Greiner J., Cuby J. G., McCaughrean M. J., 2001, Nature, 414, 522

Guetzoyan P., Aird J., Georgakakis A., Coil A. L., Barlow-Hall C., Hickox R. C., Rankine A. L., Terrazas B. A., 2024, X-Ray AGN in Boötes: Black Hole - Galaxy Assembly in Massive Populations, doi:10.48550/arXiv.2408.14297, https://ui.adsabs.harvard.edu/abs/2024arXiv240814297G

Gültekin K., et al., 2009, ApJ, 698, 198

Gunn J. E., 1978, Physica Scripta, 17, 277

HI4PI Collaboration et al., 2016, Astronomy and Astrophysics, 594, A116

Haiman Z., Thoul A. A., Loeb A., 1996, The Astrophysical Journal, 464, 523

Hale C. L., et al., 2021, Publications of the Astronomical Society of Australia, 38, e058

Harrison C., 2014, PhD thesis, Durham University

Harrison C. M., 2017, Nature Astronomy, 1, 0165

Hasinger G., Miyaji T., Schmidt M., 2005, Astronomy and Astrophysics, 441, 417

Hawking S. W., 1965, Physical Review Letters, 15, 689

Heckman T. M., Best P. N., 2014, Annual Review of Astronomy and Astrophysics, 52, 589

Heger A., Woosley S. E., 2002, The Astrophysical Journal, 567, 532

Hickox R. C., Alexander D. M., 2018, Annual Review of Astronomy and Astrophysics, 56, 625

Hicks E. K. S., Malkan M. A., 2008, The Astrophysical Journal Supplement Series, 174, 31

Hirano S., Hosokawa T., Yoshida N., Umeda H., Omukai K., Chiaki G., Yorke H. W., 2014, The Astrophysical Journal, 781, 60

Ho L. C., 2009, ApJ, 699, 638

Hogg D. W., 2001, AJ, 121, 1207

Hopkins P. F., Richards G. T., Hernquist L., 2007, The Astrophysical Journal, 654, 731

Ilbert O., et al., 2006, Astronomy and Astrophysics, 457, 841

Ilbert O., et al., 2009, The Astrophysical Journal, 690, 1236

Ilbert O., et al., 2013, Astronomy and Astrophysics, 556, A55

Inayoshi K., Visbal E., Haiman Z., 2020, Annual Review of Astronomy and Astrophysics, 58, 27

Jin C., Done C., Ward M., Gardner E., 2017, MNRAS, 471, 706

Johnson J. L., 2013, in Wiklind T., Mobasher B., Bromm V., eds, Astrophysics and Space Science Library Vol. 396, The First Galaxies. p. 177 (arXiv:1105.5701), doi:10.1007/978-3-642-32362-1_4

Kalfountzou E., Civano F., Elvis M., Trichas M., Green P., 2014, Monthly Notices of the Royal Astronomical Society, 445, 1430

Katz H., Sijacki D., Haehnelt M. G., 2015, Monthly Notices of the Royal Astronomical Society, 451, 2352

Kerr R. P., 1963, Physical Review Letters, 11, 237

Khorunzhev G. A., et al., 2021, Astronomy Letters, 47, 123

Klessen R. S., Glover S. C. O., 2023, Annual Review of Astronomy and Astrophysics, 61, 65

Kocevski D. D., et al., 2018, ApJS, 236, 48

Kocevski D. D., et al., 2024, arXiv e-prints, p. arXiv:2404.03576

Kokorev V., et al., 2024, A Census of Photometrically Selected Little Red Dots at 4 < z < 9 in JWST Blank Fields (arXiv:2401.09981), http://arxiv.org/abs/2401.09981

Komossa S., Voges W., Xu D., Mathur S., Adorf H.-M., Lemson G., Duschl W. J., Grupe D., 2006, AJ, 132, 531

Kormendy J., Ho L. C., 2013, Annual Review of Astronomy and Astrophysics, 51, 511

Kormendy J., Richstone D., 1995, ARA&A, 33, 581

Koushiappas S. M., Bullock J. S., Dekel A., 2004, Monthly Notices of the Royal Astronomical Society, 354, 292

Kovács O. E., et al., 2024, The Astrophysical Journal, 965, L21

Kraft S., et al., 2005, in Citterio O., O'Dell S. L., eds, Society of Photo-Optical Instrumentation Engineers (SPIE) Conference Series Vol. 5900, Optics for EUV, X-Ray, and Gamma-Ray Astronomy II. pp 297–308, doi:10.1117/12.638934

Kudritzki R.-P., Puls J., 2000, Annual Review of Astronomy and Astrophysics, 38, 613

Kuhn L., et al., 2024, Astronomy and Astrophysics, 684, A52

Laigle C., et al., 2016, The Astrophysical Journal Supplement Series, 224, 24

Laird E. S., et al., 2009, The Astrophysical Journal Supplement Series, 180, 102

Laloux B., et al., 2023, Monthly Notices of the Royal Astronomical Society, 518, 2546

Laloux B., et al., 2024, Accretion Properties of X-ray AGN: Evidence for Radiation-Regulated Obscuration with Redshift-Dependent Host Galaxy Contribution, doi:10.48550/arXiv.2403.07109, https://ui.adsabs.harvard.edu/abs/2024arXiv240307109L

Lang D., Hogg D. W., Mykytyn D., 2016, Astrophysics Source Code Library, p. ascl:1604.008

Larson R. B., 1998, Monthly Notices of the Royal Astronomical Society, 301, 569

Larson R. L., et al., 2023, The Astrophysical Journal, 953, L29

Lawrence A., 1991, Monthly Notices of the Royal Astronomical Society, 252, 586

Lawrence A., 2007, in Karas V., Matt G., eds, IAU Symposium Vol. 238, Black Holes from Stars to Galaxies – Across the Range of Masses. pp 117–122, doi:10.1017/S1743921307004814

Le Fèvre O., et al., 2020, Astronomy and Astrophysics, 643, A1

Liddle A. R., 2015, An introduction to modern cosmology, Third Edition

Liu H., Luo B., Brandt W. N., Brotherton M. S., Gallagher S. C., Ni Q., Shemmer O., Timlin III J. D., 2021, The Astrophysical Journal, 910, 103

Longair M. S., ed. 1998, Galaxy formation

Luo B., et al., 2017, The Astrophysical Journal Supplement Series, 228, 2

Lusso E., Risaliti G., 2016, The Astrophysical Journal, 819, 154

Lusso E., Valiante R., Vito F., 2023, The Dawn of Black Holes, doi:10.1007/978-981-16-4544-0_116-1. , https://ui.adsabs.harvard.edu/abs/2023hxga.book..122L

Lynden-Bell D., 1969, Nature, 223, 690

Machalski J., 1998, Astronomy and Astrophysics Supplement Series, 128, 153

Madau P., Dickinson M., 2014, Annual Review of Astronomy and Astrophysics, 52, 415

Madau P., Rees M. J., 2001, The Astrophysical Journal, 551, L27

Madsen K., et al., 2011, in AAS/High Energy Astrophysics Division #12. p. 43.08

Magdziarz P., Zdziarski A. A., 1995, Monthly Notices of the Royal Astronomical Society, 273, 837

Maio U., Borgani S., Ciardi B., Petkova M., 2019, Publications of the Astronomical Society of Australia, 36, e020

Maiolino R., et al., 2023, JADES. The Diverse Population of Infant Black Holes at 4, doi:10.48550/arXiv.2308.01230, https://ui.adsabs.harvard.edu/abs/2023arXiv230801230M

Maiolino R., et al., 2024, JWST meets Chandra: a large population of Compton thick, feedback-free, and intrinsically X-ray weak AGN, with a sprinkle of SNe (arXiv:2405.00504), https://arxiv.org/abs/2405.00504

Marchesi S., et al., 2016, The Astrophysical Journal, 827, 150

Margon B., 1984, Annual Review of Astronomy and Astrophysics, 22, 507

Marinucci A., et al., 2022, Monthly Notices of the Royal Astronomical Society, 516, 5907

Marshall N., Warwick R. S., Pounds K. A., 1981, MNRAS, 194, 987

Matsuoka Y., et al., 2023, The Astrophysical Journal, 949, L42

Matthee J., et al., 2024, The Astrophysical Journal, 963, 129

Mayer L., 2019, Super-Eddington Accretion; Flow Regimes and Conditions in High-z Galaxies, doi:10.1142/9789813227958_0011. , https://ui.adsabs.harvard.edu/abs/2019ffbh.book..195M

McConnell N. J., Ma C.-P., 2013, ApJ, 764, 184

McCracken H. J., et al., 2012, Astronomy and Astrophysics, 544, A156

McLure R. J., Dunlop J. S., 2004, Monthly Notices of the Royal Astronomical Society, 352, 1390

Medvedev P., et al., 2020, Monthly Notices of the Royal Astronomical Society, 497, 1842

Miyaji T., Hasinger G., Schmidt M., 2001, Astronomy and Astrophysics, 369, 49

Miyoshi M., Moran J., Herrnstein J., Greenhill L., Nakai N., Diamond P., Inoue M., 1995, Nature, 373, 127

Moffat J. W., 2020, arXiv e-prints, p. arXiv:2011.13440

Moneti A., et al., 2023, VizieR Online Data Catalog, 2373, II/373

Mukhanov V., 2005, Physical Foundations of Cosmology, doi:10.2277/0521563984.

Muzzin A., et al., 2013, The Astrophysical Journal Supplement Series, 206, 8

Nakauchi D., Inayoshi K., Omukai K., 2020, The Astrophysical Journal, 902, 81

Nandra K., et al., 2013, arXiv e-prints

Nandra K., et al., 2015, The Astrophysical Journal Supplement Series, 220, 10

Nanni R., Vignali C., Gilli R., Moretti A., Brandt W. N., 2017, Astronomy and Astrophysics, 603, A128

Netzer H., 2013, The Physics and Evolution of Active Galactic Nuclei. Cambridge University Press, New York, UNITED STATES, http://ebookcentral.proquest.com/lib/ed/detail.action?docID=1113069

Netzer H., 2015, Annual Review of Astronomy and Astrophysics, 53, 365

Ni Y., Di Matteo T., Gilli R., Croft R. A. C., Feng Y., Norman C., 2020, Monthly Notices of the Royal Astronomical Society, 495, 2135

O'Dell S. L., et al., 2000, in Flanagan K. A., Siegmund O. H., eds, Society of Photo-Optical Instrumentation Engineers (SPIE) Conference Series Vol. 4140, X-Ray and Gamma-Ray Instrumentation for Astronomy XI. pp 99–110, doi:10.1117/12.409104

O'Dell S. L., et al., 2003, in Truemper J. E., Tananbaum H. D., eds, Society of Photo-Optical Instrumentation Engineers (SPIE) Conference Series Vol. 4851, X-Ray and Gamma-Ray Telescopes and Instruments for Astronomy.. pp 77–88, doi:10.1117/12.461493

O'Dell S. L., et al., 2005, in Siegmund O. H. W., ed., Society of Photo-Optical Instrumentation Engineers (SPIE) Conference Series Vol. 5898, UV, X-Ray, and Gamma-Ray Space Instrumentation for Astronomy XIV. pp 212–223, doi:10.1117/12.619442

O'Dell S. L., et al., 2007, in Siegmund O. H., ed., Society of Photo-Optical Instrumentation Engineers (SPIE) Conference Series Vol. 6686, UV, X-Ray, and Gamma-Ray Space Instrumentation for Astronomy XV. p. 668603, doi:10.1117/12.734594

Onken C. A., et al., 2007, ApJ, 670, 105

Onodera M., et al., 2012, The Astrophysical Journal, 755, 26

Oppenheimer J. R., Snyder H., 1939, Physical Review, 56, 455

Orofino M. C., Ferrara A., Gallerani S., 2018, Monthly Notices of the Royal Astronomical Society, 480, 681

Padovani P., et al., 2017, Astronomy and Astrophysics Review, 25, 2

Page M. J., et al., 1996, Monthly Notices of the Royal Astronomical Society, 281, 579

Pâris I., et al., 2017, Astronomy and Astrophysics, 597, A79

Pâris I., et al., 2018, Astronomy and Astrophysics, 613, A51

Park T., Kashyap V. L., Siemiginowska A., van Dyk D. A., Zezas A., Heinke C., Wargelin B. J., 2006, The Astrophysical Journal, 652, 610

Peebles P. J. E., Page Lyman A. J., Partridge R. B., 2009, Finding the Big Bang

Peterson B. M., 1993, PASP, 105, 247

Pickles A. J., 1998, Publications of the Astronomical Society of the Pacific, 110, 863

Pierre M., et al., 2016, Astronomy and Astrophysics, 592, A1

Planck Collaboration et al., 2014, A&A, 571, A1

Polletta M., et al., 2007, The Astrophysical Journal, 663, 81

Pons E., McMahon R. G., Banerji M., Reed S. L., 2020, Monthly Notices of the Royal Astronomical Society, 491, 3884

Pouliasis E., et al., 2024, AGN X-ray Luminosity Function and Absorption Function in the Early Universe ($3\leq z \leq 6$), doi:10.48550/arXiv.2401.13515, https://ui.adsabs.harvard.edu/abs/2024arXiv240113515P

Predehl P., et al., 2021, Astronomy and Astrophysics, 647, A1

Ranalli P., Comastri A., Setti G., 2005, Astronomy and Astrophysics, 440, 23

Rau A., et al., 2013, The Hot and Energetic Universe: The Wide Field Imager (WFI) for Athena+, doi:10.48550/arXiv.1308.6785, https://ui.adsabs.harvard.edu/abs/2013arXiv1308.6785R

Rau A., et al., 2016, in den Herder J.-W. A., Takahashi T., Bautz M., eds, Society of Photo-Optical Instrumentation Engineers (SPIE) Conference Series Vol. 9905, Space Telescopes and Instrumentation 2016: Ultraviolet to Gamma Ray. p. 99052B (arXiv:1607.00878), doi:10.1117/12.2235268

Reed S. L., et al., 2019, Monthly Notices of the Royal Astronomical Society, 487, 1874

Rees M. J., 1984, Annual Review of Astronomy and Astrophysics, 22, 471

Reines A. E., Comastri A., 2016, Publications of the Astronomical Society of Australia, 33, e054

Reynolds C. S., et al., 2023, in Siegmund O. H., Hoadley K., eds, Society of Photo-Optical Instrumentation Engineers (SPIE) Conference Series Vol. 12678, UV, X-Ray, and Gamma-Ray Space Instrumentation for Astronomy XXIII. p. 126781E (arXiv:2311.00780), doi:10.1117/12.2677468

Robbins M., 2014, Final Test Guideline

Roming P. W. A., et al., 2005, Space Sci. Rev., 120, 95

Ross N. P., Cross N. J. G., 2020, MNRAS, 494, 789

Ross N. P., et al., 2013, The Astrophysical Journal, 773, 14

Salvato M., et al., 2009, The Astrophysical Journal, 690, 1250

Salvato M., et al., 2011, The Astrophysical Journal, 742, 61

Salvato M., et al., 2018, Monthly Notices of the Royal Astronomical Society, 473, 4937

Sanders D. B., et al., 2007, The Astrophysical Journal Supplement Series, 172, 86

Sawicki M., et al., 2019, Monthly Notices of the Royal Astronomical Society, 489, 5202

Schlafly E. F., Finkbeiner D. P., 2011, The Astrophysical Journal, 737, 103

Schleicher D. R. G., Galli D., Glover S. C. O., Banerjee R., Palla F., Schneider R., Klessen R. S., 2009, The Astrophysical Journal, 703, 1096

Schmidt M., 1968, ApJ, 151, 393

Schmidt M., Schneider D. P., Gunn J. E., 1995, AJ, 110, 68

Scholtz J., et al., 2023, JADES: A Large Population of Obscured, Narrow Line AGN at High Redshift, doi:10.48550/arXiv.2311.18731, https://ui.adsabs.harvard.edu/abs/2023arXiv231118731S

Schulz H., Komossa S., 1999, arXiv e-prints, pp astro–ph/9905118

Scoville N., et al., 2007, The Astrophysical Journal Supplement Series, 172, 1

Selsing J., Fynbo J. P. U., Christensen L., Krogager J. K., 2016, A&A, 585, A87

Seward F. D., Charles P. A., 2010, Exploring the X-ray Universe. https://ui.adsabs.harvard.edu/abs/2010exru.book.....S

Seyfert C. K., 1943, ApJ, 97, 28

Shakura N. I., 1973, Soviet Ast., 16, 756

Sharma R., Sharma M., 2024, The Origin of Supermassive Black Holes at Cosmic Dawn (arXiv:2310.06898), http://arxiv.org/abs/2310.06898

Shen Y., 2013, Bulletin of the Astronomical Society of India, 41, 61

Shen X., Hopkins P. F., Faucher-Giguère C.-A., Alexander D. M., Richards G. T., Ross N. P., Hickox R. C., 2020, Monthly Notices of the Royal Astronomical Society, 495, 3252

Shuntov M., et al., 2022, Astronomy and Astrophysics, 664, A61

Sillassen N. B., et al., 2022, Astronomy and Astrophysics, 665, L7

Simon S. H., 2013, The Oxford Solid State Basics. https://ui.adsabs.harvard.edu/abs/2013ossb.book.....S

Singha M., et al., 2022, Astronomy and Astrophysics, 659, A123

Soltan A., 1982, Monthly Notices of the Royal Astronomical Society, 200, 115

Somerville R. S., Davé R., 2015, Annual Review of Astronomy and Astrophysics, 53, 51

Somerville R. S., Hopkins P. F., Cox T. J., Robertson B. E., Hernquist L., 2008, Monthly Notices of the Royal Astronomical Society, 391, 481

Subramanian K., 2016, Reports on Progress in Physics, 79, 076901

Sunyaev R., et al., 2021, A&A, 656, A132

Szalay A. S., Connolly A. J., Szokoly G. P., 1999, The Astronomical Journal, 117, 68

Tagliacozzo D., et al., 2023, Monthly Notices of the Royal Astronomical Society, 525, 4735

Tanaka Y., et al., 1995, Nature, 375, 659

Tananbaum H., et al., 1979, ApJ, 234, L9

Tang J.-J., et al., 2019, MNRAS, 484, 2575

Taniguchi Y., et al., 2015, Publications of the Astronomical Society of Japan, 67, 104

Tashiro M. S., 2022, International Journal of Modern Physics D, 31, 2230001

Tegmark M., Silk J., Rees M. J., Blanchard A., Abel T., Palla F., 1997, The Astrophysical Journal, 474, 1

Thomas D., Maraston C., Schawinski K., Sarzi M., Silk J., 2010, Monthly Notices of the Royal Astronomical Society, 404, 1775

Tinker J., Kravtsov A. V., Klypin A., Abazajian K., Warren M., Yepes G., Gottlöber S., Holz D. E., 2008, ApJ, 688, 709

Tombesi F., Tazaki F., Mushotzky R. F., Ueda Y., Cappi M., Gofford J., Reeves J. N., Guainazzi M., 2014, Monthly Notices of the Royal Astronomical Society, 443, 2154

Trakhtenbrot B., et al., 2016, ApJ, 825, 4

Trinca A., Schneider R., Valiante R., Graziani L., Ferrotti A., Omukai K., Chon S., 2024, Monthly Notices of the Royal Astronomical Society, 529, 3563

Ueda Y., Akiyama M., Hasinger G., Miyaji T., Watson M. G., 2014, ApJ, 786, 104

Urry C. M., Padovani P., 1995, Publications of the Astronomical Society of the Pacific, 107, 803

Vestergaard M., Osmer P. S., 2009, The Astrophysical Journal, 699, 800

Vestergaard M., Peterson B. M., 2006, The Astrophysical Journal, 641, 689

Vignali C., Brandt W. N., Fan X., Gunn J. E., Kaspi S., Schneider D. P., Strauss M. A., 2001, AJ, 122, 2143

Vito F., Gilli R., Vignali C., Comastri A., Brusa M., Cappelluti N., Iwasawa K., 2014, Monthly Notices of the Royal Astronomical Society, 445, 3557

Vito F., et al., 2018, Monthly Notices of the Royal Astronomical Society, 473, 2378

Vito F., et al., 2019, A&A, 630, A118

Volonteri M., Begelman M. C., 2010, MNRAS, 409, 1022

Wang F., et al., 2019, ApJ, 884, 30

Warren S. J., Hewett P. C., Osmer P. S., 1991, ApJS, 76, 23

Weaver J. R., et al., 2022, The Astrophysical Journal Supplement Series, 258, 11

Weaver J., Zalesky L., Allen N., Taamoli S., 2023, Astrophysics Source Code Library, p. ascl:2312.016

Weisskopf M. C., Brinkman B., Canizares C., Garmire G., Murray S., Van Speybroeck L. P., 2002, Publications of the Astronomical Society of the Pacific, 114, 1

Wells A., et al., 1992, in Hoover R. B., ed., Society of Photo-Optical Instrumentation Engineers (SPIE) Conference Series Vol. 1546, Multilayer and Grazing Incidence X-Ray/EUV Optics. pp 205–220, doi:10.1117/12.51259

Wenger M., et al., 2000, A&AS, 143, 9

Whalen D. J., Fryer C. L., 2012, The Astrophysical Journal, 756, L19

White S. D. M., Rees M. J., 1978, MNRAS, 183, 341

Widrow L. M., 2002, Reviews of Modern Physics, 74, 775

Wilkins D. R., 2023, Monthly Notices of the Royal Astronomical Society, 526, 3441

Willingale R., Pareschi G., Christensen F., den Herder J.-W., 2013, The Hot and Energetic Universe: The Optical Design of the Athena+ Mirror, doi:10.48550/arXiv.1307.1709, https://ui.adsabs.harvard.edu/abs/2013arXiv1307.1709W

Willott C. J., et al., 2010, The Astronomical Journal, 140, 546

Wise M., 1997, Chandra News, 5, 22

Wise J. H., Regan J. A., O'Shea B. W., Norman M. L., Downes T. P., Xu H., 2019, Nature, 566, 85

Wolf J., et al., 2021, A&A, 647, A5

Wolf J., et al., 2022, arXiv e-prints, p. arXiv:2211.13820

Wolter H., 1952, Annalen der Physik, 445, 94

Woods T. E., et al., 2019, Publications of the Astronomical Society of Australia, 36, e027

Woosley S. E., Weaver T. A., 1995, ApJS, 101, 181

Xue Y. Q., 2017, New Astronomy Reviews, 79, 59

Yang G., et al., 2023, The Astrophysical Journal, 950, L5

Yue M., et al., 2024, The Astrophysical Journal, 966, 176

Zhu Q., Li Y., Li Y., Maji M., Yajima H., Schneider R., Hernquist L., 2020, arXiv e-prints, p. arXiv:2012.01458

Zhu Q., Li Y., Li Y., Maji M., Yajima H., Schneider R., Hernquist L., 2022, Monthly Notices of the Royal Astronomical Society, 514, 5583

Zhu P., Kewley L. J., Sutherland R. S., 2023, The Astrophysical Journal, 954, 175

Zoglauer A., et al., 2011, in AAS/High Energy Astrophysics Division #12. p. 43.07

Zubovas K., King A., 2021, MNRAS, 501, 4289

de Graaff A., et al., 2024, arXiv e-prints, p. arXiv:2409.05948

van Paradijs J., Kouveliotou C., Wijers R. A. M. J., 2000, ARA&A, 38, 379